UNIVERSIDAD DE OVIEDO

Programa de Doctorado en Materiales

DESIGN OF SEMICONDUCTOR PHOTOCATALYSTS FOR POLLUTANT DEGRADATION AND SELECTIVE CONVERSION OF BIOMASS-DERIVED COMPOUNDS

DISEÑO DE FOTOCATALIZADORES SEMICONDUCTORES PARA LA DEGRADACIÓN DE CONTAMINANTES Y LA CONVERSIÓN SELECTIVA DE COMPUESTOS DERIVADOS DE BIOMASA
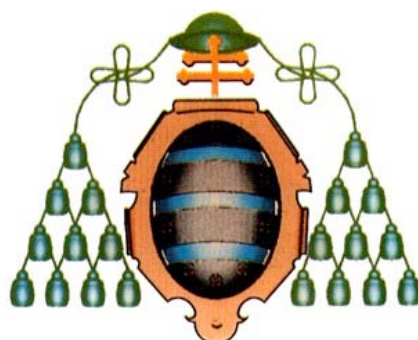
TESIS DOCTORAL

Igor Krivtsov

Mayo 2017

UNIVERSIDAD DE OVIEDO

Programa de Doctorado en Materiales

DESIGN OF SEMICONDUCTOR PHOTOCATALYSTS FOR POLLUTANT DEGRADATION AND SELECTIVE CONVERSION OF BIOMASS-DERIVED COMPOUNDS

DISEÑO DE FOTOCATALIZADORES SEMICONDUCTORES PARA LA DEGRADACIÓN DE CONTAMINANTES Y LA CONVERSIÓN SELECTIVA DE COMPUESTOS DERIVADOS DE BIOMASA

TESIS DOCTORAL

Directores: Prof. José Rubén García Menéndez

Prof. Salvador Ordóñez García

RESUMEN DEL CONTENIDO DE TESIS DOCTORAL

1.- Título de la Tesis	
Español: Diseño de fotocatalizadores semiconductores para la degradación de contaminantes y la conversión selectiva de compuestos derivados de biomasa	**Inglés:** Design of Semiconductor Photocatalysts for Pollutant Degradation and Selective Conversion of Biomass-Derived Compounds.

2.- Autor	
Nombre: Igor Krivtsov	DNI/Pasaporte/NIE:
Programa de Doctorado: Materiales (RD 99)	
Órgano responsable: Departamento de Ciencia de los Materiales e Ingeniería Metalúrgica	

RESUMEN (en español)

En la presente Tesis Doctoral se han desarrollado métodos para la modificación sintética y post-sintética de fotocatalizadores basados en dióxido de titanio y en nitruro de carbono.

Se han sintetizado materiales compuestos sílica-titania que mejoran el comportamiento foto-destructivo del dióxido de titanio. La presencia de óxido de silicio disminuye la velocidad de la cristalización de la titania, favoreciendo el crecimiento cristalino y la hidroxilación superficial de los *composites* SiO_2–TiO_2. Tanto la cristalinidad como la funcionalización de la superficie, con separación de carga más eficiente y adsorción de contaminantes en la proximidad de los centros fotoactivos, contribuyen al aumento en la actividad foto-catalítica de los nuevos materiales, que presentan una velocidad de degradación del azul de metileno bajo radiación ultravioleta (UV) superior a la del foto-catalizador comercial TiO_2-P25.

Se ha desarrollado un nuevo procedimiento de síntesis de titania que, basado en el intercambio de disolventes, incluye la precipitación de peroxotitanato de amonio. Las nanopartículas obtenidas poseen una estabilidad térmica sin precedentes de la fase anatasa, permaneciendo exentas de fase rutilo hasta 1000 ºC. El comportamiento observado se incardina con la aparición de defectos reticulares durante la calcinación. La actividad foto-catalítica (UV-asistida) de las nanopartículas de TiO_2-anatasa en la degradación de azul de metileno resulta superior a la del mejor material comercial, TiO_2-P25.

Mediante calcinación en aire del peroxotitanato de amonio, se generaron especies oxidadas (NO_x) en posiciones intersticiales del TiO_2-anatasa, que provocaron la aparición de vacantes de oxígeno en la primera esfera de coordinación del titanio. La eliminación térmica de las especies nitrogenadas generó defectos en el entorno del titanio y desequilibrios de carga en el material resultante (TiO_{2-x}), con posterior captura y difusión de oxígeno atmosférico. Los materiales dopados con nitrógeno (N-TiO_2) favorecen la selectividad en la oxidación parcial del 5-hidroximetil-2-furfural (HMF), un compuesto derivado de biomasa, hasta 2,5-furnadicarboxaldehido (FDC). Las especies nitrogenadas presentes en el catalizador reducen la cinética de la reacción foto-catalítica, por lo que la transformación de N-TiO_2 a titania oxigenada presenta un efecto positivo en la velocidad de foto-degradación de contaminantes orgánicos, aunque influye negativamente en la selectividad de los procesos de foto-oxidación parcial.

Los materiales N-TiO$_2$ foto-oxidan selectivamente alcoholes hasta sus correspondientes aldehídos, aunque con escasa selectividad, especialmente en medio acuoso (< 30% para la oxidación de HMF a FDC). La búsqueda de nuevos foto-catalizadores que incrementen el rendimiento condujo al estudio del nitruro de carbono grafítico (g-C$_3$N$_4$), ya que las características electrónicas de este semiconductor impiden la aparición de radicales ˙OH, de baja selectividad, en el medio de reacción. Este material demostró su eficiencia en la foto-oxidación del HMF hasta el FDC, aunque el g-C$_3$N$_4$ prístino, preparado por condensación térmica de melamina, presenta baja reactividad en reacciones foto-catalíticas, con valores de selectividad solo levemente superiores a los obtenidos usando dióxido de titanio. La exfoliación térmica del g-C$_3$N$_4$ incrementó su área superficial específica, simultáneamente a la eliminación de fragmentos no condensados (–NH$_2$ y –NH–) residuales en el g-C$_3$N$_4$ prístino, que atenúan la selectividad en la síntesis de FDC. Como consecuencia, se triplicó la conversión del HMF, se duplicó la selectividad en la producción de FDC, y se incrementó hasta diez veces la reactividad del g-C$_3$N$_4$ (50% de selectividad hacia la formación de FDC) cuando se utilizó luz solar como alternativa a la radiación UV.

RESUMEN (en Inglés)

In the present Ph. D. Thesis, the questions of modification of two widespread semiconductor photocatalys titanium dioxide and graphitic carbon nitride by synthetic methods and post-synthetic procedures have been addressed.

Silica-titania composites have been synthesized with a purpose of improving photo-degradation performance of TiO$_2$. A stable solution of aqueous titanium peroxo complex and oligomeric silicic acid is used as a precursor for hydrothermal synthesis of TiO$_2$ anatase nanoparticles covered with dispersed SiO$_2$ species. Silica slows down the rate of titania crystallization, thus favouring TiO$_2$ crystal growth, and it also promotes surface hydroxylation of the SiO$_2$–TiO$_2$ composites. These two properties, crystallinity and surface functionalization, contribute to the photocatalytic activity of the composite by providing an efficient charge separation and adsorption of pollutants on the surface in the proximity of the photoactive semiconductor. The proposed composite material demonstrates superior degradation rate of methylene blue under ultraviolet (UV) irradiation than the commercial P25 photocatalyst.

A solvent-exchange method including precipitation of aqueous ammonium peroxotitanate with organic solvents has been developed, in order to produce titania nanoparticles with unprecedented thermal stability of anatase phase, since no rutile is observed in the material treated up to 1000 ºC. The extraordinary stabilization of a metastable anatase phase is made possible due to the formation of crystal defects upon calcination. The prepared highly thermally stable TiO$_2$ anatase nanoparticles have shown superior photocatalytic activity in UV-assisted degradation of methylene blue compared to that of the commercial P25 photocatalyst if treated at temperatures higher than 600 ºC.

Nitrogen dopants might be introduced into TiO$_2$ structure by calcination of ammonium peroxotitanate under air. The N-species are present in the oxidized NO$_x$ form and occupy interstitial positions in TiO$_2$ anatase structure. The incorporation of nitrogen dopants provokes formation of oxygen vacancies in the first coordination shell

of titanium. Calcination of N-TiO_2 under elevated temperatures causes elimination of the nitrogen species leaving defect sites in the titanium environment, thus producing a net-charge imbalance in the titania structure. This triggers the capture of atmospheric oxygen, which subsequently diffuses from the surface to the interior of TiO_2 as to re-establish the charge neutrality. In this way, oxygen-rich titania containing interstitial oxygen species is formed. We have established that nitrogen-doping favours selectivity of the partial oxidation of a biomass-derived compound 5-hydroxymethyl-2-furfural (HMF) to 2,5-furnadicarboxaldehyde (FDC). The conversion of N-TiO_2 to oxygen-rich titania has a positive effect on photo-degradation of organic pollutants, but diminishes the selectivity in partial photo-oxidation reactions.

g-C_3N_4 because of its favourable band positions, making impossible the formation of notoriously unselective $^{\cdot}OH$ radicals, is proved to be efficient photocatalyst for the HMF to FDC photo-oxidation. It has been established that thermal exfoliation of graphitic carbon nitride does not only increase specific surface area of the material, but also it eliminates a part of uncondensed carbon nitride species containing $-NH_2$ and $-NH-$ groups, which are found to be detrimental for the selectivity toward FDC production. Thermal exfoliation procedure allows triplicating the HMF conversion rate and increasing the selectivity from 28 % for the as-prepared g-C_3N_4 to 44 % for the thermally exfoliated g-C_3N_4. Moreover, application of the natural solar light as an energy source instead of the laboratory UV-lamps based set-up results in the increase of the reaction rate up to 10 times and selectivity is found to be in the range of 50 %.

SR. PRESIDENTE DE LA COMISIÓN ACADÉMICA DEL PROGRAMA DE DOCTORADO EN MATERIALES.

Acknowledgements

On the first place I would like to thank the professors who supervised this work Rubén García and Salvador Ordoñez for all the faith they put in me, for directing, advising, supporting and simply for being excessively kind and understanding in many occasions.

I express my gratitude to all the friends and colleagues from University of Oviedo I have had pleasure to work with in the recent years, to prof. Santiago García Granda, to Marina, Alla, Alex, Rafa, Mohammed, Zakariae, Camino, Arancha and of course to Sergei and Elena, who made everything started. Many thanks to CRC group for their help in the experimental work which would have been impossible without Eva, Yolanda, Laura, Jorge, Jenny, Diego, Raquel. I would like to acknowledge all the technical and scientific assistance I received from the SCTs staff Alfonso, David, Emilio, Carlos, Azucena, Óscar.

I am enormously grateful to the group of professor Palmisano, to Elisa, Giuseppe, Rita, Francesco, Marianna for accommodating me in Palermo and giving me the possibility to not only do a fruitful research, but also spend a great time.

Thanks for a great deal of support I have received from my home University and especially to Viacheslav Avdin and all of my colleagues at the Department of Chemistry and Center for Nanotechnology.

Finally, I give my gratitude to all of my friends and family I have seen so little in the ultimate years, but who supported me in spite of the distance.

Abstract

The need of incorporating sustainable processes into the modern industry gave a start to the development of solar energy based devices, that is why semiconductor metal oxides and polymeric organic photocatalysts have gained enormous attention in recent years. Heterogeneous photocatalysis targets two general purposes: *i)* Photocatalytic degradation of water and air pollutants and *ii)* partial photo-oxidation, which aims to produce valuable organic compounds. The properties of the two most promising photoactive materials titanium dioxide (TiO_2) and graphitic carbon nitride (g-C_3N_4) are thoroughly studied up to the present date. Nevertheless, in order to increase their efficiency in above mentioned applications new modification methods are still to be developed.

Silica-titania composites have been synthesized with a purpose of improving photo-degradation performance of TiO_2. Production of materials for environmental applications calls for environmentally benign techniques for their synthesis. Use of titanium peroxo complexes is considered to be a greener alternative to widely applied titanium alkoxides, thanks to the fact that it makes application of organic solvents or structure-directing agents in the synthesis unnecessary. A stable solution of aqueous titanium peroxo complex and oligomeric silicic acid are used as precursors for hydrothermal synthesis of TiO_2 anatase nanoparticles covered with dispersed SiO_2 species. Silica slows down the rate of titania crystallization, thus favouring TiO_2 crystal growth, and it also promotes surface hydroxylation of the SiO_2–TiO_2 composites. These two properties, crystallinity and surface functionalization, contribute to the photocatalytic activity of the composite by providing an efficient charge migration and adsorption of pollutants on the surface in the proximity of the photoactive semiconductor. The proposed composite material demonstrates superior degradation rate of methylene blue under ultraviolet (UV) irradiation than the commercial P25 photocatalyst.

A new solvent-exchange method including precipitation of aqueous ammonium peroxotitanate with organic solvents has been developed, in order to produce titania nanoparticles with unprecedented thermal stability of anatase phase, since no rutile is observed in the material treated up to 1000 ℃. The extraordinary stabilization of an energetically less favourable anatase phase is made possible due to the formation of crystal defects upon calcination. This property is of key importance for the application of TiO_2-based materials in the production of photoactive ceramics. The prepared highly thermally stable TiO_2 anatase nanoparticles have shown superior photocatalytic activity in UV-assisted degradation of methylene blue compared to the commercial P25 photocatalyst if both photocatalysts are treated at temperatures higher than 800 ℃.

The question of non-metal TiO_2 doping has been addressed in great details, pursuing the purpose of finding the relation between the type of dopants, defects they produce and the photocatalytic performance of the prepared titanium dioxide materials. Doping of titanium dioxide with non-metals is known to be successful method for extending its activation to the visible-light range. Nitrogen dopants might be introduced into TiO_2 structure by calcination of ammonium peroxotitanate in air. The N-species are present in the oxidized NO_x form and occupy interstitial positions in TiO_2 anatase structure. The incorporation of nitrogen dopants provokes formation of oxygen vacancies in the first coordination shell of titanium. Calcination of N-TiO_2 under elevated temperatures causes elimination of the nitrogen species leaving defect sites in the titanium environment and producing a net-charge imbalance in the titania structure. This triggers the capture of atmospheric oxygen, which subsequently diffuses from the surface to the interior of TiO_2 as to re-establish the charge neutrality. In this way, oxygen-rich titania containing interstitial oxygen species is formed. The presence of different types of dopants affects photocatalytic properties of the material to a great extent. We have established that nitrogen-doping favours selectivity of the partial oxidation of a biomass-derived compound 5-hydroxymethyl-2-furfural (HMF) to 2,5-furnadicarboxaldehyde (FDC). Also, the N-species play the role of recombination centers reducing the photocatalytic reaction rate. The conversion of N-TiO_2 to oxygen-rich titania has a positive effect on photo-degradation of organic pollutants, but diminishes the selectivity in partial photo-oxidation reactions.

Oxidation of alcohols to the corresponding carbonyls is the reaction of a great value in organic synthesis and conversion of raw chemicals. Despite N-doped TiO_2 is able to selectively photo-oxidise alcohols to aldehydes, it usually gives unsatisfactory selectivity values, especially in water medium, reaching only 30 % of selectivity in the above mentioned oxidation process. Hence, other photocatalytic material must be found to promote such important reaction. g-C_3N_4 because of its favourable VB position, making impossible the formation of notoriously unselective $^{\bullet}OH$ radicals, is proved to be efficient photocatalyst for the HMF to FDC photo-oxidation. However, the as-prepared g-C_3N_4, obtained by thermal condensation of melamine, under UV-irradiation demonstrates low reaction rates and the selectivity values only slightly superior than that of TiO_2. It has been established that thermal exfoliation of graphitic carbon nitride does not only increase specific surface area of the material, but also it eliminates a part of uncondensed carbon nitride species containing –NH_2 and –NH– groups, which are found to be detrimental for the selectivity toward FDC production. Thermal exfoliation procedure allows triplicating the HMF conversion rate and increasing the selectivity from 28 % for the as-prepared g-C_3N_4 to 44 % for the thermally exfoliated g-C_3N_4. Moreover, application of natural solar light as an energy source instead of the laboratory UV-lamps based set-up results in the increase of the reaction rate up to 10 times, and selectivity is found to be in the range of 50 %.

Resumen

La necesidad de avanzar en el aprovechamiento tecnológico de la energía solar ha inspirado la búsqueda de nuevos foto-catalizadores heterogéneos basados en óxidos metálicos y en polímeros orgánicos, con dos objetivos principales: *i)* la degradación foto-catalítica de contaminantes orgánicos, y *ii)* la síntesis foto-oxidativa de compuestos orgánicos de alto valor añadido. En ambos procesos, el dióxido de titanio y el nitruro de carbono son materiales fotoactivos muy prometedores, demandando el incremento en su eficiencia el desarrollo de nuevos métodos de síntesis que permitan la optimización de sus propiedades.

Se han sintetizado materiales compuestos sílica-titania que mejoran el comportamiento foto-destructivo del dióxido de titanio. En su obtención, como alternativa ecológica a los habituales alcóxidos de titanio, en lugar de disolventes orgánicos y agentes directores estructurales, se utilizaron disoluciones acuosas estables de especies complejas de peróxido de titanio y de ácido silícico en estado oligomérico, precursoras mediante síntesis hidrotermal de nanopartículas de TiO_2-anatasa parcialmente recubiertas de sílica. La presencia de óxido de silicio disminuye la velocidad de la cristalización de la titania, favoreciendo el crecimiento cristalino y la hidroxilación superficial de los *composites* SiO_2–TiO_2. Tanto la cristalinidad como la funcionalización de la superficie, con migración de carga más eficiente y adsorción de contaminantes en la proximidad de los centros fotoactivos, contribuyen al aumento en la actividad foto-catalítica de los nuevos materiales, que presentan una velocidad de degradación del azul de metileno bajo radiación ultravioleta (UV) superior a la del foto-catalizador comercial TiO_2-P25.

Se ha desarrollado un nuevo procedimiento de síntesis de titania que, basado en el intercambio de disolventes, incluye la precipitación de peroxotitanato de amonio. Las nanopartículas obtenidas poseen una estabilidad térmica sin precedentes de la fase anatasa, permaneciendo exentas de fase rutilo hasta 1000 ºC. El comportamiento observado es

determinante para la aplicación de materiales basados en TiO_2 en cerámicas fotoactivas y se incardina con la aparición de defectos reticulares durante la calcinación. La actividad foto-catalítica (UV-asistida) de las nanopartículas de TiO_2-anatasa en la degradación de azul de metileno resulta superior a la del mejor material comercial, TiO_2-P25.

La incorporación de elementos no metálicos al dióxido de titanio es un método eficaz para la extensión de su actividad foto-catalítica en el rango de la luz visible. Utilizando dos diferentes tipos de dopaje nitrógeno u oxígeno, se han relacionado los defectos inducidos en el material con sus propiedades foto-catalíticas. Calcinando del peroxotitanato de amoniaco en aire, se generaron especies oxidadas (NO_x) en posiciones intersticiales del TiO_2-anatasa, que provocaron la aparición de vacantes de oxígeno en la primera esfera de coordinación del titanio. La eliminación térmica de las especies nitrogenadas generó defectos en el entorno del titanio y desequilibrios de carga en el material resultante (TiO_{2-x}), con posterior captura y difusión de oxígeno atmosférico. Los materiales dopados con nitrógeno (N-TiO_2) favorecen la selectividad en la oxidación parcial del 5-hidroximetil-2-furfural (HMF), un compuesto derivado de biomasa, hasta 2,5-furnadicarboxaldehido (FDC). Las especies nitrogenadas presentes en el catalizador reducen la cinética de la reacción foto-catalítica, por lo que la transformación de N-TiO_2 a titania oxigenada presenta un efecto positivo en la velocidad de foto-degradación de contaminantes orgánicos, aunque influye negativamente en la selectividad de los procesos de foto-oxidación parcial.

Los materiales N-TiO_2 foto-oxidan selectivamente alcoholes hasta sus correspondientes aldehídos, aunque con escasa selectividad, especialmente en medio acuoso (< 30% para la oxidación de HMF a FDC). La búsqueda de nuevos foto-catalizadores que incrementen el rendimiento condujo al estudio del nitruro de carbono grafitico (g-C_3N_4), ya que las características electrónicas de este semiconductor impiden la aparición de radicales $^\bullet OH$, de baja selectividad, en el medio de reacción. Este material demostró su eficiencia en la foto-oxidación del HMF hasta el FDC, aunque el g-C_3N_4 prístino, preparado por condensación térmica de melamina, presenta baja reactividad en reacciones foto-catalíticas, con valores de selectividad solo levemente superiores a los obtenidos usando dióxido de titanio. La exfoliación térmica del g-C_3N_4 incrementó su área superficial específica, simultáneamente a la eliminación de fragmentos no condensados (–NH_2 y –NH–) residuales en el g-C_3N_4 prístino, que atenúan la selectividad en la síntesis de FDC. Como consecuencia, se triplicó la

conversión del HMF, se duplicó la selectividad en la producción de FDC, y se incrementó hasta diez veces la reactividad del g-C_3N_4 (50% de selectividad hacia la formación de FDC) cuando se utilizó luz solar como alternativa a la radiación UV.

Contents

List of Figures

Nomenclature

UV – Ultraviolet

VIS – Visible

PXRD – Powder X-ray diffraction

SSA – Specific Surface Area

FTIR – Fourier-Transform Infrared

DR UV-vis – Diffusive-Reflectance Ultraviolet-Visible

XPS – X-ray Photoelectron Spectroscopy

XAS – X-ray Absorption Spectroscopy

EXAFS – Extended X-ray Absorption Fine Structure

XANES – X-ray Absorption Near-Edge Structure

TEM – Transmission Electron Microscopy

HRTEM –High-Resolution Transmission Electron Microscopy

EELS – Electron Energy-Loss Spectroscopy

SEM – Scanning Electron Microscopy

TG – Thermogravimetry

DTA – Differential Thermal Analysis

TOC – Total Organic Carbon

GC-MS – Gas Chromatography Mass-Spectrometry

HPLC – High Performance Liquid Chromatography

BG – Band-Gap

VB – Valence Band

CB – Conduction Band

$N\text{-}TiO_2$ – Nitrogen-Doped Titanium Dioxide

$g\text{-}C_3N_4$ – Graphitic Carbon Nitride

P25 – Titanium Dioxide Photocatalyst (Aeroxide P25, Evonik P25, Degussa P25)

CVD – Chemical Vapour Deposition

SE – Solvent-Exchange

PL – Photoluminescene

HMF – 5-hydroxymethyl-2-furfural

FDC – 2,5-furandicarboxaldehyde

MB – Methylene Blue

Índices de calidad

De acuerdo con el Reglamento de los Estudios de Doctorado aprobado por el Consejo de Gobierno de la Universidad de Oviedo el 17 de Junio de 2013 (Boletín Oficial del Principado de Asturias Nº 146, de 25-06-2013), para presentar la Tesis Doctoral como Compendio de Publicaciones es necesario incluir en la presente Memoria un informe con el factor de impacto de las publicaciones presentadas, junto con un detalle informativo sobre la calidad de las mismas, basado en el índice de impacto y en la posición que ocupa la revista científica dentro de una determinada categoría. El informe correspondiente a los índices de impacto de las revistas en las que se han publicado, o están en trámite de publicación, los artículos que forman parte de la presente Memoria de Tesis Doctoral se resume en la siguiente Tabla.

Relación de las publicaciones derivadas de la presente Tesis Doctoral
(datos obtenidos de Journal Citations Reports®).

Revista	Año	Índice de Impacto	Área	Nº de orden / nº total	Cuartil
Journal of Colloid and Interface Science	2015	3.782	Chemistry, Physical	41/144	Q2
RSC Advances	2015	3.289	Chemistry, Multidisciplinary	49/163	Q2
Applied Catalysis B: Environmental	2017	8.328	Chemistry, Physical Engineering, Chemical Engineering, Environmental	14/144 3/135 1/50	Q1 Q1 Q1
Journal of Physical Chemistry C	2017	4.509	Chemistry, Physical Material Science, Multidisciplinary. Nanoscience & Nanotechnology	30/144 40/271 22/83	Q1 Q1 Q2

Comunicaciones a Congresos

1. I. Krivtsov, M. Ilkaeva, Z. Amghouz, S. Khainakov, J.R. García, E. Díaz, S. Ordóñez. *Application of Nitrogen-Doped TiO$_2$ for Selective Photocatalytic Oxidation of 5-Hydroxymethylfurfural*. 9th European Meeting on Solar Chemistry and Photocatalysis: Environmental Applications (SPEA), Strasbourg, France, 13–16 June 2016. Poster and Flash Oral.

2. I. Krivtsov, M. Ilkaeva, Z. Amghouz, S. Khainakov, J.R. García, E. Diaz, S. Ordóñez. *Defective TiO$_2$ Anatase Nanoparticles for Selective Photocatalytic Oxidation of 5-Hydroxymethylfurfural*. 16th International Congress on Catalysis (ICC 16), Beijing, China, 2016. Poster.

3. I. Krivtsov, E.I. García-López, G. Marcì, L. Palmisano, J.R. García, E. Díaz, S. Ordónez. *Application of Thermally Exfoliated g-C$_3$N$_4$ for a Green Selective Photocatalytic Oxidation of 5-Hydroxymethyl-2-Furfural*. 40th Meeting of Iberian Adsorption Society (40 RIA), Evora, Portugal, 5-7 Septembre, 2016. Oral.

Chapter 1   Introduction

1.1   Principles of Photocatalytic Reactions

Photocatalysis is a phenomenon which can be defined as: A change in the rate of chemical reactions or their generation under the action of light in the presence of substances called photocatalysts that absorb light quanta and are involved in the chemical transformations of the reaction participants [1]. First mentioning of photocatalytic activity of TiO_2 is dated back to 1920s [2]. However, a true upraise of interest toward this process occurred only in 1970s right after the work of Fujishima and Honda on TiO_2-induced photocatalytic water splitting had been published [3]. In the following years, the growing preoccupation of industry and society with the running out fossil fuels and environmental pollution catalysed the development of photocatalytic materials further more.

Photocatalysts might be divided in homogeneous [4] and heterogeneous [5], however the present chapter as well as the entire work will be entirely devoted to the heterogeneous photocatalysis, which normally does not produce any wastes and photo-active material is easily recovered after being used in reactions. If particles of a solid photocatalyst are irradiated with an energy superior to its band gap (BG), i.e. with an energy sufficient for providing the transfer of electron from the valence band to the conduction band, making an electron (e^-) and a corresponding positively charge hole (h^+) to be generated (Fig. 1.1). After, the semiconductor is excited, the fate of the photogenerated charges is either to recombine and release energy in the form of heat or light (1), or they can migrate to the surface and interact with various molecules producing radical reactive species (2,3). The migration of the

photogenerated charges to the surface is ensured by well-crystalline nature of the material, while the bulk defects usually play the role of recombination sites. Bulk properties of the photocatalyst, as to speak high regularity of its structure, are not the only ones governing the charge separation process. When the electrons and holes reach the surface, the presence of molecules adsorbed on the exterior of photocatalyst capturing both the e^- and h^+ at the same time is necessary to inhibit the charge recombination rate. Charge separation is a crucial concept determining the photocatalytic reaction rate, and for the efficient photoreaction to take place the above mentioned conditions are to be satisfied.

$$e_{cb}^- + h_{vb}^+ \rightarrow energy \qquad (1)$$

$$e_{cb}^- + O_2 \rightarrow \cdot O_2^- \qquad (2)$$

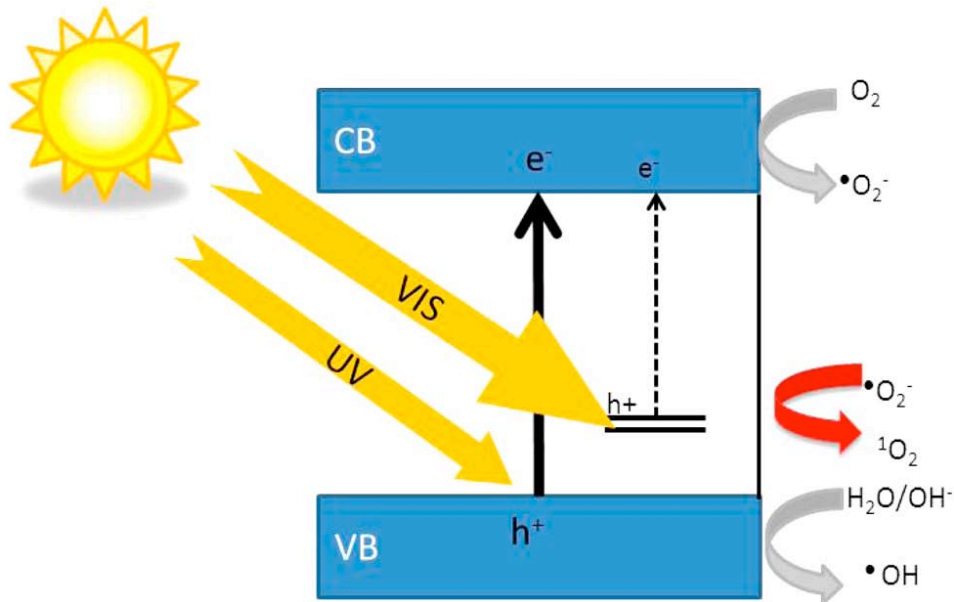$$h_{vb}^+ + H_2O \rightarrow \cdot OH + H^+ \qquad (3)$$
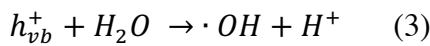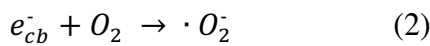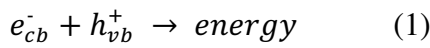
Figure 1.1 – Representation of the photocatalysis mechanism [6].

The most common solid-state photocatalytic materials are metal oxides, which have very different electronic structures (Fig. 1.2). VB and CB positions of semiconductor determine

the charge separation process and the subsequent formation of reactive species. For environmental application, as to say for photocatalytic degradation of pollutants in water or air, it is desirable to achieve total mineralization of organic substrate. Several reactive species are formed on the surface of photocatalyst, although ·OH radicals are unanimously considered as the most powerful for providing complete degradation of organics to H_2O and CO_2, NO_x, SO_x depending on the pollutant nature [7]. Hydroxyl radicals might be produced via two pathways, one of them is accomplished by the interaction of a photogenerated electron with O_2 and the series of consecutive reactions finally leading to the ·OH formation, according to the mechanism (4). However, the rates of photocatalytic generation of H_2O_2 on metal oxide semiconductors, which is a limiting step in the present reaction, are usually low [8-10]. The other way is more direct (3), although it demands that the VB of semiconductor to have a sufficient potential for direct oxidation of water molecule. Among the metal oxide semiconductors TiO_2 and ZnO possess optimal band positions permitting efficient charge separation as well as able to interact with water producing hydroxyl radicals (Fig. 1.2). Both of them have been extensively studied in various photocatalytic degradation reactions, but titanium dioxide based photocatalysts have gained major attention due to its better chemical and photo-stability [11].

$$e_{cb}^- + O_2 \rightarrow \cdot O_2^- + 2H^+ \rightarrow H_2O_2 + e_{cb}^- \rightarrow \cdot OH \quad (4)$$
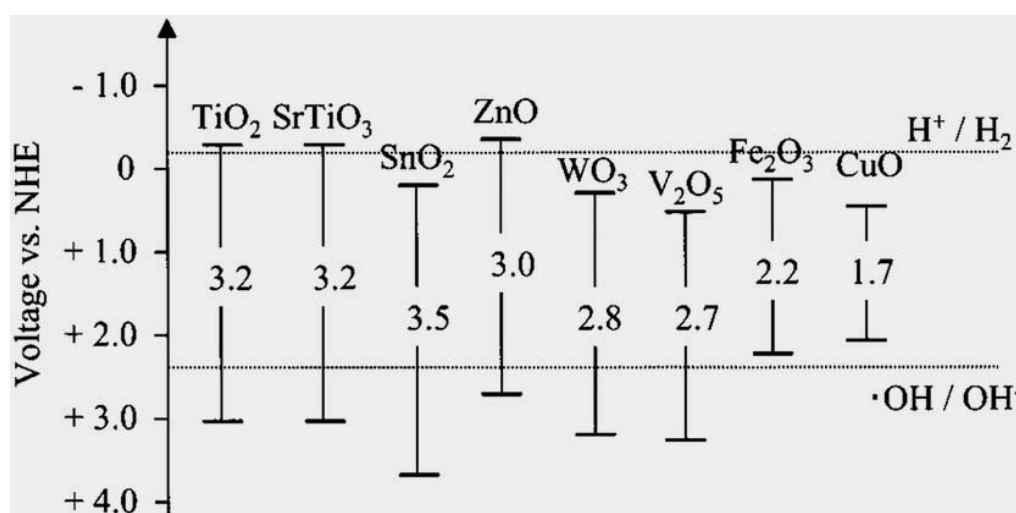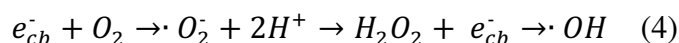
Figure 1.2 – Band positions of the widespread metal oxide semiconductor photocatalysts [12].

The main reactive species formed by photo-generated electrons are superoxide radicals. If in case of titanium dioxide, photocatalytic reaction is dominated largely by the action of hydroxyl radicals, the photo-initiated processes in presence of other materials, unable to produce them directly by water oxidation, benefits from the active oxygen species $^{\bullet}O_2^-$. One of such photocatalysts, which VB has a potential insufficient to oxidise water molecule, is g-C_3N_4 (Fig. 1.3) [13,14]. Superoxide radicals do not provide sufficient mineralization degree of organic molecules; instead they can be used for partial oxidation reactions (for more details, see Chapter 1.4).

From the above discussed, one can conclude that the universal photocatalyst suitable for various applications does not exist. It is crucial that the BG value, VB and CB positions, chemical and photostability are to be taken into consideration for any specific purpose the photocatalyst is destined to and modified accordingly.
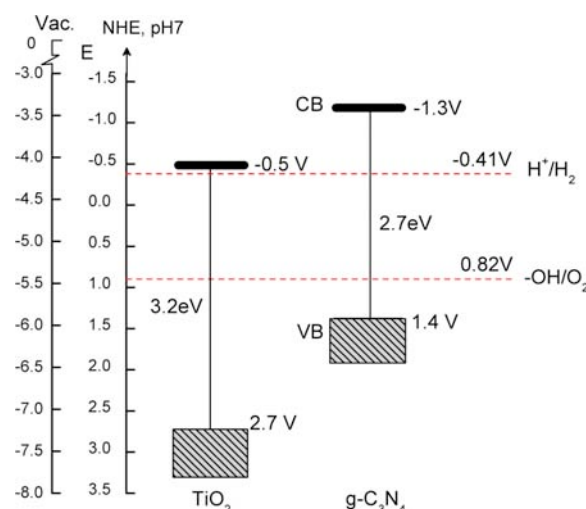
Figure 1.3 – Band positions of anatase titanium dioxide and g-C_3N_4 [14].

1.2   TiO$_2$-Based Materials for Degradation of Organic Pollutants

1.2.1   Pristine TiO$_2$ for photocatalytic applications

Titanium dioxide has gained enormous attention due to its outstanding photocatalytic activity and excellent chemical, thermal, and photo-stability. Although many synthetic modifications of titanium dioxide are known, the most commonly it is present in the form of three natural polymorphs anatase, brookite, rutile and a synthetic one TiO$_2$(B) (Fig. 1.4) [15-17]. Brookite (orthorhombic) is a relatively rare titania modification, as it is very difficult to obtain in a pure form. Despite some papers report high activity of brookite in photocatalytic reactions [18], its application is hardly can be justified because of complications and costs its synthesis brings along [19]. Rutile is the most widespread mineral of TiO$_2$, as it is thermodynamically stable crystalline modification. It is easily prepared in the form of large single-crystals [20] as well as nanoparticles even under mild conditions [21,22]. TiO$_2$ rutile is widely used in the photocatalytic process for H$_2$ production [23] and contaminated water remediation [24,25]. It is true that rutile is an active photocatalyst and in some specific applications its use is reasonable, but most usually the activity of the metastable anatase phase is far more superior.
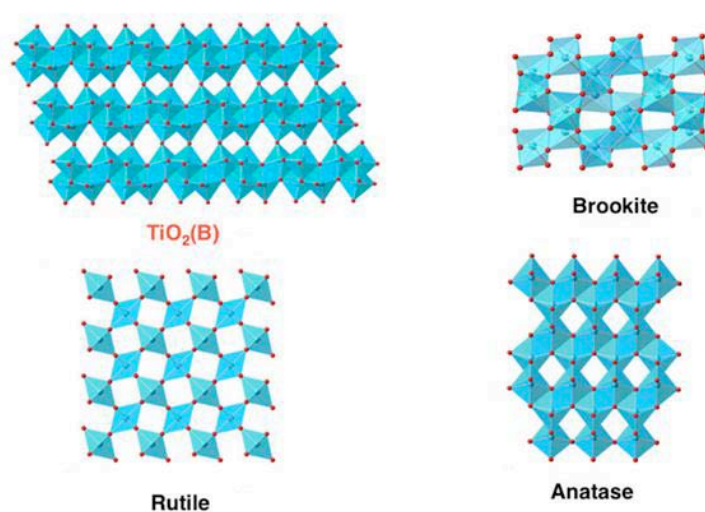
Figure 1.4 – The most common titania polymorphic modifications [16].

5

Titania anatase phase is only stable in the particle size range below 15 nm [26]. Luttrell et al. [27] established that the bulk properties of anatase and rutile are responsible for a drastic difference in their photocatalytic performance. Kakuma et al. [28] by carrying out a detailed spectroscopic study of the photogenerated reactive species on the surface of different phase TiO_2 materials explained the enhanced reaction rates, observed for anatase phase, by its favourability for ${}^{\bullet}OH$ production, while rutile promotes the formation of ${}^{\bullet}O_2^{-}$ and the consecutive H_2O_2 generation. Apart from photocatalytic degradation of organic pollutants, the difference in charge photogeneration mechanisms of rutile and anatase makes the latter more efficient material for hydrogen production [29]. It may seem that anatase is a perfect choice for photocatalytic applications, however the mixed-phase TiO_2 became famous for its outstanding activity, and it was commercialized as P25 firstly by Degussa, then it got known under the names of Evonik P25 and Aeroxide P25. Despite this photocatalyst is on the market for more than 20 years, the scientific bases explaining its extraordinary reactivity had not been known for a long time, before Hurum et al. postulated that this was due to smaller rutile BG, slow recombination rate on the rutile-anatase interface, and small rutile crystallite size [30]. In 2013, Scanlon et al. demonstrated that, in spite of the earlier accepted model, the electron affinity of anatase is higher than that of rutile, thus forcing electrons to flow from rutile to anatase (Fig. 1.5). Band alignment on anatase-rutile interface facilitates electron-hole separation, leading to the increased photoactivity of the mixed-phase material over its individual counterparts [31]. Later, this concept of band alignment was applied to develop methods allowing controllable electron migration between rutile and anatase phases [32]. Until now P25 is considered as the "gold standard" in photocatalysis. Mixed phase TiO_2 thankfully to its remarkable properties is successfully used in water decontamination from organic pollutants [33] and toxic metals [34], as well as for hydrogen production [35]. Because of enormous value of anatase and mixed phase TiO_2 for use in photocatalysis, a number of efficient sol-gel, solid-state, solvothermal, CVD methods for its production have been developed up to now. Many reviews summarized various approaches for the preparation of titania with controllable phase composition, crystal facets orientation, particle size, morphology and SSA [36-40]. Despite the mixed-phase P25 titanium dioxide is still the reference in the world of photocatalysis, there is a need to improve its properties, in order to

meet the expectations of industry for willing its use in real-life conditions. There are several major drawbacks of pristine TiO_2 materials, among them are: wide BG, which limits its activation to the UV range; low SSA of well-crystalline titania; thermal stability of photocatalytically active phase is usually limited to 400-500 ºC, which does not permit the use of TiO_2 for photoactive ceramics preparation; relatively low adsorption capacity of the titania surface, which reduces the photocatalytic reaction rate, as it normally takes place on the surface of photocatalyst. The ways of improvement of some of the above mentioned TiO_2 properties by preparation of mixed oxides and non-metal doping will be addressed in the following chapters.
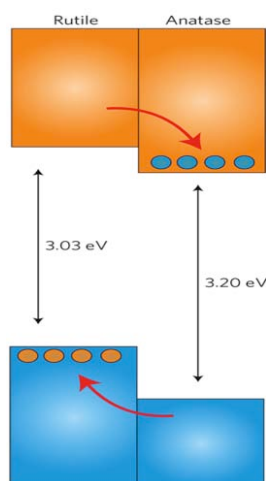
Figure 1.5 – Flow of electrons in the mixed-phase anatase-rutile system [31].

1.2.2   Synthesis of TiO_2 materials

Titanium dioxide is usually used in photocatalysis in a powder or a thin film form. The application of thin films is preferable for the solar energy harvesting in DSSC [41] and photocatalytic degradation of organic pollutants in air [42]. The most common methods of preparation of TiO_2 thin films are magnetron sputtering [43], CVD [44], sol-gel, which is a very flexible method allowing obtaining various types of materials (Fig. 1.6) [45], or hydrothermal synthesis [46].

Similar approaches are implemented to obtain titania nanoparticles in a powder form. Titania powders can be made by $TiCl_4$ oxidation in industrial flame aerosol reactors at high temperatures and moderate, near atmospheric pressures by the so-called "chloride process" at a rate of 100 ton/day [47,48]. This is a major process making more than half of the annual world-wide consumption of over 3 million tons of TiO_2 aimed mostly for pigments and to a lesser extent as a paper filler, plastics, cosmetics, catalysts and even ceramic membranes [49,50]. Sol-gel approach is more common in a laboratory scale synthesis as it is more suitable for tailoring porosity, particle size, crystalline phase, and surface modification. Although one can distinguish numerous types of sol-gel procedures applicable for titania preparation, we will consider only the following three: Pechini, non-hydrolytic and hydrolytic syntheses. Pechini sol-gel synthesis is accomplished via the pyrolysis of a polymeric titania resin precursor formed, as a rule, by complexing of oxo-titanium species by citric acid and encapsulated into the polymeric matrix of citric acid and ethylene glycol, which polymerization is catalysed by HNO_3 addition [51].

Titanium alkoxides and $TiCl_4$ are the precursors of choice in non-hydrolytic sol-gel synthesis of titania. This approach is of special interest as it enables avoiding the least controllable stages of hydrolysis and polycondensation, thus the materials with finely tuned morphology might be produced [52]. In the absence of water molecules titanium-containing compound reacts directly with an oxygen-donor such as an alcohol or with a structure-directing agent, which might be a tri-block-copolymer, surfactant, carboxylic acid or an amine [53-55]. Finally, increasing of the reaction temperature or addition of a base catalyst terminates the process of crystalline TiO_2 formation. Although, the advantages of non-hydrolytic sol-gel are unquestionable, this method brings along many complications, which stand on the road of the scaling up. The excessive cost of production of titania via this way is due to the application of organic oxygen donors, solvents and structure-directing agents, as well as it owns to the necessity of manipulating the precursors under water-free conditions and inert atmosphere. Hydrolytic sol-gel synthesis of titania photocatalysts is the most widespread in the scientific community. In most of the cases it is carried out using titanium isopropoxide or titanium butoxide as precursors. Titanium alkoxides undergo fast hydrolysis

in the presence of water, so the preparation must be done in non-aqueous solvents, generally aliphatic alcohols, having certain quantity of water and catalyst to promote hydrolysis and subsequent polycondensation reaction are applied [56-58]. After the termination of the sequence of TiO_2 formation stages normally amorphous material is obtained, demanding the implementation of an additional step of thermal treatment for removing the organic residue and obtaining crystalline titanium dioxide ready to be used in photocatalysis.
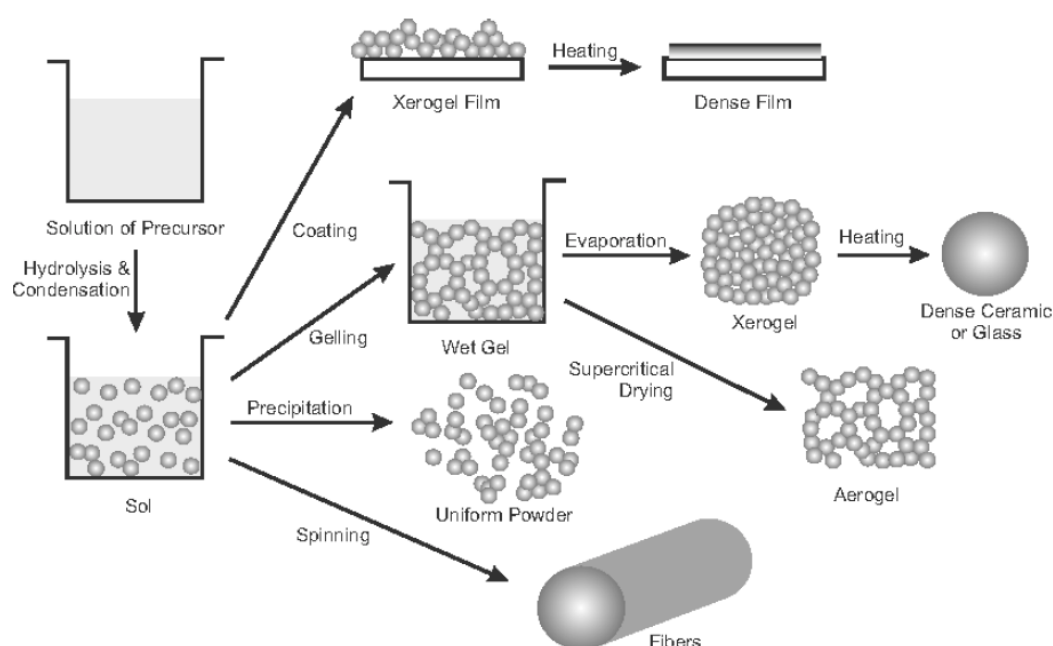
Figure 1.6 – Synthesis of metal oxides via the sol-gel approach [56].

Alkoxide-based sol-gel synthesis results in the production of high purity and high SSA titanium dioxides, while the control of these parameters is complicated if inorganic salt based processing is implemented. The elimination of the anions of titanium salts such as chlorides and sulphates is not so straightforward, and simple washing is insufficient in most of the cases. The anions composing the titanium salts tend to be incorporated into TiO_2 structure under pH below the pH of its isoelectric point, while cations of the hydrolysing agents are adsorbed on the titania when its surface is negatively charged. The second drawback of application of inorganic titanium salts for TiO_2 synthesis is the low stability of titanium oxo-species to the hydrolysis, which is limited only to very acidic solutions. The development of efficient method of the preparation of this important functional material via inorganic

aqueous pathway is highly desirable, as it would probably be the cheapest of all the processes used until now. Kakihana et al. proposed the variety of titanium peroxo complexes aiming to replace titanium alkoxides in TiO_2 synthesis [59]. Since then, many other successful techniques based on titanium peroxo complexes were developed [60-66].

Hydrothermal, or in a more general term solvothermal, processing enables reducing the preparation temperature of metal oxide materials by carrying out the synthesis under pressures superior to the atmospheric one. The already crystalline material is produced after the treatment, thus excluding the need for high temperature calcination. The temperature range of solvothermal reactions is wide, it starts from 100 ºC for water and other low boiling point solvents and reaching 240 ºC for glycothermal procedures. Despite there are many other techniques suitable for reactions at far higher temperatures, they are not considered in the present work. Solvothermal conditions favour dissolution of the material, which is not soluble under atmospheric pressure. The dissolved species then form seeds and the crystallization occurs. A vast variety of titania architectures are obtained by this method. Among them one encounters nanoparticles [67], nanorods [68], nanotubes [69], nanowires [70], flower-like structures [71], TiO_2 with exposed {001} facet [72], etc.

The great deal of the accumulated data on preparation of TiO_2 nanostructures allows us to find the most suitable approach for obtaining materials with tailored properties for some specific applications. However, in the recent years the research in the field of catalytic material preparation took a turn towards greener and economic procedures, thus the synthesis is preferably should be carried out in aqueous medium, using non-volatile, non-toxic, stable precursors and low-temperature processing.

1.2.3 TiO_2-Based Mixed Oxides

Formation of composite materials based on TiO_2 aspires achieving several goals such as stabilization of TiO_2 anatase phase, creation of electron sink zones for improved charge separation, increasing SSA, or surface modification. Stabilization of anatase phase is a well-developed process made possible by the incorporation of TiO_2 in a matrix of other metal

oxide. For instance, Hirano et al. by applying the hydrothermal pre-treatment obtained silica-titania composite having an extraordinary anatase stability up to 1300 ºC [73]. Similar role can play a ZrO_2 source addition to a TiO_2 precursor [74] and Al_2O_3 in the TiO_2-Al_2O_3 composites [75]. Ceria and copper oxides, beside playing roles of electron sinks and oxidation catalysts, are as well known for being able to inhibit anatase-to-rutile phase transformation [76].

If titania is coupled with a metal oxide semiconductor having BG smaller than 3.2 eV (i.e. inferior that of TiO_2) it can result in improved charge separation [77]. The metal of doping oxide traps the photo-excited electrons from the TiO_2 CB, thus generating the metal species with a lower oxidation state [78,79]. A number of metal oxides functioning according to this mechanism are known to improve titania photocatalytic properties among them are WO_3 [79,80], vanadia [81], and molybdena [82]. According to Di Paolo et al. [80] not all TiO_2-based mixed oxides with WO_3, V_2O_5, MoO_3, Cr_2O_3 are better photocatalysts than pure titania. It is obvious that the preparation, impregnation and treatment of the mixed oxides are crucial steps in obtaining active interface between the two components of such system. Kubacka et al. demonstrated that TiO_2-V_2O_5 has the maximum activity at the intermediate V-loadings, owing to the complete incorporation of V-species into TiO_2 structure [81]. Other oxide with similar properties, which gained a significant attention is CeO_2. Cerium (IV) due to its ability to capture photogenerated electrons forming Ce^{3+} sites and subsequently interact with atmospheric oxygen producing superoxide radicals, promotes the total photocatalytic activity of TiO_2-CeO_2 composites [83].

The increase of SSA is important from the point of view of promoting interaction of organic substrate with photocatalytically active TiO_2 in liquid phase, as well as in gas phase reactions. Silica with its outstanding textural properties and porous structure is commonly used as a support for TiO_2 nanoparticles. Kibombo et al. published an exhausting review describing the synthetic approaches and the role of silica in TiO_2-SiO_2 composite photocatalysts [84]. The flexibility of silica properties allows obtaining materials with high SSA and controllable porosity, but most importantly the degree of homogeneity of composites can be tailored via the preparation procedure manipulation [85]. Beside the above mentioned effect, modification with SiO_2 produces changes in the surface hydrophilicity and

acidity of the TiO_2-SiO_2 composites, which would undoubtedly effect the photocatalytic performance [85,86].

Numerous preparation techniques for SiO_2-TiO_2 mixed oxide have been developed up to now. In general, these procedures might be separated into to subclasses: hydrolytic and non-hydrolytic sol-gel routes. Non-hydrolytic pathways are known for providing efficient control over molecular homogeneity, crystal structure, and crystal size distribution [84,87]. However, extreme care must be taken while handling metal organic precursors, hence inert atmosphere and dry boxes are necessary, in order to avoid the precipitation of the separated metal oxide phases during the synthesis. Such aspects of the synthetic procedures might be highly impractical for the industrial scale preparation, making the hydrolytic route to be the one which is generally preferred.

The principal problem of SiO_2-TiO_2 mixed oxide preparation is the homogeneous distribution of one oxide in the matrix of the other. Titanium atom (Ti^{IV}) has a significantly large positive partial charge (+0.6) derived from its higher electrophilic character that imparts higher reactivity with water than that of the Si atom (Si^{IV}) in tetra-alkoxysilanes, hence it implies that special measures have to be taken for equalising their hydrolysis and polycondensation rates [84]. Pre-hydrolysis of silica source, usually tetraethyl orthosilicate (TEOS), or, contrary, decreasing the reactivity of Ti-alkoxides are the two most common ways of achieving homogeneity in this system. Although, the application of a single-source precursor is also reported [86], this approach is less frequently applied. Pre-hydrolysis of silica source is easily achieved by addition of certain quantities of water and catalyst to its solution in an organic solvent [88]. The stabilization of Ti source, often it is titanium tetraisopropoxide $Ti(OPri)_4$, can be provided by various stabilizing agents such as acetic acid, 2-methoxyethanol, acetylacetone, etc [84]. The above mentioned approaches are viable only for organic solvent medium, while it is very desirable for production purposes to fabricate homogeneous SiO_2-TiO_2 from aqueous solutions. Working in aqueous medium demands other ligands to be applied. Kessler et al. summarized the approaches for TiO_2-based materials preparation from the carboxylate complexes [89] and some of the similar methods were used to obtain silica-titania mixed oxides using carboxylic acid and chitosan [85,89-91].

Although many methods allowing highly homogeneous distribution in the mixed oxide system were developed, it is not always beneficial for the application of the mixed oxide in photocatalysis, as the charge recombination takes place on the doping sites, crystallization of TiO_2 is usually suppressed by the doping oxide, and also the incorporation of other metal might consume indispensable for hydroxyl radical generation surface titanyl groups [92]. For photocatalytic applications it is advisable to adjust the silica-titania mixture in that way to have a sufficient interface area between two oxides, providing that the crystallinity of TiO_2 is not compromised by the large quantity of defect sites. The optimization of the composite oxide properties would allow silica to play the role of an adsorbent for the dissolved substrate molecule delivering them to the surface of TiO_2 (Fig.1.7).
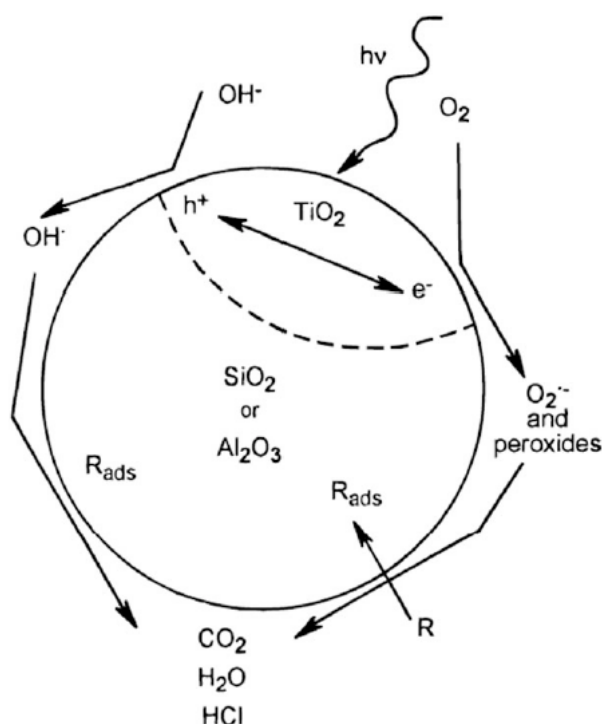
Figure 1.7 – Photocatalytic reaction on the mixed Al_2O_3-TiO_2 oxide system [74].

Despite sol-gel is the most common technique allowing synthesis of these mixed oxides with controllable properties, hydrothermal procedure could be even more useful, especially for preparation of photocatalysts, which must be in a crystalline state. There are only few works reported the successful application of this technique for SiO_2-TiO_2 synthesis [93-95].

1.2.4   Non-metal doping of TiO$_2$

The primary goal of non-metal doping of titania photocatalysts is the reduction of BG aiming to take advantage of a larger part of the visible-light range of the solar spectrum. Non-metal species such as B, C, S, F, and N incorporate into TiO$_2$ structure forming substitutional or interstitial doping sites [96-99]. Substitutional non-metal doping mainly affects VB states of TiO$_2$, as the position of the N, C, and B dopants is located 0.13, 1.39, and 2.18 eV above the VB level, respectively (Fig. 1.8). Contrary to that, F 2p state lies 1.19 eV below the bottom O 2p VB, hence no visible-light activity is observed for F-TiO$_2$ [97]. It is assumed that only substitutional doping reduces the BG of TiO$_2$, while interstitial species form interband states resulting in appearance of mid-BG [100,101]. Although, the interstitials dopants might not decrease titania BG, mid-BG states can be the source of titania visible-light activity, which by absorbing the light with wavelengths >400 nm sensitize TiO$_2$. This effect was confirmed for S and N dopants [102,103]. Besides the obvious positive effect of non-metal doping, several other consequences of heteroatom introduction into TiO$_2$ are to be considered. The excess of N concentration in titania structure favours formation of crystal defects with Ti^{III} sites, which are responsible for faster photogenerated charges recombination [104]. The anion-doping is not strictly speaking a bulk phenomenon; it is also inevitably results in surface modification. Obviously, the most reactive surface TiO$_2$ species are hydroxyl groups, which can be eliminated during the doping process, thus significantly changing TiO$_2$ photo-reactivity [105] because of the key role of surface OH in generation of $^{\bullet}$OH. Hence, in order to produce the materials with visible-light activity while retaining a high level of UV excitation of the material, the practical aspects of TiO$_2$ anion doping should be addressed with great care considering all the positive and negative effects it might cause on titania photocatalytic performance. Among all anion dopants N-doping received the most attention. Belver et al. studied in details photocatalytic and structural properties of N-TiO$_2$ synthesized in liquid phase with an assistance of various amines as nitrogen sources [106,107]. They found nitrogen species to occupy both substitutional and interstitial positions in titania network and being responsible for O-vacancies creation. However, no correlation between the nitrogen positions or its content with photocatalytic activity was established.

According to Belver et al. photocatalytic activity of N-TiO$_2$ results to be a function of a joint effect of N-dopants and oxygen vacancies, which content has to be optimized for the highest photoactivity of TiO$_2$ under visible light to be achieved [107].

Asahi et al. in the review entirely devoted to N-doping of TiO$_2$ classified all known preparation procedures of nitrogen-doped titania into two main categories: dry processes and wet processes [108]. Titanium nitride (TiN) can be oxidized by treating it under O$_2$ at high temperature producing N-TiO$_2$. Despite a significant shift of the absorption band to the visible-light range was achieved for the photocatalyst prepared in this way, the material contained traces of TiN and mainly is present in rutile phase [109]. Another dry process used for N-TiO$_2$ synthesis is NH$_3$ treatment of the pristine titanium dioxide under high temperatures. Control of NH$_3$ flow and treatment temperatures allows manipulating the loading of the dopant. High temperatures of this process, superior to 550 ºC, cause decomposition of NH$_3$ to N$_2$ and H$_2$, thus high quantity of oxygen vacancies are created by hydrogenation of titanium dioxide [110,111]. Mechanochemical synthesis of N-TiO$_2$ was also reported [112,113], although one must take into account that the application of amines or urea as nitrogen sources might lead to the formation of TiO$_2$ co-doped with C and N, or even to C$_3$N$_4$-doped titania, as urea is able condense on titania surface at high temperatures producing photoactive carbon nitride modifications [114].

Wet processes provide a vast variety of procedures for N-TiO$_2$ preparation such as a simple precipitation of titanium-containing inorganic precursors with NH$_3\cdot$H$_2$O, or in the presence of NH$_4$Cl [115], sol-gel syntheses applying metal-organic Ti complexes and using organic N-sources such as amines or amino acids [116], and finally hydrothermal synthesis, which is able to reduce the preparation temperature and produce fine N-TiO$_2$ nanoparticles [117].
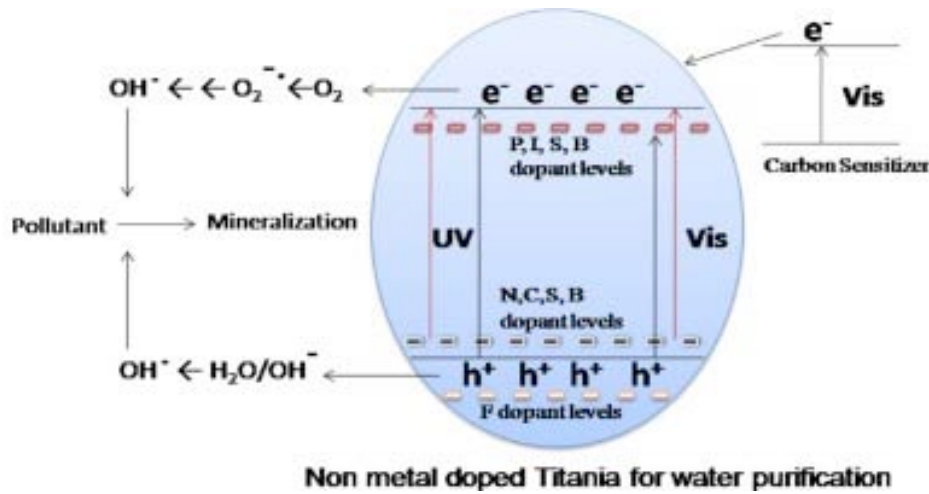
Figure 1.8 – Non-metal doping of TiO$_2$ anatase [99].

1.2.5 Stabilization of TiO$_2$ anatase phase

Anatase is known to be the most photocatalytically active titania polymorph, however this crystalline modification of TiO$_2$ is metastable. According to thermodynamic calculations made by Zhang and Banfield [118], anatase becomes more preferable modification of titania if the crystal size is reduced below the upper limit of 14 nm. Although, one can prepare small titania crystals in the low-temperature range, the calcination of TiO$_2$ at temperatures superior to 400-500 ºC is inevitably leads to crystal growth and anatase-to-rutile transformation. The stabilization of anatase phase permits the treatment of the material at high temperatures, in order to obtain photocatalyst with desired crystallinity or even approach TiO$_2$ sintering temperatures without its transformation to rutile. The latter feature is of great importance for some emerging titania applications such as fabrication of photo-active ceramics [119].

Both anatase, space group I4/amd, and rutile, space group P42/mnm, are tetragonal symmetry. Both crystal structures consist of TiO$_6$ octahedra, sharing four edges in anatase and two in rutile [120,121]. These structures are illustrated in Figure 1.4. The anatase to rutile transformation is reconstructive, which means that the transformation involves the breaking and reforming of bonds [122]. This is in contrast to a displacive transformation, in which the original bonds are distorted but retained. The reconstructive anatase to rutile transformation

involves a contraction of the *c*-axis and an overall volume contraction of 8% [123-125]. This volume contraction explains the higher density of rutile relative to anatase. In the course of the transition to rutile, the (112) planes in anatase are retained as the (100) planes in the rutile product [126,127]. The c-axis of anatase appears to be significantly longer than that of rutile only because anatase has more atoms per unit cell than rutile has.

In Section 1.2.3 has already been mentioned that antase phase demonstrates much higher stability in TiO_2-M_xO_y mixed metal oxide systems. However, many other ways of retardation of formation of rutile modification are known. The presence of brookite phase [128], or preferential orientation of titania crystals in a certain direction [129] increase the temperature of polymorphic anatase to rutile transformation. Although cation doping is widely applied for the purposes of stabilization, a detrimental effect on photocatalytic activity of transition metal sites in TiO_2 playing the role of recombination centers is often reported [130,131]. Anion doping, apart from the enriching TiO_2 with visible light activity, is also responsible for the creation of oxygen vacancies in this way contributing to the enhanced anatase thermal stability. Fluorine, sulphur, and nitrogen dopants are proved to be efficient for anatase stabilization up to temperatures of 900-950 ℃ [132-134]. In spite of numerous reports on anion-doping induced stabilization of TiO_2 anatase phase, no clear mechanism of this process is still proposed.

1.3   Graphitic Carbon Nitride Photocatalysts

1.3.1   Synthesis of g-C_3N_4

Looking on the recent outburst of publications about g-C_3N_4, one might think of it as of a relatively new achievement in polymer chemistry. It is true that many of its properties have only become known in the last two decades, but the discovery of carbon nitride named "melon" dates back to the first half of 19th century and belongs to Liebig [135]. Graphitic carbon nitride is the most stable allotrope of carbon nitride and it possesses numerous outstanding properties. It is one of the most thermally stable organic polymers decomposing only at temperatures higher than 600 ℃ even in air, it is highly stable in acids, bases and organic solvents, and it is a medium BG semiconductor. Despite the widely used term

"carbon nitride", its composition is never stoichiometric C_3N_4 and should be rather put as $C_xN_yH_z$. Although it is predicted that a nearly ideal carbon nitride would have hardness superior that of diamond [136], in practice it is very difficult to obtain a single-phase sp^3-hybridized carbon nitride due to its low thermodynamic stability [137,138]. Up to the present date, the developed synthetic procedures have only been able to produce slightly disordered low-crystalline material. It is generally accepted that C_3N_3 triazine rings cross-linked by the trigonal N atoms are the principal building blocks of g-C_3N_4 (Fig. 1.9).

The BG of g-C_3N_4 makes this material especially attractive in the field of photocatalysis, having the absorption edge of 420 nm it is able to use a larger portion of visible-light than it does TiO_2 [139]. BG value of g-C_3N_4 varies significantly depending on the preparation methods [140] and the precursor used [141-144]. However, even before the outburst of works using g-C_3N_4 for photocatalysis, many attempts to prepare carbon nitride materials were reported. Khabashesku et al. proposed powder method based on the reaction of cyanuric chloride and lithium nitride [145]. The material with very close stoichiometry to that of C_3N_4 was obtained, although it contained certain amount of chlorine as impurity. Sometime later, the same group of researchers described the templated procedure for preparation of spherical carbon nitride particles [146]. Solvothermal synthesis was also intended, although it asked for very harsh reaction conditions. Hydrazine was used as a solvent and the synthesis was carried out at the pressure of 3 GPa and in the temperature range of 800-850 ℃ [147]. An alternative way was to treat 1,3,5-trichlorotriazine and lithium nitride in benzene at temperatures between 300 and 400 ℃ and pressures of 5-7 MPa producing mainly the mixture of α-C_3N_4 and ß-C_3N_4 [139,148]. The catalytically assisted solvothermal synthesis in presence of $NiCl_2$ could give carbon nitride nanotubes with CN stoichiometry [149].
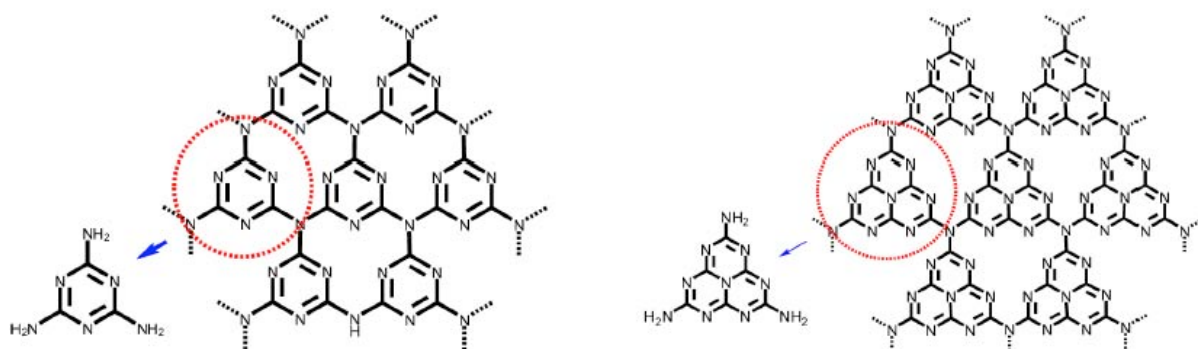
Figure 1.9 – s-Triazine (left) and tri-s-triazine as tectons of g-C$_3$N$_4$ [138].

As soon as the outstanding photocatalytic properties of g-C$_3$N$_4$ was discovered, new methods for its preparation appeared. Several available and inexpensive precursors became widely applied for carbon nitride synthesis via simple solid-state condensation reaction. The condensation pathways of the precursor used for the synthesis determine the bulk properties of the resulting g-C$_3$N$_4$ and as a consequence its BG. Melamine undergoes deammonification under high temperatures and condenses directly forming tri-s-triazine structures (Fig. 1.10). Urea and thiourea firstly condense to give melamine and melamine-urea or melamine-thiourea co-polymerization products [150] (Fig. 1.11). If urea and thiourea are used as the precursors the inclusion of heteroatoms such as O and S into the g-C$_3$N$_4$ is unavoidable and it affects significantly the light absorption of the formed carbon nitride product. Doping with fluorine, boron, phosphorus, copolymerization, hydrogenation or protonation is also known to modify the electronic structure of this semiconductor to a great extent [151-156].

1.3.2   Optimization of g-C$_3$N$_4$ properties

Beside the electronic properties of g-C$_3$N$_4$, which many researchers aim to optimize, in order to harvest a broader range of the solar spectrum, another concern is low SSA of bulk carbon nitride prepared by a simple thermal condensation of its precursors. Apart from the obvious decrease of catalyst-substrate interaction for low SSA g-C$_3$N$_4$, bulk material also shows high recombination rates of photogenerated charges in respect to nanocasted g-C$_3$N$_4$ [157]. Usually, the condensation of melamine in the temperature range of 520-550 ºC produces the material, although with high yields, but with SSA of only about 10 m^{2}g^{-1} [158].
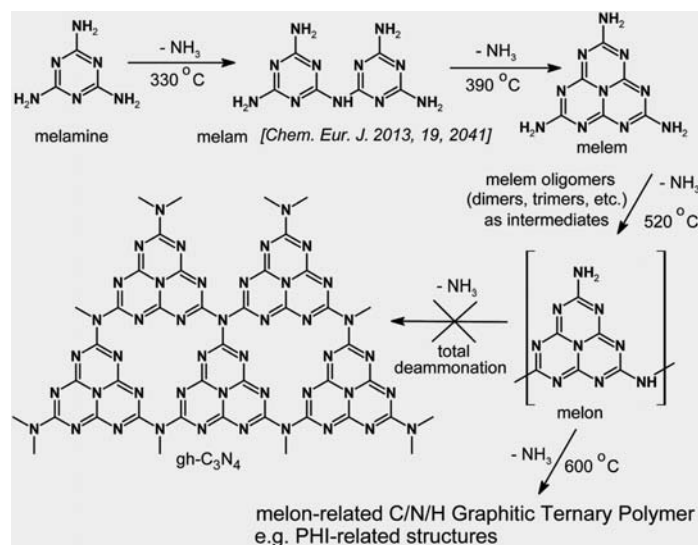
Figure 1.10 – Melamine thermal condensation pathway to g-C$_3$N$_4$ [150].

Several efficient methods have been developed allowing overcoming this obstacle. The synthetic approach to high SSA carbon nitride synthesis consists in application of hard and soft templates [159]. First class of soft templates used in g-C$_3$N$_4$ preparation is amphiphilic surfactants and block co-polymers. Application of non-ionic, cationic, and anionic surfactants is very common in preparation of micro- and mesoporous inorganic catalytic materials. Use of Triton X-100 non-ionic surfactant with dicyandiamide as a precursor gives g-C$_3$N$_4$ with SSA of 76 m^{2}g^{-1} [160]. Yan achieved SSA value of 90 m^{2}g^{-1} for g-C$_3$N$_4$ prepared with the assistance of triblock-copolymer Pluronic P123 as a template [161]. Ionic liquids are also able to promote the formation of porous carbon nitrides [162]. However, this method is not ideal as usually thermal treatment is unable to eliminate all the carbonaceous residue coming from the template, thus g-C$_3$N$_4$ with an excessive carbon content is obtained [163].
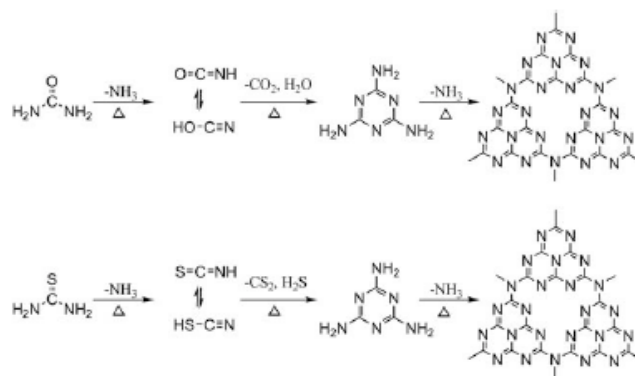
Figure 1.11 – Urea and thiourea thermal condensation pathways to g-C$_3$N$_4$ [141].

Hard templating, also known as nanocasting, is a technique providing a very versatile selection of morphologies and structures to be formed. Hard templates have one significant advantage before the soft ones, they have fixed structures thus simplifying the control of the material properties. Expectedly, the hard template of choice is silica, which in its turn as well produced by a templating approach. Vinu et al. was the first to obtain hexagonally ordered mesoporous carbon nitride by casting ethylenediamine over SBA-15 [164]. The material prepared in this way possessed SSA of 505 m^2g^{-1}, although it was rather a nitrogen-doped carbon, than g-C$_3$N$_4$ [165]. The exchange of the N-containing precursor to cyanamide and dicyandiamide resulted in the formation of carbon nitride with C/N ratio of 0.72, which is closer to the theoretical value [166]. Several other reports on preparation of high SSA carbon nitrides having of up to 450 m^2g^{-1} were published in recent years [167-169]. The major drawback of silica hard template casting is the necessity of its elimination after the thermal condensation step. Highly corrosive substances such as HF or NH$_4$HF$_2$ dissolve the template leaving mesoporous carbon nitride, thus this approach is hardly can be considered as environmentally friendly. Anodic alumina oxide is an alternative hard template for the nanocasting of carbon nitride. Li *et al* [170] by applying this technique synthesized nanocasted g-C$_3$N$_4$ more efficient in photocatalytic hydrogen production than bulk carbon nitride.

1.3.3   Application of g-C$_3$N$_4$ materials

Graphitic carbon nitride has a wide range of applications in sensing, catalysis and photocatalysis [171]. It was demonstrated that by simply changing melamine condensation temperature one can control the photoluminescence properties of g-C$_3$N$_4$ [172]. Highly stable photoluminescence intensity makes carbon nitride an ideal candidate for sensing even trace quantities of metals such as copper, iron, lead, mercury, and chromium [173-175]. Also, biocompatibility of g-C$_3$N$_4$ makes it a promising material for biomedical applications [176] and coating fabrication [177].

Although many potential uses of carbon nitride based polymeric materials exist, owing to its numerous outstanding properties photocatalytic applications attract the major interest of scientific community. Narrow BG, making this material active under visible-light, and VB and CB positions, favourable for promoting photocatalytic water-splitting, are the prerequisites for its extensive use for solar energy harvesting (5, 6).

$$H_2O \rightarrow O_2 + 4H^+ + 4e^- \qquad +0.82 \text{ V} \qquad (5)$$

$$2H^+ + 2e^- \rightarrow H_2 \qquad -0.41 \text{ V} \qquad (6)$$
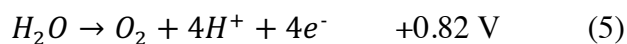
The set of other extraordinary characteristics rare for organic photocatalysts complements the electronic properties of carbon nitride giving a very promising material for hydrogen production. This material is photo-stable, oxygen tolerable, and possesses nitrogen functionalities, both Lewis and Bronsted sites, permitting anchoring of substrate molecules on the surface of the semiconductor [178]. Hence, g-C$_3$N$_4$ is capable of reducing H$_2$ from water in the presence of a suitable electron donor, such as triethanolamine even in the absence of noble metals [179], however the reaction rates are still low and usually Pt co-catalyst is applied.

Another important field of g-C$_3$N$_4$ application is photocatalytic degradation of organic pollutants in water. Considering the fact that the carbon nitride VB potential is too low to oxidise H$_2$O subsequently producing hydroxyl radicals, the development of the methods for

using this material for environmental remediation attracts significantly less attention than hydrogen production. Despite this, the researchers do not give up attempts to modify g-C_3N_4 properties for hazardous compounds degradation. Zou et al. tested boron-doped g-C_3N_4 for dyes photo-degradation, and they established that even low oxidation potential of the carbon nitride VB is sufficient to degrade rhodamine B [152]. Still the processes occurring on the CB of g-C_3N_4 are of more interest. Photogenerated electrons can interact with H_2O_2 reducing it to hydroxyl radicals, which mineralize the organic substrate [139].

If the preference of g-C_3N_4 for application in environmental remediation processes before TiO_2 seems rather doubtful, its superior selective oxidation of hydrocarbons and alcohols is almost unquestionable. The question of partial photocatalytic oxidation in the presence of g-C_3N_4 will be addressed in detail in the following chapter.

1.4 Partial Photocatalytic Oxidation Processes on TiO_2 and g-C_3N_4

Selective oxidation is one of the most important reactions in organic synthesis, widely applied in the production of an uncountable range of valuable chemicals. The common conditions used for carrying out this kind of reactions are usually harsh, demanding high temperatures and pressures [180], or use of expensive noble metals [181], organic solvents [182], toxic oxidative agents [183] resulting in the elevated cost of the processes, formation of large amounts of by-products and toxic wastes. The economic reasoning and environmental restrictions force industry to find alternative methods for selective oxidation. Heterogeneous photocatalysis being an environmentally benign and zero-waste process is on the spotlight of the scientific community looking for the replacement of outdated chemical oxidation approaches. Moreover, the fact that a unique energy source required for photocatalysis to take place is a cost-free solar irradiation would be able to drastically reduce the expenses of the chemical synthesis. Photocatalysis for many years had been thought of being an unselective process mainly serving for the oxidative destruction of organic pollutants in water medium, but eventually the molecular recognition properties of TiO_2 for certain molecules attracted attention [184,185]. Expectedly, in the beginning of the selective

photocatalysis exploration the material of choice for the majority of the researchers was titanium dioxide. Due to the readiness of notoriously unselective $^{\bullet}$OH radicals formation on the surface of TiO_2 in water or in the presence of water vapour, many partial oxidation reactions promoted by this semiconductor were performed in organic solvents under water-free conditions. Numerous studies reported selective photo-oxidation of benzyl alcohol in acetonitrile [186-188] and in benzotrifluoride [189] with good selectivity. Amines were also successfully photo-converted to imines in the presence of titanium dioxide [190,191]. Hydrocarbons were photocatalytically oxidised in benzotrifluoride or acetonitrile [192,193] and with the assistance of H_2O_2 [194].

The advantages of the replacing organic solvents with water are obvious from the point of view of the process costs and environmental impact. Unfortunately, a highly polar solvent such as water competes for the adsorption sites on the titania surface, thus complicating the interaction of a substrate with reactive species on the surface of the semiconductor and favours producing unselective $^{\bullet}$OH radicals through the reaction of water molecules with positively charged holes. The reduction processes initiated by photogenerated electrons leads to the formation of superoxide radicals, which might selectively oxidise hydrocarbons and alcohols to the corresponding carbonyl products, but also certain quantities of hydrogen peroxide might be produced in this way (4). Hydrogen peroxide by receiving photogenerated electrons from the CB of a semiconductor forms hydroxyl radicals, which destroy organic substrate unselectively.

Figure 1.12 shows the hypothesized oxidation mechanisms of alcohols in water (Fig. 1.12a) and in organic solvent (Fig. 1.12b) [195,196]. Partial photocatalytic oxidation in aqueous phase has as a major process a direct interaction of the substrate with positively charged hole resulting in deprotonation and formation of aldehyde from alcohol, while the oxidation with superoxide radicals is only the secondary reaction (Fig. 1.12a). This mechanism was supported by the application of Cu^{2+} ions as electron scavengers in TiO_2-assisted benzyl alcohol photo-oxidation in water under oxygen-free atmosphere. Copper ion by capturing an electron is reduced to a lower oxidation state, leaving the hole to react with benzyl alcohol [197]. Zhang et al. [195,196] studied the mechanism of the photocatalytically oxidative

transformation of alcohols performed in benzotrifluoride (BTF) by using bare TiO_2 anatase. They discovered the oxygen transfer from molecular O_2 to the alcohol. The oxygen atom of the alcohol is completely replaced by one of the oxygen atoms of the dioxygen molecule, i.e. the process occurs by the selective cleavage of the C–OH bond with the concomitant formation of a C=O bond to obtain the final product, where O comes from O_2. The mechanism proposed by authors (Fig. 1.12b) is the following one. The alcohol molecule is adsorbed onto the surface of TiO_2 by a deprotonation process, hence it reacts with the photogenerated hole on the TiO_2 surface forming a carbon radical whereas the electron transforms Ti(IV) into Ti(III). Both carbon radical and Ti(III) easily react with O_2 and a Ti peroxide intermediate is formed. The cleavage of this species gives rise to carbonyl species, coming from the partial oxidation of the alcohol.

The commercially available TiO_2 materials usually demonstrate very limited selectivity in partial photo-oxidation reactions in water medium [198]. It is assumed that the incorporation of certain types of defects is necessary to suppress the formation of hydroxyl radicals on titania surface. Thus, only poorly crystalline titanium dioxide containing high percentage of amorphous phase is normally applied to selectively oxidise aromatic alcohols [199]. The least crystalline titania anatase samples were found to be more efficient in partial oxidation of 4-methoxybenzyl alcohol reaching the selectivity for 4-methoxybenzyl aldehyde formation of 42% [200,201]. Rutile poorly crystalline nanoparticles were also active in the same reaction [202]. High concentration of crystal defects in such materials inhibits the reaction rate, however there is still no consensus among the researchers about the types of defects favouring selective photo-oxidation. Obviously, the percentage of the amorphous phase in titania photocatalyst is not the property solely determining the selectivity. The whole photo-oxidation process is considered as a sequence of adsorption (substrate)-oxidation-desorption (product), hence the surface properties might play an important role in controlling the adsorption phenomena on TiO_2 [203,204]. Augugliaro et al. [203] by comparing the selective photocatalytic oxidation properties of the home prepared titania nanoparticles and commercial Degussa P25, highlighted the importance of surface chemistry of the titanium dioxides over the properties of the bulk phase. They established that high content of the amorphous phase gave rise to higher hydrophilicity of TiO_2 surface in respect to well-crystalline Degussa P25. The latter is due to the fact that the surface hydroxyls readily

adsorbed aromatic alcohols and mineralize them to CO_2 and water, while the disordered regions on the home prepared titania had higher affinity to molecular water than to the organic substrate, which was probed by in-situ FTIR [204]. On one hand, such competition between the adsorption of organic substrate and water resulted in much lower reaction rates for the home prepared titania, but, on the other hand, it significantly enhanced the selectivity towards the formation of corresponding aldehydes. The desorption of the less polar product (aldehyde) was also more favourable from the more hydrophilic surface, which constituents the second advantage of the home prepared TiO_2 before the commercial photocatalyst. Despite the reasonable selectivity values for aromatic alcohols to aldehydes oxidation were achieved for the low-crystalline TiO_2, ranging within 40-70%, depending on the type of the substituents on the benzyl ring, the drop of the reaction rate in respect to highly crystalline titania would limit its utilization in industry. Since it is widely accepted that the photocatalytic activity and selectivity are dependent on the adsorption properties of photocatalyst, many researchers assumed that the easiest way to tailor this characteristic is to cover titania particles with those of other oxide [75,205-208]. Indeed, in the above mentioned works higher reaction rates were achieved compared to pristine titania photocatalysts. Later, Tsukamoto et al. [209] demonstrated that titania covered with a shell of WO_3 is also an efficient material for selective photo-oxidation of benzyl alcohol to benzaldehyde.

Band positions of g-C_3N_4 described earlier in Chapter 1.3 eliminate one of the fundamental problems of selective photocatalytic oxidation of organic compounds, i.e. their mineralization by ˙OH radicals produced via the reaction of positively charged holes with water. Contrary to TiO_2, the potential of the VB of carbon nitride is insufficient not only to generate hydroxyl radical, but also to oxidise alcohols to aldehydes by hydrogen abstraction on holes. It is uniformly accepted that the main reaction species responsible for the partial photo-oxidation of organic compounds by g-C_3N_4 are superoxide radicals formed by the reaction of photogenerated electron with molecular oxygen [14]. Expectedly, the appropriate electronic properties of g-C_3N_4 allow reaching very high selectivity values $\geq$ 99% of aromatic hydrocarbons [151] and alcohols [14] oxidation to corresponding aldehydes in organic solvent medium. Application of higher than room temperatures along with irradiation

significantly enhances reaction rate without affecting the selectivity of the process. The group of Antonietty reported high yields of aldehydes/ketones resulting from the photo-oxidation of aromatic alcohols by mesoporous g-C_3N_4 with molecular oxygen in trifluorotoluene [14]. They also established that both electron-donating and electron-withdrawing substituents in a substrate molecule enhanced the rate of the reaction (Fig. 1.13).

Although C–H and O–H oxidation promoted by g-C_3N_4 is of primary interest due to high industrial value of these processes, some other interesting selective photo-reactions have also been reported. Oxidation of amines to imines under the visible-light is one of them (Fig. 1.14) [210]. Metal catalysts used for amine-to-imine oxidation are tend to be deactivated rapidly by the poisoning with heteroatoms, thus making the photocatalytic process a promising replacement for the conventional catalytic reactions.
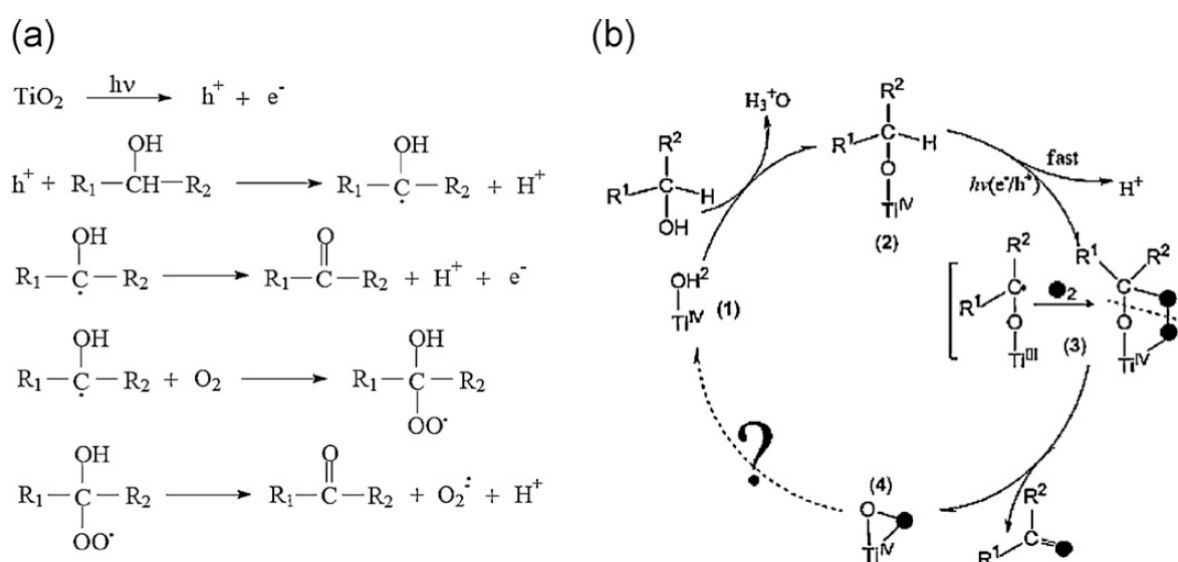
Figure 1.12 – Mechanism of TiO_2-assisted alcohols photo-oxidation in water (a) and benzotrifluoride media (b) [211].

27

	R¹	R	time, h	concn, %	seectivity, %
1	phenyl	CH_3	3	57	>99
2	phenyl	H	3	77	>99
3	4-methylphenyl	H	3	86	90[a]
4	4-chlorophenyl	H	3	79	>99
5[b]	4-methoxyphenyl	H	1.8	100	95[c]
6	4-methylbenzoate	H	3	80	>99
7	$PhCH{=}CH_2$	H	3	92	64[d]
8	pentyl	CH_3	5	35	>99
9	phenyl	cyclopropyl	5	32	90[d]

[a]Acid (10%) was formed. [b]4-Methoxybenzyl alcohol 0.65 mmol. [c]Acid (5%) was formed. [d]Benzaldehyde (36%) was detected. [e]1-(1,2-Dicyclopropyl-2-phenylethyl)benzene (10%) was formed.

Figure 1.13 – Selective photocatalytic oxidation of aromatic alcohols in the presence of g-C_3N_4 in benzotrifluoride [14].

The position of the VB for g-C_3N_4 almost completely eliminates the possibility of the formation of hydroxyl radicals, and the generation $^\bullet$OH is only possible via the reduction pathway mediating through the production of H_2O_2, which demands the presence of certain type of dopants [212,213]. Strangely, despite that fact, most of the selective photocatalytic reaction using carbon nitride are carried out in organic solvents, then the reports on application of water as a green medium for such reactions are scarce [214,215].

Figure 1.14 – g-C_3N_4 promoted photocatalytic oxidation of amines to imines [13].

Selective photocatalytic processes attract great deal of interest of research community resulting in the exponential growth of scientific publications on this topic in recent years. Yet, to the best of author's knowledge, the industrial use and commercialization of these reactions are still to be put in practice. The current fossil fuel and environmental crises cause that enormous investments are made into the sector of biomass valorisation. Photocatalysis being an environmentally benign, energy-saving and zero-waste technology meet the requirements of the modern-day industry and it is ready to be introduced into the production of high-value chemicals from a renewable feedstock. Colmenares and Luque summarized and discussed the recent works on the photocatalytic conversion of the most abundant biomass source lignocellulosic compounds [216]. High stability and difficulties related to the dissolution of lignocellulose complicate the use of photocatalysis to its direct conversion, while saccharides resulting from lignocellulose hydrolysis [217] and their oxidised derivatives are much more probable objects for the transformation by light-initiated processes. The oxidation of six-carbons sugars yields 5-hydroxymethyl-2-furfural (HMF), which can be furtherly converted to 2,5-furandicarboxaldehyde (FDC) and 2,5-furandicarboxylic acid (FDCA), which are the precursors for biopolymers fabrication [218-220]. Several approaches for HMF oxidation, using noble metals [221,222] or transition metal phosphates [223,224] as catalysts, have been explored. However, the application of high temperatures, as well as expensive noble metals [221] makes this process energy-consuming and environmentally unfriendly. The oxidant properties of TiO_2 are exalted by the relatively lower stability of the pentatomic furanic ring compared to the hexatomic aromatic structures, and consequently it is not surprising that the highest selectivity of HMF photooxidation to FDC achieved so far is only 22% [225].

Chapter 2   Objectives

The principle objective of the present Ph. D. Thesis is to develop methods for synthetic and post-synthetic modification of titanium dioxide (TiO_2) and graphitic carbon nitride (g-C_3N_4) photocatalysts, which would permit tailoring their properties in such a way as to achieve high efficiency in photo-degradation of organic pollutants in water medium or to maximize selectivity of partial photo-oxidation reactions destined to produce chemicals with high added value. In order to reach the established goals, the following specific objective are proposed:

- Synthesize silica-titania nanoparticles and estimate the effect of silica on structural features and surface properties of the composite and their role in methylene blue photo-degradation performance under UV irradiation.

- Develop a new environmentally benign procedure for preparation of thermally stable anatase titania nanoparticles using titanium peroxo complex as a precursor. Evaluate photocatalytic properties of the synthesized photocatalysts in reaction of UV-assisted methylene blue degradation and compare their performance with that of the commercial TiO_2 photocatalyst.

- Evaluate the role of nitrogen and oxygen dopants in titania structure on titanium local order and photocatalytic performance in the reaction of photo-degradation of aqueous pollutant p-cresol and partial photo-oxidation of 5-hydroxymethyl-2-furfural (HMF) to 2,5-furandicarboxyaldehyde (FDC) in water medium.

- Study the applicability of various precursors for high-yield and high-activity graphitic carbon nitride preparation and implement thermal exfoliation method, in order to enhance specific surface area of g-C_3N_4 photocatalyst. Establish the principal properties governing photocatalytic activity and selectivity of UV- and solar light assisted conversion of HMF to FDC.

Objetivos

El objetivo principal de esta Tesis Doctoral es el desarrollo de métodos sintéticos y post-sintéticos para la modificación de foto-catalizadores que, basados en dióxido de titanio (TiO_2) y nitruro de carbono grafítico (g-C_3N_4), alcancen elevada eficiencia en la foto-degradación de contaminantes orgánicos en medio acuoso o maximicen la selectividad de reacciones de foto-oxidación parcial para la generación de productos químicos de alto valor añadido. Con este objetivo general, se establecen los siguientes objetivos específicos:

- Sintetizar nanopartículas de sílica-titania y estimar el efecto de la presencia de sílice en las características estructurales y en las propiedades de superficie de los nuevos materiales, incluyendo su influencia en la capacidad de foto-degradación de azul de metileno bajo irradiación UV.

- Desarrollar un nuevo procedimiento, ambientalmente benigno, para la preparación de nanopartículas de anatasa, térmicamente estables, utilizando peroxocomplejos de titanio como precursores, evaluando las propiedades foto-catalíticas de los nuevos materiales en la degradación de azul de metileno bajo irradiación UV.

- Evaluar el efecto del nitrógeno y el oxígeno como dopantes de titania, determinando la influencia del entorno local del titanio en el comportamiento foto-catalítico en medio acuso de los nuevos materiales, tanto en la foto-degradación de p-cresol como en la foto-oxidación parcial de 5-hidroximetil-2-furfural (HMF) a 2,5-furandicarboxialdehído (FDC).

Evaluar diferentes precursores para la obtención, mediante exfoliación térmica, de nitruro de carbono grafítico con elevado rendimiento y alta actividad foto-catalítica, estableciendo los

factores que rigen su comportamiento en la conversión de HMF en FDC asistida por irradiación UV y luz solar.

Chapter 3   Materials and Methods

3.1   Materials

For the synthesis of TiO_2 and TiO_2-based materials a non-volatile and stable under ambient conditions titanium oxysulfate hydrate ($TiOSO_4 \cdot H_2O$) precursor, containing 17 wt% of sulfuric acid, was used. The source of SiO_2 was 27 wt% solution of sodium silicate ($Na_2Si_3O_7$) in water purchased from Aldrich. Sodium hydroxide (Prolabo, 99% purity) and 20% ammonia (Prolabo) were used as precipitation agents and for the pH correction, as well was nitric acid (Prolabo). Hydrogen peroxide 30 wt% solution was obtained from VWR. Apart from water, ethanol and acetone were used as solvents. To compare the properties of the synthesized photocatalysts with the commercial products Aeroxide P25 and TiO_2 anatase powder (99% purity) were purchased from Aldrich.

The starting materials for graphitic carbon nitride synthesis were melamine, urea, and thiourea. All the chemicals were of analytical grade and used as received from Aldrich without additional purification.

Several substrates were used in order to assess the photocatalytic performance of the prepared materials. Methylene blue dye and *p*-cresol (Aldrich) were used for estimation of photo-degradation abilities of the synthesized photocatalysts. HMF (Aldrich, 98% purity) was the substrate chosen for the study of its partial photocatalytic oxidation to FDC. FDC (Aldrich, 97% purity) and 5-formyl-2-furoic acid (FFA) (Aldrich, 99% purity) were used to calibrate GC-MS and HPLC systems.

3.2 Synthesis

3.2.1 Silica-titania preparation

On the first stage of the synthesis, 50 mL of sodium silicate solution with concentrations 0.0, 0.025, 0.05, 0.1, 0.14 and 0.18 mol·L^{-1} was added to 50 mL of 0.1 M solution of TiOSO$_4$. The samples were designated as 0TS, 0.1TS, 0.4TS, 0.9TS, 1.3TS, and 1.6TS (where the numbers indicate SiO$_2$/TiO$_2$ molar ratio in the synthesized samples, determined by elemental analysis). Then the mixtures were hydrolysed with 1.5 M solution of sodium hydroxide, the addition of NaOH ended when pH value reached 3.2 (4.0 for 0TS and 0.1TS). The gel-like precipitates obtained after alkali addition were centrifuged at 3000 r.p.m. and thoroughly washed with deionized water eight times, until the negative reaction for sulphate ions. On the next stage, 0.5 mL of 3 M ammonia was added to the precipitate following by ultrasonication in 50 mL of distilled water. Then, to the dispersed precipitates 4 mL of H$_2$O$_2$ solution was added and pH of the reaction mixtures was adjusted to 7.0 by the addition of ammonia solution in order to obtain water-soluble titanium peroxo complexes. Soon, clear transparent yellow solutions of titanium peroxo complex and silicic acid were formed. The findings concerning dissolution of silica–titania hydrogel in hydrogen peroxide were described elsewhere [90,226]. After that, 3 M nitric acid was dropwise introduced to the solution until pH reached the value of 2.0. It is worth mentioning that after the addition of acid all solutions stayed clear with the exception of samples 0TS and 0.1TS, where the formation of sol was observed. Then, the volume of the prepared mixtures was adjusted to 80 mL by deionized water and they were transferred to Teflon-lined stainless steel autoclaves having total volume of 140 mL for hydrothermal treatment. Hydrothermal treatment was carried out under autogenous pressure at 180 ºC during 48 h. In order to establish the role of the precursor, silica–titania materials with the equimolar SiO$_2$/TiO$_2$ composition in the reaction mixture were also synthesized under conditions of pH not being controlled by ammonia and nitric acid addition (PTA–SiO$_2$), by hydrothermal treatment of the gel in the absence of hydrogen peroxide after ammonia and nitric acid were added (GelTS), and using separately prepared titanium peroxo complex and sodium silicate solution (NH$_3$PT–SiO$_2$). When the treatment was over, the precipitates were isolated by centrifugation at 3000 r.p.m., washed with

deionized water eight times and dried at 60 ºC for 24 h. In order to eliminate adsorbed water, the samples were calcined in static air at 400 ºC for 2 h, but a part of each sample was left as-synthesized as well.

3.2.2   Preparation of thermally stable titania anatase nanoparticles

Firstly, titanium hydroxide was precipitated from 25 mL of 0.2 M titanium oxysulfate solution in sulfuric acid by addition of 3 M NH_3 aqueous solution, the final pH of the precipitate was 9.0. Then, it was centrifuged at 7000 r.p.m. and washed with deionized water until a negative reaction for sulphate ions was achieved. The aqueous titanium peroxo complexes were synthesized by addition of 4 mL of 30 wt% hydrogen peroxide to the precipitates and gradual adjustment of the pH value of the reaction mixture to 9.5 by adding ammonia. Finally, clear bright yellow stable solutions were formed and their volumes were adjusted to 25 mL. The solutions were cooled in an ice bath in order to prevent fast decomposition of H_2O_2, as well as evaporation of ethanol and acetone. The cooled solutions of titanium peroxo complexes were mixed with equal volumes of ethanol or acetone. The mixed solutions became turbid immediately, because the hydrous titania particles were formed. The obtained suspensions were left for 24 h and then centrifuged at 8000 r.p.m. for 5 min, after that the pale-yellow precipitates were isolated and washed several times with water. For the sake of comparison, the sample prepared in the absence of any organic solvents was also investigated. Because the aqueous solution of titanium peroxo complex synthesized as mentioned above was stable, it was heated at 50 ºC for 2 h in order to induce titanium hydrolysis and precipitation of peroxotitanate gel. The samples prepared by (i and ii) isolation of hydrous titania with ethanol or acetone and (iii) gelation of aqueous complex solution were designated as TiEt, TiAc and TiAq, respectively. All precipitates were dried at 70 ºC for 24 h before subjecting to investigation. Also, the samples were thermally treated in a muffle furnace at specific temperatures (500 ºC, 800 ºC, 900 ºC and 1000 ºC) at the heating rate of 5 ºC min^{-1} and left for 30 min at each specific temperature before being cooled down.

3.2.3   Preparation of nitrogen-doped and oxygen-rich titania

The titanium dioxide photocatalysts were prepared by the method similar to that described by Etacheri et al. [227]. Although titanium oxysulfate hydrate was used instead of titanium tetrachloride, a stable water-soluble peroxotitanium complex was eventually formed in both cases. Briefly, titanium oxysulfate hydrate containing 5 mmol of TiO_2 was dissolved in deionized water and then precipitated with 4 mL of 20% ammonia water solution. The resulting precipitate of titanium hydroxide was centrifuged at 3000 r.p.m. and thoroughly washed with deionized water until the sulphates were no longer detected. On the next step of the synthesis, the precipitate was dissolved by adding 3 mL of H_2O_2 (30 %) and the titanium peroxo complex was formed. Ammonia (3 M) was used to adjust pH value of the peroxo complex to 9.5, while it was ice-cold. Then, the peroxo complex solution was heated at 50 °C while stirring until the complex was gelled. The gel was dried at 70 °C overnight, powdered in an agate mortar and calcined in a muffle furnace in air at 400 °C, 500 °C, 600 °C, and 800 °C. The heating rate was 3 °C·min^{-1} and the samples were left for 2 h at the fixed temperatures. The prepared photocatalysts were designated as T_x, where x indicates the calcination temperature.

3.2.4   Preparation and exfoliation of g-C$_3$N$_4$

Bulk graphitic carbon nitride (g-C$_3$N$_4$) samples were prepared via thermal condensation method from different precursors as previously reported [158, 228]. 10 g of melamine, 20 g of urea or 10 g of thiourea were placed in a ceramic crucible covered with a lid and heated in a muffle furnace at 2 °C min^{-1} up to 520 °C, then left for 2 h at the reached temperature and slowly cooled down. The g-C$_3$N$_4$ samples derived from the different sources, melamine, urea and thiourea, were labelled as MCN, UCN and TuCN, respectively. The bulk carbon nitride prepared from melamine (MCN) was used as the precursor for the thermally exfoliated g-C$_3$N$_4$ nanosheets [229]. To this purpose, 6 g of bulk carbon nitride were powdered in a mortar, evenly spread on the bottom of a ceramic bowl with a diameter of 14 cm, calcined in a static air atmosphere at 450 °C, 500 °C, 520 °C and 540 °C by using a temperature ramp of 2 °C min^{-1} and maintained for 4 h at each of the final temperatures. The thermally exfoliated carbon nitride samples were coded as MCN 450, MCN 500, MCN 520, and MCN 540.

3.3   Characterization

Thermal analysis of the prepared materials was carried out by means of two thermoanalytical systems: NETZSCH 449C simultaneous TG/DTA analyser and Mettler Toledo TGA/SDTA851. The studied materials were put in the corundum crucible and heated at the heating rate of 10 ºC min^{-1} under air (20 mL min^{-1}) or oxygen (50 mL min^{-1}) flows from 25 ºC to 1000 ºC. The TG, DTA or SDTA curves were registered, the DTG curve was obtained by a numerical differentiation of the TG data.

The crystalline structure of the photocatalysts was determined at room temperature by powder X-ray diffraction analysis (PXRD) carried out by using a Panalytical Empyrean apparatus, equipped with CuKα (λ = 0.15418 nm) radiation source and PixCel1D (tm) detector or Rigaku Ultima IV with the similar characteristics. The mean crystal size of the TiO$_2$ samples was estimated by Scherrer equation from the (101) reflection of anatase and (110) reflection for the rutile phases (7).

$$D = \frac{K\lambda}{\beta Cos\theta} \qquad (7),$$

where D is the mean crystal size, k is a dimensionless shape factor, λ is the X-ray wavelength, ß is the broadening at half the maximum intensity, and θ is the Bragg angle.

The amount of amorphous phase content in titania samples was determined by the internal standard method. The PXRD data, collected from the samples mixed with 20 wt% of CaF$_2$, were refined using MAUD software and the quantity of the amorphous TiO$_2$ was calculated using the following expression:

$$W_{am} = \left(1 - \frac{W_{std}}{W_{xrd}}\right) * 100\% \qquad (8),$$

where W_{am} is a weight percentage of the amorphous phase, W_{std} is the fraction of CaF_2 added to the sample, and W_{xrd} is the fraction of CaF_2 in the mixture with the titania samples determined by PXRD quantitative phase analysis.

Thermodiffraction analysis was carried out using an X'pert Pananlytical diffractometer in air starting from room temperature up to 1000 $^{\circ}$C.

Micromeritics ASAP 2020 was used to obtain adsorption–desorption isotherms of N_2 at 77 K. The surface area, pore volume and pore-size distribution were calculated from the low-temperature nitrogen adsorption data using BET and BJH approaches. Prior to the experiment the samples were degassed under vacuum at 250 ºC or 350 ºC for 4 h.

SEM images were obtained by using JEOL JSM-7001F field emission scanning electron microscope and equipped with EDX detector; the samples were gold-coated prior to observation. The EDX analysis was mainly used to confirm the absence of sulphur in the TiO_2 samples.

Transmission electron microscopy (TEM), high resolution transmission electron microscopy (HRTEM), selected area electron diffraction (SAED), nanobeam electron diffraction (NBD), and EELS (electron energy loss spectroscopy) studies were performed on a JEOL JEM-2100F transmission electron microscope operated at an accelerating voltage of 200 kV, equipped with a field emission gun (FEG) and an ultra-high resolution pole-piece that provided a point-resolution better than 0.19 nm. The samples for TEM were dispersed in ethanol, sonicated and sprayed on a holey carbon film coated copper grid and then allowed to air-dry, finally, Gatan SOLARUS 950 was used before observation.

Bruker Tensor 27 FTIR and FTIR-8400 Shimadzu spectrometers were used to collect infrared spectra of the samples in KBr (Aldrich) pellets with 4 cm^{-1} resolution and 256 scans.

RT emission spectra were measured using a standard spectrofluorometer Edinburgh Instruments FLSP920 (Edimburgh, Scotland, UK), equipped with a 450W Xe lamp excitation source, at an excitation wavelength of 365 nm.

Diffuse reflectance spectra (DRS) were obtained in air at room temperature in the 250–800 nm wavelengths range by means of a Shimadzu UV-2401 PC and a Shimadzu UV-2700

spectrophotometers, with $BaSO_4$ as the reference material. The BG values were calculated from the Kubelka-Munk transformed spectra considering the indirect nature of BG of the used semiconductor photocatalysts.

The binding energies of Ti, O, Si, N, C, and N in the TiO_2, SiO_2-TiO_2, and pristine and exfoliated g-C_3N_4 samples were measured by X-ray photoelectron spectroscopy (XPS) by using a SPECS system equipped with a Hemispherical Phoibos analyser operating in a constant pass energy, using MgKα radiation (h·ν = 1253.6 eV). Surface elemental composition of the studied materials was estimated using CasaXPS software. The deconvolution of the XPS peaks were carried in accordance with the NIST binding energies database, using Shirley function to create a baseline and Gaussians function to make spectra fit.

The solid-state ^{29}Si MAS-NMR and ^{1}H–^{29}Si cross-polarization MAS-NMR (CPMAS) measurements were recorded on a Bruker Avance III 400WB spectrometer at 79.49 MHz for ^{29}Si. The experiment was done at room temperature with a sample spinning rate of 4500 Hz (45° pulse width of 2.5 μs). For calibration of the ^{29}Si signal position, Q8M8 reference material was used. For the MAS-NMR measurement a pulse delay of 180 s was chosen, and the number of scans was 3000. For the CPMAS-NMR experiment a pulse delay was 5 s, and the number of scans was 1000.

XANES and EXAFS measurements of titania samples were carried out at Spanish CRG BM25A SpLine beamline (REF-A) at ESRF (The European Synchrotron Radiation Facility, Grenoble, France (Fig. 2.1)) [230]. X-ray absorption data were collected around Ti K-edge using a -70 ℃ ethanol cooled double Si(111) crystal, which gave an energy resolution of $\Delta E/E = 1.5 \times 10^{-4}$. The experiment was performed at room temperature in fluorescence mode at standard 45° geometry (Fig. 2.2). For fluorescence detection, Sirius liquid nitrogen cooled multi-element solid state X-ray detector from e2v was employed. The detector includes 13 Si(Li) crystal sensors mounted on a low noise electrically restored FETs. Pure commercial TiO_2 anatase (Aldrich), the nitrogen-doped and the oxygen-rich samples were measured in the energy range from 4.8 to 5.7 keV.

Demeter package software was used for data processing [231]. Background removal and Tröger self-absorption correction in the raw data were carried out using Athena software [232]. Artemis software was used to complete the EXAFS data analysis. Pure commercial TiO_2 anatase sample data were used to build the structural model. Two coordination shells around central Ti atoms were fitted in the range from 1.4 Å to 3.5 Å.

Figure 2.1 – The European Synchrotron Radiation Facility.

Figure 2.2 – Experimental setup for XAS experiments.

3.4   Photocatalytic reactions

3.4.1   Photocatalytic degradation of organic pollutants

Synthesized silica–titania materials were tested in aqueous phase photocatalytic degradation of methylene blue (MB) in a stirred batch reactor. For the experiment, 25 mg of each sample calcined in air at 400 ºC for 2 h was taken into a quartz reactor. Then 50 mL of aqueous solution of MB with concentration 20 mg·L^{-1} was added to the catalyst. Firstly, the adsorption of MB by the photocatalyst was determined, for this the suspension was magnetically stirred in the dark until it reached the adsorption equilibrium (for Degussa P25, 0TS, 0.1TS, 0.4TS and 0.9TS the equilibrium was reached after 30 min, while longer time

was needed to the 1.3TS and 1.6TS samples). Then, the concentration of MB was photometrically determined by the absorbance at 664 nm using Shimadzu UV-2700 spectrophotometer. After the dark experiment the suspension was exposed to ultraviolet irradiation. The source of UV-light was the Osram high-pressure mercury 125 W lamp. It was equipped with the visible-light filter, which decreased the lamp's photon flux by half. The suspension of the sample and MB solution was constantly mixed and cooled. After irradiation started, the aliquots of 5 mL were taken every 30 min during the first 150 min of the experiment and then every 60 min to the total of 330 min. The solution was separated from the catalyst at 8000 r.p.m. using air-cooling centrifuge, and concentration was photometrically determined (absorbance measured at 664 nm). Then, the solution and the catalyst were returned back to the reactor, and irradiation continued. Photolysis of the MB solution was carried out under the same experimental conditions, but in the absence of photocatalyst. The error of MB concentration determination, calculated from the data obtained for replicate runs, did not exceed 7%. The total organic carbon (TOC) was measured using a Shimadzu TOC-V CSH Analyzer for the MB solution and the most active sample after 330 min of irradiation.

Synthesized by the solvent-exchange method titania materials were tested in aqueous-phase photocatalytic decomposition of methylene blue (MB) in a stirred batch reactor. For the experiments, 25 mg of each sample previously calcined in air at 500, 800 and 1000 ℃ for 30 min was placed into a quartz reactor. Later, 50 mL of MB aqueous solution (20 mg·L^{-1}) was added to the catalyst. Before irradiation, the suspension was magnetically stirred in the dark until the adsorption equilibrium was reached in 30 min. Afterward, the suspension was exposed to ultraviolet irradiation. The UV-light source was 500 W lamp (Helios Italquartz) having maximum emission at 365 nm and equipped with a water-cooling jacket. The reactor with suspension was positioned at a distance of 50 cm from the lamp, which gives a light intensity of 2.7 W·m^{-2}. The suspension was constantly stirred during the UV-irradiation and 5 mL aliquots were taken every 30 min during 240 min. The solution was separated from the photocatalyst using a centrifuge, and the concentration was determined photometrically by the absorbance at 664 nm using a Perkin Elmer Lambda 20 spectrophotometer. After that, the solution, together with the catalyst powder were returned back into the reactor and irradiation has continued. Photolysis of the MB solution in the absence of catalyst was carried out under

the same experimental conditions. It was found that only 1.5% of MB was decomposed under these conditions.

The photocatalytic properties of the N-doped and oxygen rich titania samples were evaluated in the reactions of photo-degradation and partial photo-oxidation using *p*-cresol HMF as model compounds, respectively. The tests were carried out in aqueous phase in a stirred batch Pyrex reactor containing 1 g·L^{-1} of the photocatalysts suspended in 100 mL of the substrate solutions. The light source was a 500 W lamp (Helios Italquartz) with emission maximum at 365 nm and equipped with a water-cooling jacket and positioned at a distance of 10 cm from the reaction vessel. The selected photocatalytic runs were carried out using a UV-cutoff filter solution of $NaNO_2$ (2 M). The optimum quantity of the photocatalysts was established based on the radiometric studies, and it ensures almost complete light absorption for all the samples. Before the radiation started the photocatalysts were suspended in the reaction solution with an assistance of ultrasonication and then mixed in the dark for 30 min, in order to complete the adsorption-desorption equilibrium. The concentrations of the substrates were 10 mg·L^{-1} (0.093 mM) for *p*-cresol, as a pollutant, which is normally found in water at low concentration levels, and 40 mg·L^{-1} (0.32 mM), 200 mg·L^{-1} (1.6 mM), and 400 mg·L^{-1} (3.2 mM) for HMF. The aliquots of approximately 2.5 mL were withdrawn from the reactor at the fixed time intervals, filtered through a PTFE 0.2 µm filter, and the concentrations of all compounds of interest extracted from water solutions in ethyl acetate were determined using a Shimadzu 2100 Ultra GC-MS system equipped with a Teknokroma TRB-5MS (95%) dimethyl (5%) diphenylpolysiloxane copolymer column. The analysis was carried out in a split regime, the injection port was at 250 ºC, the initial column temperature was 60 ºC, then the column was heated at 15 ºC·min^{-1} up to 180 ºC, then the temperature increased to 270 ºC at a rate of 40 ºC·min^{-1} and left for 2 min. Prior to each analytical run GC-MS system was calibrated for *p*-cresol or for HMF and FDC depending on the type of the reaction.

3.4.2 Photocatalytic conversion of biomass platform molecule HMF in the presence of g-C$_3$N$_4$

The irradiation experiments were carried out in a Pyrex cylindrical photoreactor (internal diameter: 32 mm, height: 188 mm, containing 150 mL of aqueous suspension, irradiated by six external Actinic BL TL MINI 15 W/10 Philips fluorescent lamps emitting in the 340–420 wavelength range with the main emission peak at 365 nm (Fig. 2.3). The reaction was carried out at about 25 ºC as the reactor open to the atmosphere was provided by a thimble where water was allowed to circulate. Selected experiments were carried out in anaerobic condition by continuously bubbling N$_2$ throughout the runs to estimate the influence of O$_2$ on the reaction. The initial HMF concentration was 0.5 mM at the natural pH. The amount of solid photocatalyst used for the experiments was 50 mg, except for the pristine carbon nitrides MCN, UCN, TuCN and MCN 450, for which 100 mg were used, due to their poorer light absorbance compared to the other samples. In this way, all the entering photons were virtually absorbed by the suspension. The impinging radiation energy in the range 315–400 nm was measured by a radiometer Delta Ohm DO9721 with an UVA probe and its average value was 3.4 W·m^{-2}. Some experiments were performed by reusing one of the best materials (MCN 520) in order to verify its performance in a series of four consecutive runs. Selected scavengers were used in order to establish the reactive species responsible for HMF conversion and the selectivity to FDC. Sodium formate (HCOONa) was used as a hole scavenger, tert-butylalcohol (t-BuOH) as an $^\bullet$OH radical scavenger, copper (II) chloridedihydrate to trap electrons, and p-benzoquinone to scavenge $^\bullet$O$_2^-$ radicals. The concentration of sodium formate and tert-butyl alcohol scavengers was 5 mM, whereas for CuCl$_2$ and p-benzoquinonethe concentration was reduced to 1 mM, which enabled to avoid the precipitation of copper hydroxide during the photocatalytic run and to decrease the effect of the formed p-hydroxiquinone on the light absorbance by the suspension.

The photocatalytic reactions under the natural solar irradiation were carried out on clear sunny days of 6th, 9th and 18th May 2016 in Palermo (Italy) from 9:30 to 13:30. Typically, 75 mL of 0.5 mM HMF solution and 25 mg of MCN_520 and MCN_540 samples were introduced inside a round-shaped Pyrex batch reactor having a total volume of 125 mL and a diameter of 10 cm (Fig. 2.4). The reactor was closed and no gases were fed during the tests as

preliminary experiments indicated that O_2 deriving from air and present in the system was sufficient to induce the oxidation. The suspensions of the carbon nitride samples in HMF solution were continuously magnetically stirred and approximately 2.5 mL were withdrawn every 30 min and analysed by using the previously described analytical procedure. The photon flux was measured every 10 minutes throughout the photocatalytic tests. Moreover, selected additional experiments were carried out by using MCN_520 and MCN_540 photocatalysts under solar light filtered by means of 1M $NaNO_2$ solution ($\lambda > 400$ nm).

Samples of the irradiated solution were withdrawn at fixed time intervals and immediately filtered through 0.25 μm membranes (HA, Millipore) to separate the photocatalyst particles. Liquid aliquots were analyzed by a Thermo Scientific Dionex Ulti-Mate 3000 HPLC equipped with a Diode Array detector to identify and to determine the concentration of HMF, FDC and 5-formyl-2-furoic acid (FFA). A REZEK ROA. Organic acid H^+ column was used with a mobile phase of aqueous 2.5 mM H_2SO_4 solution at flow rate of 0.6 mL·min^{-1}. Standards purchased from Sigma-Aldrich with a purity >99% were used to identify the products formed during the reaction and to obtain the calibration curves. Additionally, the reaction products were identified and selectivity values were confirmed by a GC-MS technique using a Shimadzu 2100 Ultra GC-MS equipped with a Teknokroma TRB-5MS dimethyl (5%) diphenylpolysiloxane copolymer column.

Figure 2.3 – UV-lamps equipped photocatalytic reactor for HMF conversion.

Figure 2.4 – Photocatalytic setup for the natural solar light promoted oxidation of HMF.

Chapter 4   Results and discussion

4.1   Materials for photocatalytic degradation of organic pollutants

Chapter 4.1 is devoted to the design of TiO_2-based photocatalysts aimed for the application in photocatalytic degradation of organic pollutants in water medium. This chapter is divided into two sub-chapters addressing the questions of increasing the efficiency and reaction rates of water contaminants degradation. The controlled crystal growth process and modification of the titania surface with dispersed silica species are the factors constituting the improved photocatalytic performance of the silica-titania composites. The second part proposes a new method for the preparation of titanium dioxide with the increased thermal stability of the most active TiO_2 anatase phase free of the presence of heteroatoms in its structure, thus making a step further to the development of photoactive ceramic materials.

4.1.1   Silica-titania mixed oxides

Preparation of silica-titania composite materials in different forms is well-known method of improving certain properties of TiO_2-based photocatalysts. Core-shell structures appeared to be one of the main type of SiO_2-TiO_2 mixed oxides used in photocatalysis. Silica spherical particles, which are easily obtained using Stöber process [233] or via templating procedures [234], can support TiO_2 nanoparticles crystallized by thermal treatment of the deposited titania precursor [235]. Similar architectures show high photocatalytic activity due to the exposed titania crystals providing efficient light utilization [236]. Further enhancement of the

photo-degradation rates might be achieved eliminating the silica constituent by chemical etching with alkali leaving a hollow structure [237]. It is also possible to obtain a reverse core-shell composites, where crystalline TiO_2 anatase nanoparticles are covered with silica layer. In this way, titania gets protection from undesirable effects of high temperature treatment one of which is polymorphic anatase-rutile transition [238]. Also, the textural properties of silica layer can be tuned producing surface porous structure permitting and regulating the access of organic substrate molecules to the photocatalyst surface.

Sol-gel and solvothermal methods are most commonly used for synthesis of SiO_2-TiO_2 architectures. Use of silicon and titanium alkoxides in organic water-free solvents along with structure directing agents allows efficient control over hydrolysis, condensation and nucleation of Si and Ti oxo-species, hence the desired composition and morphology of the composites are achieved [84]. Despite the intended results are obtained, the application of alkoxides in organic media for the synthesis brings certain disadvantages for scaling up and commercialization. High cost of the above mentioned reactants, low chemical and thermal stability of alkoxides, and the necessity of taking certain measures of prevention the contact of the precursors with water vapors complicate the industrial production of such materials. Although, examples of synthesis of silica-titania materials using inorganic sources of matrix-forming elements are known [239], they have not got a wide distribution due to complicated control of the products properties. Titanium is the element causing most of the problems when it gets to hydrolysis of its salts or complexes. Owing to its much higher electropositive charge, in comparison with that of Si, it is very susceptible to nucleophilic attack from H_2O. Fast hydrolysis of Ti compared to that of Si hinders the preparation of homogeneously mixed SiO_2-TiO_2.

Kakihana et al. [59] carried out an exhaustive study of titanium peroxo complexes and they concluded that these compounds are suitable precursors for synthesis of various TiO_2 structures even in water medium. The reports on silica-titania preparation from peroxo complexes of titania are scarce, however it was demonstrated that one can control a degree of homogeneity in the SiO_2-TiO_2 system [226]. The mutual mixing of two oxide species is another important factor to be considered in synthesis of photocatalytically active materials.

Titanium atoms are able to isomorphically substitute Si^{4+} in SiO_2, and also titanium oxo-species can be dispersed within highly porous silica matrix. These two phenomena provoke retardation of titania crystal growth or formation of small TiO_2 nanocrystals with large amount of defect sites caused by the interaction with SiO_2 units. Such effects, although favorable for catalytic application, are undesirable in photocatalysis, where high semiconductor crystallinity is required. The above mentioned fact states a difficult problem of obtaining silica-titania composite, where high content of TiO_2 crystalline phase would meet the benefits silica contributes to the mixed oxide such as high surface area, mesoporosity and surface hydroxylation.

In the following work, the stated problem is solved by applying two-step sol-gel-hydrothermal process using stable, inexpensive and widely available Si and Ti inorganic sources sodium silicate and titanium oxysulfate, respectively. On the first synthetic stage a water-based titanium peroxo complex containing certain quantity of oligomeric silica species is produced. The subsequent hydrothermal treatment allows obtaining highly crystalline TiO_2 anatase nanoparticles covered with a thin silica layer. The synthetic conditions are chosen such as to inhibit the incorporation of Ti-species into silica and to promote titania crystal growth. The thorough study of the properties of the prepared materials using XRD, XPS, FTIR, and ^{29}Si MAS-NMR methods along with the test of photocatalytic properties of silica-titania samples reveals the mechanisms of the composite formation and the causes of superior photocatalytic performance of the mixed oxide over pure TiO_2. According to the obtained data, highly hydroxylated silica species attached to the surface of titania crystals adsorb pollutant molecules in the proximity of the surface of photocatalytically active titania.

Article I

"A Hydrothermal Peroxo Method for Preparation of Highly

Crystalline Silica-Titania Photocatalysts"

A hydrothermal peroxo method for preparation of highly crystalline silica–titania photocatalysts

CrossMark

Igor Krivtsov [a,b,*], Marina Ilkaeva [a,c], Viacheslav Avdin [b,c], Sergei Khainakov [a], Jose R. Garcìa [a], Salvador Ordòñez [d], Eva Dìaz [d], Laura Faba [d]

[a] Department of Organic and Inorganic Chemistry, University of Oviedo, Julian Claveria s/n, Oviedo 33006, Spain
[b] Nanotechnology Education and Research Center, South Ural State University, Lenina Ave. 76, Chelyabinsk 454080, Russia
[c] Department of Chemistry, South Ural State University, Lenina Ave. 76, Chelyabinsk 454080, Russia
[d] Department of Chemical and Environmental Engineering, University of Oviedo, Julián Clavería s/n, Oviedo 33006, Spain

GRAPHICAL ABSTRACT

ARTICLE INFO

ABSTRACT

A new completely inorganic method of preparation of silica–titania photocatalyst has been described. It has been established that the addition of silica promotes crystallinity of TiO_2 anatase phase. Relative crystallinity and TiO_2 crystal size in the silica–titania particles increase with the silica content until SiO_2/TiO_2 molar ratio of 0.9, but at higher molar ratios they start to decrease. The single-source precursor containing peroxo titanic (PTA) and silicic acids has been proved to be responsible for high crystallinity of TiO_2 encapsulated into amorphous silica. It has been proposed that peroxo groups enhance rapid formation of crystalline titania seeds, while silica controls their growth. It has been concluded from the TEM that the most morphologically uniform anatase crystallites covered with SiO_2 particles are prepared at SiO_2/TiO_2 molar ratio of 0.4. This sample, according to ^{29}Si NMR, also shows the high content of hydroxylated silica Q^3 and Q^2 groups, and it is the most photocatalytically active in UV-assisted decomposition of methylene blue among the tested materials. It has been determined that the increase in the amount of the condensed Q^4 silica in the mixed oxides leads to the decrease in photocatalytic performance of the material, despite its better crystallinity. High crystallinity, low degree of incorporation of Ti atoms in SiO_2 in the mixed oxide and adsorption of methylene blue in the vicinity of photoactive sites on the hydroxylated silica have been considered as the main factors determining the high degradation degree of methylene blue in the presence of silica-titania.

© 2014 Elsevier Inc. All rights reserved.

1. Introduction

Titania is an excellent photocatalyst, whose applications, properties, structural and morphological features are well known and summarized in the number of comprehensive reviews [1–12]. However, the search for the procedures able to ensure TiO_2 with better qualities for photocatalytic applications is still a key issue. Recently, the industry and researchers have turned towards

"green" and more economically reasonable technologies. In the field of oxide materials it means that alternative ways for preparation of oxides have to be found, instead of the most widespread alkoxide-based procedures. As a consequence, several reviews on the utilization of peroxo complexes of transition metals [13] and titanium in particular [14,15] have been published. Water-soluble peroxo complexes of transition metals are considered as "green" and inexpensive sources of nanostructured metal oxide catalysts, since application of toxic alkoxides or solvents and organic ligands is not needed. Aqueous titanium peroxo complexes can exist in the wide range of pH values in low-nuclear forms, which allows controlling their phase composition, obtaining 100% pure anatase, rutile or brookite phases [16,17]. Also the peroxo route of TiO_2 synthesis is found to be flexible enough to control shape, sizes and preferential orientation of titania crystals [18–22]. In spite of the fact that this method is inexpensive and allows controlling various titania properties, it has seldom been applied for preparation of mixed silica–titania oxides, which could posses improved photocatalytic properties. The information on application of the peroxo route to SiO_2/TiO_2 synthesis is scarce; being limited to the thin film preparation or impregnation of the preformed silica colloidal particles with titanium peroxo complex [23]. However, modification of titanium oxide with silica is a widespread method [24] aiming to increase the thermal stability of its most photocatalytically active polymorph anatase [25], tune the sizes of its crystals [26], increase the surface area [27], improve adsorption properties [26], and introduce mesoporosity to the mixed SiO_2/TiO_2 material [28]. This modification can be achieved by preparation of a highly homogeneous mixed oxide [29], by covering the preformed crystalline titania particles with silica layer [30], or making it otherwise, crystallizing anatase on the surface of colloidal SiO_2 spheres [31]. Sol–gel technique is found to be the most applicable to the abovementioned purposes. Hydrothermal method, on the other hand, is less common for SiO_2/TiO_2 particles preparation; only several reports on the application of this procedure were published [26,32,33].

Besides the obvious advantages that silica contributes to the mixed silica–titania, it also gives a significant drawback. As a rule, silica in the mixed oxide causes formation of defects and suppresses the growth of TiO_2 crystals [29,34–37]. However, it is known that high crystallinity is an important feature, as the electron pairs recombination takes place on the crystalline defects; this reduces the activity of the photocatalyst [38–40]. In spite of a common view attributing the enhancement of the photocatalytic activity to the decrease of the anatase particles [41,42], it might be supposed that the increase of the TiO_2 crystal sizes could favor lowering recombination rate and improve its catalytic properties. The benefit that silica introduces to the mixed oxide is difficult to combine with high crystallinity of TiO_2. In order to achieve reasonable crystallinity in silica–titania, heat treatment at temperatures up to 800 °C is applied [25]. However, we have not found any reports on the preparation of highly crystalline SiO_2/TiO_2 oxides under mild conditions. In the present study we describe a new method of silica–titania particles synthesis and the unusual effect that silica has on the crystallization of TiO_2 under hydrothermal conditions, as it promotes titania crystallinity rather than suppresses it. The test of the prepared materials in the photocatalytic degradation of methylene blue dye shows their high activity.

2. Experimental

2.1. Chemicals

Non-volatile and stable under ambient conditions titanium oxysulfate hydrate ($TiOSO_4 \cdot H_2O$), containing not more than 17 wt% of sulfuric acid, and 27 wt% solution of sodium silicate ($Na_2Si_3O_7$) in water were purchased from Aldrich and used as the sources of titania and silica, respectively. Sodium hydroxide (Prolabo, 99% purity) was used as precipitation agent, 20% ammonia solution in water (Prolabo) and nitric acid (Prolabo) were applied for pH correction. Hydrogen peroxide 30 wt% solution was obtained from Aldrich. Methylene blue was of analytical grade.

2.2. Synthesis

On the first stage of the synthesis, 50 mL of sodium silicate solution with concentrations: 0.0, 0.025, 0.05, 0.1, 0.14 and 0.18 mol/L was added to 50 mL of 0.1 M solution of $TiOSO_4$. The samples were designated as 0TS, 0.1TS, 0.4TS, 0.9TS, 1.3TS, and 1.6TS (where the numbers indicate SiO_2/TiO_2 molar ratio in the synthesized samples, determined by elemental analysis). Then the mixtures were hydrolyzed with 1.5 M solution of sodium hydroxide, the addition of NaOH ended when the pH value reached 3.2 (4.0 for 0TS and 0.1TS). The gel-like precipitates obtained after alkali addition were centrifuged at 3000 r.p.m. and thoroughly washed with deionized water eight times, until the negative reaction on sulfate ions. On the next stage, 0.5 mL of 3 M ammonia was added to the precipitate following by ultrasonication in 50 mL of distilled water. Then to the dispersed precipitates 4 mL of H_2O_2 solution was added and the pH of the reaction mixtures was adjusted to 7.0 by the addition of ammonia solution in order to obtain water-soluble titanium peroxo complexes. Soon, the clear transparent yellow solutions of titanium peroxo complex and silicic acid were formed. The findings concerning dissolution of silica–titania hydrogel in hydrogen peroxide were described elsewhere [43,44]. The pH of the solution was adjusted to 7.0 with ammonia. After that, 3 M nitric acid was dropwise introduced to the solution until pH reached the value of 2.0. It is worth mentioning that after the addition of acid all solutions stayed clear with an exception of the samples 0TS and 0.1TS, where the formation of sol was observed. Then the volume of the prepared mixtures was adjusted to 80 mL by deionized water and they were transferred to Teflon-lined stainless steel autoclaves having total volume of 140 mL for hydrothermal treatment. Hydrothermal treatment was carried out under autogenic pressure at 180 °C during 48 h. In order to establish the role of the precursor, silica–titania materials with the equimolar SiO_2/TiO_2 composition in the reaction mixture, were also synthesized under conditions of pH not being controlled by ammonia and nitric acid addition (PTA–SiO_2), by hydrothermal treatment of the gel in the absence of hydrogen peroxide after ammonia and nitric acid were added (GelTS), and using separately prepared titanium peroxo complex and sodium silicate solution (NH_3PT–SiO_2). When the treatment was over, the precipitates were isolated by centrifugation at 3000 r.p.m., washed with deionized water eight times and dried at 60 °C for 24 h. In order to eliminate adsorbed water, the samples were calcined in static air at 400 °C for 2 h, but a part of each sample was left as-synthesized as well.

2.3. Characterization

X-ray diffraction patterns were registered using Rigaku Ultima IV diffractometer, operating at Cu K_α radiation (λ = 0.15418 nm) at voltage of 30 kV with a help of high-speed DTEX detector. Scherrer equation was applied to estimate the mean crystallite size of TiO_2 by the (101) reflection, the uncertainty of the estimation is near 5%. Unit cell parameters for anatase crystals were refined using GSAS software [45]. Relative crystallinity was estimated from the ratio of anatase peak intensity of (101) reflection to that of the 0TS sample calcined at 400 °C [46,47]. Scanning electron microscope Jeol JSM 7001F with Oxford Instruments EDS-attachment was used to investigate morphology and to determine elemental

composition of the prepared materials. The samples were preliminary coated by magnetron sputtering with approximately 3 nm thick gold layer Transmission electron microscopy (TEM) images were carried out using a Jeol 200 EX-II and a Jeol JEM 2100F, the elemental composition of the particles was obtained by EDS-attachment to the microscope. The samples were dispersed in ethanol and then few drops of the suspension were put on a copper grid prior to investigation Infrared spectra were collected from the samples powdered with KBr and pressed in pellets, by Bruker Tensor 27 FTIR spectrometer. Diffusive-reflectance ultraviolet–visible light (DR UV) spectra were registered from the powdered samples supported on barium sulfate pellets in a Shimadzu UV-2700 UV–vis spectrophotometer with an integrated sphere attachment. Band gap energy was determined from the DR UV spectra by Kubelka-Munk method. Micromeritics ASAP 2020 was used to obtain adsorption–desorption isotherms of N_2 at 77 K. The surface area and pore volume were calculated from the low-temperature nitrogen adsorption data using BET and BJH approaches. Prior to the experiment the samples were degassed under vacuum at 400 °C for 4 h. The solid state ^{29}Si MAS NMR and ^1H–^{29}Si cross-polarization MAS NMR (CPMAS) measurements were recorded on a Bruker Avance III 400WB spectrometer at 79.49 MHz for ^{29}Si. The experiment was done at ambient temperature with a sample spinning rate of 4500 Hz (45° pulse width of 2.5 µs). For calibration of the ^{29}Si signal position Q8M8 reference material was used. For the NMR MAS measurement a pulse delay of 180 s was chosen, and the number of scans was 3000. For the CPMAS NMR experiment a pulse delay was 5 s, and the number of scans was 1000. The surface composition and binding energy of Si, Ti and O in pure titania and mixed oxides were measured by X-ray Photoelectron Spectroscopy (XPS), using a SPECS system equipped with a Hemispherical Phoibos detector operating in a constant pass energy, using Mg Kα radiation ($h \cdot \upsilon = 1253.6$ eV). The content of sulfur was determined using CHNS Elementar vario MACRO analyzer.

2.4. Photocatalytic activity test

Synthesized silica–titania materials were tested in the aqueous-phase photocatalytic degradation of methylene blue (MB) in a stirred batch reactor. For the experiment 25 mg of each sample calcined in air at 400 °C for 2 h was taken into a quartz reactor. Then 50 mL of the aqueous solution of MB with concentration 20 mg L^{-1} was added to the catalyst. Firstly, the adsorption of MB by the catalyst was determined, for this the suspension was magnetically stirred in the dark until it reached the adsorption equilibrium (for the Degussa P25, 0TS, 0.1TS, 0.4TS and 0.9TS the equilibrium was reached after 30 min, while longer time was needed to the 1.3TS and 1.6TS samples), then the concentration of MB was photometrically determined by the absorbance at 664 nm using Shimadzu UV-2700 spectrophotometer. After the dark experiment the suspension was exposed to ultraviolet irradiation. The source of UV-light was the Osram high-pressure mercury 125 W lamp. It was equipped with the visible-light filter, which decreased the lamp's photon flux by half. The suspension of the sample and MB solution was constantly mixed and cooled. After irradiation started, the aliquots of 5 mL were taken every 30 min during the first 150 min of the experiment and then every 60 min to the total of 330 min. The solution was separated from the catalyst at 8000 r.p.m. using air-cooling centrifuge, and concentration was photometrically determined (absorbance measured at 664 nm). Then the solution and the catalyst were returned back to the reactor, and irradiation continued. Photolysis of the MB solution was carried out under the same experimental conditions, but in the absence of a catalyst. The error of MB concentration determination, calculated from the data obtained for replicate runs, did not exceed 7%. The total organic carbon (TOC) was measured using

Shimadzu TOC-V CSH Analyzer for the MB solution and the most active sample after 330 min of irradiation.

3. Results and discussion

3.1. EDS and XRD study of SiO_2/TiO_2 particles

When the samples were recovered after hydrothermal treatment, their elemental compositions were analyzed by EDS method. The slight decrease in silica content after synthesis in comparison with the one in the reaction mixture was observed for all of them. The variations between the SiO_2/TiO_2 molar ratios in the reaction mixture and in the solid phase are shown in Table 1. Despite the pH of the reaction mixture after synthesis equaling 3.0 for all the samples, which is explained by decomposition of PTA during heat treatment, the concentration of silica left in the solution is too small to polymerize and it has been removed at washing. Elemental CHNS analysis has proved the absence of sulfur in the prepared silica–titania materials (<0.1 wt%), with the exception for the pure TiO_2 and the 0.1TS samples, where *ca* 1 wt% of sulfur has been detected.

Anatase is known to be the most photocatalytically active polymorph of TiO_2. The increase in its crystallinity and crystallite size could results in lowering the recombination rate, hence provide better photocatalytic activity. That is why the determination of the TiO_2 crystalline phase and its crystal sizes is of great importance. The XRD data (Fig. 1) reveal that all the samples contain only the anatase phase of TiO_2 (ICDD PDF2 99-101-0957), except 0.9TS, where near 2 wt% of rutile phase (ICDD PDF2 99-101-0954) is detected. The as-prepared samples and the ones calcined at 400 °C show no differences in their structural features, crystallite sizes, or any other properties determined by spectroscopic techniques. For the sake of comparison three other silica–titania samples (PTA–SiO_2, GelTS and NH_3PT–SiO_2) have been synthesized, using different combinations of the reagents, and their XRD patterns have been registered (Supplementary Information Fig. S1). From Table 1, where the crystallite sizes estimated by (1 0 1) reflection for the anatase phase using Scherrer equation are presented, it is clear that the sizes of anatase crystals and relative crystallinity are significantly higher in the SiO_2/TiO_2 mixed oxides synthesized by the proposed peroxo route, than they are for the gel subjected to hydrothermal treatment (GelTS), separately prepared titanium peroxo complex and sodium silicate (NH_3PT–SiO_2), or for the sample prepared without any pH adjustment after hydrogel dissolution (PTA–SiO_2). The samples prepared via non-peroxo route were excluded from the further study on the basis of they poorer crystallinity.

Addition of silica has been found to have no significant effect on the changing of *a*-parameter of the TiO_2 unit cell; however, *c*-parameter shows noticeable variations (Table 1). The decrease in the anatase unit cell volume might indicate the formation of Si–O–Ti linkages causing the formation of defects. The lowest value of *c*-parameter is observed for 0.4TS. The variation of this dimension at high silica loadings is not so significant, taking the calculation error into account.
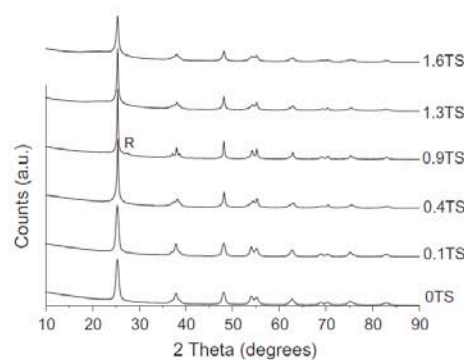
The formation of titania crystallites of larger size, while using the single-source precursor containing titanium peroxo complex and silicic acid, compared to the methods applied to prepare GelTS, PTA–SiO_2 and NH_3PT–SiO_2, can be explained in the following way. The conventional sol–gel or co-precipitation procedures, that routinely serve to synthesize SiO_2/TiO_2 materials, lead to formation of the mixture, which is very homogeneous on the molecular level [25,29]. It is suggested that the incorporation of titania into silica matrix takes place, thus resulting in retardation of TiO_2 crystallization up to high temperatures, and decreased crystallite size of

Table 1
The elemental composition, mean crystallite size, calculated by Scherrer equation, relative crystallinity and the unit cell parameters for anatase in the silica–titania samples (confidence interval of unit cell parameters in brackets).

Sample	Reaction mixture SiO$_2$/TiO$_2$ molar ratio	Solid phase SiO$_2$/TiO$_2$ molar ratio	Mean crystallite size (nm)	Relative crystallinity	Unit cell parameters (Å)	
					a	c
0TS	0	0	10	1	3.785(1)	9.502(1)
0.1TS	0.2	0.1	13	1.12	3.784(4)	9.499(1)
0.4TS	0.5	0.4	24	1.49	3.777(1)	9.428(2)
0.9TS	1.0	0.9	33	1.55	3.782(4)	9.464(3)
1.3TS	1.4	1.3	26	1.37	3.782(1)	9.450(1)
1.6TS	1.8	1.6	16	1.02	3.781(5)	9.459(1)
PTA–SiO$_2$	1.0	0.9	22	1.24	3.784(5)	9.463(5)
GelTS	1.0	1.0	17	1.26	3.780(1)	9.491(3)
NH$_3$PT–SiO$_2$	1.0	0.9	20	1.22	3.781(3)	9.456(2)

Fig. 1. XRD patterns of the silica–titania samples. R – indicates the reflection corresponding to the rutile phase (all the other peaks correspond to anatase).

Table 2
XPS surface composition of the mixed oxides and a relative ratio of the silica species obtained from NMR data.

Sample	Si:Ti surface ratio (at%)	$Q^1/Q^2/Q^3/Q^4$ Ratio from ^{29}Si MAS NMR
0TS	0	
0.4TS	1.5:1	1/1.2/7.2/7.3
0.9TS	3.4:1	–/1/4.2/12.3
1.6TS	6.9:1	

3.2. XPS, ^{29}Si MAS NMR, FTIR and DR UV spectroscopic studies

It is obvious now that silica modifies the crystal structure of anatase and controls the sizes of TiO$_2$ crystals. However, the role of silica species is still unclear, as it is present in the samples in the amorphous state and cannot be established by XRD analysis only. XPS gives some valuable information about the interactions of silica and titania units in the mixed oxides and their surface composition. Silica enriches the surface regions of the silica–titania samples (Table 2), thus making SiO$_2$ species mainly responsible for the adsorption processes on the silica–titania particles. The shifting of the Ti 2p peak on the XPS spectrum (Fig. 2a) with the increasing silica content indicates the substitution of Si atoms in the SiO$_2$ network by Ti ones. The displacement of this maximum for the 0.4TS and 0.9TS samples in comparison with 0TS is not significant due to high crystallinity of TiO$_2$ in the mixed oxides, and as a consequence low degree of Ti incorporation in the silica matrix. At the same time the obvious decrease of binding energy of Ti in 1.6TS correlates with its low crystallinity, as it reflects the incorporation of Ti^{4+} ions in silica matrix. The variations of the binding energy of oxygen are of particular interest in such systems. The band of O ion of Ti–O–Ti and Si–O–Si matrices is observed at 530.5 and 533.5 eV respectively, and the intermediate value of the binding energy is often attributed to the oxygen of Si–O–Ti bonds [24]. It is assumed that the increase of silica content in the mixed oxide gradually shifts the peak of oxygen to higher binding energies. However the peak of oxygen is split in two on the spectra of the mixed oxides with 0.4 and 0.9 SiO$_2$/TiO$_2$ molar ratios, indicating on the separation of oxide phases due to high crystallinity of TiO$_2$ anatase (Fig. 2b). When the SiO$_2$/TiO$_2$ molar ratio is increased up to the value of 1.6, the presence of Si–O–Ti linkages becomes evident, as the peak of O 1s is found at 532 eV. From the data obtained by XPS one can conclude that the lowest content of Si–O–Ti bonds is found in the 0.4TS sample.

Although, XPS data say in favor of the separation of the two oxides in the mixed one, more clear understanding of the state of silica is required. The form of the silica species and some information about silicon local structure can be obtained from the solid state ^{29}Si NMR. Two samples with high crystallinity and separation degree of the oxides were investigated using this method. Fig. 3
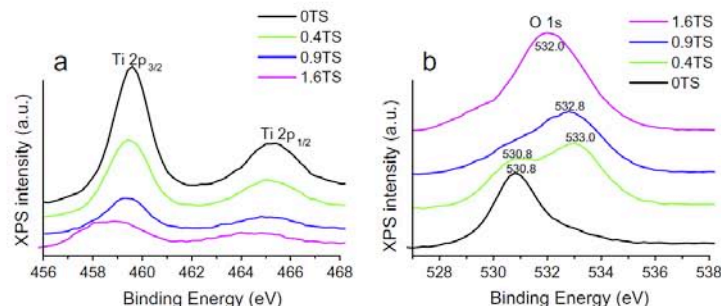
anatase [25]. However, in the case of the precursor used, one can propose a different interaction mechanism of silica and titania. During the co-precipitation stage Si–O–Ti heterolinkages are formed, but the addition of hydrogen peroxide and ammonia causes their cleavage, and titanium peroxo complex is obtained, while silica stays in oligomeric forms [44]. As Si–O–O–Ti bridges are not likely to appear in this system [48], the degree of titania incorporation in SiO$_2$ matrix would be less than it is while conventional preparation techniques are applied. When the precursor solution undergoes heating, several processes take place. The rate of hydrogen peroxide and peroxo group decomposition increases drastically, and small seeds of titania are formed. On this stage the state of titania source plays an important part, as it is known that the peroxo method allows decreasing the temperatures of anatase crystallization from the amorphous PTA precursor in comparison with amorphous titania [49]. The initial pH value of 2.0 is determined to be the point when the silica polymerization is low [50], that is why, instead of formation of Si–O–Si network in the whole volume of the reaction mixture, silica species are preferably adsorbed on the surfaces of the formed TiO$_2$ particles, thus the titania seeds become separated by SiO$_2$ layer. The rate of diffusion of the dissolved low-concentrated titania species through the silica layer surrounding TiO$_2$ crystallites is low, and these conditions favor growth of the crystals already existing in the mixture, instead of the formation of new small seeds. The optimal conditions for crystal growth at the given concentrations of silica and titania are reached when the SiO$_2$/TiO$_2$ ratio in the solid phase equals 0.9. It is likely that the further increase in silica content favors more rapid polymerization of silica, resulting in the assembling of more rigid SiO$_2$ network, where diffusion is too hindered to provide the growth of large crystals.
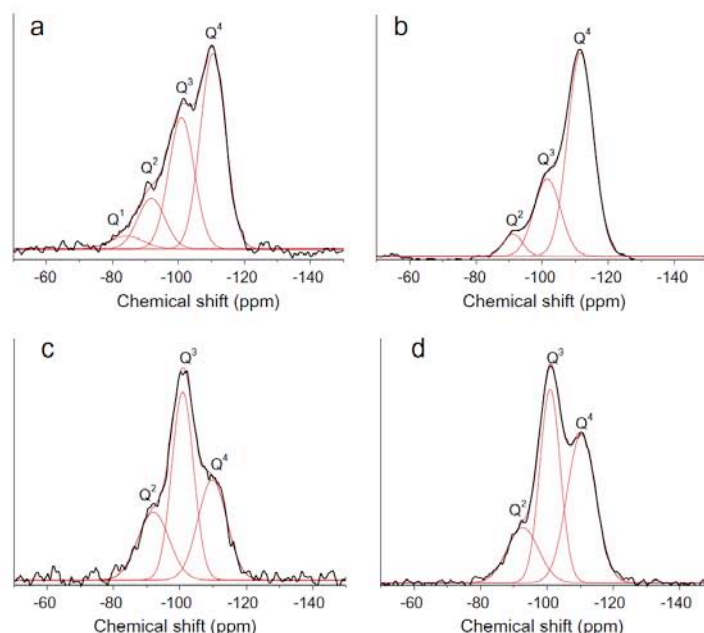
Fig. 2. XPS spectra of Ti 2p (a) and O 1s (b) regions.

Fig. 3. ^{29}Si MAS and ^{29}Si–^{1}H CPMAS NMR spectra of the (a) 0.4TS, (b) 0.9TS and (c) 0.4TS, (d) 0.9TS samples respectively.

shows the ^{29}Si MAS NMR and ^{29}Si CPMAS NMR spectra of the most crystalline 0.4TS and 0.9TS samples, where the peaks at chemical shifts of approximately 110, 101, and 90 ppm, attributed to the different silica species, are clearly resolved. From Fig. 3a and b it is obvious that the 0.4TS sample contains less amount of highly condensed Q^4 [Si(SiO)$_4$] than its amount in the 0.9TS one (the ratios of the Q^4, Q^3, Q^2 and Q^1 species, calculated from the deconvoluted spectra, are shown in Table 2). The higher content of the low condensed silica can be caused by incorporation of Ti atoms into the SiO_2 matrix, thus forming Si–O–Ti linkages [29], but also by high dispersion of silica particles on titania. Nur observed formation of low condensed units, such as Q^2, after colloidal silica had been dispersed onto preformed titania particles [51]. The influence of Ti incorporation into SiO_2 and OH groups on the chemical shift can be distinguished using ^{29}Si CPMAS NMR. In the case that Ti incorporation gave the main contribution into the formation of Q^2 and Q^3 groups, the enhancement of the intensity of these signals on ^{29}Si CPMAS NMR spectra would be insignificant, but a different picture is seen in Fig. 3c and d. The obvious increase in intensity at

101 and 90 ppm on the spectra of the both samples is clear, while the signal corresponding to Q^1 is not enhanced. This means that the most part of the silicon nuclei is directly bonded to hydroxyl groups, but the silicon of Q^1 species is possibly attributed to the presence of Si–O–Ti. The results of the solid state NMR are in good agreement with those obtained from XPS, as they confirm high degree of separation of silica and titania on the molecular level in the mixed oxides. Moreover, it has been shown that the 0.4TS sample contains higher amount of hydroxyl groups of silica Q^3 and Q^2 species, than the 0.9TS one. However, the presence of Si–O–Ti bonds should not be totally excluded, since they have to be present in some quantities, in order to provide attachment to the surface of titania particles.

The FTIR spectra of the 0TS and 0.1TS samples are almost featureless, only the weak bands corresponding to SO_4^{2-} groups at 1100 cm^{-1} and the broad band centered at 670 cm^{-1}, attributed to vibrations in octahedral TiO_6, are worth mentioning (Fig. 4). The asymmetric stretching vibrations of Si–O–Si bridges at 1070 cm^{-1} in silica become clearly seen and as intense as Ti–O–
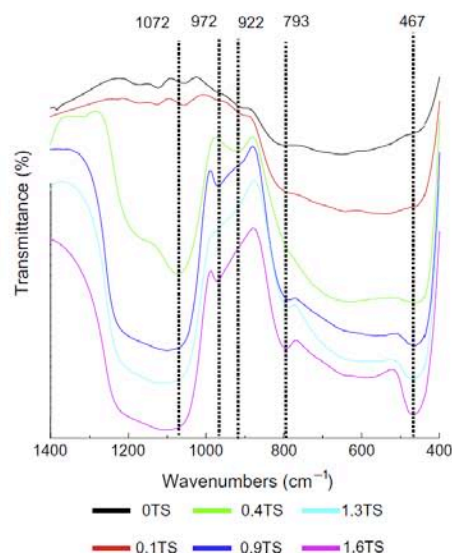
Fig. 4. FTIR spectra of the silica–titania samples.

Ti stretching on the spectrum of the sample with SiO_2/TiO_2 molar ratio equaling 0.4. The peak of Si–O–Si symmetric stretching vibrations near 790–800 cm^{-1}, usually present in the spectra of silica compounds, is not observed on the spectrum of the 0.4TS sample, which can be considered as the indication of the low quantity of highly condensed silica species (Q^4) due to small silica loading and its high dispersion on titania particles. The spectrum of 0.4TS sample shows no presence of this band, while for 0.9TS a peak in this region is observed showing the presence of the condensed SiO_2 network. The bands at 793 cm^{-1} and 467 cm^{-1} increase their intensity and become more prominent with the increase of silica content, and the peak of the asymmetric stretching of Si–O–Si (1100–1070 cm^{-1}) shifts towards higher wavenumbers. It might be suggested that the sample 0.4TS contains lower amount of highly condensed silica, which is in accordance with NMR study. The absorption in the region of 920–980 cm^{-1} corresponds to the joint contribution from silanol groups and Si–O–Ti heterolinkage vibrations, according to numerous reports [25,29,52]. However, the position of this peak is different for 0.4TS and the samples with higher silica content. Considering the XPS results, which evidence the separation of SiO_2 and TiO_2 in the 0.4TS sample and clearly indicate the formation of Si–O–Ti linkages in the 1.6TS sample, one can conclude that the shifting of the peak from 922 cm^{-1} (for the 0.4TS sample) to 972 cm^{-1} (for the 1.6 sample) is assigned to the increasing contribution of Si–O–Ti bond vibration. This feature is more likely to correspond to the higher incorporation degree of Ti atoms into silica network.

The other spectroscopic technique used for the characterization of materials allows calculating band gap energy of semiconductors, which is a feature of high importance for photocatalysts. Expectedly, the band gap energy increases, as the silica content in the SiO_2/TiO_2 samples rises, but this relationship is not linear (S.I. Fig. S2). The widening of the band gap reflects the defectiveness of anatase structure; however the difference of the band gap energy between pure titania and silica–titania is not large. Li and Kim [27] found that the addition of silica caused significant blue shift of the absorption edge, as silica containing samples possessed band gap energy of 3.54 eV, while for pure TiO_2 that value equaled 3.20 eV. In our case not so significant change in the band gap

energies can be attributed to high crystallinity of the anatase in the mixed oxides.

### 3.3. Surface area and porosity measurements

Special attention of the researchers, investigating photocatalytic properties of titania, is attracted to its porous characteristics. Usually, highly crystalline anatase has low surface area [53–55], only seldom exceeding 100 m^2/g [56], which hinders accessibility of active sites for organic molecules. Silica provides TiO_2 with such indispensable properties as mesoporosity and developed surface that result, according to some reports, in enhanced photocatalytic activity [57,58]. We have found the effect of silica addition, when the proposed peroxo route is used, to be different to that is usually observed for the sol–gel materials. The synthesized titania (0TS) shows isotherm type IV with H2 type of the hysteresis loop, typical of mesoporous solids, according to IUPAC classification (Fig. 5a). This sample, having crystallite size of 10 nm, expectedly has high value of surface area (Table 3) and also narrow pore size distribution (S.I. Fig. S3a). Silica at low loadings does not make the surface of the mixed oxide more developed; on the contrary, the surface area of 0.4TS has smaller value in comparison with pure TiO_2 (Table 3). The reduction of the surface area for 0.4TS is undoubtedly related to the increase of TiO_2 crystallite size. The 0.4TS and 0.9TS samples have the isotherm type IV and barely distinguishable hysteresis loops of H1 type (Fig. 5b and c). Pore size distribution analysis has shown the presence of the meso- and macropores (0.9TS sample exhibits two maximums in the pore size distribution, one corresponding to mesopores and another to macropores) in these samples (S.I. Fig. S3b and c), which are likely to be attributed to the interparticle voids. Higher silica content favors developing the surface area of the mixed oxide. The mixed oxide with the highest SiO_2/TiO_2 molar ratio has surface area slightly exceeding the same value obtained for 0TS (Table 3). It is also noticeable that the form of the hysteresis loop is different than it is for previously discussed samples. The H1 type hysteresis loop (Fig. 5d) indicates the formation of mesopores, which are in the range of 10–50 nm (S.I. Fig. S3d).

Silica has a drastic effect on the porosity and surface area of the mixed oxides: it promotes TiO_2 crystallinity and bonds to the anatase crystals forming larger particles, the pores in which are partially blocked by the SiO_2, thus contributing to decrease of the surface area. After the highest degree of silica coverage of TiO_2 particles has been reached, as it is for the 0.4TS sample, SiO_2 starts to form more condensed network, which is confirmed by NMR study, leading to the enhanced surface area of the mixed oxide (0.9TS and 1.6TS) and appearance of mesoporosity at high loadings of SiO_2 (1.6TS).

3.4. SEM and TEM investigations

The evolution of morphology of the prepared mixed oxides is seen in Fig. 6. Pure titania sample (Fig. 6a) is composed of small particles assembled in large shapeless aggregates. The particles of the 0.4TS sample are well separated from each other; they have spherical or slightly elongated forms (Fig. 6b). The most crystalline sample 0.9TS (Fig. 6c) has some similarity to the 0.4TS; however, it is not so uniform. Further increase in silica content results in formation of the dispersed small grains of the mixed oxide surrounding the larger particles (Fig. 6d). The samples 0.4TS and 0.9TS are represented by the aggregates with the mean size 70–90 nm, composed of small spheres having diameter about 10 nm. This observation is inconsistent with the XRD data, as it has been determined that the crystalline sizes of TiO_2 in these samples, calculated by (1 0 1) reflection, equal 24 and 33 nm, respectively. Such disagreement forces us to conclude that these particles are titania
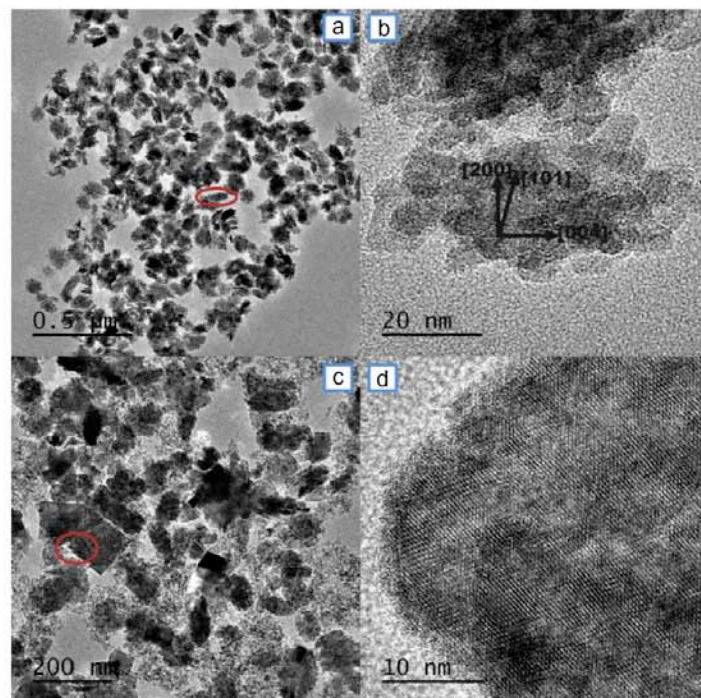
Fig. 7. TEM-images of the 0.4TS sample: (a) a general image of the sample, (b) high resolution micrograph; and the 0.9TS sample: (c) a general image of the sample, (d) high resolution micrograph.

[1 0 1] directions is estimated to be equal to 2.2. These changes in morphology of this sample are likely to be responsible for the significant difference of the unit cell parameter (Table 1), as the effect of silica incorporation seems to be less probable in a view of the XPS results.

The greater amount of silica in the mixed oxide samples has resulted in larger crystallites of TiO_2, and has also caused separation of pure silica particles from anatase crystals. Titania exists in the form of crystals having various shapes and sizes, each of them is covered with a layer of adsorbed silica particles (S.I. Fig. S6).

Mostly the particles of the 1.6TS sample are the agglomerates of small titania crystallites, where crystalline anatase is embedded in amorphous SiO_2 matrix. They do not possess any definite shape and the material resembles the one usually obtained in the result of conventional sol–gel procedure. However, the presence of large crystals, similar to those observed for 0.9TS sample, is noticeable (S.I. Fig. S7).

Summarizing the results obtained from different characterization techniques, the following formation mechanism of silica–titania particles can be proposed. In absence of silica titania peroxo species condense rapidly with each other and the solid phase is formed, even the appearance of the sol in the acidic medium indicates that they tend to coalesce. This limits the crystal sizes of TiO_2 within 10 nm, thus the material has high surface area, and uniformity of the particles provides unimodal pore-size distribution (S.I. Fig. 3a). The addition of silica results in its adsorption on the titania species, thus decreasing the rate of their condensation and preventing coalescence. This slows down the crystallization process. It is also important to mention that the Si–O–Ti linkages are cleaved by addition of hydrogen peroxide and PTA and silicic acid present in the reaction mixture separately [44]. These two important features provide slower crystal growth, where the diffusion of dissolved titania species towards formed seeds is controlled by the

layer of silica particles formed on their surfaces. At this stage of synthesis the low pH value plays an important part, as silica has low polymerization rate at these conditions [50], so it does not form rigid network around TiO_2 seeds. Indeed, silica in this material is not in the highly condensed state that is evidenced from NMR study. Silica particles cover the titania crystals with a thin amorphous layer having high concentration of hydroxyl groups in the vicinity of the photocatalytically active TiO_2.

It is reasonable that the ability of TiO_2 crystals to accommodate silica species on their surface is limited. When the SiO_2/TiO_2 ratio reaches 0.9, the presence of highly condensed silica becomes obvious from NMR data. We attribute the increase in crystallinity in this sample to the slower rate of condensation of titania species and slower diffusion of dissolved species towards the formed seeds through the silica layer. At this point the mechanism of formation of silica–titania particles changes. In the 1.6TS sample the polymerization of SiO_2 goes faster due to its higher concentration in the reaction mixture, so the mixture of small and large crystallites of TiO_2 embedded in the amorphous SiO_2 is formed. The incorporation of Ti atoms into silica network reaches the highest degree for all investigated samples, which suppresses TiO_2 crystallinity.

3.5. Photocatalytic test

The photocatalytic properties of the prepared mixed oxides are found to be enhanced in comparison with pure titania synthesized under the same conditions and Degussa P25. In Fig. 8a one can see the general trend of MB photodegradation on the titania and silica–titania catalysts. It is noticeable that the 0.4TS and 1.6TS samples have the highest adsorption capacity for MB due to the thin layer of hydroxyl-rich SiO_2 in one case and the presence of Ti–O–Si linkages causing more amorphous character of the oxide in the other (Table 4). The increased crystallinity and the presence of high
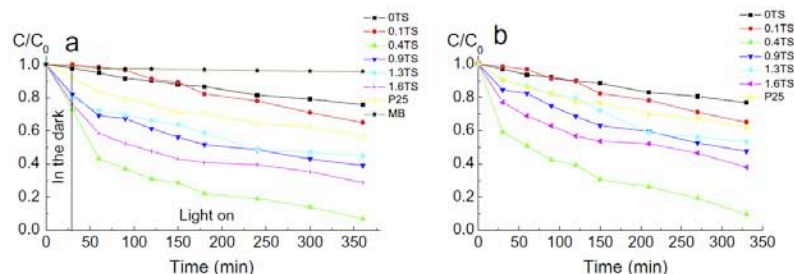
59

Fig. 8. Photocatalytic decomposition of MB solution on the titania and silica–titania materials (a) showing the values of adsorption of MB on the samples; (b) excluding adsorption stage.

Table 4
First-order kinetic constant (min^{-1}) of MB degradation and adsorption capacity for MB of the pure titania and silica–titania samples.

Sample	0TS	0.1TS	0.4TS	0.9TS	1.3TS	1.6TS	Degussa P25
k_1 (ks^{-1} L g TiO$_2^{-1}$)	0.031	0.043	0.288	0.130	0.104	0.200	0.053
Adsorption (mmol(MB) g^{-1})	1	1	18	11	15	17	5

amount of highly condensed silica species (Q^4) reduce the adsorption capacity of the 0.9TS sample.

The clearer picture of photodecomposition process may be obtained from Fig. 8b, where the adsorption stage is excluded, and the concentration of MB left in the solution after adsorption is taken as C$_0$. The 0.4TS sample shows activity, which is superior compared with other catalysts. It adsorbs and decomposes more than 90% of MB (S.I. Fig. S8), and, according to TOC determination, 60% of carbon is removed from the solution after adsorption and photocatalysis. In order to discuss the effect of various material properties on the catalyst performance, reaction curves have been fit to a pseudo-first order reaction model (S.I. Fig. S9), the kinetic constant for each material is reported in Table 3. Other kinetic models, such as zero-th order, second order or Langmuir–Hinshelwood models have also been tested, but these models do not provide good fit of the experimental results.

As it has been described earlier, usually the enhanced photocatalytic activity of TiO$_2$ in mixed silica–titania oxides is attributed to its improved surface area and mesoporosity that silica brings to the binary system, or to the small crystal size of titania. However, it is clear for us that the influence that the porous structure has on the SiO$_2$/TiO$_2$ activity is negligible. Crystallinity of the active phase has greater influence on the MB decomposition rate. As the anatase crystal size and its relative crystallinity increase, the decomposition rate increases drastically, this is clearly seen for the 0.4TS, 0.9TS and 1.3TS samples. However, it cannot be the determinative parameter, as there is no correlation between activity and crystallinity. This leads to the consideration of another important factor, adsorption mechanism. The most photocatalytically active 0.4TS sample has the highest adsorption capacity for MB, which is not related to surface area or high silica content, but this value only slightly exceeds the one for the 1.6TS sample, so it clearly cannot be the explanation for the 0.4TS superior performance. The adsorption process and interaction of TiO$_2$ anatase with the target molecules in the 0.4TS and other silica-rich samples are not similar. It is proved by NMR and TEM analyses that silica in the 0.4TS sample is not in the highly condensed state and it uniformly covers titania crystals. Also it might be suggested that adsorption of organic molecules on the thin layer of amorphous silica is preferred, as it provides the immobilization of target molecules near the photocatalytically active TiO$_2$. Thus, MB is immobilized on the hydroxyl groups in the vicinity of highly crystalline anatase, while

in the samples with high silica loadings it is adsorbed on the silanol groups of the highly condensed SiO$_2$ network separated from TiO$_2$ crystals, which could not favor the transfer of the oxidants from anatase surface to MB.

It is difficult to define the property that determines the photocatalytic activity of silica–titania materials to the greater extent, since no direct correlations were found (S.I. Fig. S10), but it is obvious that the presence of thin silica layer rich in hydroxyls, high crystallinity of anatase and the ability to adsorb methylene blue are among the most important.

4. Conclusions

In the present study we have proposed a new completely inorganic method of preparation of the silica–titania photocatalysts, using titanium peroxo complex and silicic acid as the single-source precursor. We have found that in contrast to conventional alkoxide-based or inorganic sol–gel processes, silica does not suppress titania crystal growth; on the contrary, it favors improving TiO$_2$ crystallinity. It has been proposed that this is caused by the low degree of Ti incorporation in SiO$_2$ in the precursor and by the adsorption of silica species on the titania seeds separating them from each other, thus controlling diffusion and saturation conditions in the reaction mixture. The sample with the SiO$_2$/TiO$_2$ ratio of 0.9 has the highest relative crystallinity and the largest titania crystallite size. The sample with SiO$_2$/TiO$_2$ molar ratio equaling 0.4 is found to be the most uniform in the sense of particle size distribution, and also it has shown the superior performance in photocatalytic decomposition of methylene blue. We attribute the enhanced photocatalytic activity of the synthesized mixed oxides compared to pure TiO$_2$ to the adsorption of methylene blue on the thin silica layer rich in hydroxyls in the vicinity of highly crystalline anatase TiO$_2$.

Appendix A. Supplementary material

The XRD patterns of the PTA–SiO$_2$, GelTS and NH$_3$PT–SiO$_2$ samples, pore size distribution analysis, the results of band gap energy determination and TEM-EDS analysis of the silica–titania particles. Supplementary data associated with this article can be found, in the online version, at http://dx.doi.org/10.1016/j.jcis.2014.12.044.

References

[1] G. Liu, L. Wang, H.G. Yang, H-M. Cheng, G.Q. (Max) Lu, J. Mater. Chem. 20 (2010) 831–843.
[2] H. Chen, C.E. Nanayakkara, V.H. Grassian, Chem. Rev. 112 (2012) 5919–5948.
[3] S. Liu, J. Yu, M. Jaroniec, Chem. Mater. 23 (2011) 4085–4093.
[4] A.A. Ismail, D.W. Bahnemann, J. Mater. Chem. 21 (2011) 11686–11707.
[5] R. Daghrir, P. Drogui, D. Robert, Ind. Eng. Chem. Res. 52 (2013) 3581–3599.
[6] D.J. Stacchiola, S.D. Senanayake, P. Liu, J.R. Rodriguez, Chem. Rev. 113 (2013) 4373–4390.
[7] W.Y. Teoh, J.A. Scott, R. Amal, J. Phys. Chem. Lett. 3 (2012) 629–639.
[8] M. Pagliaro, G. Palmisano, R. Ciriminna, V. Loddo, Energy Environ. Sci. 2 (2009) 838–844.
[9] U.G. Akpan, B.H. Hameed, J. Hazard. Mater. 170 (2009) 520–529.
[10] I.A. Konstantinou, T.A. Albanis, Appl. Catal., B: Environ. 49 (2004) 1–14.
[11] Z. Weng, G. Guo, G. Liu, S. Wu, K.W.K. Yeng, P.K. Chu, RSC Adv. 3 (2013) 24758–24775.
[12] A. Kubacka, M. Fernández-García, G. Colon, Chem. Rev. 112 (2012) 1555–1614.
[13] J.-Y. Piquemal, E. Briot, J.-M. Bregeault, Dalton Trans. 42 (2013) 29–45.
[14] M. Kakihana, M. Kobayashi, K. Tomita, V. Petrykin, Bull. Chem. Soc. Jpn. 83 (2010) 1285–1308.
[15] V.G. Kessler, J. Sol–Gel. Sci. Technol. 68 (2013) 464–470.
[16] K. Tomita, V. Petrykin, M. Kobayashi, M. Shiro, M. Yoshimura, M. Kakihana, Angew. Chem. 188 (2006) 2438–2441.
[17] Y. Zhang, L. Wu, Q. Zheng, J. Zhi, J. Phys. Chem. C 112 (2008) 16457–16462.
[18] N. Murakami, Y. Kurihara, T. Tsubota, T. Ohno, J. Phys. Chem. C 113 (2009) 3062–3069.
[19] J.A. Chang, M. Vithal, I.C. Baek, S.I. Seok, J. Solid State Chem. 182 (2009) 749–756.
[20] V.R. De Mendoca, C. Ribeiro, Appl. Catal., B: Environ. 105 (2011) 298–305.
[21] Y. Miao, J. Gao, J. Solid State Chem. 196 (2012) 372–378.
[22] M. Kobayashi, V. Petrykin, K. Tomita, M. Kakihana, J. Cryst. Growth 337 (2011) 30–37.
[23] A. Ennaoui, B.R. Sankapal, V. Skryshevsky, Mch. Lux-Steiner, Cell 90 (2006) 1533–1541.
[24] H.S. Kibombo, R. Peng, S. Rasalingam, R.T. Koodali, Catal. Sci. Technol. 2 (2012) 1737–1766.
[25] H.S. Kibombo, D. Zhao, A. Gonshorowski, S. Budhi, M.D. Koppang, R.T. Koodali, J. Phys. Chem. C 115 (2011) 6126–6135.
[26] Z. Li, B. Hou, Y. Xu, D. Wu, Y. Sun, W. Hu, F. Deng, F. Comparative, J. Solid State Chem. 178 (2005) 1395–1405.
[27] Y. Li, S.-J. Kim, J. Phys. Chem. B 109 (2005) 12309–12315.
[28] W. Dong, Y. Sun, C.W. Lee, W. Hua, X. Lu, Y. Shi, S. Zhang, J. Chen, D.J. Zhao, J. Am. Chem. Soc. 129 (2007) 13894–13904.
[29] R.J. Davis, Z. Liu, Chem. Mater. 9 (1997) 2311–2324.
[30] Y. Ren, Y. Zhang, L. Wu, Langmuir 26 (2010) 11391–11396.
[31] X. Li, J. He, ACS Appl. Mater. Interfaces 5 (2013) 5282–5290.
[32] Z.Y. Wu, Y.F. Tao, Z. Lin, L. Liu, X.X. Fan, Y. Wang, J. Phys. Chem. C 113 (2009) 20335–20348.
[33] B. Mahltig, E. Gutmann, D.C. Meyer, Mater. Chem. Phys. 127 (2011) 285–291.
[34] M. Andrianainarivelo, R. Corriu, D. Leclercq, P.H. Mutin, A. Vioux, J. Mater. Chem. 6 (1996) 1665–1671.
[35] G. Liu, Y. Liu, G. Yang, S. Li, Y. Zu, W. Zhang, M. Jia, J. Phys. Chem. C 113 (2009) 9345–9351.
[36] A. Budnyk, A. Damin, S. Bordiga, A. Zecchina, J. Phys. Chem. C 116 (2012) 10064–10072.
[37] M. Hirano, K. Ota, H. Iwata, Chem. Mater. 16 (2004) 3725–3732.
[38] X. Chen, S. Shen, L. Guo, S.S. Mao, Chem. Rev. 110 (2010) 6503–6570.
[39] X. Wang, L. Cao, D. Chen, R.A. Caruso, ACS Appl. Mater. Interfaces 5 (2013) 10926–10932.
[40] F. Amano, A. Yamakata, K. Nogami, M. Osawa, B. Ohtani, J. Am. Chem. Soc. 130 (2008) 17650–17651.
[41] M. Anpo, T. Shima, S. Kodama, Y. Kubokawa, J. Phys. Chem. 91 (1987) 4305–4310.
[42] N. Xu, Z. Shi, Y. Fan, J. Dong, J. Shi, M.Z-C. Hu, Ind. Eng. Chem. Res. 38 (1999) 373–379.
[43] I.V. Krivtsov, M.V. Ilkaeva, V.D. Samokhina, V.V. Avdin, S.A. Khainakov, D.A. Uchaev, J.R. Garcia, J. Sol–Gel. Sci. Technol. 67 (2013) 665–669.
[44] M. Ilkaeva, I. Krivtsov, V. Avdin, S. Khainakov, J.R. Garcia, Colloids Surf., A. – Physicochem. Eng. Asp. 456 (2014) 120–128.
[45] A.C. Larson, R.B. Von Dreele, General Structure Analysis System (GSAS), Los Alamos National Laboratory Report LAUR, 1994, pp. 86–748.
[46] X. Wang, T. Dornom, M. Blackford, R.A. Caruso, J. Mater. Chem. 22 (2012) 11701–11710.
[47] J. Yu, F. Fan, K. Lv, Nanoscale 2 (2010) 2144–2149.
[48] W. Lin, H. Frei, J. Am. Chem. Soc. 124 (2002) 9292–9298.
[49] H. Ichinose, M. Terasaki, H. Katsuki, J. Ceram. Soc. Jpn. 104 (1996) 715–718.
[50] R.K. Iler, The Chemistry of Silica, Wiley & Sons, New York, 1979.
[51] H. Nur, Mater. Sci. Eng., B 133 (2006) 49–54.
[52] D.M. Pickup, G. Mountjoy, G.M. Wallidge, R. Anderson, J.M. Cole, R.J. Newport, M.E. Smith, J. Mater. Chem. 9 (1999) 1299–1305.
[53] W. Li, Y. Bai, C. Liu, Z. Yang, X. Feng, X. Lu, N.K. Van der Laak, K-Y. Chan, Environ. Sci. Technol. 43 (2009) 5423–5428.
[54] S.C. Pillai, P. Periyat, R. George, D.E. McCormack, M.K. Seery, H. Hayden, J. Colreavy, D. Corr, S.J. Hinder, J. Phys. Chem. C 111 (2007) 1605–1611.
[55] P. Periyat, S.C. Pillai, D.E. Mccormack, J. Colreavy, S.J. Hinder, J. Phys. Chem. C 112 (2008) 7644–7652.
[56] P. Wen, H. Itoh, W. Tang, Q. Feng, Langmuir 23 (2007) 11782–11790.
[57] X. Chen, X. Wang, X. Fu, Energy Environ. Sci. 2 (2009) 872–877.
[58] X. Fu, L.A. Clark, Q. Yang, M.A. Anderson, Environ. Sci. Technol. 30 (1996) 647–653.

SUPPLEMENTARY INFORMATION

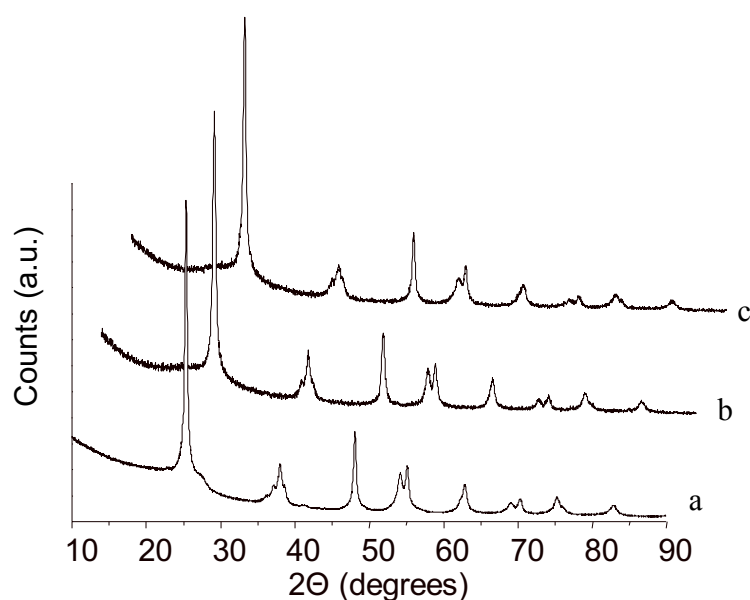## A hydrothermal peroxo method for preparation of highly crystalline silica–titania photocatalysts

Igor Krivtsov [a,b,⇑], Marina Ilkaeva [a,c], Viacheslav Avdin [b,c], Sergei Khainakov [a], Jose R. Garcìa [a], Salvador Ordòñez [d], Eva Dìaz [d], Laura Faba [d]

[a] Department of Organic and Inorganic Chemistry, University of Oviedo, Julian Claveria s/n, Oviedo 33006, Spain

[b] Nanotechnology Education and Research Center, South Ural State University, Lenina Ave. 76, Chelyabinsk 454080, Russia

[c] Department of Chemistry, South Ural State University, Lenina Ave. 76, Chelyabinsk 454080, Russia

[d] Department of Chemical and Environmental Engineering, University of Oviedo, Julián Clavería s/n, Oviedo 33006, Spain
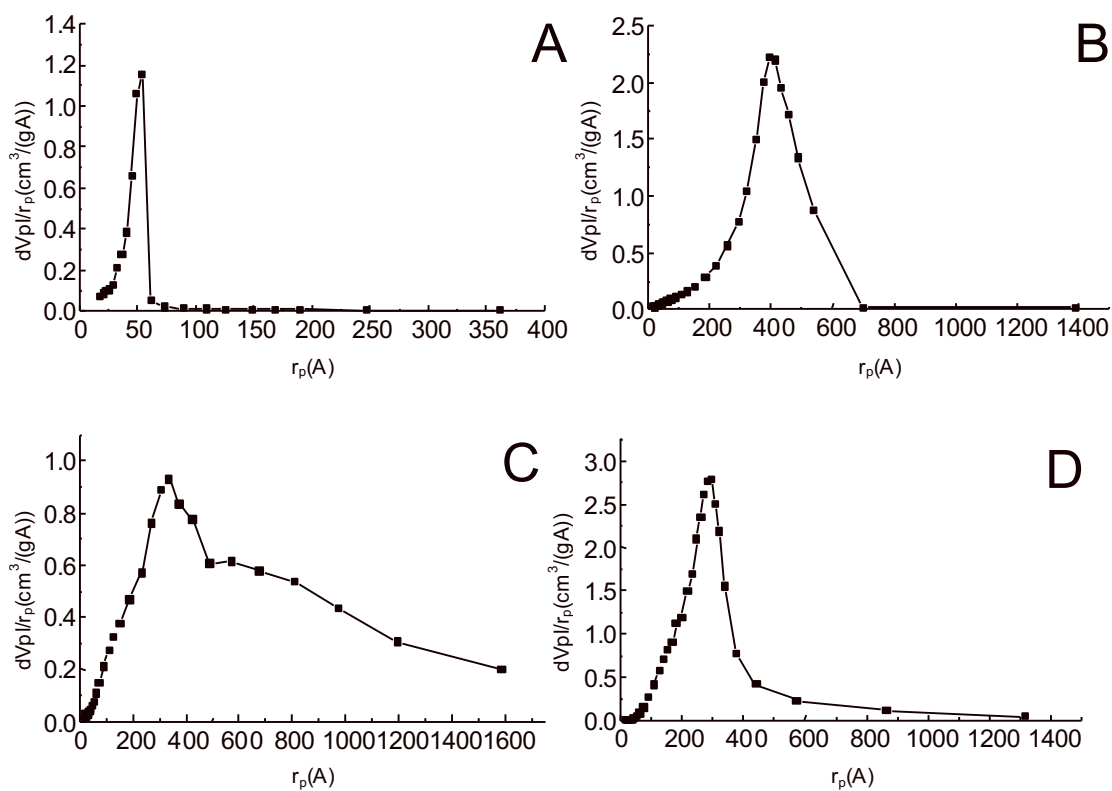
Fig. S1. XRD patterns of (a) PTA-SiO$_2$, (b) GelTS and (c) NH$_3$PT-SiO$_2$ samples.
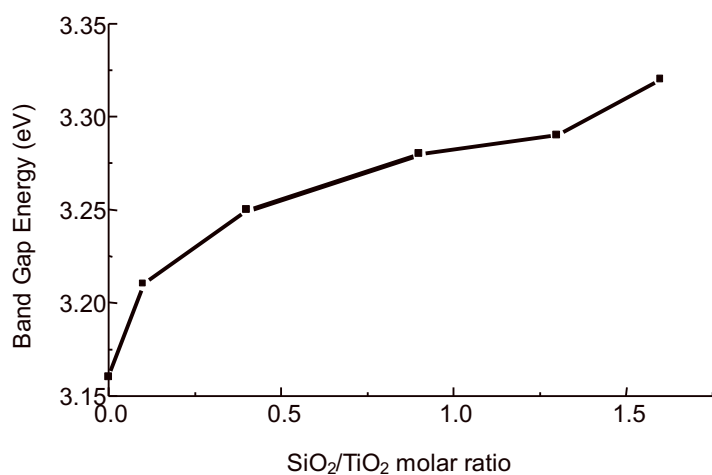
Fig. S2. Band gap energy versus SiO_2/TiO_2 molar ratio in the mixed oxide samples.

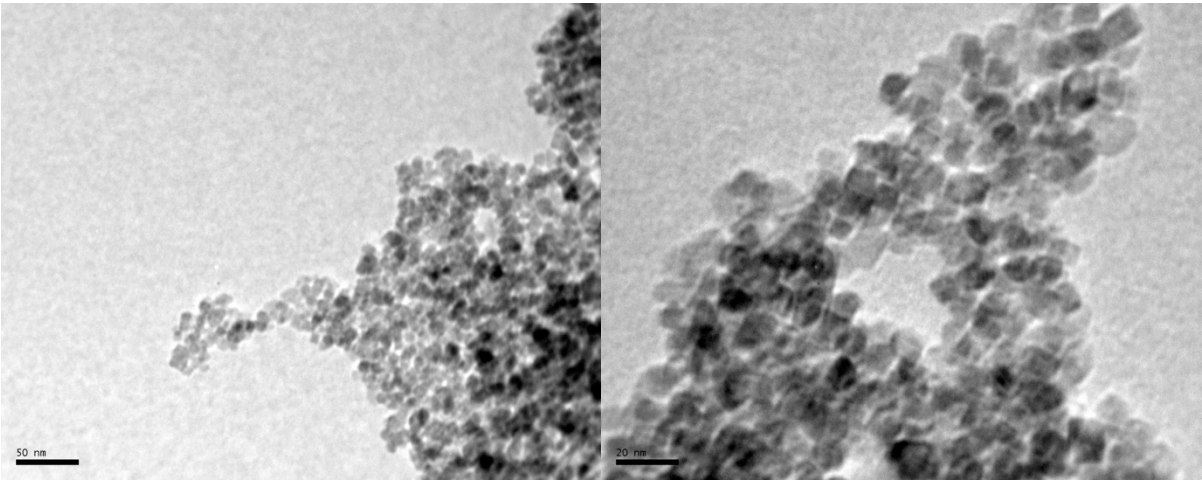**Fig. S3.** Pore size distribution of the samples (a) 0TS, (b) 0.4TS, (c) 0.9TS, and 1.6TS.
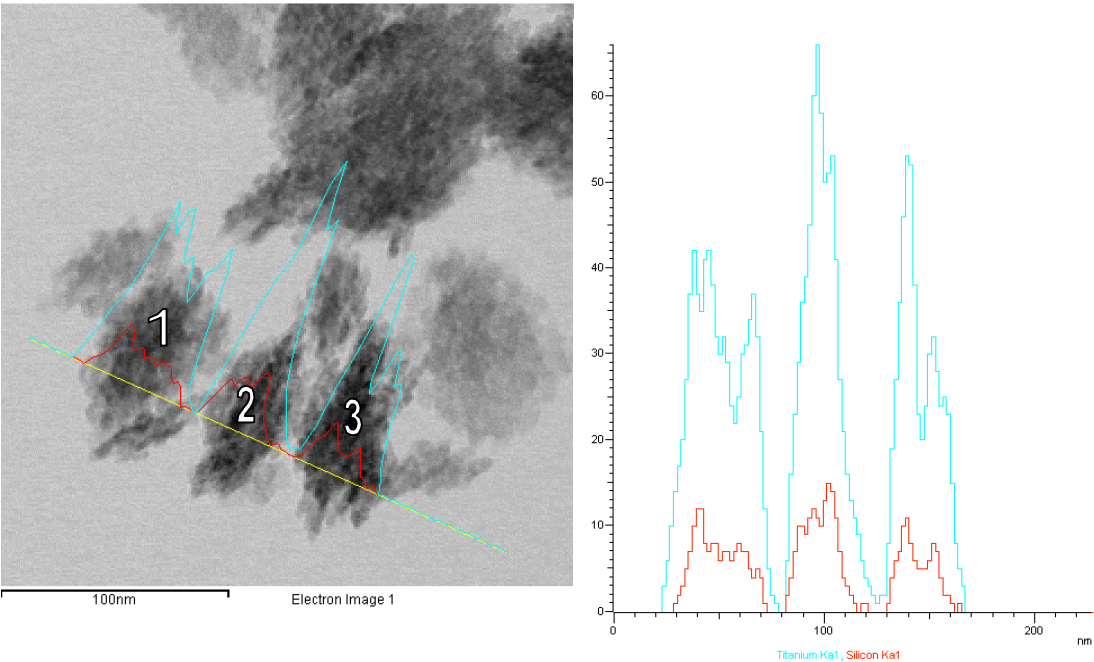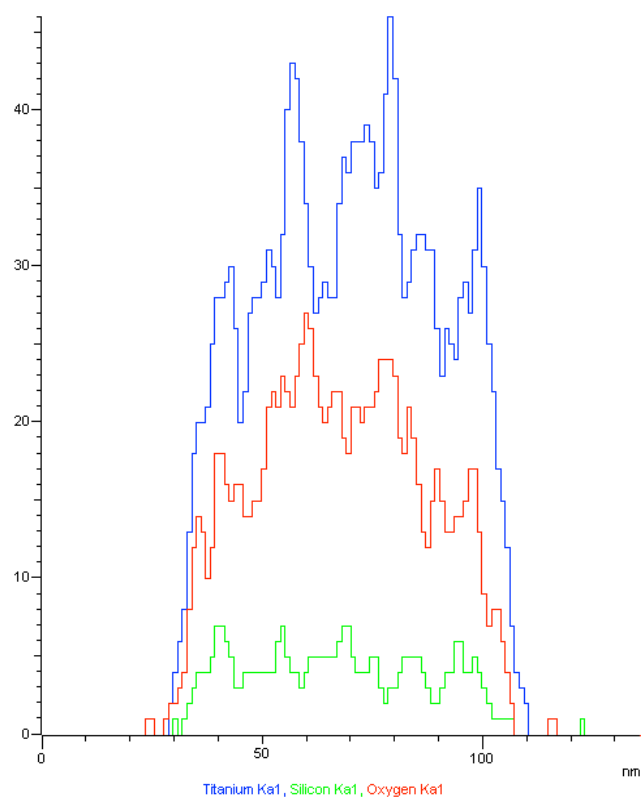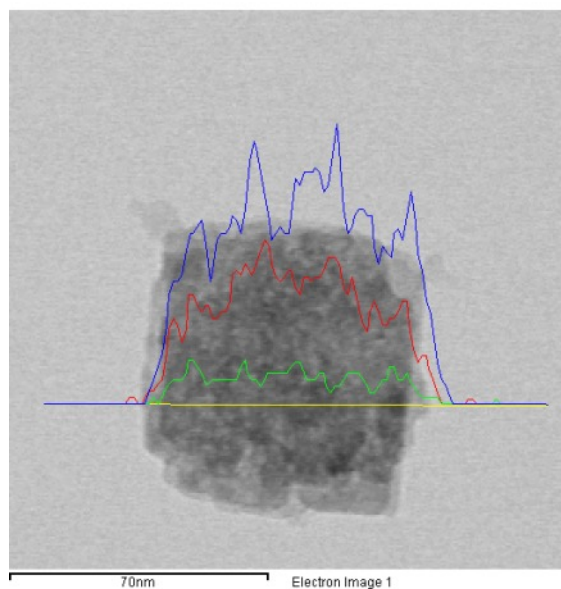
Fig. S4. TEM-images of the 0TS sample.

Spectrum	O	Si	Ti

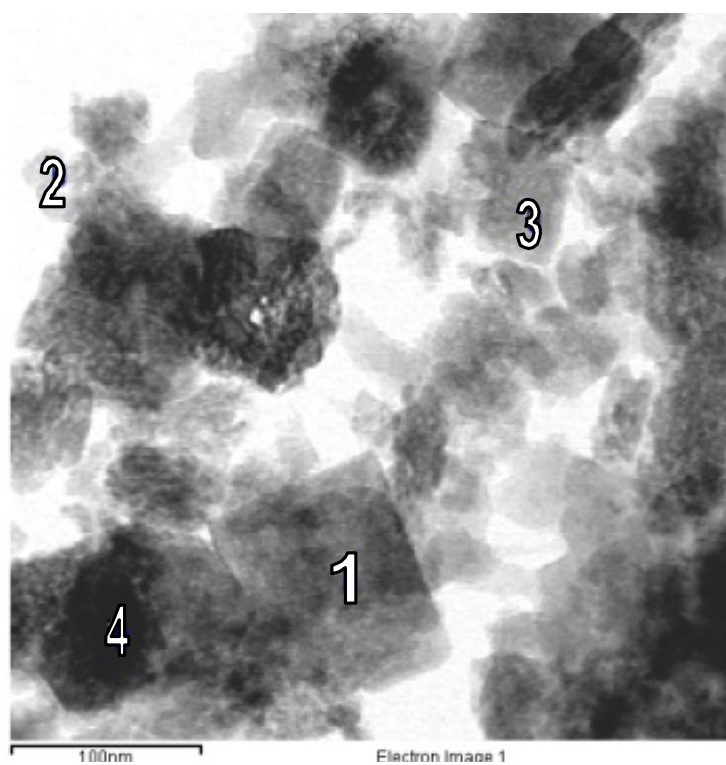|			
1	60.94	10.77	28.29
2	62.43	11.25	26.33
3	26.48	20.82	52.69

*All results in the atomic percents

Fig. S5. EDS elemental analysis of 0.4TS sample.

Spectrum	O	Si	Ti
1	62.79	6.80	30.41
2	53.56	8.56	37.89
3	56.05	7.73	36.22
4	64.05	15.17	20.78

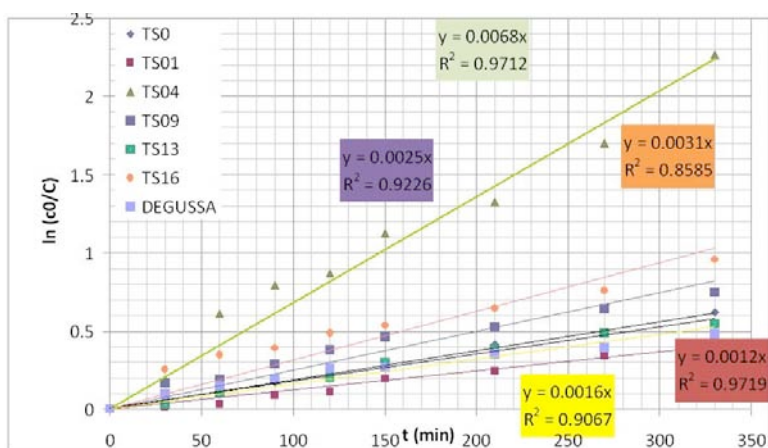*All results in the atomic percents

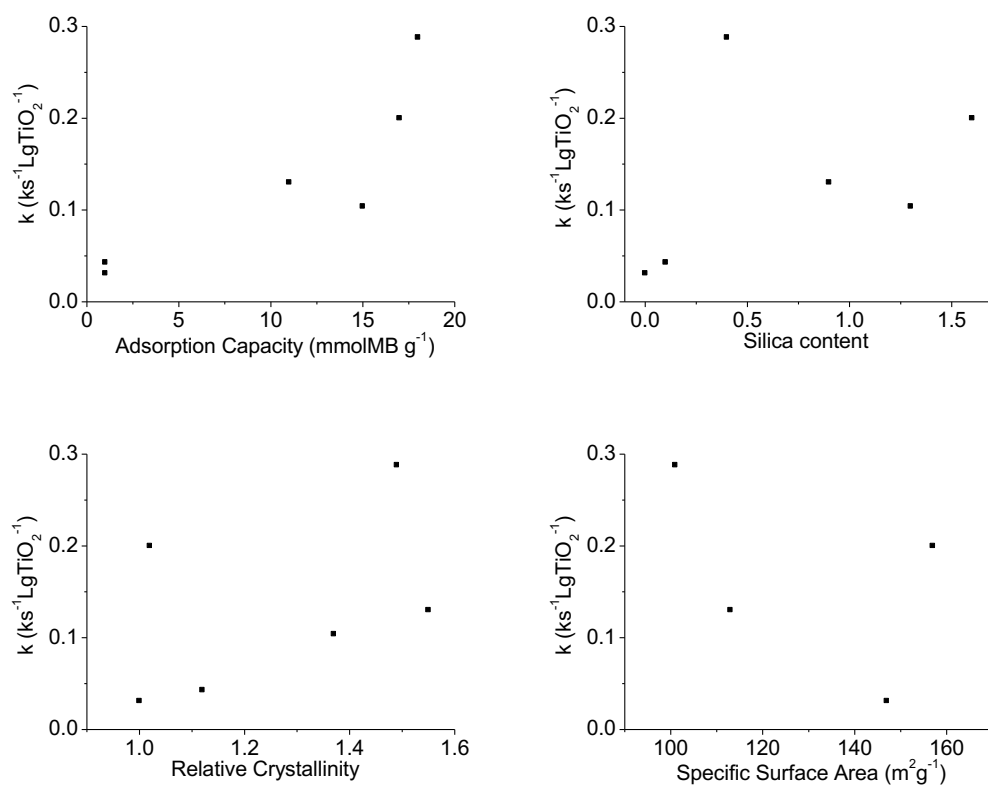**Fig. S6.** EDS elemental analysis of 0.9TS sample.
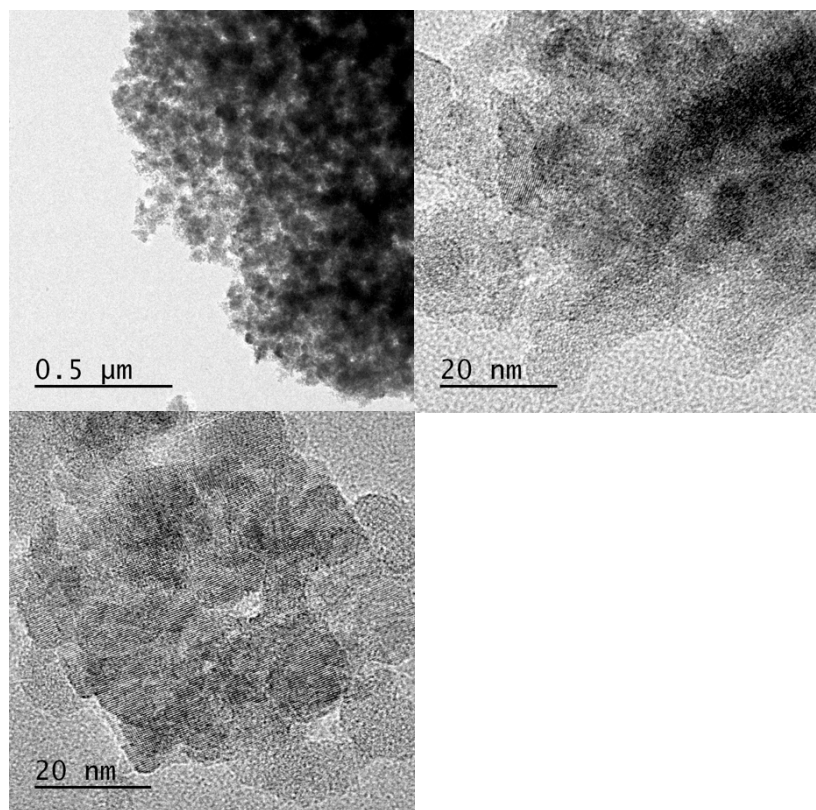
Figure S7. TEM images of the 1.6TS sample
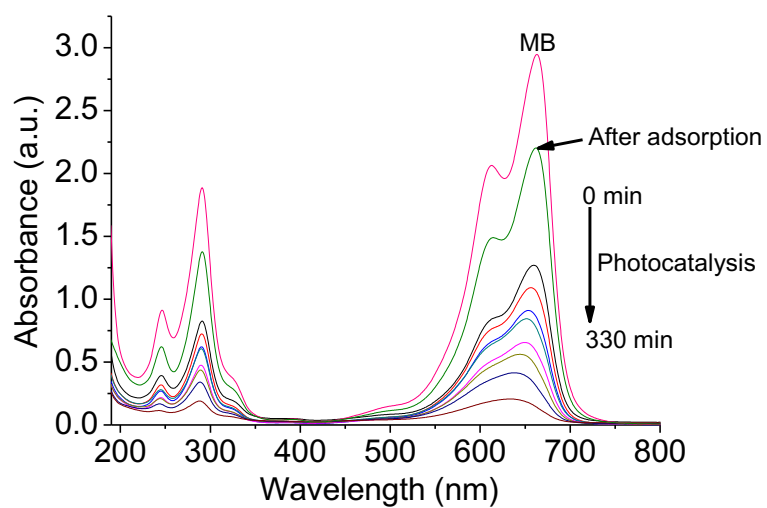
Fig. S8. The spectra of MB solution during photocatalytic decomposition in presence of the 0.4TS sample.

Fig. S9. Fitting the reaction to the pseudo-first order

Fig. S10. Effect of different parameters on photocatalytic activity of the silica-titania samples

3.1.2 Thermally Stable Titania Anatase Nanoparticles

Some aspects of thermal stability of a metastable anatase phase, widely considered as the most photocatalytically active one among other titania polymorphs, were discussed in Introduction Chapter 1.2.5.

Pillai et al. persuaded the idea of obtaining highly stable anatase nanoparticles for application in self-cleaning and self-disinfecting ceramics, and they developed numerous methods of anatase stabilization [132-134]. Despite the majority of such procedures included doping of TiO_2 with metal or non-metal species, there was one of a particular interest, where no heteroatoms were present in the titania structure, but anatase polymorph was stable up to 900 °C.

The following research paper reports a modified method for the preparation of unprecedentedly stable anatase nanoparticles, which do not suffer the polymorphic transition up to 1000 °C. In the study, we propose a new solvent-exchange (SE) method based on the precipitation of aqueous ammonium peroxotitanate complex with ethanol or acetone. The proposed procedure favours the formation of crystalline anatase phase at lower temperature than it is usually occurs. Due to the presence of ammonia in the precursor solution, in the range of thermal treatment up to 500 °C nitrogen-doped TiO_2 is formed, which is confirmed by EELS study. Despite this effect is found for the titania prepared by the SE method as well as for TiO_2 prepared by directly gelling titanium peroxo complex as did Pillai et al. [227], SE anatase nanoparticles possess higher thermal stability. HR-TEM investigation evidences the presence of high concentration of crystal defect sites in SE anatase TiO_2 nanoparticles, which most probably contributes to their extraordinary stability. Moreover, the material obtained by SE method has superior photocatalytic activity than its counterpart formed by gelation of the peroxo titanium complex, which is due to its higher SSA of 34 m^2g^{-1}. SE nanoparticles also outrun the commercial Evonik P25 TiO_2, if both photocatalysts are treated at temperatures equal or higher than 800 °C. Summarizing, this newly developed synthetic technique allows preparation of fine titania nanoparticles with high photocatalytic activity, and it holds promise for application in the production of photoactive ceramics.

Article II

"Exceptional Thermal Stability of Undoped Anatase TiO$_2$ Photocatalyst Prepared by a

Solvent-Exchange Method"

Exceptional thermal stability of undoped anatase TiO$_2$ photocatalysts prepared by a solvent-exchange method†

Igor Krivtsov,*[ab] Marina Ilkaeva,[ac] Viacheslav Avdin,[bc] Zakariae Amghouz,[d] Sergei A. Khainakov,[d] José R. García,[a] Eva Díaz[e] and Salvador Ordóñez[e]

A new solvent-exchange technique to prepare anatase nanoparticles with exceptional thermal stability and photocatalytic activity is described here. The process of preparation is accomplished by using organic solvents to precipitate hydrous titania particles from a basic aqueous medium containing a titanium peroxo complex. Undoped titanium dioxide formed *via* a solvent exchange method has unprecedented thermal stability against transformation to the rutile phase, as opposed to TiO$_2$ prepared by the common method of the gelation of an aqueous titanium peroxo complex. On the basis of X-ray thermodiffraction experiments, it has been established that the thermal treatment at 1000 °C of the titania prepared by ethanol precipitation contains 100% pure anatase phase. The stabilization of anatase is induced by the high defectiveness of the TiO$_2$ nanostructure, which is evidenced from band-gap energy estimation, PXRD and HRTEM studies. The prepared TiO$_2$ nanoparticles show an outstanding photocatalytic activity comparable to the commercial **Aeroxide P25** photocatalyst in the UV-assisted decomposition of methylene blue.

1. Introduction

Despite the large number of alternatives,[1] titanium dioxide is considered to be the most appropriate semiconductor photocatalyst, because it is inexpensive, non-toxic and thermally stable according to many comprehensive reviews.[2–11] Anatase, generally considered the most active phase for photocatalytic applications, is a metastable polymorph which usually transforms into the stable rutile phase in the temperature range of approximately 500–700 °C. The development of new methods tailored to prepare anatase with increased thermal stability up to the sintering temperature range is of great importance, not only for photocatalysis, but also in other emerging applications such as self-cleaning and antibacterial ceramic production.[12] There are two general procedures to stabilize anatase: doping TiO$_2$ with metal cations,[13] fluorine,[14] or sulfur,[15] and

preparation of mixed TiO$_2$/M$_x$O$_y$ oxides.[16,17] The most significant drawback of these methods is that the dopants reduce crystallinity of TiO$_2$, which increases the recombination rate of electron–hole pairs. However, the preparation of stable undoped anatase is also discussed in the literature. Wu *et al.*[18] found that the anatase phase, prepared from titanium isopropoxide in the presence of tetramethylammonium hydroxide, was stable up to 950 °C. They attributed the retardation of anatase-to-rutile phase transition to the formation of the rod-like crystals. Similar observation about the effect of crystallite size and morphology on the stability of anatase phase was reported by Mao *et al.*[19] Li *et al.*[20] showed that the formation of intermediate brookite phase would enhance the stability of anatase at high temperatures. Application of simple alkoxide-based sol–gel procedures using urea or formic acid as modifying agents also led to improved stability of the desired titania polymorph.[21,22] But recently, the emerging class of precursors based on peroxo complexes have been used for metal oxide synthesis.[23,24] Moreover, shape of anatase crystals was successfully controlled *via* hydrothermal treatment of titanium peroxo complexes.[25,26] Etacheri *et al.*[27] used peroxo titanic acid to prepare visible light active TiO$_2$ photocatalyst with 100% anatase phase after heat treatment at temperature as high as 900 °C.

Herein, we report a new facile solvent-exchange method for preparing TiO$_2$ nanoparticles. We have found that titanium peroxo complex is insoluble in ethanol and acetone, as a consequence, hydrous titania suspensions were precipitated using these solvents. The proposed technique does not require

[a]Department of Organic and Inorganic Chemistry, University of Oviedo-CINN, 33006 Oviedo, Spain. E-mail: uo247495@uniovi.es; zapasoul@gmail.com; Tel: +34 684348116

[b]Nanotechnology Education and Research Center, South Ural State University, 454080, Chelyabinsk, Russia

[c]Department of Chemistry, South Ural State University, 454080 Chelyabinsk, Russia

[d]Servicios Científico-Técnicos, Universidad de Oviedo, 33006 Oviedo, Spain

[e]Department of Chemical and Environmental Engineering, University of Oviedo, 33006 Oviedo, Spain

utilization of toxic, unstable and volatile alkoxide precursors as well as complex organic structure-directing agents or templates. Thus, it can be considered as an environmentally friendly approach for preparing high performance titania photocatalysts. The prepared TiO_2 nanoparticles exhibit temperatures of anatase-to-rutile phase transformation higher than those previously reported.[15,18,21,22,27]

2.   Experimental

2.1   Chemicals

Titanium oxysulfate hydrate containing not more than 17% of H_2SO_4, as well as 30 wt% hydrogen peroxide (H_2O_2) water solution were purchased from Aldrich. Ammonium hydroxide 20% water solution, ethanol and acetone (all VWR Chemicals) were of analytical grade and used as received without additional purification. The commercial photocatalyst **Aeroxide P25** (Degussa P25) was purchased from Aldrich. The concentration of titanium oxysulfate was determined gravimetrically prior to its use in synthesis. Titanium oxysulfate has been chosen as precursor due to its high stability under ambient conditions, which is not the case for titanium tetrachloride or titanium alkoxides.

2.2   Synthesis

Firstly, titanium hydroxide was precipitated from 25 mL of 0.2 M titanium oxysulfate solution in sulfuric acid by addition of 3 M NH_3 aqueous solution, the final pH of precipitate was 9.0. Then, it was centrifuged at 7000 rpm and washed with deionized water until a negative reaction for sulfate ions was achieved. The aqueous titanium peroxo complexes were synthesized by addition of 4 mL of 30 wt% hydrogen peroxide to the precipitates and gradual adjustment of the pH value of the reaction mixture to 9.5 by adding ammonia. Finally, clear bright yellow stable solutions were formed and their volumes were adjusted to 25 mL. The solutions were cooled in an ice bath in order to prevent fast decomposition of H_2O_2, as well as evaporation of ethanol and acetone. The cooled solutions of titanium peroxo complexes were mixed with equal volumes of ethanol or acetone. The mixed solutions became turbid immediately, because the hydrous titania particles were formed. The obtained suspensions were left for 24 h and then centrifuged at 8000 rpm for 5 min, after that the pale-yellow precipitates were isolated and washed several times with water. For the sake of comparison, the sample prepared in the absence of any organic solvents was also investigated. Because the aqueous solution of titanium peroxo complex synthesized as mentioned above was stable, it was heated at 50 °C for 2 h in order to induce titanium hydrolysis and precipitation of peroxo titanate gel. The samples prepared by (i and ii) isolation of hydrous titania with ethanol or acetone and (iii) gelation of aqueous complex solution were designated as **TiEt**, **TiAc** and **TiAq**, respectively. All precipitates were dried at 70 °C for 24 h before subjecting to investigation. Also the samples were thermally treated in a muffle furnace at specific temperatures (500 °C, 800 °C, 900 °C and 1000 °C) with a heating rate of 5 °C min^{-1} and left for 30 min at each specific temperature before cooling down.

2.3   Characterization

Powder XRD patterns were registered on a Rigaku Ultima IV diffractometer, using Ni-filtered CuK_α radiation source. The PXRD data were refined, where unit cell parameters and anatase phase content were estimated using MAUD software and crystal sizes were calculated by Scherrer equation for anatase (101) reflection. Thermodiffraction analysis was carried out using the X'pert Pananlytical diffractometer for **TiEt** sample calcined at 400 °C for 2 h prior to measurement. **TiEt** was heated up to 1000 °C at a heating rate of 5 °C min^{-1} and the XRD patterns were collected every 30 min during 5 h at this temperature. A Shimadzu UV-2700 spectrophotometer with integrated sphere attachment was used to obtain diffuse reflectance (DR) spectra of the samples using barium sulfate as a reference. Band gap energy was estimated by Kubelka–Munk method. Bruker Tensor 27 spectrometer was used to collect FTIR spectra. Thermal analysis were carried out by means of NETZSCH 449C simultaneous TG/DTA analyzer at a heating rate of 10 °C min^{-1} under air flow. SEM images were obtained by using JEOL JSM-7001F field emission scanning electron microscope equipped with EDX detector; the samples were gold-coated prior to observation. The EDX analysis confirmed the absence of sulfur in the TiO_2 samples. A Micromeritics ASAP 2020 was used to obtain N_2 adsorption–desorption isotherms at 77 K. Before the experiment, the samples were outgassed under vacuum at 400 °C. Surface area and pore volume were calculated using BET and BJH methods. TEM, HRTEM, selected area electron diffraction (SAED), nanobeam electron diffraction (NBD), and EELS (electron energy loss spectroscopy) studies were performed on a JEOL JEM-2100F transmission electron microscope operated at an accelerating voltage of 200 kV, equipped with a field emission gun (FEG) and an ultra-high resolution pole-piece that provided a point-resolution better than 0.19 nm. The samples for TEM were dispersed in ethanol, sonified and sprayed on a Holey carbon film coated copper grid and then allowed to air-dry, finally, Gatan SOLARUS 950 was used before observation.

2.4   Photocatalytic activity test

Synthesized titania materials were tested in the aqueous-phase photocatalytic decomposition of methylene blue (**MB**) in a stirred batch reactor. For the experiments, 25 mg of each sample previously calcined in air at 500 °C, 800 °C and 1000 °C for 30 min was placed into a quartz reactor. Later, 50 mL of **MB** aqueous solution (20 mg L^{-1}) was added to the catalyst. Before irradiation, the suspension was magnetically stirred in the dark until the adsorption equilibrium was reached in 30 min. Afterward, the suspension was exposed to ultraviolet irradiation. The UV-light source was 500 W lamp (Helios Italquartz) having maximum emission at 365 nm and equipped with a water-cooling jacket. The reactor with suspension was positioned at a distance of 50 cm from the lamp, which gives a light intensity of 16 mW cm^{-2}. The suspension was constantly stirred during the UV-irradiation and 5 mL aliquots were taken every 30 min during 240 min. The solution was separated from the catalyst using a centrifuge, and the concentration was determined photometrically by the absorbance at 664 nm using a

Perkin Elmer Lambda 20 spectrophotometer. After that, the solution, together with the catalyst powder were returned back into the reactor and irradiation has continued. Photolysis of the **MB** solution in the absence of catalyst was carried out under the same experimental conditions. It was found that only 1.5% of **MB** was decomposed under these conditions.

3. Results and discussion

All the as-synthesized samples were found to be amorphous (see ESI, Fig. S1†), except **TiAq** sample that shows a broad peak centered at $2\theta = 9.2°$ on the XRD pattern, which was attributed to the ammonia peroxo titanate complex.[28] FTIR spectra (Fig. 1) of the as-prepared samples reveal some differences in the structural features of the precipitates. The most intense band at 1385 cm^{-1} confirms the presence of ammonia in all the samples. The intense and well-defined band at 900 cm^{-1}, observed in the spectrum of the peroxo titanate gel (**TiAq**), corresponds to the stretching O–O vibrations, while the peak at 696 cm^{-1} indicates the presence of Ti–O–O bonds. However, the bands corresponding to the peroxo groups are not clearly seen in **TiAc** and **TiEt** spectra. A similar observation was made by Liao *et al.*[26] when the solvothermal method is applied to synthesize TiO$_2$ from the mixture of peroxo titanate complex and organic solvent. We suppose that the reaction between organic solvents and peroxo groups has caused the decomposition of the latter, which in turn, led to the oxolation of hydrous titania species. The broad absorption band centered at 616 cm^{-1} in **TiAc** and **TiEt** spectra is attributed to Ti–O–Ti stretching vibrations, this is most likely due to the very high degree of condensation of oxo-species in these precipitates. Likewise, the decomposition of peroxo groups while preparing the **TiAc** and **TiEt** samples is also evidenced by DR-UV-vis spectroscopy study (Fig. S2†). The **TiAq** sample absorbs light in the visible region due to the presence of peroxo groups on titania. Contrarily, the visible light absorbance is considerably decreased in the case of the **TiAc** and **TiEt** samples (Fig. S2†). Moreover, this method provides additional information about structural features of titania particles and coordination state of titanium. The sharp absorption peak at 219 nm in **TiAq** spectrum can be attributed to the charge transfer process in isolated TiO$_4$ units.[29] The shifting of absorbance bands towards longer wavelengths
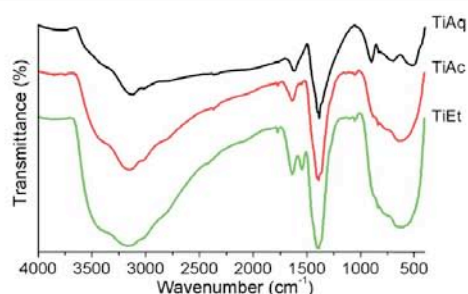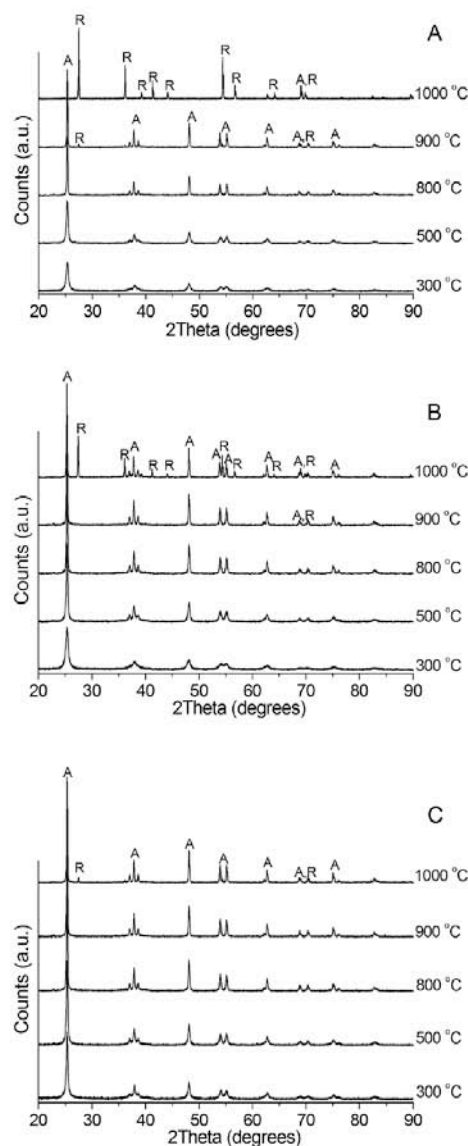

Fig. 1 FTIR spectra of the as-synthesized samples.

Fig. 2 Powder XRD patterns of (A) TiAq, (B) TiAc and (C) TiEt samples treated at different temperatures in a muffle furnace, where A indicates reflections of anatase phase and R for rutile.

indicates the presence of large titania particles. The absorbance bands at 334 nm in the **TiEt** and **TiAc** spectra suggest that these samples show more condensed TiO$_2$ phase compared to **TiAq** sample. Thermal analysis of the as-synthesized samples was carried out in order to determine the temperatures for the elimination of volatile components and exothermic effects associated with phase transitions. Thermal decomposition of **TiAq** is similar to that one reported previously.[28] The DTA curve shows one endothermic and three well-defined exothermic

Table 1 The results of powder XRD analysis and band gap energy estimation

| Sample | T (°C) | Unit cell parameters (Å) | | Crystal size (nm) | Anatase : rutile ratio (wt%) | Band gap energy (eV) |
		a	c			
TiAq	500	3.785(4)	9.508(4)	22	100 : 0	3.02
	800	3.782(2)	9.525(2)	49	100 : 0	3.15
	900	3.783(1)	9.534(1)	49	96 : 4	
	1000				0 : 100	2.93
TiAc	500	3.785(2)	9.507(4)	29	100 : 0	3.24
	800	3.785(2)	9.516(1)	41	100 : 0	3.30
	900	3.785(4)	9.518(1)	52	100 : 0	
	1000	3.782(1)	9.517(1)	64	69 : 31	3.20
TiEt	500	3.784(4)	9.503(4)	31	100 : 0	3.23
	800	3.784(4)	9.509(2)	44	100 : 0	3.32
	900	3.784(3)	9.513(1)	48	100 : 0	
	1000	3.783(1)	9.516(2)	76	96 : 4	3.24

peaks corresponding to the elimination of adsorbed and chemically bonded water, decomposition of peroxo groups and crystallization process of amorphous titania (Fig. S3a†). However, thermal decomposition of **TiAc** and **TiEt** samples prepared *via* solvent-exchange method is different (Fig. S3b and c†). Similarly to **TiAq** sample, there are three exothermic peaks on the DTA curves for **TiAc** and **TiEt**, but unlike the **TiAq** sample, the first two exothermic peaks observed at low temperature correspond to the combustion process of the organic residue. The as-prepared samples start to crystallize around 300 °C and with further heat treatment their crystallinity increases (Fig. 2). The results of XRD analysis are summarized in Table 1. Titania sample **TiAq** prepared from the aqueous peroxo titanate gel has the lowest thermal stability among all samples, however, its stability is much higher than TiO_2 prepared *via* conventional non-peroxo techniques.[27] Rutile phase is detected in the **TiAq** sample after treatment at 900 °C and the complete anatase-to-rutile transition takes place at 1000 °C. The **TiAc** sample is more stable, it contains pure anatase phase after being subjected to 900 °C for 30 min. Furthermore, titania prepared by solvent-exchange method using ethanol (**TiEt**) shows a remarkably higher stability, it retains 96 wt% of anatase phase even after heat treatment in muffle furnace at temperature as high as 1000 °C. In order to investigate the process of anatase-to-rutile transformation *in situ*, X-ray thermodiffraction study was performed for **TiEt** sample (Fig. 3a). It shows that the **TiEt** sample possesses unprecedented stability towards formation of rutile phase, it retains 60 wt% of anatase phase after being treated at 1000 °C for 5 h (Fig. 3b). The slight controversy observed in the percentage of rutile phase, when **TiEt** sample is thermally treated in muffle furnace or during the thermodiffraction experiment, is attributed to overheating of the sample in the furnace, which leads to the formation of 4% of rutile phase after 30 min, while 150 min in the diffractometer heating chamber was necessary to reach the same percentage of transformation. According to XRD data, we cannot attribute the hindering of anatase-to-rutile phase transformation to the crystallite size effect, because the differences in this parameter are insignificant. The differences in the *c*-axis lattice parameter

indicate that crystalline anatase formed from **TiAc** and **TiEt** precursors contains higher concentration of defects than that prepared from **TiAq** one. The above hypothesis is corroborated
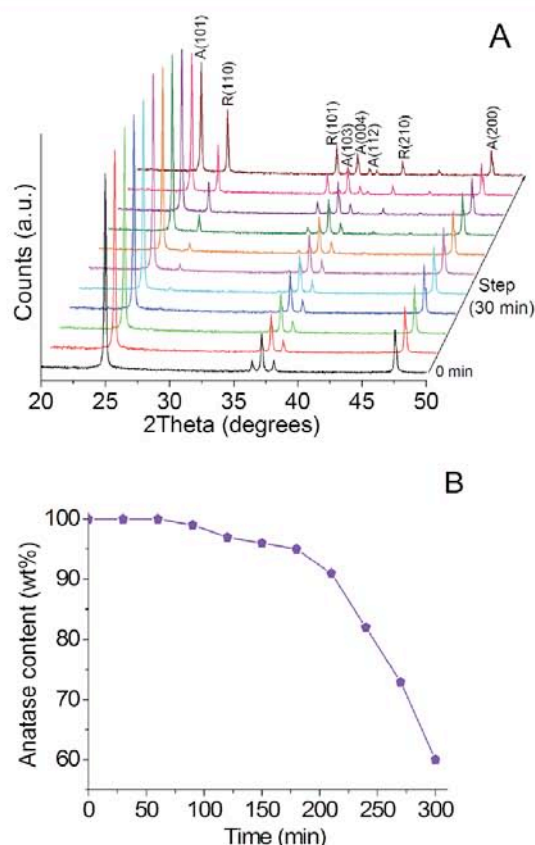

Fig. 3 TiEt sample at 1000 °C: (A) HT-pXRD patterns as a function of the treatment time (the pXRD scans were taken every 30 min) and (B) changes in anatase/rutile content.

by the results of band-gap (BG) energy estimation (Table 1). Usually BG energy of anatase TiO_2 is 3.2 eV, however, this value varies depending on the presence of dopants and degree of crystallinity. Like Etacheri et al.[27] we observe the band gap shrinkage when TiO_2 anatase is prepared via aqueous titanium peroxo complex route (**TiAq**). It can be attributed to the nitrogen-doping effect in the samples calcined not higher than 500 °C, as the presence of nitrogen is evident from the EELS data (Fig. S4†). After thermal treatment at 800 °C its BG value increases, but it is still less than 3.2 eV, due to the presence of oxygen vacancies formed on sites of the removed N atoms (Table 1). However, **TiAc** and **TiEt** samples obtained by solvent-exchange route show broader BG, even though nitrogen-doping occurring when they are treated at 500 °C, and then no nitrogen is detected at calcination temperatures higher than 800 °C (Fig. S4†). This indicates high concentration of defects in the structure, and it also means that nitrogen-doping could play some noticeable role, but cannot be solely responsible for the defects formation at elevated temperatures. The formation of defects is likely to be due to rapid loss of ligands, i.e. peroxo groups, which are not stable in organic solvents. This leads to fast assembling process of the oxide network. On the contrary, the aqueous peroxo titanate gel containing peroxo groups is stable up to high temperatures,[30] and because peroxo groups hinder the condensation of titania species, the crystallization rate becomes slow. As a result, less defective structure is formed. TEM and HRTEM images and electron diffraction (ED) patterns of pure anatase **TiAq** and **TiEt** samples calcined at 800 °C are shown in Fig. 4 and 5. Both samples show the presence of crystal grains with the average size of ca. 45 nm and 50 nm for **TiEt** and **TiAq** (Fig. 4a–d and S5†), respectively, in agreement with the results obtained from XRD analysis. From a careful inspection of SAED patterns (Fig. 4e and f) and NBD patterns for individual crystal grains (Fig. 4g and h), the degree of crystallinity seems to be similar for both samples and all ED patterns have been indexed as anatase phase. No detectable traces of rutile phase have been found by indexing the ED patterns. TEM images reveal mesoporous crystal grains with pore diameters in the range 3–12 nm in the case of **TiEt** sample (Fig. 5a). HRTEM images displayed in Fig. 5c–f for both samples show an interplanar spacing of 0.35 nm corresponding to (101) atomic planes. Several line defects, such as dislocations, along the (101) plane have been observed in the case of **TiEt** (Fig. 5c and e), while very distinguishable planar defects, such as grain boundaries, are manifested in the case of **TiAq** (Fig. 5b and f). Obviously, the blurred lattice fringes observed in HRTEM images in the case of **TiEt**, such as Fig. 5e, are an indication of the defects induced from the lattice distortion, probably attributed to the crystallization process. EELS spectra for **TiAq** and **TiEt**, are shown in Fig. S6.† Because of the octahedral coordination of Ti atoms, the L3 and L2 edges are then both subdivided into two edges by the strong crystal-field splitting arising from the surrounding O atoms.[31] The splitting of Ti L2, 3 edges is slightly higher in **TiAq**, which may reflect that the local octahedral coordination is weakly present in the case of **TiEt**, probably due to the degree of crystallinity and/or the structural defects as confirmed by HRTEM study. The splitting of O–K
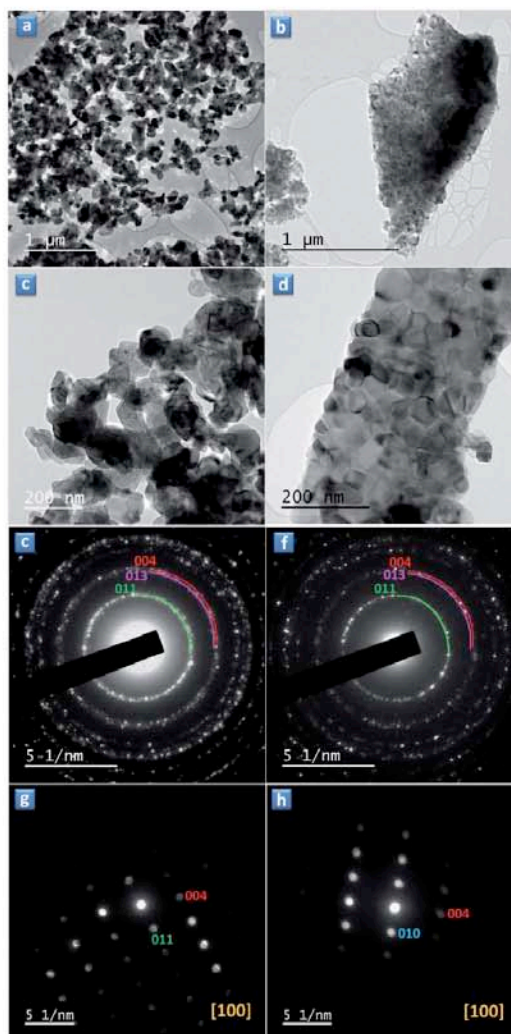

Fig. 4 (a–d) TEM images, (e and f) selected area electron diffraction (SAED) and (g and h) nanobeam electron diffraction (NBD) for TiEt (left) and TiAq (right) thermally treated at 800 °C.

edge with a separation of 2.4 eV for **TiAq** and **TiEt** (Fig. S6†) confirms the anatase phase.[32] TEM and SEM images of **TiAq** calcined at 800 °C (Fig. 4b and d and S7a†) show the presence of sintered oxide composed of large densely packed grains, while the images of **TiEt** (Fig. 4a and c and S7c†) show unagglomerated TiO_2 grains and with the increase of calcination temperature leads to the formation of densely packed large particles (Fig. S7d†).

TiEt sample exhibit high photocatalytic activity for the decomposition of **MB** when compared to **TiAc** and **TiAq** samples calcined at 500 °C (Fig. S8†). The crystallinity of TiO_2 is improved after calcination at higher temperatures (Table 1),
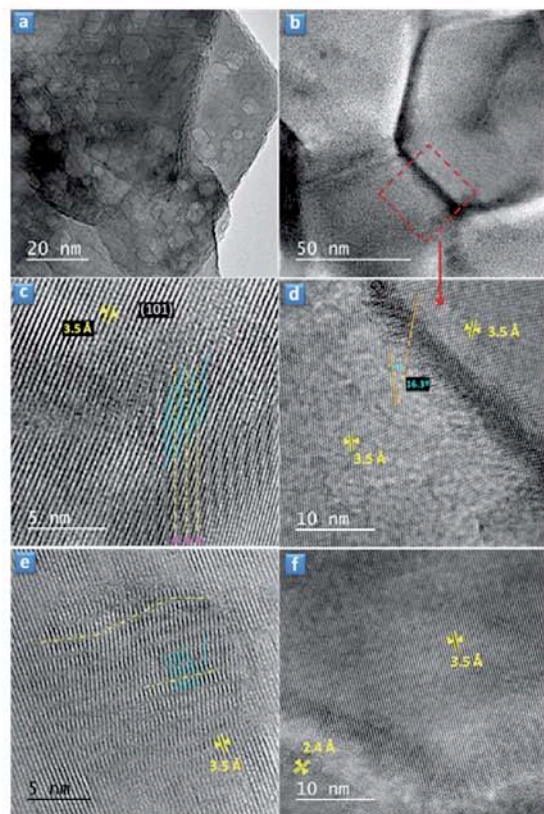
77

Fig. 5 TEM and HRTEM images of TiEt (a, c and e) and TiAq (b, d and f) samples calcined at 800 °C. The dislocations observed in TiEt are indicated by cyan lines and directions of slip are indicated by yellow dashed lines.
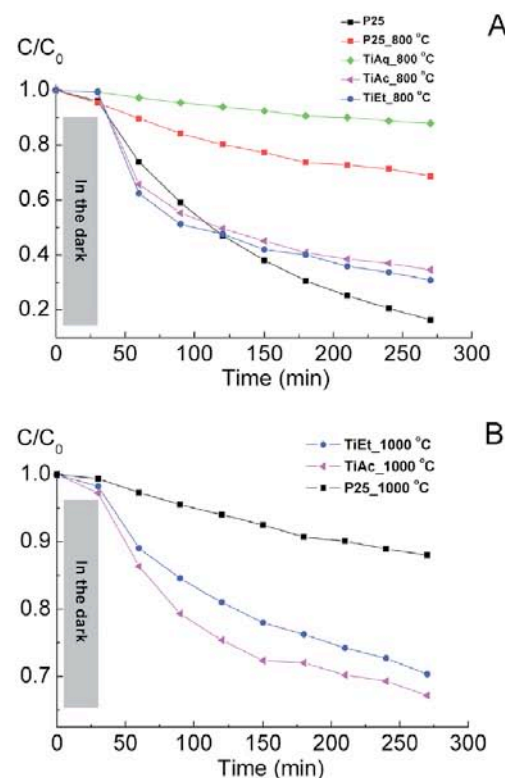

Fig. 6 Decomposition of MB under UV radiation in the presence of TiAq, TiAc and TiEt samples synthesized in this work, compared with Aeroxide P25, as a function of the calcination temperature: (A) 800 °C and (B) 1000 °C.

this fact may lead to enhancement of photocatalytic activity. Despite the crystallinity of **TiAq** sample is improved by thermal treatment at 800 °C, this sample does not show any increase of photocatalytic activity, which is probably attributed to its densification and therefore resulting in low BET surface area of just 9 m^2 g^{-1} (Fig. S9†). However, **TiEt** sample treated at the same temperature retains higher surface area (34 m^2 g^{-1}) and mesopore volume (Fig. S10†). The decomposition rates of **MB** in the presence of **TiEt** or **TiAc** samples calcined at 800 °C reach almost the values obtained by the commercial photocatalyst **Aeroxide P25** (Fig. 6a). This known commercial photocatalyst has proved to be very efficient; however it shows poor thermal stability compared to **TiEt** and **TiAc** samples. The calcination of **Aeroxide P25** at temperatures higher than 800 °C induced the full transition from anatase phase to the photocatalytic less-active rutile phase (Fig. S11†). Obviously, 100% pure anatase phase up to 900 °C, high surface area and mesoporosity of **TiEt** and **TiAc** samples are the main contributors to the outstanding photocatalytic activity (Fig. 6a). When **TiEt** and **TiAc** are thermally treated at 1000 °C, their photodecomposition rate of **MB** decreases. However, their photocatalytic activity is still nearly

twice higher than for **Aeroxide P25** treated at the same temperature (Fig. 6b). Moreover, the degree of **MB** photo-degradation in **TiAc** sample was slightly enhanced compared to **TiEt**, which could be attributed to the better charge separation on the anatase–rutile interface.[33,34]

4. Conclusion

In summary, we have developed and described a new solvent-exchange method for the preparation of undoped TiO_2 photocatalysts with unprecedented anatase thermal stability and outstanding photocatalytic activity. We have succeeded in preparing mesoporous pure anatase TiO_2 nanoparticles which are stable up to 1000 °C. The preparation procedure is completed by using ethanol to precipitate hydrous titania particles from basic medium containing titanium peroxo complex. High thermal stability against anatase-to-rutile phase transformation is caused by the defectiveness of the formed TiO_2 structure, which is the consequence of the rapid decomposition of titania peroxo species. The photocatalytic activity of the prepared TiO_2 materials, thermally treated at temperatures higher than 800 °C, is superior to the commercial **Aeroxide P25**

photocatalyst treated at the same conditions. The thermal stability of anatase up to the sintering temperatures, along with its high photocatalytic activity, offer new possibilities to prepare a wide range of self-cleaning and anti-bacterial TiO_2-based ceramic materials to meet medical and domestic needs.

Acknowledgements

References

1 M. D. Hernández-Alonso, F. Fresno, S. Suárez and J. M. Coronado, Development of Alternative Photocatalysts to TiO_2: Challenges and Opportunities, *Energy Environ. Sci.*, 2009, **2**, 1231–1257.

2 X. Lang, W. Ma, C. Chen, H. Ji and J. Zhao, Selective Aerobic Oxidation Mediated by TiO_2 Photocatalysis, *Acc. Chem. Res.*, 2014, **47**, 355–363.

3 A. Kubacka, M. Fernández-García and G. Colon, Advanced Nanoarchitectures for Solar Photocatalytic Applications, *Chem. Rev.*, 2012, **112**, 1555–1614.

4 X. B. Chen and S. S. Mao, Titanium Dioxide Nanomaterials: Synthesis, Properties, Modifications, and Applications, *Chem. Rev.*, 2007, **107**, 2891–2959.

5 M. R. Hoffmann, S. T. Martin, W. Choi and D. W. Bahnemann, Environmental Applications of Semiconductor Photocatalysis, *Chem. Rev.*, 1995, **95**, 69–96.

6 A. A. Ismail and D. W. Bahnemann, Mesoporous titania photocatalysts: preparation, characterization and reaction mechanisms, *J. Mater. Chem.*, 2011, **21**, 11686–11707.

7 D. J. Stacchiola, S. D. Senanayake, P. Liu and J. R. Rodriguez, Fundamental Studies of Well-Defined Surfaces of Mixed-Metal Oxides: Special Properties of $MOx/TiO_2(110)$ {M = V, Ru, Ce, or W}, *Chem. Rev.*, 2013, **113**, 4373–4390.

8 W. Y. Teoh, J. A. Scott and R. Amal, Progress in Heterogeneous Photocatalysis: From Classical Radical Chemistry to Engineering Nanomaterials and Solar Reactors, *J. Phys. Chem. Lett.*, 2012, **3**, 629–639.

9 M. Cargnello, T. R. Gordon and C. B. Murray, Solution-Phase Synthesis of Titanium Dioxide Nanoparticles and Nanocrystals, *Chem. Rev.*, 2014, **114**, 9319–9345.

10 K. Liu, M. Cao, A. Fujishima and L. Jiang, Bio-Inspired Titanium Dioxide Materials with Special Wettability and Their Applications, *Chem. Rev.*, 2014, **114**, 10044–10094.

11 L. Liu and X. Chen, Titanium Dioxide Nanomaterials: Self-Structural Modifications, *Chem. Rev.*, 2014, **114**, 9890–9918.

12 M. Machida, K. Norimoto and T. Kimura, Antibacterial Activity of Photocatalytic Titanium Dioxide Thin Films with Photodeposited Silver on the Surface of Sanitary Ware, *J. Am. Ceram. Soc.*, 2005, **88**, 95–100.

13 J. Choi, H. Park and M. R. Hoffmann, Effects of Single Metal-Ion Doping on the Visible-Light Photoreactivity of TiO_2, *J. Phys. Chem. C*, 2010, **114**, 783–792.

14 S. C. Padmanabhan, S. C. Pillai, J. Colreavy, S. Balakrishnan, D. E. McCormack, T. S. Perova, Y. Gun'ko, S. J. Hinder and J. M. Kelly, A Simple Sol–Gel Processing for the Development of High-Temperature Stable Photoactive Anatase Titania, *Chem. Mater.*, 2007, **19**, 4474–4481.

15 P. Periyat, S. C. Pillai, D. E. McCormack, J. Colreavy and S. J. Hinder, Improved High-Temperature Stability and Sun-Light-Driven Photocatalytic Activity of Sulfur-Doped Anatase TiO_2, *J. Phys. Chem. C*, 2008, **112**, 7644–7652.

16 M. Hirano, K. Ota and H. Iwata, Direct Formation of Anatase (TiO_2)/Silica SiO_2) Composite Nanoparticles with High Phase Stability of 1300 °C from Acidic Solution by Hydrolysis under Hydrothermal Condition, *Chem. Mater.*, 2004, **16**, 3725–3732.

17 J.-Y. Kim, C.-S. Kim, H.-K. Chang and T.-O. Kim, Effects of ZrO_2 Addition on Phase Stability and Photocatalytic Activity of ZrO_2/TiO_2 Nanoparticles, *Adv. Powder Technol.*, 2010, **21**, 141–144.

18 J. Wu, S. Hao, J. Lin, M. Huang, Y. Huang, Z. Lan and P. Li, Crystal Morphology of Anatase Titania Nanocrystals Used in Dye-Sensitized Solar Cells, *Cryst. Growth Des.*, 2008, **8**, 247–252.

19 Y. Mao and S. S. Wong, Size- and Shape-Dependent Transformation of Nanosized Titanate into Analogous Anatase Titania Nanostructures, *J. Am. Chem. Soc.*, 2006, **128**, 8217–8226.

20 W. Li, Y. Bai, C. Liu, Z. Yang, X. Feng, X. Lu, N. K. Van der Laak and K. Y. Chan, Highly Thermal Stable and Highly Crystalline Anatase TiO_2 for Photocatalysis, *Environ. Sci. Technol.*, 2009, **43**, 5423–5428.

21 S. C. Pillai, P. Periyat, R. George, D. E. McCormack, M. K. Seery, H. Hayden, J. Colreavy, D. Corr and S. J. Hinder, Synthesis of High-Temperature Stable Anatase TiO_2 Photocatalyst, *J. Phys. Chem. C*, 2007, **111**, 1605–1611.

22 N. T. Nolan, M. K. Seery and S. C. Pillai, Spectroscopic Investigation of the Anatase-to-Rutile Transformation of Sol–Gel-Synthesized TiO_2 Photocatalysts, *J. Phys. Chem. C*, 2009, **113**, 16151–16157.

23 J.-Y. Piquemal, E. Briot and J.-M. Bregeault, Preparation of Materials in the Presence of Hydrogen Peroxide: from Discrete or "Zero-Dimensional" Objects to Bulk Materials, *Dalton Trans.*, 2013, 29–45.

24 M. Kakihana, M. Kobayashi, K. Tomita and V. Petrykin, Application of Water-Soluble Titanium Complexes as Precursors for Synthesis of Titanium Containing Oxides *via* Aqueous Solution Process, *Bull. Chem. Soc. Jpn.*, 2010, **83**, 1285–1308.

25 N. Murakami, Y. Kurihara, T. Tsubota and T. Ohno, Shape-Controlled Anatase Titanium(ɪv) Oxide Particles Prepared by Hydrothermal Treatment of Peroxo Titanic Acid in the Presence of Polyvinyl Alcohol, *J. Phys. Chem. C*, 2009, **113**, 3062–3069.

79

26 J. Liao, L. Shi, S. Yuan, Y. Zhao and J. Fang, Solvothermal Synthesis of TiO$_2$ Nanocrystal Colloids from Peroxotitanate Complex Solution and Their Photocatalytic Activities, *J. Phys. Chem. C*, 2009, **113**, 18778–18783.

27 V. Etacheri, M. K. Seery, S. J. Hinder and S. C. Pillai, Oxygen Rich Titania: A Dopant Free, High Temperature Stable, and Visible-Light Active Anatase Photocatalyst, *Adv. Funct. Mater.*, 2011, **21**, 3744–3752.

28 H. Ichinose, M. Terasaki and H. Katsuki, Synthesis of peroxo-modified anatase sol from peroxo titanic acid solution, *J. Ceram. Soc. Jpn.*, 1996, **104**, 715–718.

29 G. N. Vayssilov, Structural and Physicochemical features of titanium silicalites, *Catal. Rev.*, 1997, **39**, 209–251.

30 M. Ilkaeva, I. Krivtsov, V. Avdin, S. Khainakov and J. R. Garcia, Comparative Study of Structural Features and Thermal Behavior of Mixed Silica-Titania Xerogels Prepared *via* the Peroxo Method and the Conventional Co-Precipitation Technique, *Colloids Surf.*, 2014, **456**, 120–128.

31 M. Okada, P. Jing, Y. Yamada, M. Tazawa and K. Yoshimura, Low-Energy Electron Energy Loss Spectroscopy of Rutile and Anatase TiO$_2$ Films in the Core Electron Excitation Regions, *Surf. Sci.*, 2004, **566–568**, 1030–1034.

32 A. Gloter, C. Ewels, P. Umek, D. Arcon and C. Colliex, Electronic Structure of Titania-Based Nanotubes Investigated by EELS Spectroscopy, *Phys. Rev. B: Condens. Matter Mater. Phys.*, 2008, **80**, 035413.

33 D. O. Scanlon, C. W. Dunnill, J. Buckeridge, S. A. Shevlin, A. J. Logsdail, S. M. Woodley, C. R. A. Catlow, M. J. Powell, R. G. Palgrave, I. P. Parkin, G. W. Watson, T. W. Keal, P. Sherwood, A. Walsh and A. A. Sokol, Band Alignment of Rutile and Anatase TiO$_2$, *Nat. Mater.*, 2013, **12**, 798–801.

34 D. C. Hurum, A. G. Agrios, K. A. Gray, T. Rajh and M. C. Thurnauer, Explaining the Enhanced Photocatalytic Activity of Degussa P25 Mixed-Phase TiO$_2$ Using EPR, *J. Phys. Chem. B*, 2003, **107**, 4545–4549.

Electronic Supporting Information

Exceptional thermal stability of undoped anatase TiO₂ photocatalysts prepared by a solvent-exchange method

Igor Krivtsov*[a,b], Marina Ilkaeva[a,c], Viacheslav Avdin[b,c], Zakariae Amghouz[d], Sergei A. Khainakov[d], José R. García[a], Eva Díaz[e] and Salvador Ordoñez[e]

[a] Department of Organic and Inorganic Chemistry, University of Oviedo-CINN, 33006 Oviedo, Spain
[b] Nanotechnology Education and Research Center, South Ural State University, 454080, Chelyabinsk, Russia
[c] Department of Chemistry, South Ural State University, 454080 Chelyabinsk, Russia
[d] Servicios Científico Técnicos, Universidad de Oviedo, 33006 Oviedo, Spain
[e] Department of Chemical and Environmental Engineering, University of Oviedo, 33006 Oviedo, Spain

1
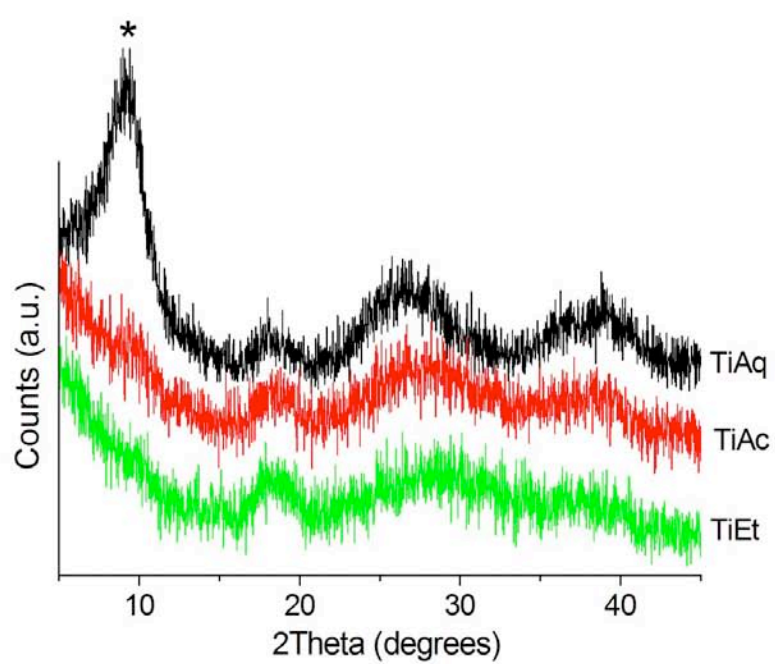
Fig. S1. Powder XRD patterns of the as-prepared samples

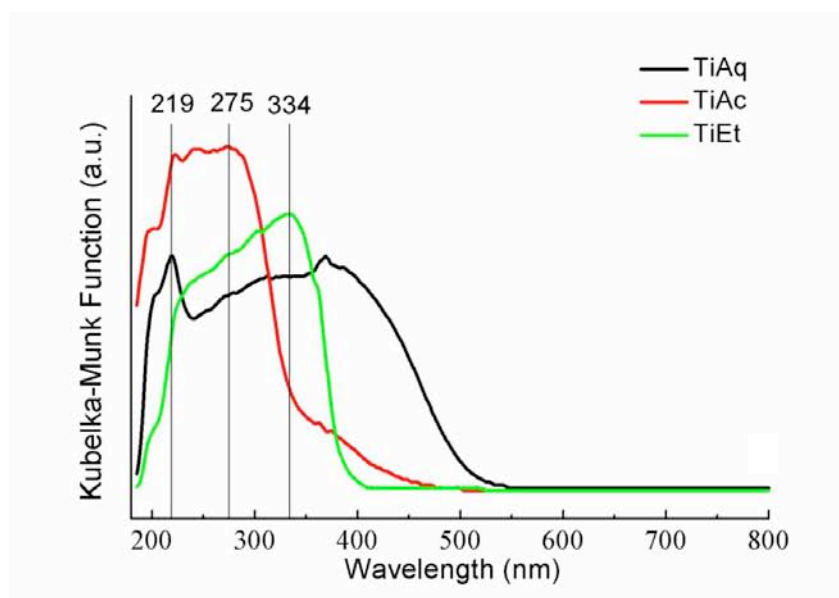Fig. S2 DR UV-vis spectra of the as-prepared TiAq, TiAc and TiEt samples
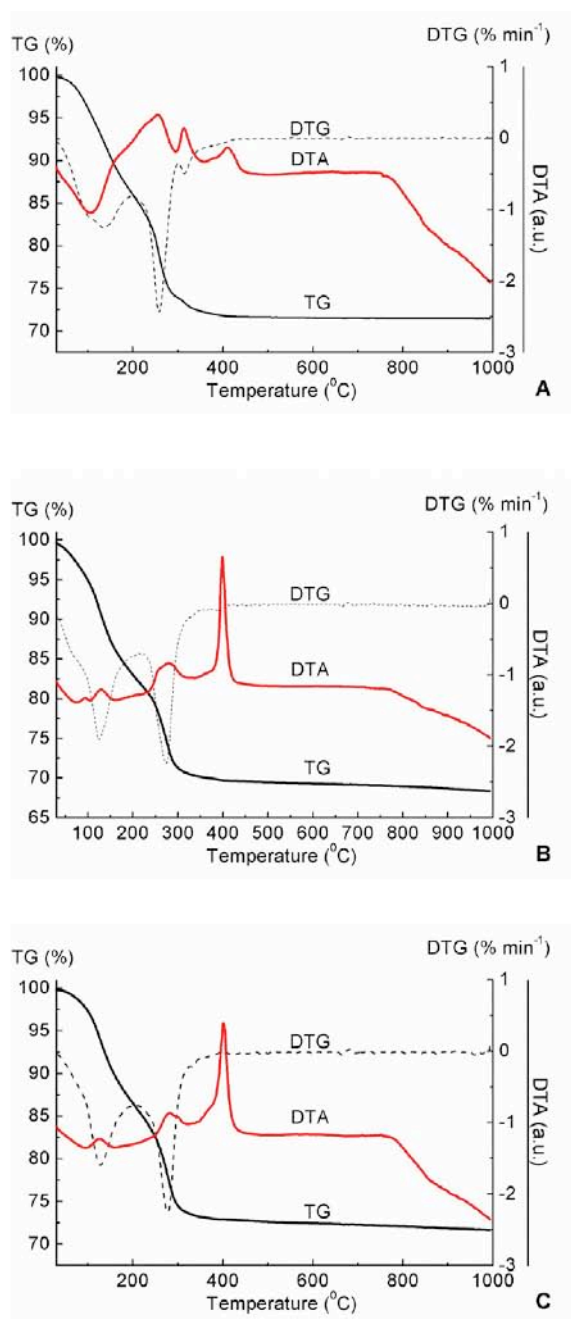
Fig. S3 TG/DTG/DTA curves of the (A) TiAq, (B) TiAc and (C) TiEt samples
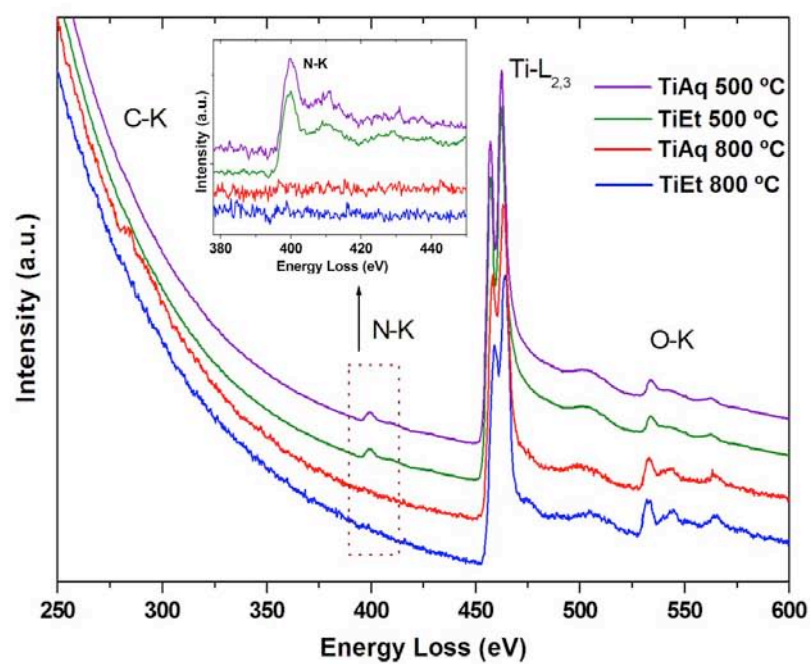
Figure S4. EELS spectra of some selected **TiEt** and **TiAq** samples; the inset shows the magnification of the nitrogen K-edge.
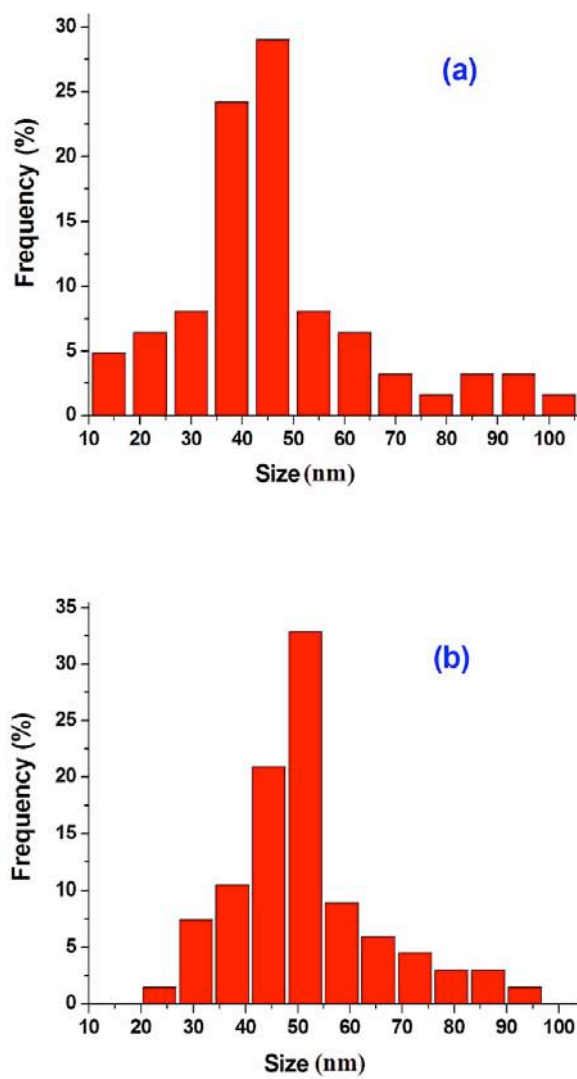
Fig. S5. Histograms of particle-size distribution for the **TiEt** (a) and **TiAq** (b) samples thermally treated at 800 ºC
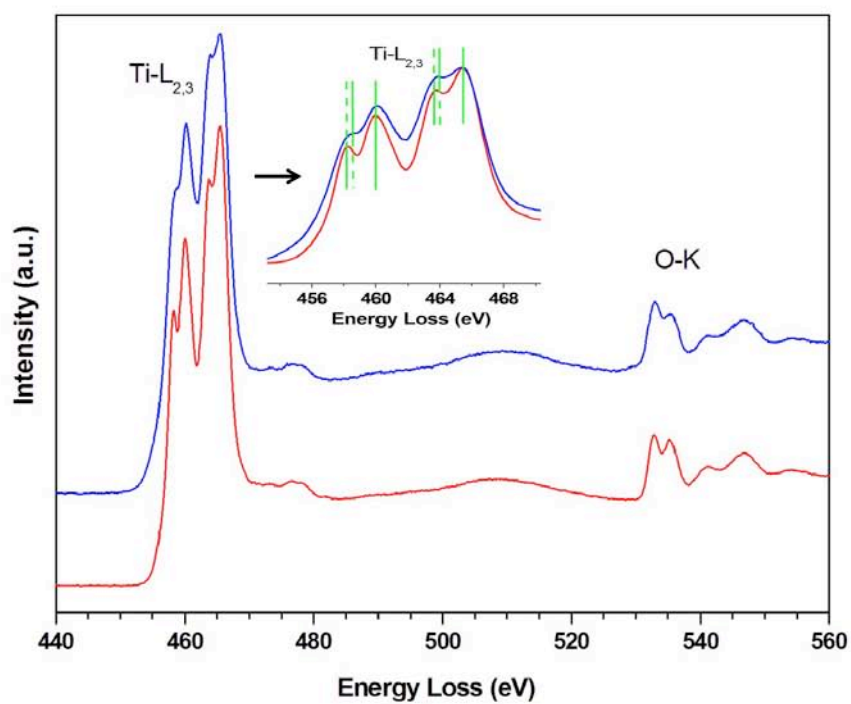
Fig. S6. Titanium L2,3 core-Loss and oxygen K core-Loss normalized EELS spectra from the **TiEt** (blue) and **TiAq** (red) samples treated at 800 ºC
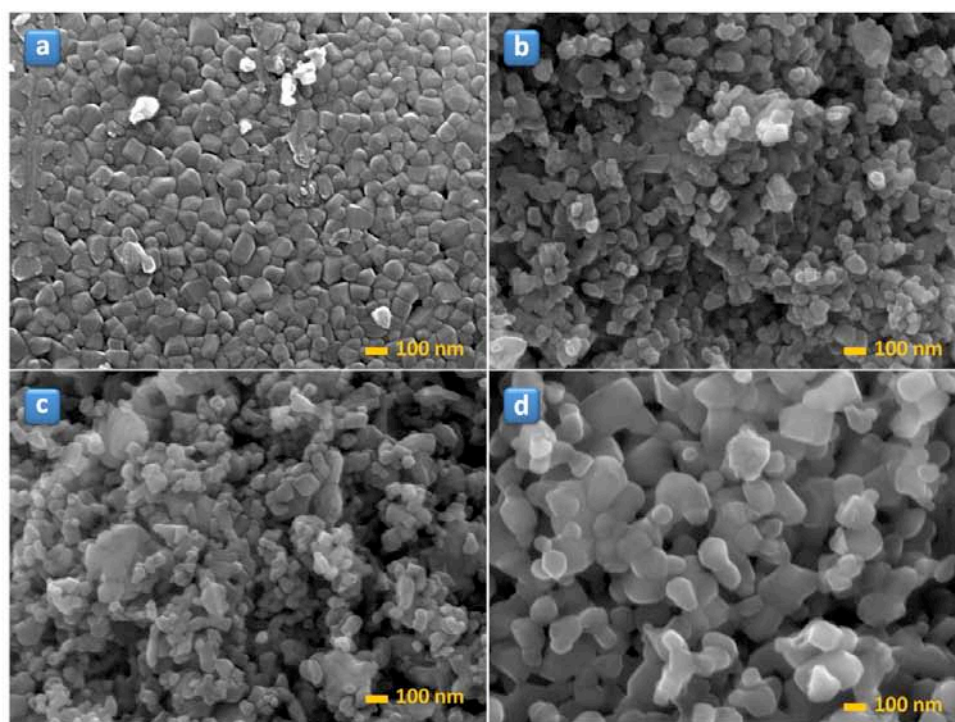
Fig. S7. SEM-images of the **TiAq** (a), **TiAc** (b), **TiEt** (c) samples thermally treated at 800 °C   and the **TiEt** treated at 1000 °C (d)
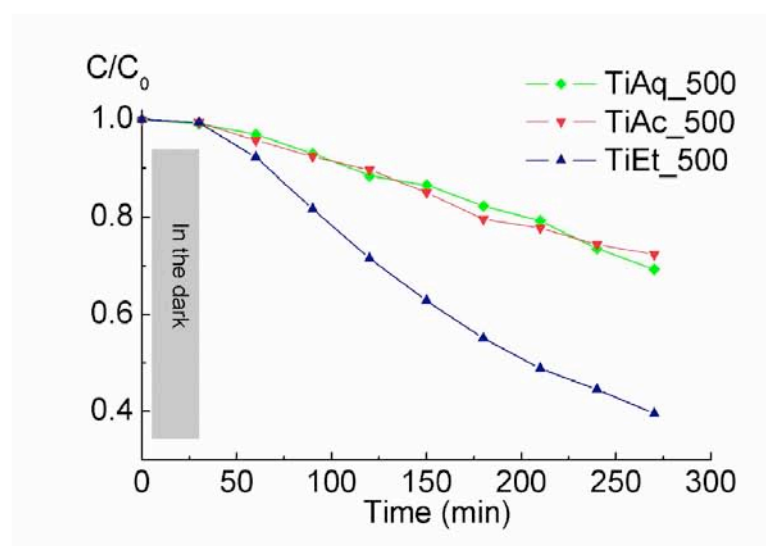
Fig. S8. Photocatalytic decomposition of **MB** in presence of the catalysts thermally treated at 500 °C

9
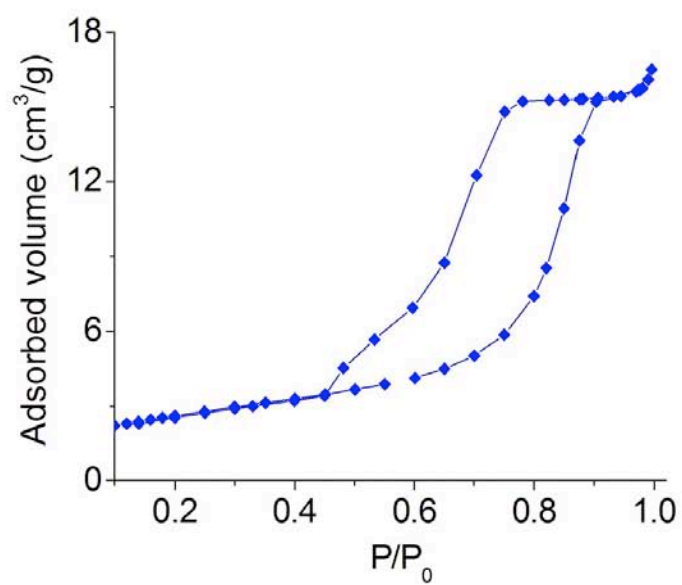
Fig. S9. N$_2$ Adsorption-desorption isotherm at 77 K for the sample **TiAq** calcined at 800
°C   (BET surface area: 9 m^2·g^{-1}; mesopores volume: 0.026 cm^3·g^{-1})
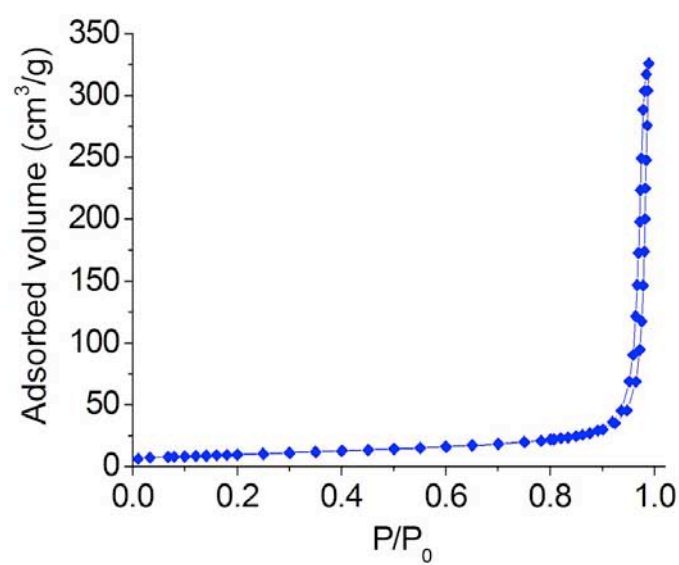
Fig. S10. N_2 Adsorption-desorption isotherm at 77 K for the sample **TiEt** calcined at 800 °C (BET surface area: 34 $m^2 \cdot g^{-1}$; mesopores volume: 0.50 $cm^3 \cdot g^{-1}$)
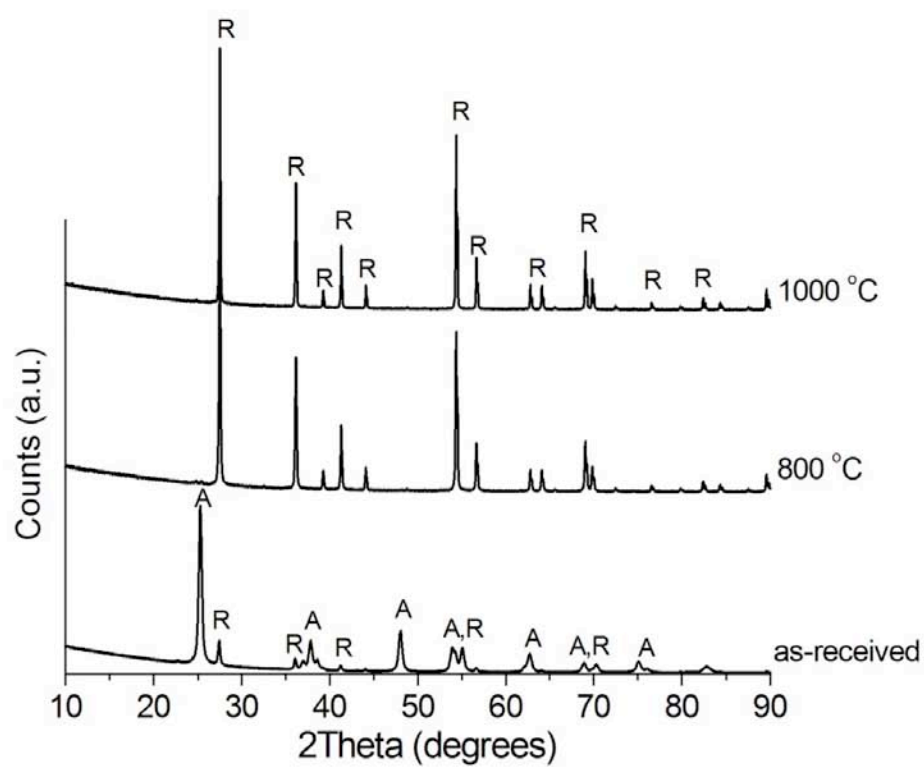
Fig. S11. Powder XRD patterns of **Evonik P25** thermally treated at different temperatures

4.2 Selective photocatalytic oxidation on semiconductor surfaces

In this chapter, selective photo-oxidation properties of two well-known semiconductor photocatalysts titanium dioxide and graphitic carbon nitride are discussed. For a long period of time, the interest towards partial oxidation of organic compounds via photocatalysis had been overshadowed by applications of this phenomenon for pollutant degradation, until the amount of accumulated knowledge about the principles governing photo-oxidation and an impressive data on tailoring of this process finally permitted to develop procedures targeting the production of certain valuable compounds through light-initiated reactions. Among the all variety of the synthesized photocatalysts g-C_3N_4 and TiO_2 are those meeting the demands for high quantum efficiency, low-cost of production, stability and non-toxicity.

4.2.1 Role of TiO_2 defects sites in promoting selectivity of the photocatalytic processes

Titanium dioxide is primarily known for its efficiency for complete degradation of noxious organic compounds to CO_2 and H_2O. Surely, the decomposition induced by photogenerated oxidative species does not lead directly to mineralization, but many intermediate compounds are formed on the course of reactions. Some of the products of partial oxidation obtained via hydrogen abstraction, $^\bullet OH$ or superoxide radical attack are valuable molecules such as aromatic aldehydes, acids or alcohols. Mild conditions of photocatalytic reactions and almost inexhaustible source of energy are found to be tempting enough for the research community to consider the application of heterogeneous photocatalysis for organic synthesis. The ways of terminating a photo-activated reaction at a certain point, when the desired compound is produced, are discussed in details in Chapter 1.4. Introducing the defect sites into TiO_2, in order to supress hydroxyl radicals generation and favour the desorption of the product, is one of those methods. Although non-metal doping of titania is widely applied, the role of N and O interstitials in the local arrangement in the titania structural units and the effect they have on photo-degradation and partial photo-oxidation performance of TiO_2 is barely studied.

It is of common opinion that poor crystallinity, or in other words the presence of high quantities of amorphous phase, responsible for bulk and surface defects in the photocatalyst, is an indispensable property of TiO_2 allowing its use in partial photocatalytic oxidation reactions in aqueous medium [199, 225]. High content of defects in disordered TiO_2 materials does not permit a proper evaluation of the effect of heteroatomic dopants on the photocatalytic performance. For this reason, in the following study a series of well-crystalline anatase titania is considered. The peroxo method of TiO_2 nanoparticles preparation described by Etacheri et al. [227] satisfies this condition providing both high crystallinity and stability of anatase TiO_2 phase. The estimation of amorphous phase content by quantitative XRD approach using internal standard CaF_2 has shown that the concentration of amorphous titania does not exceed 8% and it has not evidenced any correlation with N or O dopants content. The source of nitrogen in the present synthesis has been ammonia, which constitutes a cationic part of ammonium peroxotitanate complex. Calcination of the gelled and dried precursors solutions at temperatures 400 ºC and 500 ºC results in the formation of nitrogen-doped titania with N content of 6 and 2 at%, respectively. The incorporation of nitrogen in the form of NO_x species into interstitial positions of titania structure shifts the absorption edge of TiO_2 to 3.05 eV, and also it is responsible for appearance of interband states able to harvest visible light. The expected blue shift after the N-dopants are eliminated is not observed. Using the combination of XRD, XPS, and especially EXAFS techniques, it has been established that the introduction of nitrogen interstitials provokes formation of oxygen vacancies in the first coordination shell of Ti. The consecutive removal of N-species under high-temperature treatment leaves the net-charge of TiO_2 imbalanced, which triggers the capture of atmospheric oxygen during the calcination. The captured oxygen is firstly adsorbed on the surface of titania and then it gradually diffuses to the interior aiming to occupy the vacant sites in the titanium environment. This oxygen is present in the titania structure in the form of interstitial species causing elongation of crystallographic c parameter and expansion of anatase TiO_2 cell. The interstitial oxygens according to the calculations made by other research groups and by the experimental data demonstrated in the following study form superoxide and peroxide species, which influence the electronic properties of TiO_2 and shift its BG to lower energies.

The test of pollutant photo-decomposition properties of the prepared materials is intended to demonstrate the effect of N and O dopants on the degradation rate of p-cresol. It has been shown that the presence of N-species inhibits the UV-assisted photo-degradation of p-cresol, even despite the fact that N-TiO$_2$ samples have superior SSA. The primary reason for the inhibition is the charge separation on nitrogen-doping defect sites in TiO$_2$, which is probed by PL study. The O-doped TiO$_2$ demonstrate somewhat higher rates of p-cresol degradation exceeding that of N-doped by a factor of 1.4. Although, the values of BG observed for the both types of doped titania are almost the same, the presence of the interband states in the N-TiO$_2$ favours more efficient harvesting of visible light resulting in higher rates of p-cresol photocatalytic decomposition if the NaNO$_2$-filter, cutting-off the irradiation with wavelengths below 400 nm, is applied.

If O-doped TiO$_2$ is preferred for the application for photo-decomposition of organic pollutants, N-doped titania shows better performance if there is a need for selective formation of partial oxidation compounds. The partial photo-oxidation of a biomass platform molecule HMF to FDC, having a potential application in biopolymer production [218-220], in the presence of N-TiO$_2$ gives the selectivity to FDC formation of 34%, while this value for the O-doped TiO$_2$ at the same HMF conversion is only 20%. The higher selectivity of N-TiO$_2$ is explained by the low affinity of the partial oxidation product to the photocatalyst surface and inhibition of hydroxyl radicals formation. Thus, the following work does not only show the detailed investigation of Ti local structure in nitrogen and oxygen doped titania, but gives a basis for a rational design of TiO$_2$-based photocatalysts for specific applications.

Article III

"Consequences of Nitrogen Doping and Oxygen Enrichment on Titanium Local Order and

Photocatalytic Performance of TiO$_2$ Anatase"

The Journal of Physical Chemistry C

121 (6770–6780)

Year 2017

DOI: 10.1021/acs.jpcc.7b00354

Impact Index: 4.509

Consequences of Nitrogen Doping and Oxygen Enrichment on Titanium Local Order and Photocatalytic Performance of TiO$_2$ Anatase

Igor Krivtsov,*[†,‡] Marina Ilkaeva,[†,‡] Eduardo Salas-Colera,[§,∥] Zakariae Amghouz,[⊥] José R. García,[†] Eva Díaz,[#] Salvador Ordóñez,[#] and Silvia Villar-Rodil[∇]

[†]Department of Organic and Inorganic Chemistry, University of Oviedo-CINN, 33006 Oviedo, Spain

[‡]Nanotechnology Education and Research Center, South Ural State University, 454080 Chelyabinsk, Russia

[§]Instituto de Ciencia de Materiales de Madrid, CSIC, Sor Juana Inés de la Cruz 3, Cantoblanco, 28049 Madrid, Spain

[∥]Spanish CRG BM25 SpLine Beamline at the ESRF, 71 Avenue de Martyrs, F-38043 Grenoble, France

[⊥]Department of Materials Science and Metallurgical Engineering, University of Oviedo, Campus Universitario, 33203 Gijón, Spain

[#]Department of Chemical and Environmental Engineering, University of Oviedo, 33006 Oviedo, Spain

[∇]Instituto Nacional del Carbón, INCAR-CSIC, Apartado 73, 33080 Oviedo, Spain

S Supporting Information

ABSTRACT: Extended X-ray absorption fine structure (EXAFS) investigation of the oxygen-rich titania formed via the thermal treatment of N-doped TiO$_2$ has revealed that the removal of N-dopants is responsible for the creation of defect sites in the titanium environment, thus triggering at high temperatures (500−800 °C) the capture of atmospheric oxygen followed by its diffusion toward the vacant sites and formation of interstitial oxygen species. The effect of the dopants on Ti coordination number and Ti−O$_{int}$ and Ti−N$_{int}$ bond distances has been estimated. The photocatalytic p-cresol degradation tests have demonstrated that the interband states formed by the N-dopants contribute to a greater extent to the visible-light activity than the oxygen interstitials do. However, under the UV irradiation the oxygen-rich titania shows higher efficiency in the pollutant degradation, while the N-dopants in N−TiO$_2$ play the role of recombination sites. The presence of the surface nitrogen species in TiO$_2$ is highly beneficial for the application in partial photooxidation reactions, where N−TiO$_2$ demonstrates a superior selectivity of 5-hydroxymethyl furfural (HMF) oxidation to 2,5-furandicarboxaldehyde (FDC). Thus, this work underlines the importance of a rational design of nonmetal doped titania for photocatalytic degradation and partial oxidation applications, and it establishes the role of bulk defects and surface dopants on the TiO$_2$ photooxidation performance.
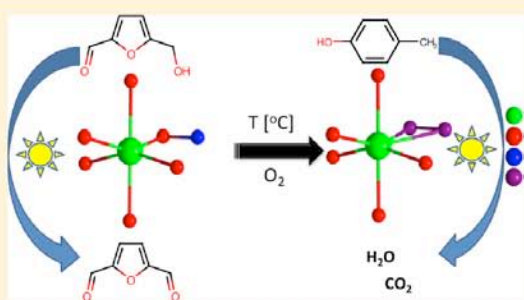
1. INTRODUCTION

Titanium dioxide is a well-known photocatalyst efficient under UV irradiation,[1−4] although nowadays the extension of its photocatalytic properties to a broader part of the solar spectrum is of key interest.[5−8] This can be achieved by nitrogen doping,[9] oxygen vacancies creation,[10] H$_2$O$_2$ modification[11] or oxygen interstitials incorporation.[12] The formation of interstitial oxygen species is observed for different metal oxide materials.[13−16] The presence of interstitial oxygen in TiO$_2$ was proposed on the basis of theoretical calculations[17−19] and confirmed experimentally for the reduced TiO$_2$ having Ti^{3+} sites[20] and rutile single crystal with oxygen vacancies,[21] and it was even observed by the electron microscopy methods for Nb-doped TiO$_2$.[22] The common feature of the reported TiO$_2$ materials containing oxygen interstitials is their defective structure formed as the result of

doping, reductive, or high-energy treatment. The presence of structural defects drives O$_2$ capture, and its consecutive incorporation into TiO$_2$ crystals aims to compensate the net-charge imbalance. Etacheri et al.[12] reported an intriguing procedure for the preparation of visible-light-active oxygen-rich TiO$_2$ anatase, where the only dopant was the interstitial oxygen incorporated into the oxide structure under calcination. Latter, Tan et al.[23−25] described a series of the preparation procedures devoted to obtain oxygen-rich titania guided mostly by the H$_2$O$_2$:Ti ratio suggested in ref 12 while using a different TiO$_2$ source. However, the properties, i.e., phase composition and band-gap (BG) energy, of the materials synthesized by Tan et

al. did not coincide with those reported in ref 12, thus forcing us to rethink the mechanism of oxygen-rich titania formation. Previously,[26] we established that a preparation procedure similar to that reported in ref 12 led to N-doping of titania at treatment temperatures up to 500 °C. N-species can occupy substitutional or interstitial positions in TiO_2 network, as demonstrated by spectroscopic studies.[27,28] Belver et al.[29,30] were the first in providing a deeper insight in the local arrangement of Ti in N-doped titania, using more sophisticated analytical methods such as in situ DRIFT studies and XAS investigation. They discovered that the N-doping was responsible for the oxygen vacancies formation in titanium dioxide. In a more recent investigation supported by DFT calculations and EXAFS, Ceotto et al. postulated that nitrogen preferentially occupies the axial position in the TiO_6 polyhedra replacing the lattice oxygen at low doping levels and forming oxygen vacancies at high dopant concentrations.[31] Several years later, Sahoo et al. found out by means of EXAFS that nitrogen interstitial doping is responsible for the reduction of Ti—O coordination number and the increase of the axial and equatorial Ti—O bond lengths.[32]

In our view, N-doping related defects in TiO_2 might be a driving force for the consecutive O-interstitials incorporation and oxygen-rich titania formation. Here, we will explore this hypothesis focusing on evaluation of the data obtained from EXAFS and other analytical techniques about the local Ti arrangement in titania anatase. We will also demonstrate not only that the type of dopants is responsible for the visible-light absorption but also that it determines the performance of TiO_2 in destructive and selective photocatalytic reactions. A bare TiO_2 having a hydroxylated surface is an efficient photocatalyst for the destruction of water pollutants, such as phenols,[33] while achieving selectivity in partial oxidation reactions in water medium usually demands the materials to be modified by dopants or its crystallinity to be reduced.[34] Thus, we propose the rational design of doped TiO_2 targeting some specific photocatalytic applications. The total photo-oxidation of p-cresol, a common water pollutant, was used to evaluate the performance of these materials for environmental purposes. Also, the conversion of HMF, a biomass-derived platform molecule used to produce 2,5-furandicarboxylic acid and 2,5-furnadicarboxaldehyde (FDC),[35−37] was studied in the present work, in order to probe the selective photo-oxidation performance of N-TiO2 and oxygen-rich titania.

2. EXPERIMENTAL SECTION

2.1. Materials and Methods. Titanium oxysulfate hydrate containing 17% H_2SO_4 was purchased from Aldrich. Ammonia−water solution (20%) and 30 wt % hydrogen peroxide (H_2O_2) water solution were of analytical grade and used as received without additional purification. The concentration of titanium oxysulfate was determined gravimetrically prior to its use in the synthesis. A commercial titanium dioxide (anatase phase) was purchased from Aldrich.

The titanium dioxide photocatalysts were prepared by the method described elsewhere,[26] which was also similar to that described by Etacheri et al.[12] Despite using titanium oxysulfate hydrate instead of titanium tetrachloride, a stable water-soluble peroxotitanium complex was eventually formed in both cases. Briefly, titanium oxysulfate hydrate containing 5 mmol of TiO_2 was dissolved in deionized water and then precipitated with 4 mL of 20% ammonia−water solution. The resulting precipitate of titanium hydroxide was centrifuged at 3000 rpm and

thoroughly washed with deionized water until the sulfates were no longer detected. On the next step of the synthesis, the precipitate was dissolved by adding 3 mL of H_2O_2 (30%), and the titanium peroxo complex was formed. Ammonia (3 M) was used to adjust pH value of the peroxo complex to 9.5 while it was ice-cold. Then, the peroxo complex solution was heated at 50 °C while stirring until the complex was gelled. The gel was dried at 70 °C overnight, powdered in an agate mortar, and calcined in a muffle furnace in air at 400, 500, 600, and 800 °C. The heating rate was 3 °C·min^{-1} and the samples were left for 2 h at the fixed temperatures. The prepared photocatalysts were designated as T_x, where x indicates a calcination temperature.

2.2. Characterization. Powder X-ray diffraction analysis (PXRD) was carried out using a Phillips X'pert diffractometer operating at Cu Kα radiation (λ = 0.15418 nm). The mean crystal size of the TiO_2 samples was estimated by Scherrer equation from the (101) reflection of anatase phase. The amount of amorphous phase in the photocatalysts was determined by the internal standard method. The PXRD data, collected from the samples mixed with 20 wt % of CaF_2, were refined using MAUD software, and the quantity of the amorphous TiO_2 was calculated using the following expression:

$$W_{am} = \left(1 - \frac{W_{std}}{W_{xrd}}\right) \times 100\%$$

where W_{am} is a weight percentage of the amorphous phase, W_{std} is the fraction of CaF_2 added to the sample, and W_{xrd} is the fraction of CaF_2 in the mixture with the titania samples determined by PXRD quantitative phase analysis.

Micromeritics ASAP 2020 was used to obtain N_2 adsorption−desorption isotherms at 77 K. Before the experiment, the samples were outgassed under vacuum at 250 °C. Specific surface area (SSA) and pore volume were calculated using BET and BJH methods. A Shimadzu UV-2700 spectrophotometer with integrated sphere attachment was used to obtain diffuse reflectance (DR) spectra of the samples using barium sulfate as a reference. BG energy was estimated by Kubelka−Munk method. Electron energy loss spectroscopy (EELS) studies were performed on a JEOL JEM-2100F transmission electron microscope The samples for TEM were dispersed in ethanol, sonicated, and sprayed on a holey carbon film coated copper grid and then allowed to air-dry. Finally, Gatan SOLARUS 950 was used before observation. The surface composition and binding energies of Ti, O, and N in the prepared photocatalysts were measured by X-ray photoelectron spectroscopy (XPS), using a SPECS system equipped with a Hemispherical Phoibos analyzer operating in a constant pass energy, using Mg Kα radiation ($h\nu$ = 1253.6 eV). Bruker Tensor 27 FTIR spectrometer was used to collect infrared spectra of the samples in KBr (Aldrich) pellets with 4 cm^{-1} resolution. RT emission spectra were measured using a standard spectrofluorometer Edinburgh Instruments FLSP920 (Edimburgh, Scotland, U.K.), equipped with a 450W Xe lamp excitation source, at an excitation wavelength of 365 nm. EXAFS measurements of the titania samples were carried out at Spanish CRG BM25A SpLine beamline (REF-A) at ESRF (The European Synchrotron Radiation Facility, Grenoble, France).[38] X-ray absorption data were collected around Ti K-edge using a −70 °C ethanol-cooled double Si(111) crystal, which gives an energy resolution of $\Delta E/E$ = 1.5 × 10^{-4}. The experiment was performed at room temperature in fluorescence mode at standard 45° geometry. For fluorescence detection, Sirius

liquid-nitrogen-cooled multielement solid-state X-ray detector from e2v was employed. The detector includes 13 Si(Li) crystal sensors mounted on a low-noise electrically restored FETs. Pure commercial TiO_2 anatase (Aldrich) and the nitrogen-doped and the oxygen-rich samples were measured in the energy range from 4.8 to 5.7 keV.

Demeter package software was used for data processing.[39] Background removal and Tröger self-absorption correction in the raw data were carried out using Athena software.[40] Artemis software was used to complete the EXAFS data analysis. Pure commercial TiO_2 anatase sample data were used to build the structural model. Two coordination shells around central Ti atoms were fitted in the range from 1.4 to 3.5 Å.

2.3. Photocatalytic Reaction. The photocatalytic properties of the prepared materials were evaluated in the reactions of photo-degradation and partial photo-oxidation using p-cresol and HMF as model compounds, respectively. The tests were carried out in aqueous phase in a stirred batch pyrex reactor containing 1 g L^{-1} photocatalysts suspended in 100 mL of the substrate solutions. The light source was a 500 W lamp (Helios Italquartz) with emission maximum at 365 nm, equipped with a water-cooling jacket and positioned at a distance of 10 cm from the reaction vessel. The selected photocatalytic runs were carried out using a UV-cutoff filter solution of $NaNO_2$ (2 M). The optimum quantity of the photocatalysts was established based on the radiometric studies, and it ensures almost complete light absorption for all the samples. Before the radiation started, the photocatalysts were suspended in the reaction solution with an assistance of ultrasonication and then mixed in the dark for 30 min, in order to complete the adsorption−desorption equilibrium. The concentrations of the substrates were 10 mg L^{-1} (0.093 mM) for p-cresol, as a pollutant, which is normally found in water at low concentration levels, and 40 mg L^{-1} (0.32 mM), 200 mg L^{-1} (1.6 mM), and 400 mg L^{-1} (3.2 mM) for HMF. Aliquots of approximately 2.5 mL were withdrawn from the reactor at the fixed time intervals, filtered through a PTFE 0.2 μm filter, and the concentrations of all compounds of interest extracted from water solutions in ethyl acetate were determined using a Shimadzu 2100 Ultra GC-MS system equipped with a Teknokroma TRB-5MS (95%) dimethyl (5%) diphenylpolysiloxane copolymer column. The analysis was carried out in a split regime. The injection port was at 250 °C; the initial column temperature was 60 °C. Then, the column was heated at 15 °C·min^{-1} up to 180 °C, and the temperature was then increased to 270 °C at a rate of 40 °C·min^{-1} and left for 2 min. Prior to each analytical run, the GC-MS system was calibrated for p-cresol or for HMF and FDC depending on the type of the reaction.

3. RESULTS AND DISCUSSION

3.1. Structural Features of N-Doped and Oxygen-Rich Titania. The phase composition of the titania prepared by the described procedure and treated in a wide temperature range was already described elsewhere.[26] Only pure anatase phase is detected for all the studied temperatures (Figure 1). High crystallinity of the TiO_2 is confirmed by the amorphous content estimation, which changes only slightly as the calcination conditions change, reaching its maximum value at the highest thermal treatment temperature (Table 1). The unit cell parameters show significant discrepancies, especially c dimension of anatase unit cell, which grows along with increasing of the annealing temperature of the samples. This parameter
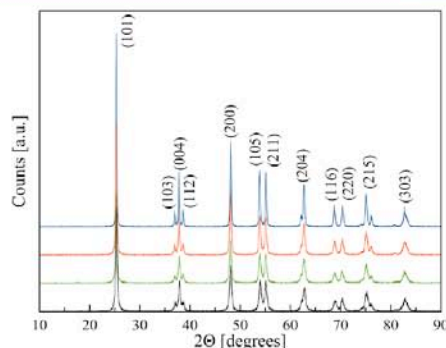
Figure 1. PXRD patterns of the titania samples: (black) T_400, (green) T_500, (red) T_600, and (blue) T_800.

exceeds that of pure commercial titania for T_600 and T_800 samples indicating the existence of certain structural perturbations (Table 1).

Considering that the precursors for the TiO_2 samples contain the sources of sulfur and nitrogen, one might attribute the changes of the anatase crystallographic parameters to the effect of nonmetal doping, especially taking into account the bright yellow color of the samples calcined at 400 and 500 °C. Indeed, sulfur is not detected by any of the used analytical methods (XPS, EELS, and CHNS-analysis), while the presence of nitrogen is obvious from the EELS data. The nitrogen content appears to be relatively high for T_400 and T_500, but it is completely removed at higher temperatures (Figure 2, Table 1). In the previous study, we observed that no nitrogen was found for the same type of TiO_2 treated at 800 °C.[26] We suppose that the application of NH_4OH for the pH adjustment of the titanium hydroxide suspension in the work of Etacheri et al. might have led to the nitrogen incorporation into the TiO_2 structure, as in the present case, although the characterization of the materials prepared at temperatures below 600 °C was not reported.[12]

Contrary to the supposition expressed in ref 12, we consider N-doping and not oxygen gas released from the decomposed peroxo complex precursor during the thermal treatment as absolutely crucial for the following development of oxygen-rich TiO_2 under higher temperatures. It was demonstrated in numerous works that the peroxo species in the titanium peroxo complexes were decomposed at temperatures not higher than 300 °C;[41−44] consequently, oxygen gas released by this reaction cannot affect the formation of TiO_2 structure at largely higher temperatures. Moreover, considering that pure TiO_2 is a stable compound in the studied temperature range, where Ti has a perfectly satisfying 6-coordinated state and exists in its highest oxidation state, there is no thermodynamic force, which would induce the incorporation of super stoichiometric oxygen into the crystal network. In contrast, the crystal defects created by the incorporation of dopants or impurities might provoke the formation of oxygen vacancies causing a charge imbalance in the TiO_2 cell, which would tend to be compensated by the reduction of Ti^{4+} to Ti^{3+} or Ti^{2+} or by trapping oxygen from the atmosphere, which would occupy the vacant sites. Although the role of nitrogen doping and its effect on the titanium local arrangement in our view is crucial for the preparation of oxygen-rich TiO_2, the importance of hydrogen peroxide concentration in the synthesis of this material must not be

Table 1. Properties of the Prepared Titania Samples

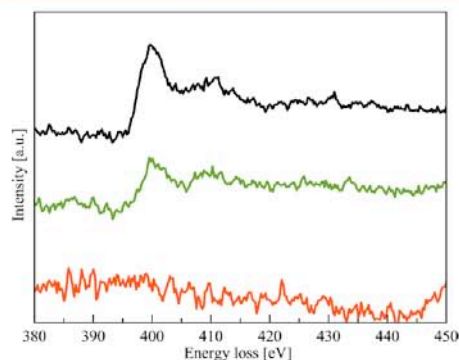| sample	crystal size (nm)	unit cell parameters (Å)		unit cell volume (Å³)	amorphous phase content (%)	BG (eV)	SSA (m²g⁻¹)	EELS N (atom %)	K (min⁻¹)
		a	c						
T_400	22 ± 1	3.7858(9)	9.5044(3)	136.22	3.4 ± 0.4	3.05	81	6	0.0179
T_500	27 ± 3	3.7848(7)	9.5084(3)	136.21	1.1 ± 0.3	3.10	59	2	0.0223
T_600	33 ± 3	3.7845(7)	9.5146(2)	136.27	2.5 ± 0.3	3.08	36	0	0.0256
T_800	54 ± 5	3.7833(5)	9.5245(2)	136.33	7.7 ± 0.3	3.05	9	0	0.0101
anatase (Aldrich)	91 ± 7	3.7844(9)	9.5135(8)	136.25	0 ± 0.1	3.20	5	0	

Figure 2. N region of EELS spectra obtained for (black) T_400, (green) T_500, and (red) T_600.

underestimated. In our opinion, high concentration of H_2O_2 provides the titanium complexation by the peroxo ligands and stabilization of ammonium peroxotitanate, thus facilitating the incorporation of nitrogen species into the TiO_2 under thermal treatment.

The electronic structure of the titania materials was studied by UV–vis spectroscopy and by measuring the valence band (VB) potential by XPS. The DR UV–vis study clearly demonstrates the effect of the nitrogen-doping on the electronic properties of T_400 and T_500 samples, as the light-absorbance is extended to the visible-light region and the BG values are estimated to be 3.05 and 3.10 eV, respectively (Figure 3A,B). Nitrogen impurities induce sub-band-gap states resulting in the appearance of the second absorption edge at about 2.3 eV observed for T_400 and T_500 (Figure 3A,B, Table 1). Bellardita et al. reported similar observations.[45] The elimination of nitrogen species, capable of reducing the titania BG, leaves its position almost unchanged, while the sub-band-gap states and the corresponding visible-light absorption disappear completely (Figure 3C,D, Table 1).

From Figure 4 is seen that both the N-doped and the N-free TiO_2 samples possess identical VB potential of 2.4 eV; thus, the subtraction of BG from the VB potential gives us the conduction band (CB) value similar to those for all the studied TiO_2 materials and close to −0.7 eV. Such a minor difference in the electronic structure of the N-doped titania from the pristine TiO_2 anatase, having BG, VB, and CB values of 3.2, 2.5, and −0.7 eV, respectively, indicates that the principal role of the N-doping is sensitizing for visible-light activation of the photocatalysts, which is related to the appearance of the sub-band-gap states in T_400 and T_500.

It is still not clear if only substitutional nitrogen species are able to shift the absorption edge of TiO_2 to the visible region, while interstitial nitrogen dopants form interband states, which
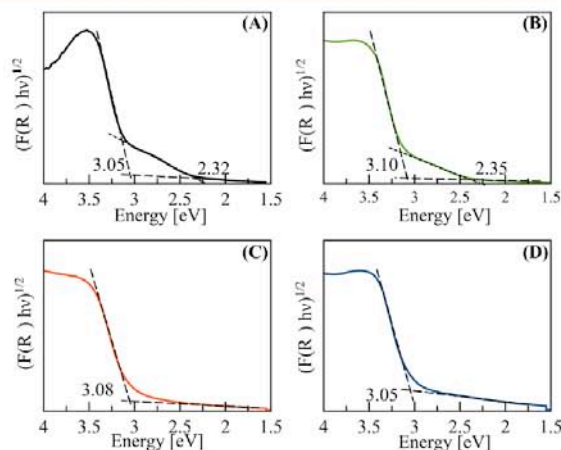
Figure 3. Tauc-plot of DR UV–vis data obtained for (A) T_400, (B) T_500, (C) T_600, and (D) T_800.
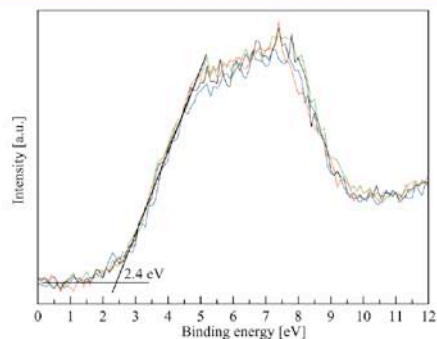
Figure 4. XPS VB spectra of (black) T_400, (green) T_500, (red) T_600, and (blue) T_800.

do not contribute to the visible-light activity of TiO_2 anatase.[27] Nonetheless, the differences in the visible-light activation at certain radiation wavelengths are not only caused by Ti–N, Ti–N–O, or Ti–O–N linkages, but also by oxygen vacancies and Ti^{3+} containing sites in doped titania.[46] Spectroscopic techniques allow us to establish a state in which the nitrogen species are found in the TiO_2 structure. The FTIR spectrum of the as-prepared dried titanium peroxo complex precursor (Figure 5) shows the presence of O–O bonds vibration at 889 cm⁻¹, adsorbed and chemically bonded water manifesting itself by the bands at 3380 and 1630 cm⁻¹, but most importantly the presence of absorption at 1431 cm⁻¹ and several bands between 2800 and 3200 cm⁻¹ are assigned to the N–H vibrations and

101
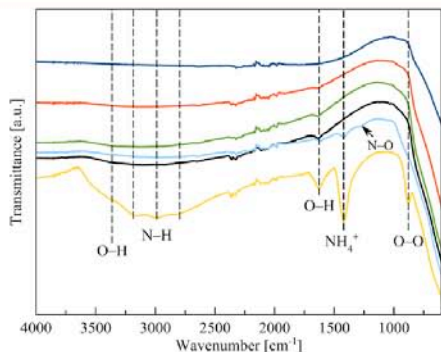
Figure 5. FTIR spectra of the titania samples (yellow) titanium peroxo complex precursor, (light blue) titanium peroxo complex precursor treated at 250 °C, (black) T_400, (green) T_500, (red) T_600, and (dark blue) T_800.

Figure 6. XPS spectra of Ti $2p_{3/2}$ region of (A) T_400, (B) T_500, (C) T_600, and (D) T_800.

attributed to the NH_4^+ of the dried ammonium peroxotitanate complex or adsorbed ammonium cation. The same observations were also made by Etacheri et al. studying FTIR data of the precursor.[12] Thermal treatment of the precursor in air at 250 °C for 2 h resulted in complete elimination of peroxo groups and significant reduction of quantity of bonded NH_4^+; instead, another absorption band at 1286 cm^{-1} appears (Figure 5). Hadjiivanov et al. pointed out that the band found at the same position is attributed to the N−O vibration of various TiO_2−NO_2 surface complexes.[47] Thus, we suppose that the ammonium cations of the precursor react with the oxygen of TiO_2 lattice forming N−O species, which are incorporated into the titania structure upon crystallization. The FTIR spectra registered for the samples calcined at higher temperatures do not show any valuable features due to low concentration of dopants residing in the titanium dioxide.

The presence of the nitrogen species in the TiO_2 was also probed by XPS; however, nitrogen was only detected in T_400, while the concentration of it in T_500 was below the detection limit (see Figure S1). Even more valuable than elemental analysis is the information about state of the atomic components of these samples obtained from XPS data. The signal coming from Ti $2p_{3/2}$ contains two major contributions, Ti-1 located at 458.9 eV and Ti-2 having a maximum at 460.2 eV, both of which have reasonable half width half-maximum (HWHM) values of about 0.8−0.9 eV for the N-doped (Figure 6A,B) as well as for the N-free samples (Figure 6C,D). The Ti-1 peak is undoubtedly attributed to the octahedrally coordinated titanium of the TiO_2 crystalline network, while the second contribution might be assigned to the bulk and surface TiO_x species with a distinct coordination number or chemical bonding. Indeed, many studies on titania-containing mixed oxide systems assign the peak shift of Ti $2p_{3/2}$ to higher energies to the changes of Ti coordination from octahedral to tetrahedral.[48−50] The Ti-1/Ti-2 peak ratio reveals a higher content of the Ti-species having a different coordination in the N-doped TiO_2 samples, namely, T_400 and T_500 compared to those of the nitrogen-free ones (Table 2). Thus, the incorporation of nitrogen in titania affects the titanium coordination, leading to some distorted TiO_x units. Further heat treatment leads to a predominant contribution of Ti signal of the crystalline TiO_2 anatase, thus indicating the reduced
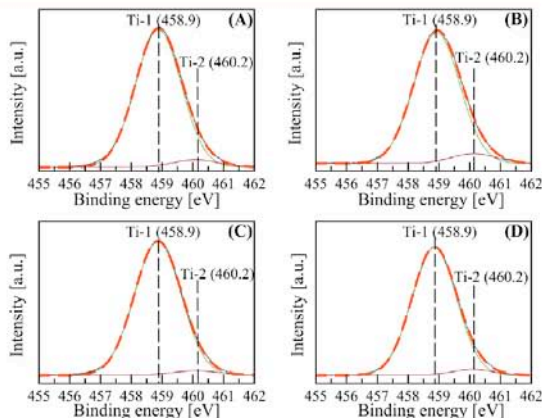
amount of the defect-sites containing Ti-species with Ti coordination number below 6 (Figure 6C,D and Table 2).

Quantitative analysis of the chemical composition of the prepared materials by XPS revealed that the oxygen content increases as treatment temperature increases (Table 2). This is most likely an indication of atmospheric O_2 capture by TiO_2. O 1s XPS spectrum of TiO_2 usually contains two major contributions corresponding to lattice oxygen and adsorbed hydroxyl groups. However, in the present case the deconvolution of O 1s band into two components (not shown) yields large HWHM values for the peaks. That is why the spectra have been fitted to three contributions centered at 530.2 (O-1), 531.8 eV (O-2), and 533.0 eV (O-3). The dominant peak at 530.2 eV (O-1) is assigned to the oxygen atoms of the TiO_2 crystalline network, the second one at 531.8 eV (O-2) corresponds to the oxygen of surface hydroxyl groups, and the third one at 533.0 eV (O-3) might be attributed to the contributions from adsorbed H_2O and chemisorbed oxygen species including those taking the form of peroxo groups.[51−53] The most heavily N-doped T_400 sample shows the highest ratio of O-1 to the sum of O-2 and O-3, indicating that oxygen in this material is mostly a part of the crystalline anatase TiO_2 (Figure 7A, Table 2). When the thermally driven elimination of the nitrogen species starts at a higher temperature, we observe a drastic change in O-2 and O-3 contributions to the O 1s spectrum of T_500 sample (Figure 7B). It is worth mentioning that among all the samples the highest relative content of disordered Ti-species and the lowest O-1 to O-2 and O-3 ratio are observed for T_500. This can be explained by the elimination of a large quantity of the N-dopants, which results in the creation of bulk defect-sites. However, the replacement of the N-containing surface sites with the surface oxygens promotes higher titania hydroxylation. It is a common notion that titanium dioxide loses its surface hydroxyl groups and adsorbed H_2O when thermally treated, which would lead to a predominance of O-1 component.[54] Here, on the contrary, we see that the area of O-2 barely decreases for samples T_600 and T_800 (Figure 7D) in respect to that of the nitrogen-doped TiO2 (Table 2), which means that some oxygen-containing species other than surface hydroxyls are formed in the TiO2 after the N-dopants are removed at higher calcination temperatures. Furthermore, the O-3 peak area even experiences

Table 2. XPS Elemental Composition (atom %) and Deconvolution Data

	Ti $2p_{3/2}$			O 1s				
sample	Ti-1, HWHM	Ti-2, HWHM	Ti-1/Ti-2 ratio	O-1, HWHM	O-2, HWHM	O-3, HWHM	O-1/O-2/O-3 ratio	O/Ti ratio
T_400	0.87	0.86	19	0.93	0.78	0.84	1/0.12/0.05	2.42
T_500	0.88	0.84	14	0.94	0.78	1.09	1/0.19/0.10	2.57
T_600	0.89	0.88	30	0.98	0.77	0.95	1/0.08/0.10	2.75
T_800	0.85	0.76	25	0.94	0.73	0.97	1/0.11/0.12	2.80
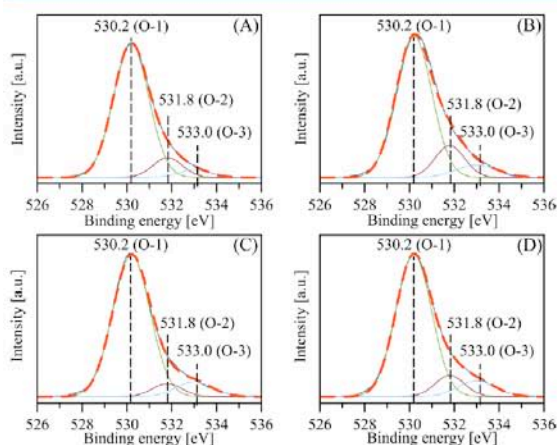
Figure 7. XPS spectra of O 1s region of (A) T_400, (B) T_500, (C) T_600, and (D) T_800.

Figure 8. Extended region fitting using ARTEMIS in R-space for (black) T_400, (green) T_500, (red) T_600, and (blue) T_800 samples.

an increase, which suggests that chemisorbed oxygen[51] or peroxo groups[52,53] compensates for the loss of absorbed H_2O.

XAS, contrary to surface sensitive XPS, allows us to obtain information on the oxidation state and the local order of Ti atoms from the bulk of TiO_2 materials, thus revealing the distortions caused by the incorporation of dopants or formation of other types of defects. If the defect-inducing species are present in the titanium dioxide at very low concentration levels and hence have only a minor effect on the long-range order of the TiO_2, then many laboratory-scale instruments are unable to characterize the Ti local arrangement in-depth.

It may occur that N-doping provokes a partial reduction of Ti^{4+} to Ti^{3+} through the formation of O-vacancies and the charge-compensation effect. The XANES spectra of four samples show the same shape and the energy edge as the TiO_2 (Ti^{4+}) anatase reference (Figure S2), thus indicating the absence of significant quantities of the reduced species, which is in accordance with the previously discussed XPS data.

EXAFS data analysis was carried out in order to determine the position of the dopants in the titania samples using an approach similar to that reported by Sahoo et al.[32] Crystallographic data for TiO_2 anatase reference phase was used to construct the model for fitting the spectra. Two coordination shells around central Ti atom were fitted in the range from 1.4 to 3.5 Å and in the k-range of the Fourier transform from 2.6 to 11.8 Å^{-1}. Three main single scattering paths were used: Ti−O_{ax}, Ti−O_{eq}, and Ti−Ti. In addition, several double scattering paths ($R_{eff} < 3.5$ Å) were taken into account, using a combination of parameters from single scattering path in order to avoid exceeding of the limit of number of free variables determined by Nyquist theorem.

One can clearly observe the differences on the spectra of the N−TiO_2 after treatment at high temperatures (Figure 8). It is
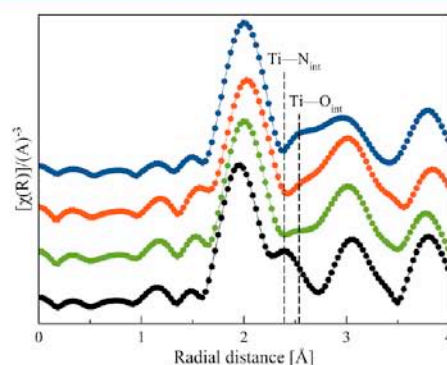
of special importance that the shoulder present on the spectrum of T_400 is gradually replaced by another maximum manifesting itself on the spectra of T_600 and T_800 samples (Figure 8). Although the shoulder seen for T_400 is not the signal directly coming from the N atoms, we attribute it to the redistribution of defects and displacement of the oxygens neighboring to the central Ti atom probably caused by the incorporation of nitrogen-dopants. Thus, the Ti−nitrogen interstitials (Ti−N_{int}) and Ti−oxygen interstitials (Ti−O_{int}) paths were included in the fit aiming to assess the influence of the dopants on the local order in the titania material. For the sake of comparison, the commercial TiO_2 anatase powder of 99% purity was measured and fitted in order to calculate S_0^2 and ΔE_0 values to be further used in the fitting model. Figure 9 displays the quality of the EXAFS spectra fitting. It is clear that a good fit is obtained for the first two coordination shells of Ti.

The highest concentration of nitrogen provokes the reduction of the coordination number Ti−O in the first coordination shell in respect to the commercial TiO_2 anatase, which is the consequence of the N-species incorporation both by axial and equatorial positions (Table 3). The N-doping in the case of T_400 barely affects the Ti−O bond distance, resulting in it being almost the same as that in the reference material, where (Ti−O)$_{eq}$ and (Ti−O)$_{ax}$ distances are 1.94 and 1.98 Å, equal to those calculated by Ceotto et al. for the pristine titania.[31] The doping certainly influences the TiO_2 microstructure by causing the formation of oxygen vacancies in the first coordination shell and creation of doping sites at a larger distance from the central atom (Figure S3A, Table 3). The fitting of the Ti−N_{int} path to the model shows that the distance between the central atom and the N-species is about 2.4 Å, which is in agreement with the axially positioned Ti−N_{int} distance calculated by Ceotto et al. using the DFT method.[31] The coordination number of Ti−N_{int} is calculated to be nearly 1, which sums with oxygens bonded to the titanium atom
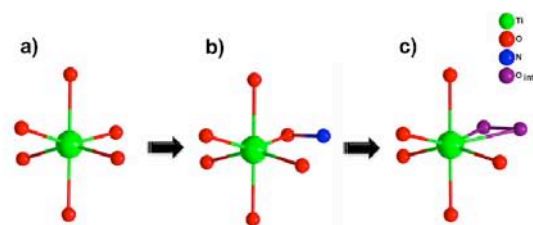
103
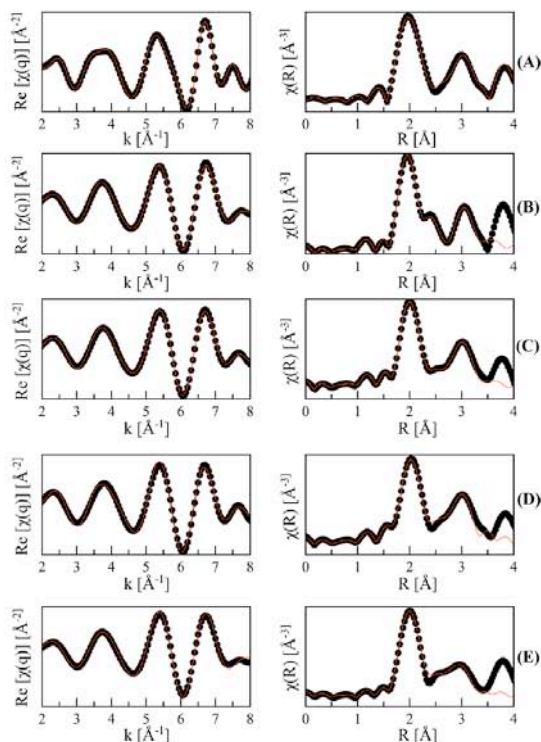
Figure 9. Fitted magnitude of the k^2-weighted Ti K-edge EXAFS spectra (left) and the corresponding EXAFS Fourier transform (right) for (A) commercial TiO_2 anatase, (B) T_400, (C) T_500, (D) T_600, and (E) T_800 samples.

Table 3. Results of EXAFS Data Fitting[a]

sample	path	coordination number	R (Å)	σ^2 (Å^2)
T_400	Ti–O equatorial	3.46(2)	1.935(2)	0.0003(1)
	Ti–O axial	1.58(2)	1.977(2)	0.0003(1)
	Ti–N _interstitial	0.99(6)	2.436(4)	0.0004(1)
	Ti–Ti	3.62(2)	3.033(1)	0.002(1)
T_500	Ti–O equatorial	3.21(2)	1.959(2)	0.0003(1)
	Ti–O axial	1.65(2)	1.975(3)	0.0003(1)
	Ti–N _interstitial	0.45(6)	2.352(2)	0.0001(1)
	Ti–O _interstitial	0.51(7)	2.581(4)	0.002(1)
	Ti–Ti	4.26(2)	3.035(1)	0.002(1)
T_600	Ti–O equatorial	3.36(2)	1.968(2)	0.0003(1)
	Ti–O axial	1.89(4)	1.976(2)	0.0003(1)
	Ti–O _interstitial	1.05(8)	2.620(7)	0.010(2)
	Ti–Ti	4.03(3)	3.039(3)	0.001(1)
T_800	Ti–O equatorial	3.61(1)	1.961(2)	0.0002(1)
	Ti–O axial	2.25(2)	1.973(2)	0.0002(1)
	Ti–O _interstitial	1.28(9)	2.537(5)	0.010(1)
	Ti–Ti	4.41(2)	3.026(2)	0.004(1)
anatase (Aldrich)	Ti–O equatorial	4.00	1.939(2)	0.0001(1)
	Ti–O axial	2.00	1.976(3)	0.0001(1)
	Ti–Ti	4.00	3.042(2)	0.0006(1)

[a] R, bond distance; σ, XAFS Debye–Waller factor.

giving the Ti coordination number of 6, thus satisfying its octahedral arrangement (Table 3). However, given the low concentrations of nitrogen found in the studied material, one must not think that this path included in the fit demonstrates the existence of titanium nitride bonds; neither does this imply that every sixth O atom in the vicinity of the Ti is replaced by one N. As nitrogen and oxygen atoms are indistinguishable by the applied analytical technique due to their very similar electron density, it is rather an indication of the presence of NO_x species at a certain distance from Ti in the TiO_2 network. Moreover, according to the XPS study, nitrogen is present in the material in the oxidized form (Figure S1), so it is most likely that the doping of the TiO_2 occurs by the incorporation of the N-interstitials forming in this way Ti–O–N bonds (Figure 10A,B). The increase of the calcination temperature under air atmosphere causes the part of nitrogen to be eliminated from the titania (Table 1, Figure 2). The N-dopants are evolved in the form of NO; thus, leaving the vacancies in the TiO_2 network and provoking a charge imbalance, which is in accordance with the XPS study demonstrating the largest quantity of the disordered TiO_x sites in T_500 among the all samples (Figure 6B, Table 2). According to the mechanism of oxygen interstitials formation in titanium dioxide doped with Nb ions proposed in ref 22, the net-charge imbalance forces atmospheric oxygen to be adsorbed on the titania surface and then slowly to diffuse to the vacant sites, as TiO_6 polyhedral units recover their charge neutrality. For T_500, we can clearly

Figure 10. Schematic representation of the N- and O-interstitial formation in the TiO_2 structure.

see a new contribution at a distance of 2.6 Å, which we attribute to the interstitial oxygen species (Table 3). Also, the equatorial Ti–O bonds influenced by the incorporation of O as the distance is significantly increased (Figure S3B, Table 3). All nitrogen dopants are removed by the thermal treatment at 600 °C and totally replaced by oxygen interstitials (Figures 8 and 10C). The distance of Ti–O$_{int}$ in this sample is maintained as almost the same as that in T_500, while the Ti–O equatorial bond length reaches its highest value (Figure S3B, Table 3). This observation is in accordance with the earlier described elongation of the crystallographic c-parameter and the expansion of the titania anatase unit cell (Table 1), as well as with the computation data presented by Lo Presti et al.,[55] where interstitial N-dopants had the similar effect on the TiO_2 crystal structure. It is important to mention that at this point the sum of Ti–O$_{eq}$, Ti–O$_{ax}$, and Ti–O$_{int}$ coordination numbers gives a value superior that of the reference anatase TiO_2 (Table

3). It is known that titanium atom acquires a coordination number of 7 in peroxo complexes,[56] and the formation of O_2^{2-} (peroxo), O_2^- (superoxo), and bridging dimer $(O_2)_o$ species in oxygen-rich titania (Figure 10C) was also proposed in ref 22. In accordance with this, our XPS study discussed above shows the contribution at 533 eV on the 1s O spectra, also suggesting the presence of some chemisorbed oxygen species or peroxo groups (Table 2). Peroxo groups coordinated to titanium are able to absorb visible-light, which is most likely a cause of a slight BG shrinkage observed for the oxygen-rich titania samples in respect to the pristine TiO_2 anatase (Table 1). The further increase of the calcination temperature almost completes the process of occupation of defect sites produced by the N-species elimination, as the coordination number of Ti to the neighboring oxygens is back to 6 in T_800 (Figure S3A, Table 3). The $Ti-O_{eq}$ bond length decreases compared to that of T_600 sample, indicating that the O_2 adsorption process is probably completed and that the internal rearrangement inside the TiO_2 cell is taking place. In our previous work[26] we found out that the calcination of this material at temperatures superior 800 °C causes it to partially transform to rutile phase, so this study is limited to the 400−800 °C range to avoid the application of another crystallographic phase being included in the model, making it less precise.

3.2. Photocatalytic Properties of N-Doped and Oxygen-Rich Titania. 3.2.1. Photocatalytic Degradation of p-Cresol.
All the studied materials are active in the UV−vis-assisted decomposition of p-cresol. The N-doped samples T_400 and T_500 show intermediate activity, totally degrading the pollutant after 240 and 210 min of the reaction, respectively (Figure 11A). Thermal treatment of TiO_2 at 600 °C results in
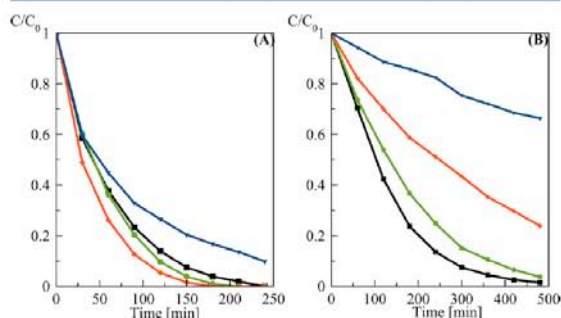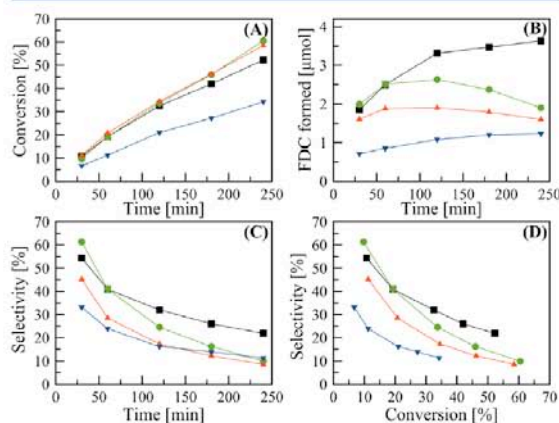

Figure 11. Photocatalytic degradation of p-cresol in the presence of (black) T_400, (green) T_500, (red) T_600, and (blue) T_800 samples under (A) UV−vis and (B) $NaNO_2$-filtered (>400 nm) irradiation.

complete elimination of the N-dopants producing the most active photocatalyst (Figure 11A). Up to this point, the activity increases despite the reduction of SSA values (Table 1). To explain this slight increase of the reaction rate after the removal of N-dopants, one might look to the PL spectra of the two most representative of the series T_400 and T_600 samples, where it is clearly seen that the recombination rate is reduced for the oxygen-rich TiO_2 sample (Figure S4). Thus, the N-species or the oxygen vacancies in the first coordination shell formed as a result of N incorporation in TiO_2 play role of recombination centers, while O-doping by filling the vacant sites in the Ti environment (Table 3) and by producing O-interstitial does not hinder the charge transfer. Further increase of the

treatment temperature leads to the sintering of the TiO_2[26] and diminishing of SSA value. This results in T_800 demonstrating the worst photocatalytic performance of the present samples (Figure 11A).

By cutting off the UV irradiation, we intended to verify the effect of the N- and O-dopants on the visible-light activation of the titania photocatalysts. T_400, containing the highest concentration of nitrogen species, is the most active under visible light (Figure 11B). The lower nitrogen content of T_500 reduces the utilization of visible-light irradiation; hence, some reduction of the p-cresol photodegradation rate is observed (Figure 11B). Contrary to the UV−vis-assisted photocatalytic study, the removal of the N-species is detrimental for the photocatalytic performance of T_600, as it loses a lot of the visible-light susceptibility (Figure 11B). Not surprisingly, the further enhancement of the calcination temperature reduces the photoactivity even more (Figure 11B). However, even if the N-dopants are completely removed, the TiO_2 samples maintain visible-light-assisted photocatalytic activity indicating on the important role of the oxygen interstitials of oxygen-rich titania in the sensitization of the photocatalyst.

3.2.2. Partial Photooxidation of HMF to FDC.
Almost all of the studied TiO_2 samples demonstrate very similar trends of HMF conversion with the exception of T_800, which is significantly less active due to its low SSA (Figure 12A). As in

Figure 12. Photocatalytic conversion of HMF to FDC in the presence of (black) T_400, (green) T_500, (red) T_600, and (blue) T_800 samples at HMF concentration of 40 mg L^{-1} (0.32 mM).

the case of the p-cresol degradation, the slight increase of the reaction rate is observed for the samples treated at temperatures of 500 and 600 °C compared to that of T_400, which is most likely to be attributed to the decreased recombination rate associated with the nitrogen removal (Figure S4). However, the reaction does not go exactly the same way for the N- and O-doped photocatalysts. The photo-oxidation of HMF in the presence of the N-doped TiO_2 compared to that of the N-free titania samples gives higher quantities of a valuable partial oxidation product FDC (Figure 12B), which might be formed in the result of a hydrogen abstraction from the OH group of HMF by photogenerated holes or $O_2^{\bullet-}$ radicals.[57,58] Although relatively high concentrations of FDC are observed during the photocatalytic runs, we should mention a certain decline of the selectivity values with the reaction time (Figure 12C). From

105

Figure 12D it is clear that the N-doped TiO_2 samples have higher selectivity values than those of the oxygen-rich titania at the same conversion degrees. The descending character of the selectivity curve with time is improved if higher concentrations of the substrate are used. Selectivities to FDC oxidation of about 30–40% are reached when T_400 is used as photocatalyst at HMF concentrations of 1.6 and 3.2 mM (Figure S5).

A partial photocatalytic oxidation of alcohols in general and HMF in particular might be promoted by the reaction with O_2^- radicals generated via oxygen reduction pathway on semiconductor photocatalysts such as g-C_3N_4, which is unable to form $OH^•$ radicals by the direct interaction of positively charged holes with water.[58] Titanium dioxide, however, possesses a VB potential favorable to $OH^•$ formation; hence, only very disordered TiO_2 materials with high contents of amorphous phase are usually applied for partial photooxidation reactions with an intention to suppress $OH^•$ generation.[34,59] High concentration of various surface and bulk defects in poorly crystalline material make it difficult to assess the influence of nitrogen doping on selective photooxidation performance of titanium dioxide, although such attempt was made,[34] which is why it is of special interest to compare crystalline N–TiO_2 and oxygen-rich TiO_2 anatase in this type of reaction. From the presented data, it is clear that N-doping favors partial oxidation of HMF to FDC, while oxygen-rich titania obviously more efficiently performs in photodegradation of the water pollutants. Considering the fact that both types of TiO_2 samples possess nearly the same electronic structure (Figures 3 and 4), which is responsible for the generation of electron–hole pairs, we find the explanation of their very different photocatalytic behavior in the modification of the surface active sites. It was mentioned in section 3.1 that ammonia contained in the precursor material reacts with Ti–O sites forming Ti–O–N linkages, thus leaving the surface poor in hydroxyl groups, which was confirmed by the XPS study (Figure 7A, Table 2). This has a 2-fold effect: It inhibits the generation of $OH^•$ radicals on the titania surface, and it complicates the interaction of the surface sites with the reaction products, thus reducing the decomposition of FDC. As a result, the selectivity values of HMF to FDC conversion obtained for the well-crystalline N–TiO_2 are close to those reported for the poorly crystalline titania and superior than that of the commercial titanium dioxide.[59]

4. CONCLUSIONS

Titanium local structure study has allowed us to reconsider the mechanism of oxygen-rich titania formation from a precursor containing a source of nitrogen. We have demonstrated that at low temperatures of thermal treatment (400–500 °C) nitrogen doping of TiO_2 anatase titania occurs, and the N-species occupy interstitial position in the titanium dioxide anatase crystal structure causing creation of defects (oxygen vacancies) in the titanium first coordination shell. The treatment under air at high temperatures completely removes the N-dopants, thus leaving the Ti coordination unsatisfied and provoking the charge imbalance in the TiO_5 units. It forces the neighboring oxygen atoms to occupy a vacant place, which in turn results in the cascade reaction of adsorption of atmospheric oxygen and its diffusion to the unoccupied sites. The captured oxygen forms interstitial O-species inside the TiO_2 network, expanding the TiO_2 crystal cell. The coordination number of Ti in the oxygen-rich titania exceeds the value of 6, thus implying the formation of O–O peroxo bridges coordinating titanium atoms.

Both types of dopants affect in a similar way the electronic properties of TiO_2, slightly reducing its BG value by shifting the VB to 2.4 eV. Despite the fact that all the samples are active under wavelengths of ≥400 nm, the interband state formed by the N-species incorporation provides better sensitization of photocatalyst than the O-dopants do, thus permitting more efficient visible-light utilization. On the basis of the photocatalytic studies, we have also suggested that N-doping and the oxygen vacancies it produces in the first coordination shell of Ti might be responsible for the reduced photocatalytic reaction rate in the case of p-cresol degradation as well as in HMF photoconversion. In contrast, the presence of the N-species on the titania modifies its surface chemistry, reducing the hydroxylation degree and making it the most probable contributing factor to a higher selectivity of N–TiO_2 in the photooxidation of HMF to FDC by hindering the transfer of the unselective $OH^•$ radicals from the catalyst surface to the substrate and the product molecules. Thus, the presented investigation not only sheds light on the question of formation of oxygen-rich TiO_2 but also demonstrates the importance of a rational design of doped titania materials for the application in different types of photocatalytic reactions.

■ ASSOCIATED CONTENT

ⓢ Supporting Information

The Supporting Information is available free of charge on the ACS Publications website at DOI: 10.1021/acs.jpcc.7b00354.

XPS, XANES, and photoreactivity data (PDF)

■ AUTHOR INFORMATION

Corresponding Author
*E-mail: uo247495@uniovi.es; zapasoul@gmail.com. Tel. +34 684348116.

ORCID
Igor Krivtsov: 0000-0003-4926-2338
Salvador Ordóñez: 0000-0002-6529-7066
Silvia Villar-Rodil: 0000-0002-5832-9971

Notes
The authors declare no competing financial interest.

■ ACKNOWLEDGMENTS

■ REFERENCES

(1) Chen, X.; Mao, S. S. Titanium dioxide nanomaterials: Synthesis, properties, modifications, and applications. *Chem. Rev.* **2007**, *107*, 2891–2959.
(2) Han, F.; Kambala, V. S. R.; Srinivasan, M.; Rajarathnam, D.; Naidu, R. Tailored titanium dioxide photocatalysts for the degradation of organic dyes in wastewater treatment: A review. *Appl. Catal., A* **2009**, *359*, 25–40.
(3) Ma, Y.; Wang, X.; Jia, Y.; Chen, X.; Han, H.; Li, C. Titanium dioxide-based nanomaterials for photocatalytic fuel generations. *Chem. Rev.* **2014**, *114*, 9987–10043.
(4) Gaya, U. I.; Abdullah, A. H. Heterogeneous photocatalytic degradation of organic contaminants over titanium dioxide: A review

of fundamentals, progress and problems. *J. Photochem. Photobiol., C* **2008**, *9*, 1−12.

(5) Pelaez, M.; Nolan, N. T.; Pillai, S. C.; Seery, M. K.; Falaras, P.; Kontos, A. G.; Dunlop, P. S. M.; Hamilton, J. W. J.; Byrne, J. A.; O'Shea, K.; et al. A review on the visible light active titanium dioxide photocatalysts for environmental applications. *Appl. Catal., B* **2012**, *125*, 331−349.

(6) Etacheri, V.; Di Valentin, C.; Schneider, J.; Bahnemann, D.; Pillai, S. C. Visible-light activation of TiO₂ photocatalysts: Advances in theory and experiments. *J. Photochem. Photobiol., C* **2015**, *25*, 1−29.

(7) Wang, Y.; Wang, Q.; Zhan, X.; Wang, F.; Safdar, M.; He, J. Visible light driven type II heterostructures and their enhanced photocatalysis properties: a review. *Nanoscale* **2013**, *5*, 8326−8339.

(8) Rehman, S.; Ullah, R.; Butt, A. M.; Gohar, N. D. Strategies of making TiO₂ and ZnO visible light active. *J. Hazard. Mater.* **2009**, *170*, 560−569.

(9) Asahi, R.; Morikawa, T.; Irie, H.; Ohwaki, T. Nitrogen-doped titanium dioxide as visible-light-sensitive photocatalyst: Designs, developments, and prospects. *Chem. Rev.* **2014**, *114*, 9824−9852.

(10) Nakamura, I.; Negishi, N.; Kutsuna, S.; Ihara, T.; Sugihara, S.; Takeuchi, K. Role of oxygen vacancy in the plasma-treated TiO₂ photocatalyst with visible light activity for NO removal. *J. Mol. Catal. A: Chem.* **2000**, *161*, 205−212.

(11) Kong, X.; Zeng, C.; Wang, X.; Huang, J.; Li, C.; Fei, J.; Li, J.; Feng, Q. Ti-O-O coordination bond caused visible light photocatalytic property of layered titanium oxide. *Sci. Rep.* **2016**, *6*, 29049.

(12) Etacheri, V.; Seery, M. K.; Hinder, S. J.; Pillai, S. C. Oxygen Rich Titania: A dopant free, high temperature stable, and visible-light active anatase photocatalyst. *Adv. Funct. Mater.* **2011**, *21*, 3744−3752.

(13) Mamontov, E.; Egami, T.; Brezny, R.; Koranne, M.; Tyagi, S. Lattice defects and oxygen storage capacity of nanocrystalline ceria and ceria-zirconia. *J. Phys. Chem. B* **2000**, *104*, 11110−11116.

(14) León-Reina, L.; Losilla, E. R.; Martínez-Lara, M.; Bruque, S.; Aranda, M. A. G. Interstitial oxygen conduction in lanthanum oxy-apatite electrolytes. *J. Mater. Chem.* **2004**, *14*, 1142−1149.

(15) León-Reina, L.; Porras-Vazquez, J. M.; Losilla, E. R.; Aranda, M. A. G. Interstitial oxide positions in oxygen-excess oxy-apatites. *Solid State Ionics* **2006**, *177*, 1307−1315.

(16) Nakamura, T.; Ling, Y.; Amezawa, K. The effect of interstitial oxygen formation on the crystal lattice deformation in layered perovskite oxides for electrochemical devices. *J. Mater. Chem. A* **2015**, *3*, 10471−10479.

(17) Kamisaka, H.; Yamashita, K. Theoretical study of the interstitial oxygen atom in anatase and rutile TiO₂: electron trapping and elongation of the r(O_O) bond. *J. Phys. Chem. C* **2011**, *115*, 8265−8273.

(18) Li, Y.-F.; Aschauer, U.; Chen, J.; Selloni, A. Adsorption and reactions of O₂ on anatase TiO₂. *Acc. Chem. Res.* **2014**, *47*, 3361−3368.

(19) Lee, H.-Y.; Robertson, J. Doping and compensation in Nb-doped anatase and rutile TiO₂. *J. Appl. Phys.* **2013**, *113*, 213706.

(20) Close, T.; Tulsyan, G.; Diaz, C. A.; Weinstein, S. J.; Richter, C. Reversible oxygen scavenging at room temperature using electro-chemically reduced titanium oxide nanotubes. *Nat. Nanotechnol.* **2015**, *10*, 418−422.

(21) Hollister, A. G.; Gorai, P.; Seebauer, E. G. Surface-based manipulation of point defects in rutile TiO₂. *Appl. Phys. Lett.* **2013**, *102*, 231601.

(22) Setvín, M.; Aschauer, U.; Scheiber, P.; Li, Y.-F.; Hou, W.; Schmid, M.; Selloni, A.; Diebold, U. Reaction of O₂ with subsurface oxygen vacancies on TiO₂ anatase (101). *Science* **2013**, *341*, 988.

(23) Tan, L.-L.; Ong, W.-J.; Mohamed, A. R. Visible-light-activated oxygen-rich TiO₂ as next generation photocatalyst: Importance of annealing temperature on the photoactivity toward reduction of carbon dioxide. *Chem. Eng. J.* **2016**, *283*, 1254−1263.

(24) Tan, L.-L.; Ong, W.-J.; Chai, S.-P.; Mohamed, A. R. Band gap engineered, oxygen-rich TiO₂ for visible light induced photocatalytic reduction of CO₂. *Chem. Commun.* **2014**, *50*, 6923−6926.

(25) Tan, L.-L.; Ong, W.-J.; Chai, S.-P.; Goh, B. T.; Mohamed, A. R. Visible-light-active oxygen-rich TiO₂ decorated 2D graphene oxide

with enhanced photocatalytic activity toward carbon dioxide reduction. *Appl. Catal., B* **2015**, *179*, 160−170.

(26) Krivtsov, I.; Ilkaeva, M.; Avdin, V.; Amghouz, Z.; Khainakov, S. A.; García, J. R.; Díaz, E.; Ordóñez, S. Exceptional thermal stability of undoped anatase TiO₂ photocatalysts prepared by a solvent-exchange method. *RSC Adv.* **2015**, *5*, 36634−36641.

(27) Di Valentin, C.; Finazzi, E.; Pacchioni, G.; Selloni, A.; Livraghi, S.; Paganini, M. C.; Giamello, E. N-doped TiO₂: Theory and experiment. *Chem. Phys.* **2007**, *339*, 44−56.

(28) Chen, H.; Nambu, A.; Wen, W.; Graciani, J.; Zhong, Z.; Hanson, J. C.; Fujita, E.; Rodriguez, J. A. Reaction of NH₃ with titania: N-doping of the oxide and TiN formation. *J. Phys. Chem. C* **2007**, *111*, 1366−1372.

(29) Belver, C.; Bellod, R.; Stewart, S. J.; Requejo, F. G.; Fernández-García, M. Nitrogen-containing TiO₂ photocatalysts. Part 2. Photo-catalytic behaviour under sunlight excitation. *Appl. Catal., B* **2006**, *65*, 309−314.

(30) Belver, C.; Bellod, R.; Fuerte, A.; Fernández-García, M. Nitrogen-containing TiO₂ photocatalysts. Part 1. Synthesis and solid characterization. *Appl. Catal., B* **2006**, *65*, 301−308.

(31) Ceotto, M.; Lo Presti, L.; Cappelletti, G.; Meroni, D.; Spadavecchia, F.; Zecca, R.; Leoni, M.; Scardi, P.; Bianchi, C. L.; Ardizzone, S. About the nitrogen location in nanocrystalline N-doped TiO₂: Combined DFT and EXAFS approach. *J. Phys. Chem. C* **2012**, *116*, 1764−1771.

(32) Sahoo, M.; Yadav, A. K.; Jha, S. N.; Bhattacharyya, D.; Mathews, T.; Sahoo, N. K.; Dash, S.; Tyagi, A. K. Nitrogen location and Ti-O bond distances in pristine and N-doped TiO₂ anatase thin films by X-ray absorption studies. *J. Phys. Chem. C* **2015**, *119*, 17640−17647.

(33) Ahmed, S.; Rasul, M. G.; Martens, N. W.; Brown, R.; Hashib, M. A. Heterogeneous photocatalytic degradation of phenols in waste-water: A review on current status and developments. *Desalination* **2010**, *261*, 3−18.

(34) Yurdakal, S.; Augugliaro, V.; Loddo, V.; Palmisano, G.; Palmisano, L. Enhancing selectivity in photocatalytic formation of *p*-anisaldehyde in aqueous suspension under solar light irradiation via TiO₂ N-doping. *New J. Chem.* **2012**, *36*, 1762−1768.

(35) Amarasekara, A. S.; Green, D.; Williams, L. D. Renewable resources based polymers: Synthesis and characterization of 2,5-diformylfuran-urea resin. *Eur. Polym. J.* **2009**, *45*, 595−598.

(36) Hui, Z.; Gandini, A. Polymeric schiff bases bearing furan moieties. *Eur. Polym. J.* **1992**, *28*, 1461−1469.

(37) Kanetaka, Y.; Yamazaki, S.; Kimura, K. Preparation of Poly(ether ketone)s derived from 2,5-furandicarboxylic acid by polymerization in ionic liquid. *Macromolecules* **2016**, *49*, 1252−1258.

(38) Castro, G. R. Optical design of the general-purpose Spanish X-ray beamline for absorption and diffraction. *J. Synchrotron Radiat.* **1998**, *5*, 657−660.

(39) Ravel, B.; Newville, M. Athena, Artemis, Hephaestus: data analysis for X-ray absorption spectroscopy using IFEFFIT. *J. Synchrotron Radiat.* **2005**, *12*, 537−541.

(40) Tröger, L.; Arvanitis, D.; Baberschke, K.; Michaelis, H.; Grimm, U.; Zschech, E. Full correction of the self-absorption in soft-fluorescence extended x-ray-absorption fine structure. *Phys. Rev. B: Condens. Matter Mater. Phys.* **1992**, *46*, 3283−3289.

(41) Ilkaeva, M.; Krivtsov, I.; Avdin, V.; Khainakov, S. A.; García, J. R. Comparative study of structural features and thermal behaviour of mixed silica-titania xerogels prepared via the peroxo method and the conventional co-precipitation technique. *Colloids Surf., A* **2014**, *456*, 120−128.

(42) Ichinose, H.; Terasaki, M.; Katsuki, H. Synthesis of peroxo-modified anatase sol from peroxo titanic acid solution. *Nippon Seramikkusu Kyokai Gakujutsu Ronbunshi* **1996**, *104*, 715−718.

(43) Liu, Y.-J.; Aizawa, M.; Wang, Z.-M.; Hatori, H.; Uekawa, N.; Kanoh, H. Comparative examination of titania nanocrystals synthe-sized by peroxo titanic acid approach from different precursors. *J. Colloid Interface Sci.* **2008**, *322*, 497−504.

107

The Journal of Physical Chemistry C

(44) Gao, Y.; Masuda, Y.; Peng, Z.; Yonezawa, T.; Koumoto, K. Room temperature deposition of a TiO2 thin film from aqueous peroxotitanate solution. *J. Mater. Chem.* **2003**, *13*, 608−613.

(45) Bellardita, M.; Addamo, M.; Di Paola, A.; Palmisano, L.; Venezia, A. M. Preparation of N-doped TiO$_2$: characterization and photocatalytic performance under UV and visible light. *Phys. Chem. Chem. Phys.* **2009**, *11*, 4084−4093.

(46) Chen, Y.; Cao, X.; Lin, B.; Gao, B. Origin of the visible-light photoactivity of NH$_3$-treated TiO$_2$: Effect of nitrogen doping and oxygen vacancies. *Appl. Surf. Sci.* **2013**, *264*, 845−852.

(47) Hadjiivanov, K.; Bushev, V.; Kantcheva, V.; Klissurski, D. Infrared spectroscopy study of the species arising during NO$_2$ adsorption on TiO$_2$ (Anatase). *Langmuir* **1994**, *10*, 464−471.

(48) Stakheev, A. Yu.; Shpiro, E. S.; Apijok, J. XPS and XAES study of TiO$_2$-SiO$_2$ system. *J. Phys. Chem.* **1993**, *97*, 5668−5672.

(49) Luan, Z.; Maes, E. M.; van der Heide, P. A. W.; Zhao, D.; Czernuszewicz, R. S.; Kevan, L. Incorporation of titanium into mesoporous silica molecular sieve SBA-15. *Chem. Mater.* **1999**, *11*, 3680−3686.

(50) Blasco, T.; Camblor, T. A.; Corma, A.; Perez-Pariente, J. The state of Ti in titanoaluminosilicates isomorphous with zeolite.beta. *J. Am. Chem. Soc.* **1993**, *115*, 11806−11813.

(51) Han, X.-G.; He, H.-Z.; Kuang, Q.; Zhou, X.; Zhang, X.-H.; Xu, T.; Xie, Z.-X.; Zheng, L.-S. Controlling morphologies and tuning the related properties of nano/microstructured ZnO Crystallites. *J. Phys. Chem. C* **2009**, *113*, 584−589.

(52) Kong, L.; Wang, C.; Zheng, H.; Zhang, X.; Liu, Y. Defect-induced yellow color in Nb-Doped TiO2 and its impact on visible-light photocatalysis. *J. Phys. Chem. C* **2015**, *119*, 16623−16632.

(53) Kong, X.; Zeng, C.; Wang, X.; Huang, J.; Li, C.; Fei, J.; Li, J.; Feng, Q. Ti-O-O coordination bond caused visible light photocatalytic property of layered titanium oxide. *Sci. Rep.* **2016**, *6*, 29049.

(54) Zhu, J.; Yang, J.; Bian, Z.-F.; Ren, J.; Liu, Y.-M.; Cao, Y.; Li, H.-X.; He, H.-Y.; Fan, K.-N. Nanocrystalline anatase TiO$_2$ photocatalysts prepared via a facile low temperature nonhydrolytic sol−gel reaction of TiCl$_4$ and benzyl alcohol. *Appl. Catal., B* **2007**, *76*, 82−91.

(55) Lo Presti, L.; Ceotto, M.; Spadavecchia, F.; Cappelletti, G.; Meroni, D.; Acres, R. G.; Ardizzone, S. Role of the nitrogen source in determining structure and morphology of N-Doped nanocrystalline TiO$_2$. *J. Phys. Chem. C* **2014**, *118*, 4797−4807.

(56) Tomita, K.; Petrykin, V.; Kobayashi, M.; Shiro, M.; Yoshimura, M.; Kakihana, M. A water-soluble titanium complex for the selective synthesis of nanocrystalline brookite, rutile, and anatase by a hydrothermal method. *Angew. Chem., Int. Ed.* **2006**, *45*, 2378−2381.

(57) Spasiano, D.; del Pilar Prieto Rodriguez, L.; Olleros, J. C.; Malato, S.; Marotta, R.; Andreozzi, R. TiO$_2$/Cu(II) photocatalytic production of benzaldehyde from benzyl alcohol in solar pilot plant reactor. *Appl. Catal., B* **2013**, *136−137*, 56−63.

(58) Krivtsov, I.; García-López, E. I.; Marcì, G.; Palmisano, L.; Amghouz, Z.; García, J. R.; Ordoñez, S.; Díaz, E. Selective photocatalytic oxidation of 5-hydroxymethyl-2-furfural to 2,5-furandicarboxyaldehyde in aqueous suspension of g-C$_3$N$_4$. *Appl. Catal., B* **2017**, *204*, 430−439.

(59) Yurdakal, S.; Tek, B. S.; Alagoz, O.; Augugliaro, V.; Loddo, V.; Palmisano, G.; Palmisano, L. Photocatalytic selective oxidation of 5-(hydroxymethyl)-2-furaldehyde to 2,5-furandicarbaldehyde in water by using anatase, rutile, and brookite TiO$_2$ nanoparticles. *ACS Sustainable Chem. Eng.* **2013**, *1*, 456−461.

108

SUPPLEMENTARY MATERIAL

Consequences of Nitrogen-Doping and Oxygen Enrichment on Titanium Local Order and Photocatalytic Performance of TiO₂ Anatase

Igor Krivtsov[1,2], Marina Ilkaeva[1,2], Eduardo Salas-Colera[3,4], Zakariae Amghouz[5], José R. Garcia[1], Eva Díaz[6], Salvador Ordóñez[6], Silvia Villar-Rodil[7]*

[1] Department of Organic and Inorganic Chemistry, University of Oviedo-CINN, 33006 Oviedo, Spain.

[2] Nanotechnology Education and Research Center, South Ural State University, 454080, Chelyabinsk, Russia.

[3] Instituto de Ciencia de Materiales de Madrid, CSIC, Sor Juana Inés de la Cruz 3, 28049, Cantoblanco Madrid, Spain.

[4] Spanish CRG BM25 SpLine Beamline at the ESRF, 71 Avenue de Martyrs, F-38043 Grenoble, France.

[5] Department of Materials Science and Metallurgical Engineering, University of Oviedo, Campus Universitario, 33203 Gijón, Spain

[6] Department of Chemical and Environmental Engineering, University of Oviedo, 33006 Oviedo, Spain

[7] Instituto Nacional del Carbón, INCAR-CSIC, Apartado 73, 33080, Oviedo, Spain
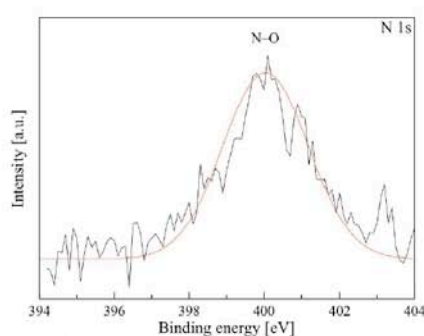
Figure S1. The N 1s region of the T_400 XP spectrum
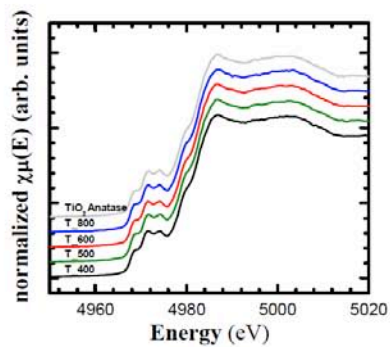
Figure S2. Comparison of XANES spectra of (——) TiO₂ Anatase reference and (——) T_400, (——) T_500, (——) T_600, and (——) T_800 samples.
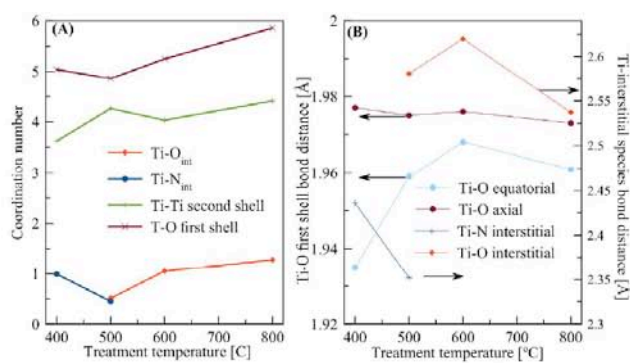
Figure S3. (A) Variations of the coordination number of O and Ti of the first and the second shell, and (B) mean bond distances between Ti atoms lattice oxygen or interstitial N and O in the titania samples calculated from the EXAFS data.
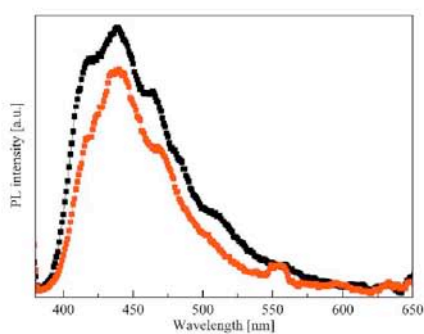
Figure S4. PL spectra of T_400 (-•-) and T_600 (-•-) samples after excitation at 365 nm.
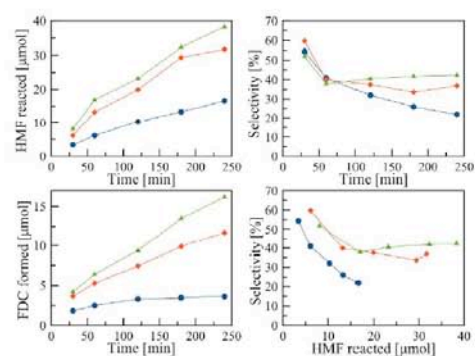
Figure S5. Effect of HMF initial concentration (•) 0.32 mM, (♦) 1.6 mM, and (Δ) 3.2 mM on the photocatalytic conversion of HMF to FDC in the presence of T_400 photocatalyst.

4.2.2   Thermally exfoliated g-C$_3$N$_4$ for selective photocatalytic oxidation of HMF in aqueous phase

As it is discussed previously in Introduction Section, the major reason behind the successful application of carbon nitride for the oxidative conversion of organic compounds aiming to produce valuable products is the inability of g-C$_3$N$_4$ to directly oxidise H$_2$O by photogenerated hole and form unselective powerful oxidants ˙OH radicals. The photocatalytic reaction promoted by this catalyst usually involves superoxide radicals, which are mild oxidative species efficiently converting alcohols and producing the corresponding aldehydes.

The most accessible way to prepare g-C$_3$N$_4$ at reasonable quantities is by direct condensation of N-containing organic precursors such as melamine, urea or thiourea (Chapter 1.3). The condensation of urea gives the most active photocatalyst, which is due to its lower VB position and higher SSA compared to the g-C$_3$N$_4$ synthesized from melamine and thiourea sources. However, it also shows the worst selectivity toward FDC formation from HMF reaching only 22%, while other precursors thiourea and melamine resulted in the formation of more efficient photocatalysts for which the same parameters are 27% and 28%, respectively. On the basis of this preliminary experiment it has been decided to continue the reaction studies using g-C$_3$N$_4$ derived from the most accessible precursor melamine, which also gives the highest yields. Unfortunately, the as-prepared carbon nitride possesses a negligible SSA of only 7 m^{2}g^{-1} complicating its efficient application in photocatalytic processes. Despite a numerous nanocasting methods were elaborated to overcome this drawback, the complications and elevated costs accompanying them have forced us to opt for a simple thermal exfoliation technique [229]. Thermal treatment applied in order to exfoliate the bulk g-C$_3$N$_4$ has found to be favourable not only for improving the reaction rate, but also it has positively affected the selectivity of HMF to FDC conversion. Even when the bulk g-C$_3$N$_4$ is treated at low temperature at 450 ºC, which does not increase the material's SSA and consequently does

not noticeably affect the reaction rate, it demonstrates much higher selectivity of HMF to FDC oxidation reaching 37%. Following increase of thermal exfoliation temperature gradually enhances the SSA and the HMF conversion rate and eventually approaching the selectivity value of 44%. The XPS study evidences the elimination of low-condensed species from g-C_3N_4 and partial removal of the surface amino-groups. One might conclude that the presence of basic functionalities on the photocatalyst surface is deteriorating for the selectivity of HMF to FDC photo-oxidation. Another outstanding carbon nitride property is its BG, which permits utilization of visible-light for photocatalyst activation. The photocatalytic oxidation of HMF carried out under natural light illumination has demonstrated a remarkable performance superior by the measures of reaction rate and selectivity than that observed for the laboratory reactor equipped with UV-lamps. The findings presented in the following research work make a step further for the application of photocatalysis for selective photo-conversion under natural solar light irradiation using water as a green solvent and oxygen as the environmentally-friendly oxidiser.

Article IV

"Selective Photocatalytic Oxidation of 5-Hydroxymethyl-2-Furfural to 2,5-

Furandicarboxyaldehyde in Aqueous Suspension of g-C$_3$N$_4$"

Selective photocatalytic oxidation of 5-hydroxymethyl-2-furfural to 2,5-furandicarboxyaldehyde in aqueous suspension of g-C$_3$N$_4$

Igor Krivtsov [a,b], Elisa I. García-López [c,*], Giuseppe Marcì [c], Leonardo Palmisano [c], Zakariae Amghouz [d], José R. García [a], Salvador Ordóñez [e], Eva Díaz [e]

[a] Department of Organic and Inorganic Chemistry, University of Oviedo-CINN, 33006 Oviedo, Spain
[b] Nanotechnology Education and Research Center, South Ural State University, 454080, Chelyabinsk, Russia
[c] "Schiavello-Grillone" Photocatalysis Group. Dipartimento di Energia, Ingegneria dell'informazione e modelli Matematici (DEIM), Università di Palermo, Viale delle Scienze, 90128 Palermo, Italy
[d] Servicios Científico Técnicos, Universidad de Oviedo, 33006 Oviedo, Spain
[e] Department of Chemical and Environmental Engineering, University of Oviedo, 33006 Oviedo, Spain

ARTICLE INFO

ABSTRACT

Graphitic carbon nitride assisted partial photocatalytic oxidation of 5-hydroxymethyl-2-furfural (HMF) in aqueous medium was investigated. Different carbon nitride precursors were considered, being melamine the one yielding the most efficient photocatalyst. The obtained 30% selectivity of HMF oxidation to 2,5-furandicarboxaldehyde (FDC) is higher than those reported up to now. A further thermal exfoliation of the g-C$_3$N$_4$ samples showed under artificial light irradiation both an enhanced photocatalytic activity in conversion of HMF, and selectivity (ca. 42–45%) to FDC. The performance of the catalysts increased when the experiments were carried out under real outdoor illumination, reaching 50% of selectivity versus FDC formation at 40% of HMF conversion. The utilization of radical scavengers revealed that O$_2$$^{\bullet-}$ was the main reactive species responsible for HMF oxidation to FDC. The photocatalytic test carried out under natural solar irradiation resulted in higher yields of FDC compared to that observed in the laboratory UV irradiated set-up, thus demonstrating the applicability of the exfoliated carbon nitride material in real-life conditions.

1. Introduction

The use of renewable feedstock for producing valuable chemicals and materials is a key point of the modern sustainable industry. Saccharides deriving from lignocellulose hydrolysis are one of the most abundant biomass-derived platform molecules [1]. The oxidation of six-carbons sugars yields 5-hydroxymethyl-2-furfural (HMF), which can be furtherly converted to 2,5-furandicarboxaldehyde (FDC) and 2,5-furandicarboxylic acid (FDCA), the precursors for biopolymers fabrication [2–4]. Several approaches for HMF oxidation, utilizing noble metals [5–7] or transition metal phosphates [8,9] as catalysts, have been explored. However, the application of high temperatures, as well as expensive noble metals [5] makes this process energy-consuming and environmentally unfriendly. Heterogeneous photocatalysis provides a greener alternative to many widely applied catalytic oxidation reactions because toxic by-products are not formed and in principle solar radiation could be used. Highly selective oxidation of aromatic alcohols to aldehydes over TiO$_2$-based photocatalysts has been extensively explored [10–12], although in most cases the reactions have been carried out in organic media [13–15]. Titanium dioxide under UV irradiation readily forms hydroxyl radicals, which can unselectively attack organic species until their mineralization to CO$_2$ and H$_2$O occurs. The oxidant properties of TiO$_2$ are exalted by the relatively lower stability of the pentatomic furanic ring compared to the hexatomic aromatic structures, and consequently it is not surprising that the highest selectivity of HMF photooxidation to FDC achieved so far is only 22% [16]. A photocatalytic material with appropriate thermodynamic requirements, which has recently attracted attention to perform selective oxidations, is graphitic carbon nitride (g-C$_3$N$_4$). It is normally prepared by thermal condensation of dicyandiamide, melamine, urea or thiourea [17]. Relatively low specific surface areas (SSA), in the range 4–7 m^2 g^{-1}, are obtained if thiourea or melamine are used as the precursors, although values close to 70 m^2 g^{-1} (but with very low yields) have been reported for samples prepared at high condensa-

tion temperatures [18–20]. There are two general ways to increase the SSA of g-C$_3$N$_4$: hard or soft templating during the synthesis [21] and post-synthetic exfoliation [22]. Hard templating demands the elimination of the structure-directing material, usually a mesoporous silica, by its dissolution in hazardous hydrofluoric acid, while the presence of soft templates during the preparation might result in the formation of undesired carbonaceous residue [21]. Liquid exfoliation successfully enhances the specific surface area of carbon nitride; however, it usually implies the application of toxic oxidative agents or aggressive media [23]. Recently, Niu et al. [24] have reported an easy thermal exfoliation method allowing to reach values of specific surface area up to ca. 300 m^2 g^{-1}.

The unique electronic structure of carbon nitride semiconductor triggered its application in the field of organic compounds conversion by selective photocatalytic oxidation [25] such as partial photooxidation of amines [26], aromatic hydrocarbons [27–29], cyclohexane [30] and aromatic alcohols with molecular oxygen [31–35]. To the best of our knowledge, despite the favourable position of its energy levels and the absence of hydroxyl groups on the surface, which would favour the direct formation of the unselective OH$^\bullet$ radicals, carbon nitride has not been utilized before for selective oxidation of non-aromatic alcohols in aqueous medium. In the present work it is reported the partial photo-oxidation of HMF in aqueous medium aimed to obtain FDC by using both as-prepared and thermally exfoliated g-C$_3$N$_4$ samples. The overall partial oxidation of HMF to FDC by using carbon nitride is also shown in Scheme 1.

2. Experimental

2.1. Photocatalyst preparation

Bulk carbon nitride (g-C$_3$N$_4$) samples were prepared *via* the thermal condensation method from different precursors as before reported [18,19]. 10 g of melamine, 20 g of urea or 10 g of thiourea were placed in a ceramic crucible covered with a lid and heated in a muffle furnace at 2 °C min^{-1} up to 520 °C, then left for 2 h at the reached temperature and slowly cooled down. The g-C$_3$N$_4$ samples derived from the different sources, melamine, urea and thiourea, were labelled as MCN, UCN and TuCN, respectively. The bulk carbon nitride prepared from melamine (MCN) was used as the precursor for the thermally exfoliated g-C$_3$N$_4$ nanosheets [24,36]. To this purpose, 6 g of bulk carbon nitride were powdered in a mortar, evenly spread on the bottom of a ceramic bowl with a diameter of 14 cm, calcined in a static air atmosphere at 450, 500, 520 and 540 °C by using a temperature ramp of 2 °C min^{-1} and maintained for 4 h at each of the final temperatures. The thermally exfoliated carbon nitride samples were coded as MCN_450, MCN_500, MCN_520, MCN_540.

2.2. Photocatalysts characterization

The crystalline structure of the samples was determined at room temperature by powder X-ray diffraction analysis (PXRD) carried out by using a Panalytical Empyrean apparatus, equipped with CuKα radiation source and PixCel1D (tm) detector. Specific surface areas (SSA) were calculated in accordance with the standard Brunauer-Emmet-Teller (BET) method from the nitrogen adsorption data using a Micromeritics ASAP 2020. Infrared spectra of the samples in KBr (Aldrich) pellets were recorded with 4 cm^{-1} resolution and 256 scans using a FTIR-8400 Shimadzu spectrometer. Diffuse reflectance spectra (DRS) were obtained in air at room temperature in the 250–800 nm wavelengths range by means of a Shimadzu UV-2401 PC spectrophotometer, with BaSO$_4$ as the reference material. Mettler Toledo TGA/SDTA851 was used to

investigate the thermal decomposition of g-C$_3$N$_4$ under an O$_2$ flow of 50 mL min^{-1} in the temperature range 25–1000 °C. The binding energies of C, N and O in the pristine and exfoliated MCN samples were measured by X-ray Photoelectron Spectroscopy (XPS) by using a SPECS system equipped with a Hemispherical Phoibos detector operating in a constant pass energy, using MgKα radiation (h·ν = 1253.6 eV). TEM studies were performed on a JEOL JEM-2100F transmission electron microscope operated at an accelerating voltage of 200 kV, equipped with a field emission gun (FEG) and an ultra-high resolution pole-piece that provided a point-resolution better than 0.19 nm. The samples for TEM were dispersed in ethanol, sonicated and sprayed on a holey carbon film coated copper grid and then allowed to air-dry; finally, Gatan SOLARUS 950 was used before carrying out observations with the microscope.

2.3. Photocatalytic set-up and procedure

The irradiation experiments were carried out in a Pyrex cylindrical photoreactor (internal diameter: 32 mm, height: 188 mm) containing 150 mL of aqueous suspension, irradiated by six external Actinic BL TL MINI 15 W/10 Philips fluorescent lamps emitting in the 340–420 wavelength range with the main emission peak at 365 nm. The reaction was carried out at about 25 °C as the reactor open to the atmosphere was provided by a thimble where water was allowed to circulate. Selected experiments were carried out in anaerobic condition by continuously bubbling N$_2$ throughout the runs to estimate the influence of O$_2$ on the reaction. The initial HMF concentration was 0.5 mM at the natural pH. The amount of solid photocatalyst used for the experiments was 50 mg, except for the pristine carbon nitrides MCN, UCN, TuCN and MCN_450, for which 100 mg were used, due to their poorer light absorbance compared to the other samples. In this way, all the entering photons were virtually absorbed by the suspension. The impinging radiation energy in the range 315–400 nm was measured by a radiometer Delta Ohm DO9721 with an UVA probe and its average value was 3.4 W m^{-2}. Some experiments were performed by reusing one of the best materials (MCN_520) in order to verify its performance in a series of four consecutive runs. Details on the procedure for the experiments of re-utilization are reported in the Supporting information. Selected scavengers were used in order to establish the reactive species responsible for HMF conversion and the selectivity to FDC. Sodium formate (HCOONa) was used as a hole scavenger, *tert*-butyl alcohol (*t*-BuOH) as an OH$^\bullet$ radical scavenger, copper (II) chloride dihydrate to trap electrons, and *p*-benzoquinone to scavenge O$_2^{\bullet-}$ radicals. The concentration of sodium formate and *tert*-butyl alcohol scavengers was 5 mM, whereas for CuCl$_2$ and *p*-benzoquinone the concentration was reduced to 1 mM, which enabled to avoid the precipitation of copper hydroxide during the photocatalytic run and to decrease the effect of the formed *p*-hydroxiquinone on the light absorbance by the suspension.

Samples of the irradiated solution were withdrawn at fixed time intervals and immediately filtered through 0.25 μm membranes (HA, Millipore) to separate the photocatalyst particles. Liquid aliquots were analysed by a Thermo Scientific Dionex UltiMate 3000 HPLC equipped with a Diode Array detector to identify and to determine the concentration of HMF, FDC and 5-formyl-2-furoic acid (FFA). A REZEK ROA Organic acid H$^+$ column was used with a mobile phase of aqueous 2.5 mM H$_2$SO$_4$ solution at a flow rate of 0.6 mL min^{-1}. Standards purchased from Sigma-Aldrich with a purity >99% were used to identify the products formed during the reaction and to obtain the calibration curves. Additionally, the reaction products were identified and selectivity values were confirmed by a GC–MS technique, using a Shimadzu 2100 Ultra GC–MS equipped with a Teknokroma TRB-5MS (95%) dimethyl (5%) diphenylpolysiloxane copolymer column.
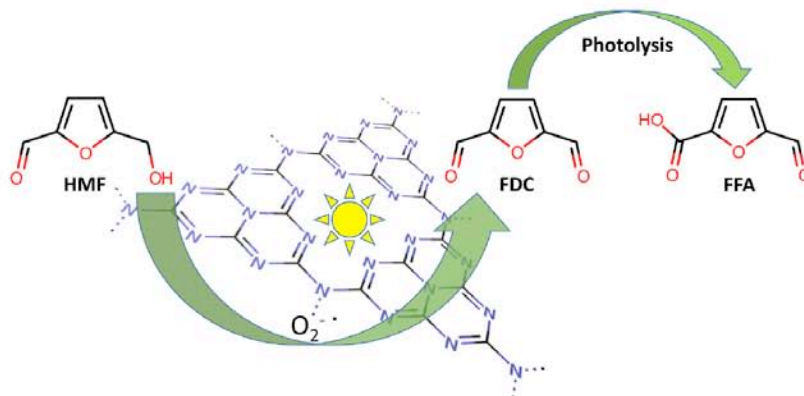
Scheme 1. Photocatalytic oxidation of HMF to FDC by using carbon nitride as photocatalyst along with the photolysis reaction of FDC producing FFA.

The photocatalytic reactions under a natural solar irradiation were carried out on clear sunny days of 6th, 9th and 18th May, 2016 in Palermo (Italy) from 9:30 to 13:30. Typically, 75 mL of 0.5 mM HMF solution and 25 mg of MCN_520 and MCN_540 samples were introduced inside a round-shaped Pyrex batch reactor having a total volume of 125 mL and a diameter of 10 cm. The reactor was closed and no gases were fed during the tests as preliminary experiments indicated that O_2 deriving from air and present in the system was sufficient to induce the oxidation. The suspensions of the carbon nitride samples in HMF solution were continuously magnetically stirred and approximately 2.5 mL were withdrawn every 30 min and analysed by using the previously described analytical procedure. The photon flux was measured every 10 min throughout the photocatalytic tests. Moreover, selected additional experiments were carried out by using MCN_520 and MCN_540 photocatalysts under solar light filtered by means of 1 M $NaNO_2$ solution ($\lambda > 400$ nm).

3. Results and discussion

3.1. Bulk g-C_3N_4 derived from the different precursors

3.1.1. Properties of bulk g-C_3N_4

It is known that the thermal condensation of the different carbon nitride precursors can significantly influence the structure and properties of g-C_3N_4. In the present case the yields of g-C_3N_4 obtained from melamine, urea and thiourea were approximately 60, 5, and 10 wt%, respectively. The two main diffraction maxima for g-C_3N_4 at 13° and 27°, reported in Fig. 1(A) can be attributed to (100) and (002) crystallographic planes of g-C_3N_4. These results are consistent with the studies reported before [18,19]. The variation of the intensity of the mentioned diffraction peaks, along with the slightly more pronounced reflections at 46.2 and 56.4 angles, assigned to (300) and (004) crystallographic planes, corresponding to the tri-s-triazine network [37], could be an indication of the degree of polymerization of g-C_3N_4, which decreases in the order MCN > TuCN > UCN.

FTIR spectroscopy of these solids confirmed the carbon nitride structure of the materials, showing no significant differences among the samples synthesized using different precursors (Supporting information, Fig. S1). UV–vis spectroscopy indicated significant discrepancies in their light absorption properties. The typical band-gap value of carbon nitride (2.73 eV) was found for the MCN sample, whilst a significant blue-shift occurred for the UCN one (2.86 eV band-gap) (Supporting information, Fig. S2), which can be attributed to its lower polymerization degree, hypothesized on the basis of PXRD results. The incorporation of S-heteroatom into the TuCN carbon nitride sample, extended the light absorption to the visible region resulting in a slight decrease of its band-gap value to 2.71 eV and the appearance of the sub-band-gap was estimated to be 2.17 eV. The low specific surface area generally observed for g-C_3N_4 materials is a drawback which could prevent their utilization as (photo)catalysts. This property depends on the precursor selected for their preparation, as shown in Table 1 and in the N_2 adsorption-desorption isotherms reported in Fig. S3. The higher SSA of UCN sample could be a consequence of a polymerization mechanism different from that of the other samples, resulting in the formation of a less condensed network, as suggested by the PXRD study.

3.1.2. Photocatalytic oxidation of HMF by using bulk g-C_3N_4

The extent of adsorption and photolysis of the substrate was determined before discussing the photoreactivity results. The adsorption of 0.5 mM HMF or FDC on the surface of the solid did not exceed 1% of the initial concentration and it can be considered negligible. On the contrary, the photolytic decomposition of HMF under UV illumination for 4 h was about 6%, but no formation of FDC was observed (Fig. S4). The photolytic stability of FDC under irradiation was lower than that of HMF, in fact, almost 20% was degraded after 4 h, and unlike the substrate, its photolysis produced FFA in large quantities (Fig. S4). Preliminary photocatalytic tests carried out in the presence of increasing amounts of MCN, from 25 to 200 mg, indicated that the optimum amount of photocatalyst was 100 mg (Fig. S5). By considering that all of the prepared materials possess similar light absorption, this amount was chosen also for the other two samples. The conversion of HMF versus irradiation time and the formation of FDC are reported in Fig. 2(A) and (B), respectively. The highest activity was observed for UCN sample, while the lowest one for TuCN, which could be related to the SSA values of the solids. The amount of FDC formed during the reaction was very similar for MCN and UCN, which implies that the selectivity to FDC formation was higher for MCN, as shown in Fig. 2(C). In addition to the influence of SSA, the bulk properties of the photocatalyst can also play some role on the reaction performance. The similar dependence of selectivity to FDC versus the HMF conversion observed for MCN and TuCN, as shown in Fig. 2(D), suggests that the bulk structure (determining the band positions) of these two materials which appeared to be similar according to the PXRD and spectroscopic data, was also responsible for the high selectivity to FDC formation. Thermal condensation of urea via a different pathway due to the presence of oxygen in the starting molecule, led to the formation of less polymerized carbon nitride network, resulting in poorer efficiency of

117
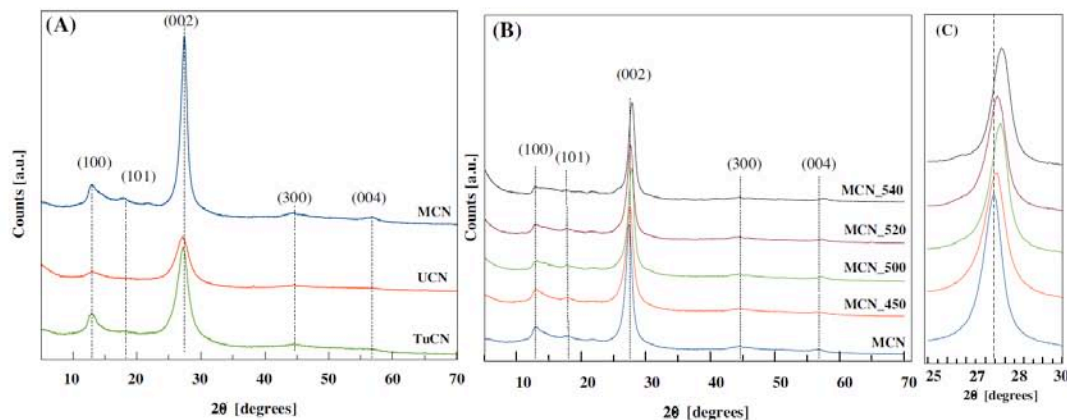
Fig. 1. PXRD patterns of (A): (___) MCN, (___) UCN, (___) TuCN samples and (B): thermo-exfoliated carbon nitride samples, i.e. Pristine MCN (___) and thermally exfoliated MCN_450 (___), MCN_500 (___), MCN_520 (___) and MCN_540 (___) samples. (C) Enlargement of the (002) in Fig. 1 (B).

Table 1
Specific surface area (SSA), band gap, HMF initial conversion rate (r), HMF conversion after 4 h of irradiation and selectivity to FDC formation at 30% of HMF conversion.

Sample	SSA [$m^2 g^{-1}$]	Band gap [eV]	HMF initial conversion rate, r [$mM\,min^{-1}$]	HMF Conversion (%)	FDC Selectivity (%)
UCN	28	2.86	0.0012	44	22
TuCN	4.0	2.71	0.0007	26	27[c]
MCN	7.0	2.73	0.0009	39	28
MCN_450	14	2.75	0.0010	38	37
MCN_500	154	2.78	0.0015	52	42
MCN_520	161	2.79	0.0018/0.0033[a]/0.0009[b]	58/81[a]/31[b]	44/47[a]/47[b]
MCN_540	169	2.90	0.0025/0.0091[a]/0.0012[b]	69/>99[a]/42[b]	43/49[a]/53[b]

[a] The value for the HMF photooxidation test under solar light.
[b] The value for the HMF photooxidation test under solar light in the presence of a 1 M $NaNO_2$ filter.
[c] The value is shown for 25% of HMF conversion.
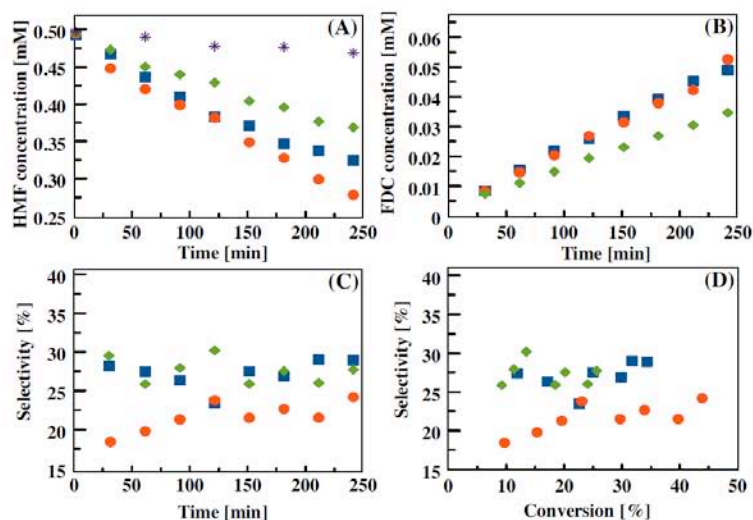
Fig. 2. HMF degradation (A); formation of FDC (B); selectivity to FDC versus irradiation time (C) and selectivity of the reaction to FDC versus HMF conversion (D) in the presence of MCN (■), UCN (●), and TuCN (◆) samples. (*) HMF photolysis in the homogeneous system.

the UCN sample in the partial photooxidation, as shown on Fig. 2(C) and (D).

A run carried out for the sake of comparison in the presence of TiO_2 Evonik P25, not reported in Fig. 2, indicated that this cat-

alyst was able to degrade HMF almost completely in 4 h but the selectivity to FDC was virtually zero at any time of the runs.

As above mentioned, the formation of FFA was found during the photolysis of FDC. The same compound in small amounts was also
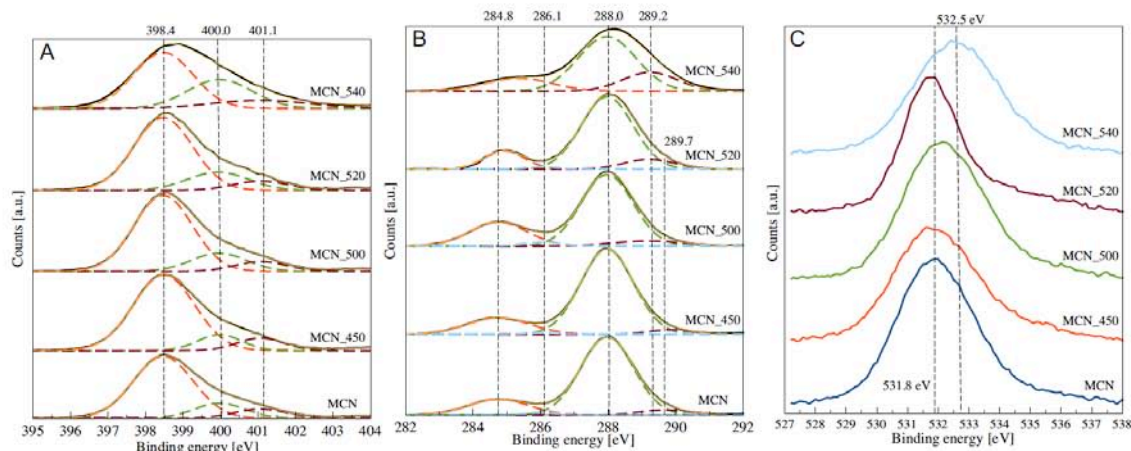
Fig. 3. XPS spectra of N 1s (A), C 1s (B) and O 1s (C) regions of the MCN and thermally exfoliated samples.

observed during the photocatalytic reactions of HMF conversion. Notably, its content did not depend on the type of the photocatalyst used for the reaction, but it was related to the FDC concentration. Therefore, the formation of FFA can be attributed to the photolysis of FDC deriving from the photooxidation of HMF (Fig. S6).

3.2. Photocatalytic conversion of HMF by using thermally exfoliated carbon nitride samples

3.2.1. Properties of the exfoliated g-C₃N₄

The preparation of carbon nitride using melamine as the precursor is preferable because it can be obtained in high yields and the selectivity for the partial photooxidation of HMF to FDC by using this photocatalyst was also high. In general, the changes caused by the thermal exfoliation follow the trends described in Refs. [23], and [34]. The diffraction patterns of the thermo-exfoliated samples prepared starting from MCN are reported in Fig. 1(B). It is clear that the exfoliation did not destroy the tri-s-triazine structure of g-C₃N₄. All the reflections corresponding to (100), (101), (002), (300), and (004) crystal planes, in fact, are retained even after treatment at 540 °C.

According to the thermal analysis (Fig. S7) the maximum decomposition rate of the pristine MCN can be observed at approximately 750 °C, while the exfoliated sample MCN_540 began to decompose at lower temperature, as indicated by the DTG peak centred at 700 °C. The lower thermal stability of the exfoliated carbon nitride could be attributed to formation of ammonia from the large amount of amino-groups, which prevents oxidation of the material.

FTIR spectroscopy confirmed the structure of the prepared carbon nitride samples. All the major bands responsible for the bonds vibration of the g-C₃N₄ matrix, such as those attributable to heptazine ring (810 cm⁻¹) and to C−N−C and C−NH−C units (900–1800 cm⁻¹) remain almost unchanged for the as-prepared and exfoliated samples (Fig. S8).

The chemical state of the surface species of the exfoliated carbon nitride was investigated by XPS. All the major band positions for C, N, and O are virtually coincident with those reported for the thermally exfoliated carbon nitride [24,36], although it is useful, for the benefit of readers, to briefly highlight some important features which play a role in the present study. Deconvolution of the N 1s XPS peak obtained for the pristine MCN reveals contributions from three different nitrogen species (Fig. 3A).

The most intense peak centred at 398.4 eV is due to the C−N=C groups of the tri-s-triazine network, while the other bands at 400.0 eV and 401.1 eV can be assigned to N−(C)₃ groups and C−N−H linkages, respectively. The integrated intensity ratio of N−(C)₃ and C−N=C signals reflects the polymerization degree of the carbon nitride [38]. According to the deconvolution data (Table S1), the thermal exfoliation favours the increase of this ratio by completing the thermal polymerization process and eliminating uncondensed NH₂ species. All the deconvoluted XPS peaks show reasonable half-width at half-height (HWHM) values below 1 eV, however it can be noticed a significant peak broadening in the spectra of MCN_520 and MCN_540, probably resulting from the appearance of some additional contributions to the N 1s signal coming from the oxidized g-C₃N₄ fragments (Table S1).

The C 1s peak in all of the carbon nitride spectra is dominated by the contribution having a maximum at 288.0 eV, corresponding to the carbon of the N−C=N groups of tri-s-triazine network (Fig. 3B). The second largest band observed at 284.8 eV can be attributed to the sp² bonded carbon of C−C bonds deriving from the adventitious hydrocarbon of the XPS instrument. The presence of C−N−H is witnessed by the small maximum at 286.1 eV. The peak near 289.7 eV in the spectrum of MCN can be attributed to C=O bonds of the carbonate species and it is due to the reaction of surface basic sites of the carbon nitride surface with atmospheric CO₂ (Fig. 3B). A HWHM value of this maximum is lower for MCN_450 sample and the signal completely disappears in the spectra of the samples treated at t ≥500 °C giving rise to a new contribution centred at 289.2 eV, which increases by increasing the g-C₃N₄ exfoliation temperature (Fig. 3B, Table S1). According to Li et al. [39], the latter maximum can be attributed to the oxidized carbon nitride surface, where sp²-hybridized carbon is directly bonded to O atom. O 1s spectra support this hypothesis because the peak at 531.8 eV (C=O bonds) in the spectrum of pristine MCN is shifted to 532.5 eV (C−O) in that of MCN_540 (Fig. 3C).

The effect of the exfoliation on SSA was negligible for temperatures below 450 °C, in fact, only a twofold increase of this value was observed for MCN_450 with respect to g-C₃N₄, whilst the corresponding value ranged from 154 to 169 m²g⁻¹ for the samples treated at t ≥500 °C. All of the adsorption isotherms correspond to IV-type with H3 hysteresis loop indicating the presence of large mesopores, as reported in Fig. S9.

TEM images showing the typical morphology of the bulk and thermally exfoliated carbon nitride are reported in Fig. 4. The pres-
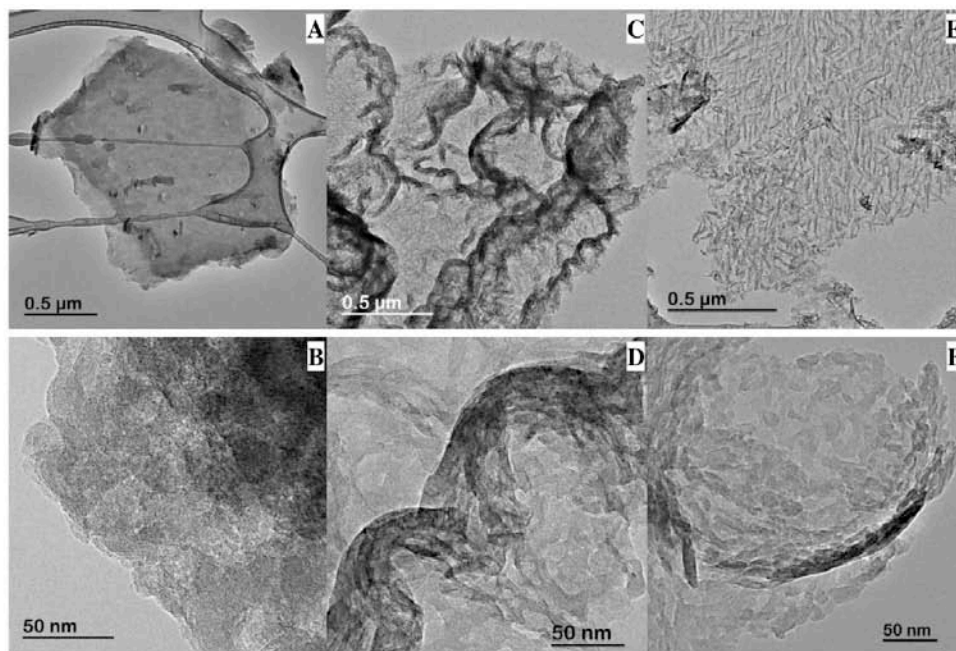
119

Fig. 4. TEM images of some selected samples: MCN (A) and (B), MCN_520 (C) and (D) and MCN_540 (E) and (F).

ence of large sheet-like particles of g-C_3N_4 showing no porosity is a feature of the material synthesized by thermal condensation of melamine (Fig. 4(A) and (B)). The thermal treatment under oxidant atmosphere results in disaggregation of the carbon nitride particles, which is probably due to the thickening and separation of layers caused by increasing treatment temperature (Fig. 4(C) to (F)).

Relatively large voids found between the particles are likely responsible for the appearance of a hysteresis loop in the N_2 adsorption-desorption isotherms (Fig. S9).

A significant blue shift of the absorption edge was observed for the thermally treated samples (Fig. S10), in good agreement with data previously reported for the exfoliated carbon nitride [36]. The band-gap energy increased from 2.73 eV for the as-prepared g-C_3N_4 to 2.90 eV for the sample exfoliated at 540 °C (Table 1). This change in the electronic properties of the material could be explained by the quantum confinement effect, which occurs as the result of separation of carbon nitride layers [24].

3.2.2. Photocatalytic oxidation of HMF by using the exfoliated g-C_3N_4

The increase of the SSA of the exfoliated carbon nitride samples resulted in a more efficient light absorption compared to the pristine MCN, thus the optimal amount of the photocatalysts was determined to be 50 mg according to radiometry measurements. The improved textural properties of MCN_500, MCN_520 and MCN_540 were also responsible for somewhat higher HMF adsorption (about 3%).

The photocatalytic HMF partial oxidation by using the thermo-exfoliated samples is reported in Fig. 5.

The observation of Fig. 5(A) and (B) indicates that the degradation rate of HMF was always higher than the formation rate of FDC for all of the samples tested. This finding indicates that the degradation of HMF proceeded at least by two parallel reactions, one of which gave rise to formation of FDC. Due to the fact that

only FDC and small amounts of FFA (deriving from the further oxidation of FCD) were found as the products, it is likely that a parallel reaction gave rise to the complete mineralization of HMF by the formation of adsorbed open-chain aliphatic compounds. However, this work was not aimed to fully characterize the intermediates, most of which were present only as traces in the bulk of solution.

The HMF conversion rate grew with the increase of the thermal treatment temperature and SSA values, therefore it is not surprising that the slight enhancement of the SSA observed for MCN_450 with respect to the pristine MCN sample ($14\,m^2\,g^{-1}$ versus $7\,m^2\,g^{-1}$) did not improve the photocatalytic efficiency of carbon nitride (Fig. 5(A)). The drastic increase of the HMF conversion observed in the presence of the samples thermally treated at t $\geq$ 500 °C, which reached the highest value of 69% in the presence of MCN_540 sample, along with the increase of the initial reaction rate by 2.5 times compared to that of the MCN sample (Table 1), could be related to the enhanced SSA of the thermally treated photocatalysts. However, the high reactivity of the exfoliated g-C_3N_4 cannot be explained only by taking into account its textural properties, because no direct correlation between these two parameters was found (see the sharp increase of the initial reaction rate observed in the presence of the sample with the higher SSA, Figs. S11A and B).

The XPS study indicates that the treatment under oxidative conditions modifies the functionality of the carbon nitride surface. The increased polymerization degree, the removal of NH_2 uncondensed basic sites playing the role of the CO_2 adsorption centres and the formation of C—O bonds on the g-C_3N_4 surface, probably account for a more efficient charge separation and interaction with a polar substrate. Moreover, the exfoliation led to band-gap broadening of g-C_3N_4, implying the increase of the conduction band potential and possibly the formation of reactive species via the reductive pathway [40]. Thus, this property could influence the oxidation rate and the selectivity of HMF conversion (Fig. S11C and D).
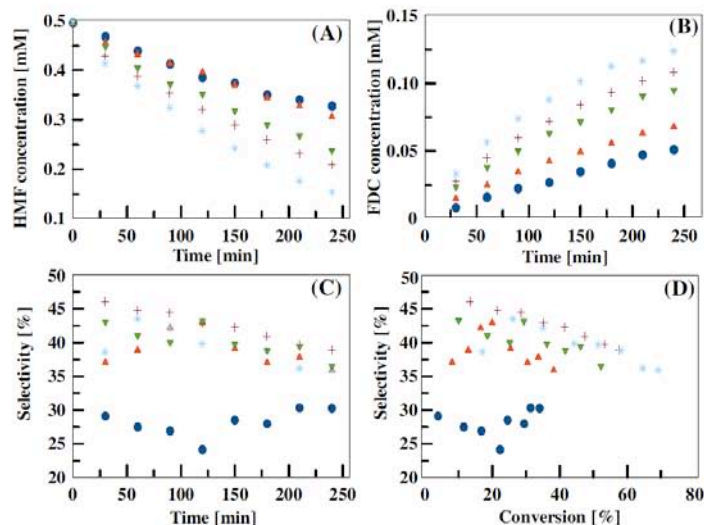
Fig. 5. HMF degradation (A); formation of FDC (B) and selectivity to FDC versus irradiation time (C) or selectivity to FDC versus HMF conversion (D) in the presence of the non exfoliated MCN (●), MCN_450 (▲), MCN_500 (▼), MCN_520 (+) and MCN_540 (✦).

The evolution of FDC gradually slowed down with time, due to the continuously decreasing concentration of HMF in the reaction medium, but the degradation of the substrate still prevailed over the FDC decomposition (Fig. 5(B)).

A satisfactory selectivity near 30% was found also in the presence of the pristine MCN (Fig. 5(C) and (D)) and it was noticeably higher than that reported for the TiO$_2$-assisted HMF photooxidation [16]. The thermal treatment of g-C$_3$N$_4$ at 450 °C did not significantly affect the activity of the photocatalyst, but the selectivity to FDC formation improved. XPS results indicate only the presence of small changes, possibly due to the elimination of the carbonate species adsorbed on the g-C$_3$N$_4$ basic sites. Such moieties interfere with the charge separation process, increasing the contribution of the reactive species which unselectively can decompose HMF. The selectivity to FDC formation reached its highest values (ca. 45%) for MCN_520 and MCN_540 samples and it was virtually identical after the same extent of conversion of HMF (Fig. 5(D)). Moreover, it decreased by increasing the conversion, because the product was subjected to further oxidative attacks, which gave rise to its decomposition, but it did not go down below 35% even after 69% of HMF conversion (Fig. 5(D)). High selectivity values observed for the exfoliated carbon nitride samples were also confirmed by GC–MS data (Fig. S12A and B).

FFA formed continuously during the photooxidation of HMF in the presence of MCN and the exfoliated carbon nitride samples (Fig. S13A). Similarly to the case of bulk g-C$_3$N$_4$ materials, the extent of FFA virtually depended only on that of FDC derived from HMF oxidation, regardless of the type of the catalyst used (Fig. S13 B).

In addition to the photolysis, the photocatalytic degradation of FDC could also take place, although the latter reaction was not significant. The inability of carbon nitride to produce OH• radicals by direct interaction of electron-holes with water, did not favour the degradation of FDC, making HMF partial oxidation the prevailing process. Indeed, only about 35% of FDC decomposed after 4 h, conversely 69% of HMF was converted in the same time in the presence of MCN_540 (See Fig. S14).

The application of a set of scavengers helped to evaluate the contribution of different reaction pathways to the HMF decomposition and selectivity to FDC, as reported in Fig. 6 and in Fig. S15.

According to many reports [41,42], *tert*-butyl alcohol is an efficient OH• scavenger. Its addition to the reaction mixture resulted in a minor change of HMF conversion rate while the selectivity remained unchanged. Therefore, one can suppose that the presence of hydroxyl radicals was not determinant for the HMF partial oxidation. When the reaction was carried out in anhydrous aprotic organic solvents, higher values of selectivity were usually achieved [31–33]. Under such conditions, the oxidation could proceed only *via* the direct interaction of the substrate and/or its intermediates with the photoproduced pairs on the photocatalyst surface or with O$_2$•$^-$ radicals. The photooxidation of HMF in acetone resulted in much lower conversion rate, but it gave higher selectivity, which was due to the absence of unselective OH• radicals and H$_2$O$_2$ (Fig. 6). Whether the substrate is decomposed *via* the direct electron-hole interaction was tested by the addition of sodium formate as a hole scavenger, which gave rise to a decrease of the HMF conversion to a significant extent, but also slightly enhanced the selectivity to FDC formation. Spasiano et al. [43] reported that the addition of cupric ions during the partial photooxidation of benzyl alcohol in water and TiO$_2$ under anaerobic conditions can promote the selectivity towards benzaldehyde formation. In that way it was established that the dominant process responsible for the selectivity of benzyl alcohol involves the formation of e$^-$- h$^+$ pairs. A similar experiment in the presence of carbon nitride resulted in a complete inhibition of the reaction. Cupric ions, indeed, can efficiently scavenge electrons, but the potential of the holes is unsuitable to oxidize HMF selectively. The application of *p*-benzoquinone as O$_2$•$^-$ radical scavenger indicated that superoxide radicals were mainly responsible for the partial oxidation of HMF to FDC. Benzoquinone effectively consumed O$_2$•$^-$ radicals hindering their interaction with HMF and yielding almost no selectivity to FDC formation.

Unexpectedly, the reaction did not completely stop under anaerobic conditions (N$_2$), although no electron scavengers were present (see Figs. 6 and S15). Almost 20% of HMF decomposed after 4 h of irradiation, and no significant selectivity to FDC was observed. The absence of any selectivity is in accordance with the absence of O$_2$•$^-$ radicals, while the observed decomposition of the substrate could be explained by considering that terminal functional groups
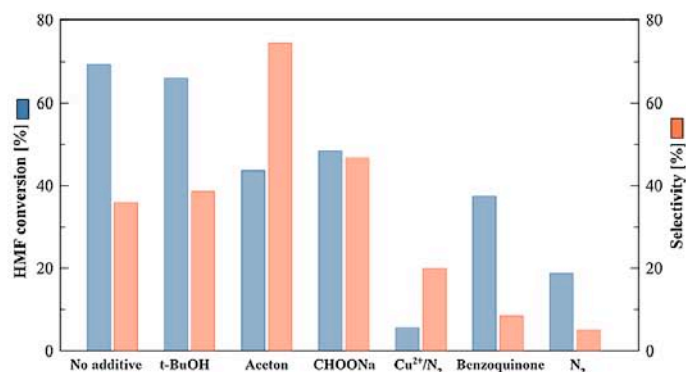
Fig. 6. Effect of scavengers (of charges and/or radicals) or of the solvent (acetone instead of water) on the HMF conversion and the corresponding selectivity to FDC after 240 min of irradiation in the presence of MCN_540.
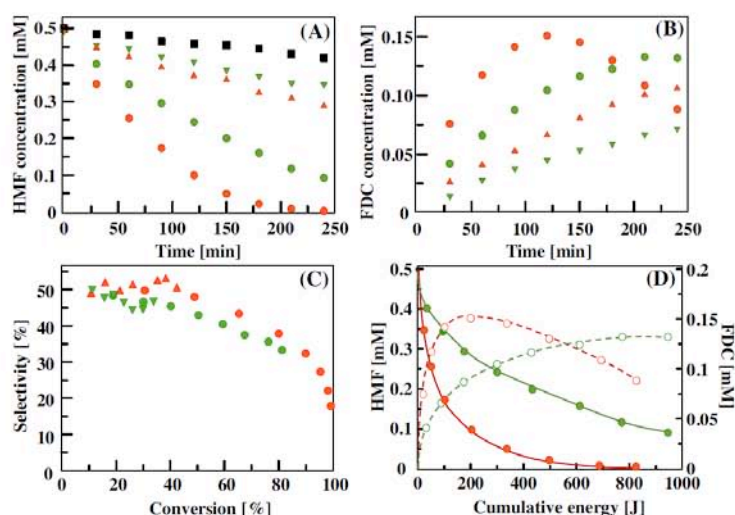

Fig. 7. HMF degradation (A); FDC formation versus irradiation time (B); selectivity of the reaction to FDC versus HMF conversion (C) and evaluation of HMF and FDC concentrations as a function of the cumulative energy entering the reactor for a reaction carried out under natural solar light irradiation (D). Symbols refer to a homogeneous photolysis experiment (■) or to runs carried out in the presence of MCN_520 or MCN_540 samples with (▼), (▲) and without (●), (●) a 1 M NaNO₂ filter. Empty symbols represent the FDC concentration during the solar experiment.

and/or adsorbed surface species on the photocatalyst could induce some extent of electron-hole separation.

Therefore, we confirm that, as in the case of photooxidation of aromatic alcohols in organic media [31], superoxide radicals formed *via* the reduction of molecular oxygen by the photogenerated electrons are the reactive species mainly responsible for the HMF partial oxidation to FDC in water. Zhang et al. reported the major role played by $O_2^{\bullet-}$ in the partial oxidation of aromatic alcohols to aldehydes with a selectivity higher than 96% by using Bi_2WO_6 as the photocatalyst in aqueous phase [44]. The higher selectivity values with respect to that obtained in this work could be attributed to the more stable benzene rings of the studied substrate molecules in Ref. [44], compared to the pentatomic furanic ring of HMF.

In order to test the stability of the catalyst some experiments were performed by reusing one of the best materials (MCN_520) in a series of four consecutive runs. The results reported in Fig.

S16 indicate that the catalyst maintained ca. the same performance during all of the runs for both the conversion of HMF (57–58%) and the selectivity versus FDC formation (38–41%).

3.2.3. Solar photo-oxidation of HMF by using exfoliated g-C₃N₄

It is generally accepted that absorption of light by a photocatalyst extended as much as possible to the visible range can contribute to its better performance under a natural solar irradiation. However, many photocatalysts based on N-TiO₂ and g-C₃N₄ are able to utilize only a small portion of the visible irradiation, thus contributing slightly to the total photocatalytic activity of the material when sunlight is used. In this work, under solar irradiation the exfoliated carbon nitride samples showed a significantly higher activity than that observed using the UV-lamps of the laboratory set-up (see Figs. 5 (A) and 7 (A)). Notably, despite the band gap values of MCN_540 and MCN_520 were 2.90 and 2.79 eV, respectively, the latter was not more active even with the NaNO₂ filter cutting-off UV irradiation

(Fig. 7). The decreased activity of the carbon nitride at λ > 400 nm indicated, contrarily to what reported in some literature [34,45], that UV-light played a determinant role in the activation of the g-C_3N_4 at least under the experimental conditions used in this work (Fig. 7A and Table 1).

By observing the formation of FDC in the presence of MCN_540 photocatalyst (see Fig. 7(B)), it can be noticed that its concentration was maximum after about 2 h of irradiation and then it began to decline. This finding can be attributed to the decomposition of most of the HMF which was preferentially photooxidized by the carbon nitride.

The selectivity to FDC formation was somewhat higher under solar irradiation reaching about 50% after 40% conversion (Fig. 7(C)) by using MCN_520 and MCN_540, compared to experiments performed under UV-lamps irradiation. The use of a UV-filter did not significantly change the selectivity, although it reduced the HMF conversion and the photolysis of substrate and product. This finding indicates that the HMF partial oxidation by using carbon nitride occurred mainly under UV irradiation, and consequently the reaction data were plotted versus the cumulative energy entering the reactor between 315 and 400 nm. Fig. 7(D) reports the reactivity data in Fig. 7(A) and (B) for runs carried out in the presence of MCN_520 and MCN_540 samples versus the cumulative energy, E, entering the reactor [46]. The E value allows to compare photoreactivity results obtained under natural sunlight irradiation with different photocatalysts, and it was calculated by measuring the natural solar irradiance with a radiometer.

4. Conclusions

Graphitic carbon nitride demonstrated an outstanding selective photocatalytic performance in aqueous medium and in the absence of organic solvents. High selectivity of g-C_3N_4 in partial photooxidation of HMF to FDC was mainly due to its inability to generate unselective hydroxyl radicals, instead promoting the formation of highly efficient dehydrogenating $O_2^{\bullet-}$ species by reaction of electrons with atmospheric O_2. The main drawback of the carbon nitride, i.e its low specific surface area, was successfully overcome by implementing a facile thermal exfoliation procedure, which allowed not only to increase the reaction rate, but also to eliminate from the g-C_3N_4 surface uncondensed NH_2 sites, which were discovered to be detrimental for the partial photooxidation of HMF to FDC. The proposed material enabled to achieve 45% selectivity to FDC formation, which is higher than that (22%) reported by using TiO_2. The photocatalytic experiments under natural solar light irradiation showed that, despite the band gap energy of the carbon nitride allows utilization of a small portion of visible light, the UV fraction of the solar spectrum contributed to a greater extent to the excitation of the photocatalytic material. It was observed also that the exfoliated g-C_3N_4 showed even better activity and selectivity to FDC formation under real outdoor illumination, reaching 50% at 40% of HMF conversion in aqueous medium. The above results suggest that this material is a promising catalyst for application in the biomass-related compounds valorisation.

Acknowledgements

Appendix A. Supplementary data

Supplementary data associated with this article can be found, in the online version, at http://dx.doi.org/10.1016/j.apcatb.2016.11.049.

References

[1] D. Murzin, O. Simakova (Eds.), Biomass Sugars for Non-Fuel Applications, 1st ed., RSC, Cambridge, 2016.
[2] A.S. Amarasekara, D. Green, L.D. Williams, Renewable resources based polymers: synthesis and characterization of 2,5-diformylfuran-urea resin, Eur. Polym. J. 45 (2009) 595–598.
[3] Z. Hui, A. Gandini, Polymeric schiff bases bearing furan moieties, Eur. Polym. J. 28 (1992) 1461–1469.
[4] Y. Kanetaka, S. Yamazaki, K. Kimura, Preparation of poly(ether ketone)s derived from 2,5-furandicarboxylic acid by polymerization in ionic liquid, Macromolecules 49 (2016) 1252–1258.
[5] T.S.A. Heugebaert, C.V. Stevens, C.O. Kappe, Singlet-oxygen oxidation of 5-hydroxymethylfurfural in continuous flow, ChemSusChem 8 (2015) 1648–1651.
[6] B. Liu, Y. Ren, Z. Zhang, Aerobic oxidation of 5-hydroxymethylfurfural into 2,5-furandicarboxylic acid in water under mild conditions, Green Chem. 17 (2015) 1610–1617.
[7] L. Ozcan, P. Yalcin, O. Alagoz, S. Yurdakal, Selective photoelectrocatalytic oxidation of 5-(hydroxymethyl)-2-furaldehyde in water by using Pt loaded nanotube structure of TiO_2 on Ti photoanodes, Catal. Today 281 (2017) 205–213.
[8] J. Ma, Z. Du, J. Xu, Q. Chu, Y. Pang, Efficient aerobic oxidation of 5-hydroxymethylfurfural to 2,5-diformylfuran, and synthesis of a fluorescent material, ChemSusChem 4 (2011) 51–54.
[9] C. Carlini, P. Patrono, A.M.R. Galletti, G. Sbrana, V. Zima, Selective oxidation of 5-hydroxymethyl-2-furaldehyde to furan-2,5-dicarboxaldehyde by catalytic systems based on vanadyl phosphate, Appl. Catal. A 289 (2005) 197–204.
[10] V. Augugliaro, M. Bellardita, V. Loddo, G. Palmisano, L. Palmisano, S. Yurdakal, Overview on oxidation mechanisms of organic compounds by TiO_2 in heterogeneous photocatalysis, J. Photochem. Photobiol. C 13 (2012) 224–245.
[11] G. Palmisano, E. García-López, G. Marcì, V. Loddo, S. Yurdakal, V. Augugliaro, L. Palmisano, Advances in selective conversions by heterogeneous photocatalysis, Chem. Commun. 46 (2010) 7074–7089.
[12] X. Lang, X. Chen, J. Zhao, Heterogeneous visible light photocatalysis for selective organic transformations, J. Chem. Soc. Rev. 43 (2014) 473.
[13] J.C. Colmenares, W. Ouyang, M. Ojeda, E. Kuna, O. Chernyayeva, D. Lisovytskiy, S. De, R. Luque, A.M. Balu, Mild ultrasound-assisted synthesis of TiO_2 supported on magnetic nanocomposites for selective photo-oxidation of benzyl alcohol, Appl. Catal. B 183 (2016) 107–112.
[14] I. Tamiolakis, I.N. Lykakis, G.S. Armatas, Mesoporous CdS-sensitized TiO_2 nanoparticle assemblies with enhanced photocatalytic properties: selective aerobic oxidation of benzyl alcohols, Catal. Today 250 (2015) 180–186.
[15] C.J. Li, G.R. Xu, B. Zhang, J.R. Gong, High selectivity in visible-light-driven partial photocatalytic oxidation of benzyl alcohol into benzaldehyde over single-crystalline rutile TiO_2 nanorods, Appl. Catal. B 115–116 (2012) 201–208.
[16] S. Yurdakal, B.S. Tek, O. Alagoz, V. Augugliaro, V. Loddo, G. Palmisano, L. Palmisano, Photocatalytic selective oxidation of 5-(hydroxymethyl)-2-furaldehyde to 2,5-furandicarbaldehyde in water by using anatase, rutile, and brookite TiO_2 nanoparticles, ACS Sustain. Chem. Eng. 1 (2013) 456–461.
[17] S. Yin, J. Han, T. Zhou, R. Xu, Recent progress in g-C_3N_4 based low cost photocatalytic system: activity enhancement and emerging applications, Catal. Sci. Technol. 5 (2015) 5048–5061.
[18] Y.W. Zhang, J.H. Liu, G. Wu, W. Chen, Porous graphitic carbon nitride synthesized via direct polymerization of urea for efficient sunlight-driven photocatalytic hydrogen production, Nanoscale 4 (2012) 5300–5303.
[19] K. Wang, Q. Li, B. Liu, B. Cheng, W. Ho, J. Yu, Sulfur-doped g-C_3N_4 with enhanced photocatalytic CO_2-reduction performance, Appl. Catal. B 176–177 (2015) 44–52.
[20] Y. Wang, Y. Di, M. Antonietti, H. Li, X. Chen, X. Wang, Excellent visible-light photocatalysis of fluorinated polymeric carbon nitride solids, Chem. Mater. 22 (2010) 5119–5121.
[21] Z. Yang, Y. Zhang, Z. Schnepp, Soft and hard templating of graphitic carbon nitride, J. Mater. Chem. A 3 (2015) 14081–14092.
[22] X. Dong, F. Cheng, Recent development in exfoliated two-dimensional g-C_3N_4 nanosheets for photocatalytic application, J. Mater. Chem. A 3 (2015) 23642–23652.
[23] J. Xu, L. Zhang, R. Shi, Y. Zhu, Chemical exfoliation of graphitic carbon nitride for efficient heterogeneous photocatalysis, J. Mater. Chem. A 1 (2013) 14766–14772.
[24] P. Niu, L. Zhang, G. Liu, H.M. Cheng, Graphene-Like carbon nitride nanosheets for improved photocatalytic activities, Adv. Funct. Mater. 22 (2012) 4763–4770.
[25] X. Wang, S. Blechert, M. Antonietti, Polymeric graphitic carbon nitride for heterogeneous photocatalysis, ACS Catal. 2 (2012) 1596–1606.

[26] F. Su, S.C. Mathew, L. Mohlmann, M. Antonietti, X. Wang, S. Blechert, Aerobic oxidative coupling of amines by carbon nitride photocatalysis with visible light, Angew. Chem. 50 (2011) 657–660.

[27] X. Chen, J. Zhang, X. Fu, M. Antonietti, X. Wang, Fe-g-C_3N_4-Catalyzed oxidation of benzene to phenol using hydrogen peroxide and visible light, J. Am. Chem. Soc. 131 (2009) 11658–11659.

[28] Z. Ding, X. Chen, M. Antonietti, X. Wang, Synthesis of transition metal-modified carbon nitride polymers for selective hydrocarbon oxidation, ChemSusChem 4 (2011) 274–281.

[29] X.H. Li, X. Wang, M. Antonietti, Solvent-free and metal-free oxidation of toluene using O_2 and g-C_3N_4 with nanopores: nanostructure boosts the catalytic selectivity, ACS Catal. 2 (2012) 2082–2086.

[30] X.H. Li, J.S. Chen, X. Wang, J. Sun, M. Antonietti, Metal-free activation of dioxygen by graphene/g-C3N4 nanocomposites: functional dyads for selective oxidation of saturated hydrocarbons, J. Am. Chem. Soc. 133 (2011) 8074–8077.

[31] F. Su, S.C. Mathew, G. Lipner, X. Fu, M. Antonietti, S. Blechert, X. Wang, Mpg-C_3N_4-Catalyzed selective oxidation of alcohols using O_2 and visible light, J. Am. Chem. Soc. 132 (2010) 16299–16301.

[32] S. Verma, R.B.N. Baig, M.N. Nadagouda, R.S. Varma, Selective oxidation of alcohols using photoactive VO@g-C_3N_4, ACS Sustain. Chem. Eng. 4 (2016) 1094–1098.

[33] J. Xu, L. Luo, G. Xiao, Z. Zhang, H. Lin, X. Wang, J. Long, $C_3N_3S_3$ Polymer/graphene hybrids as metal-free catalysts for selective photocatalytic oxidation of benzylic alcohols under visible light, ACS Catal. 4 (2014) 3302–3306.

[34] J. Xu, L. Luo, G. Xiao, Z. Zhang, H. Lin, X. Wang, J. Long, Layered $C_3N_3S_3$ polymer/graphene hybrids as metal-free catalysts for selective photocatalytic oxidation of benzylic alcohols under visible light, ACS Catal. 4 (2014) 3302–3306.

[35] B. Long, Z. Ding, X. Wang, Carbon nitride for the selective oxidation of aromatic alcohols in water under visible light, ChemSusChem 6 (2013) 2074–2078.

[36] F. Dong, Y. Li, Z. Wang, W.K. Ho, Enhanced visible light photocatalytic activity and oxidation ability of porous graphene-like g-C_3N_4 nanosheets via thermal exfoliation, Appl. Surf. Sci. 358 (2015) 393–404.

[37] F. Fina, S.K. Callear, G.M. Carins, J.T.S. Irvine, Structural investigation of graphitic carbon nitride via XRD and neutron diffraction, Chem. Mater. 27 (2015) 2612–2618.

[38] S. Gu, J. Xie, C.M. Li, Hierarchically porous graphitic carbon nitride: large-scale facile synthesis and its application toward photocatalytic dye degradation, RSC Adv. 4 (2014) 59436–59439.

[39] J. Li, B. Shen, Z. Hong, B. Lin, B. Gao, Y. Chen, A facile approach to synthesize novel oxygen-doped g-C3N4 with superior visible-light photoreactivity, Chem. Commun. 48 (2012) 12017–12019.

[40] H. Zhang, L.H. Guo, L. Zhao, B. Wan, Y. Yang, Switching oxygen reduction pathway by exfoliating graphitic carbon nitride for enhanced photocatalytic phenol degradation, J. Phys. Chem. Lett. 6 (2015) 958–963.

[41] T. Xu, P.V. Kamat, K.E. O'shea, Mechanistic evaluation of arsenite oxidation in TiO_2 assisted photocatalysis, J. Phys. Chem. A. 109 (2005) 9070–9075.

[42] M.B. Gilliard, C.A. Martin, A.E. Cassano, M.E. Lovato, Reaction kinetic model for 2,4-dichlorophenoxyacetic acid decomposition in aqueous media including direct photolysis, direct ozonation, ultraviolet C and pH enhancement, Ind. Eng. Chem. Res. 52 (2013) 14034–14048.

[43] D. Spasiano, L.P.P. Rodriquez, J.C. Olleros, S. Malato, R. Marotta, R. Andreozzi, TiO_2/Cu(II) photocatalytic production of benzaldehyde from benzyl alcohol in solar pilot plant reactor, Appl. Catal. B: Environ. 136–137 (2013) 56–63.

[44] Y. Zhang, Y.J. Xu, Bi_2WO_6: A highly chemoselective visible light photocatalyst toward aerobic oxidation of benzylic alcohols in water, RSC Adv. 4 (2014) 2904–2910.

[45] G. Mamba, A.K. Mishra, Graphitic carbon nitride (g-C3N4) nanocomposites: a new and exciting generation of visible light driven photocatalysts for environmental pollution remediation, Appl. Catal. B: Environ. 198 (2016) 347–377.

[46] V. Augugliaro, E. García-López, V. Loddo, S. Malato-Rodriguez, I. Maldonado, G. Marcì, R. Molinari, L. Palmisano, Degradation of lyncomycin in aqueous medium: coupling of slar photocatalysis and membrane separation, Sol. Energy 79 (2005) 402–408.

SUPPLEMENTARY MATERIAL

Selective Photocatalytic Oxidation of 5-Hydroxymethyl-2-Furfural to 2,5-Furandicarboxyaldehyde in Aqueous Suspension of g-C$_3$N$_4$

Igor Krivtsov[1,2], Elisa I. García-López[3], Giuseppe Marcì[3], Leonardo Palmisano[3], Zakariae Amghouz[4], José R. García[1], Salvador Ordóñez[5], Eva Díaz[5]

1. Department of Organic and Inorganic Chemistry, University of Oviedo-CINN, 33006 Oviedo, Spain.

2. Nanotechnology Education and Research Center, South Ural State University, 454080, Chelyabinsk, Russia.

3 "Schiavello-Grillone" Photocatalysis Group. Dipartimento di Energia, Ingegneria dell'informazione e modelli Matematici (DEIM), Università di Palermo, Viale delle Scienze, 90128 Palermo, Italy.

4. Servicios Scientífico Técnicos, Universidad de Oviedo, 33006 Oviedo, Spain.

5. Department of Chemical and Environmental Engineering, University of Oviedo, 33006 Oviedo, Spain

FTIR spectroscopy of these solids confirmed the carbon nitride structure of the materials, showing no significant differences between the samples synthesized from the different precursors (Fig. 1S). The bands in the regions of 1632, 1560, 1410, 1325, 1250 cm^{-1} are typical for the stretching vibrations modes of heptazine heterocyclic ring (C$_6$N$_7$) units [1]. The absorption at 887 and 804 corresponds to the N-H deformation mode and a bending mode of the triazine units respectively. Uncondensed amino groups bands can be noticed between 3500-3000 cm^{-1}.
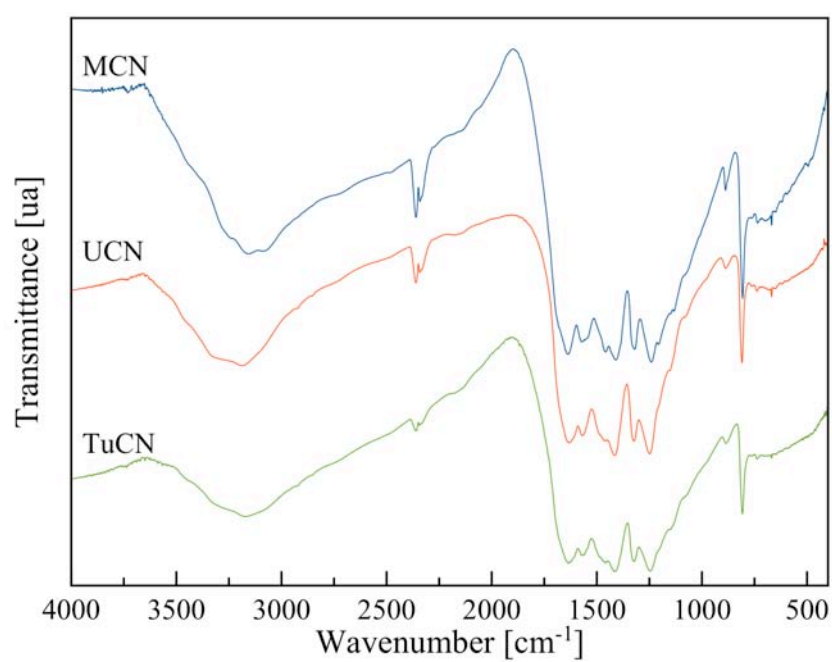
Figure S1. FTIR spectra of the carbon nitride samples prepared from different precursors.
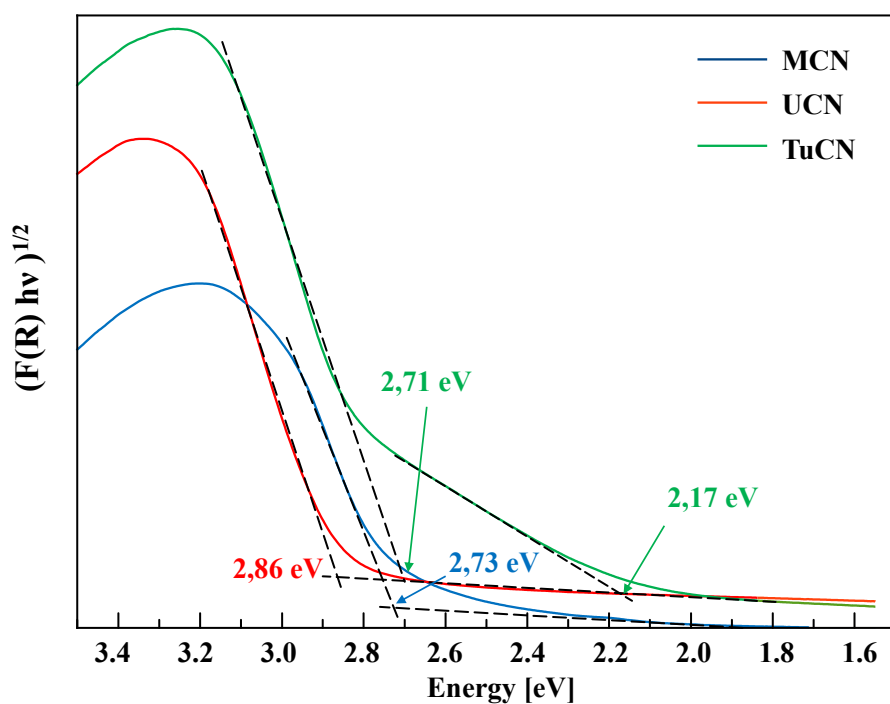
Figure S2. Tauc-plot of the g-C_3N_4 samples prepared from different precursors.
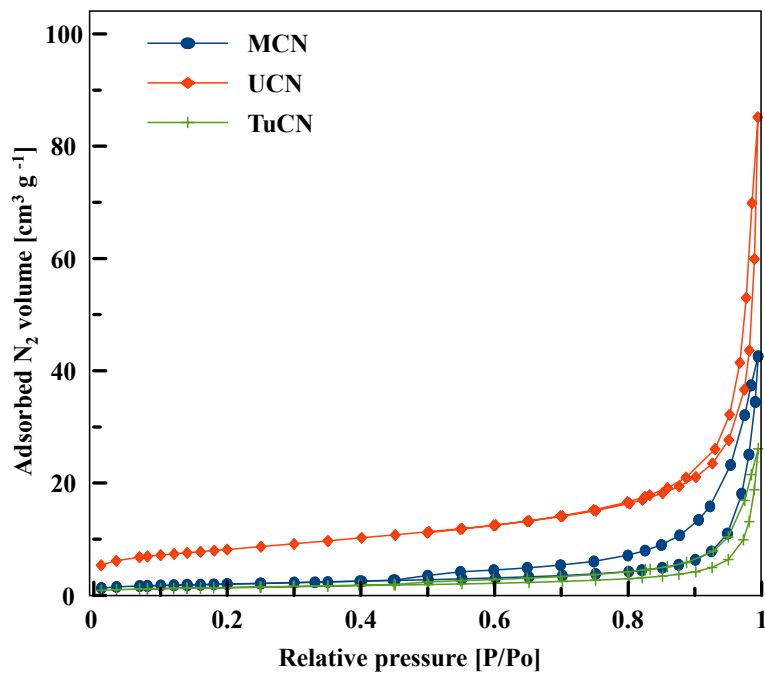
Figure S3. Adsorption-desorption N_2 isotherms obtained for (●) MCN, (♦) UCN, (+) TuCN

samples prepared from different precursors.
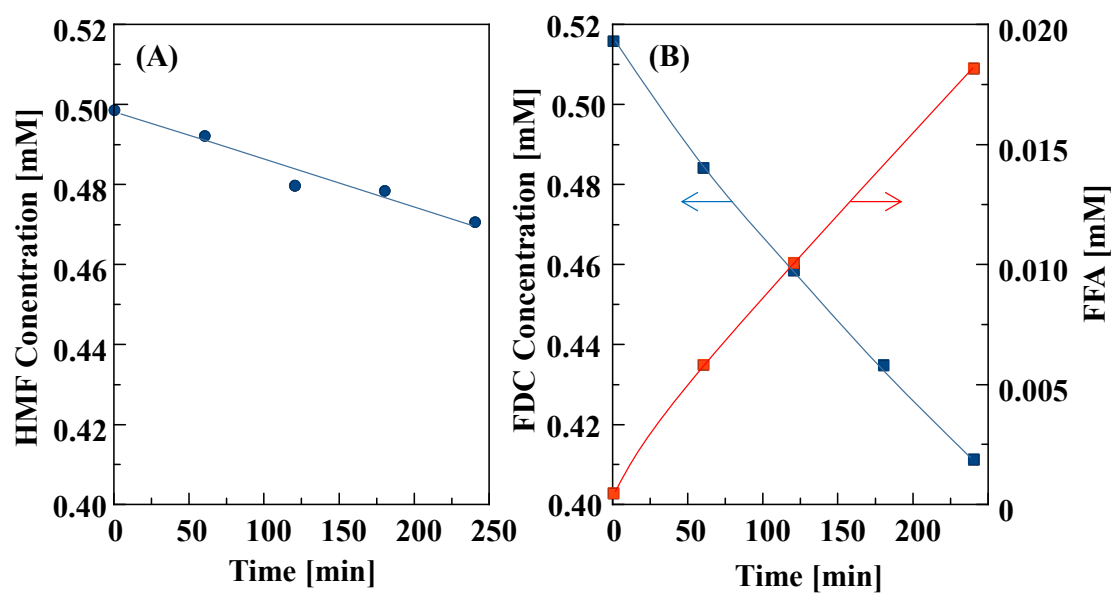
Figure S4. Photolysis under UV light of HMF (A) and FDC (B). FDC (■) and FFA (■).
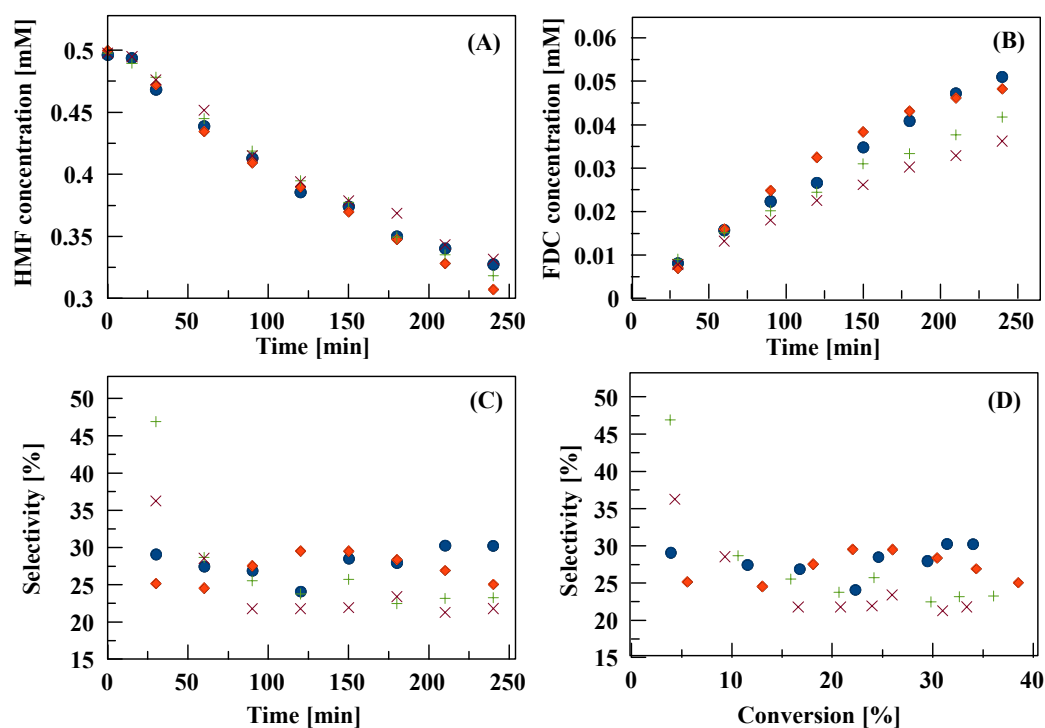
Figure S5. HMF conversion in the presence of different loadings of MCN sample: 200 mg (●); 100 mg (◆); 50 mg (+) and 25 mg (x).
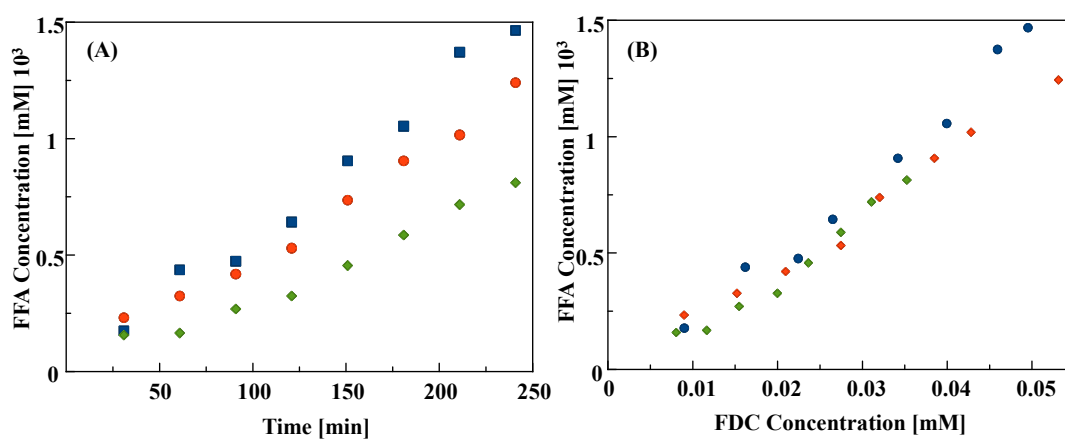
Figure S6. Evaluation of FFA concentration versus time (A) or versus the FDC concentration (B) during HMF photocatalytic partial oxidation runs carried out in the presence of MCN (■), UCN (●), and TuCN (◆) samples.
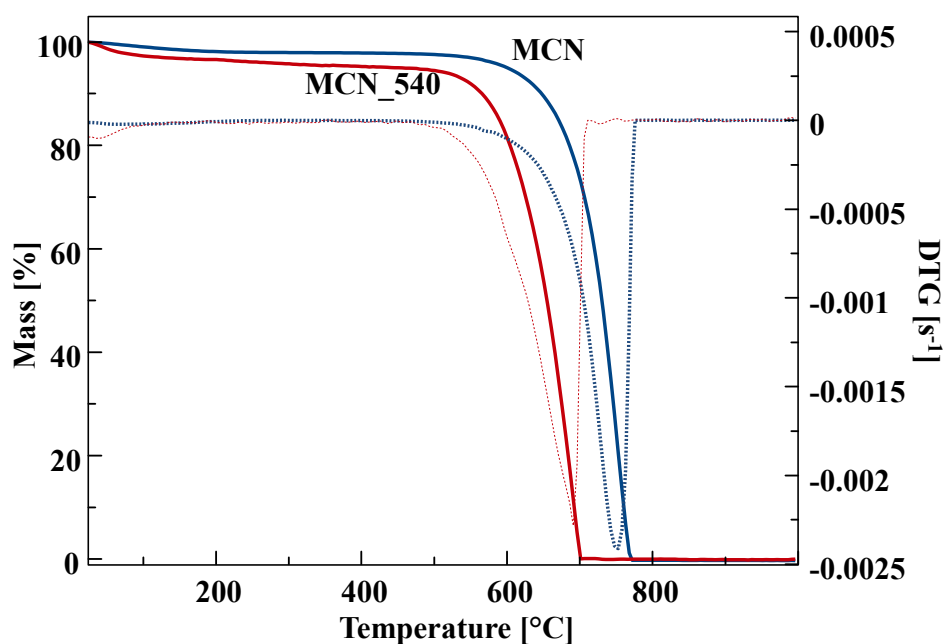
Figure S7. Thermogravimetric study of MCN and MCN_540 samples.
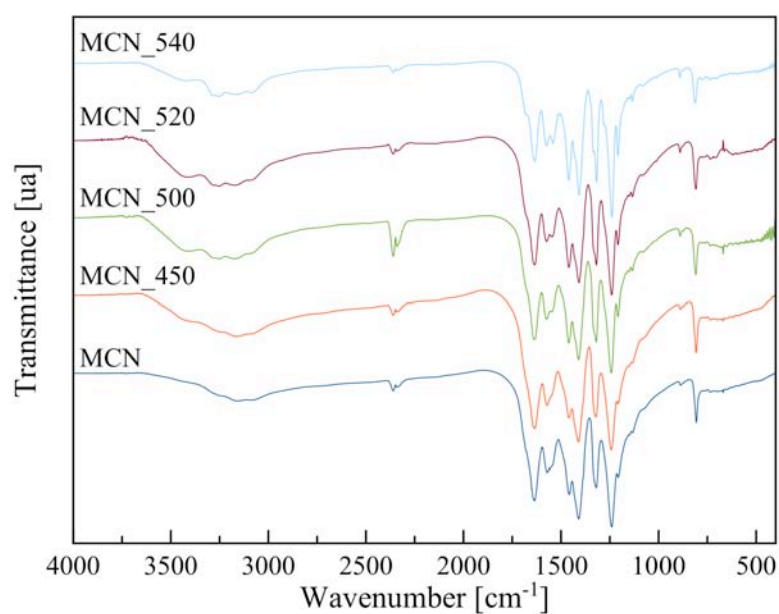
Figure S8. FTIR data of (—) MCN and thermally exfoliated (—) MCN_450, (—) MCN_500,

(—) MCN_520, and (—) MCN_540 samples.

Table S1. XPS deconvolution data

Peak position, eV	Assignment	HWHM				
		MCN	MCN_450	MCN_500	MCN_520	MCN_540
398.4	C-N=C	0.94	0.95	0.91	0.93	0.94
400.0	N(C)$_3$	0.79	0.76	0.87	0.96	1.0
401.1	C-N-H	0.82	0.75	0.8	0.86	1.5
Relative integrated peak intensity C-N=C / N(C)$_3$		1.64	1.86	1.85	1.96	3.54*
284.8	C-C	0.94	0.95	0.91	0.93	0.94
286.1	C-NH$_2$	0.79	0.76	0.87	0.96	1.0
288.0	N-C=N	0.82	0.75	0.8	0.86	1.5
289.7	C=O	0.88	0.78			
289.2	C-O			1.21	0.88	0.95

* an unrealistic value of the ratio of C-N=C/N(C)$_3$ integrated peak intensity is attributed to the enhanced contribution of some unknown nitrogen species, which also resulted in larger HWHM values
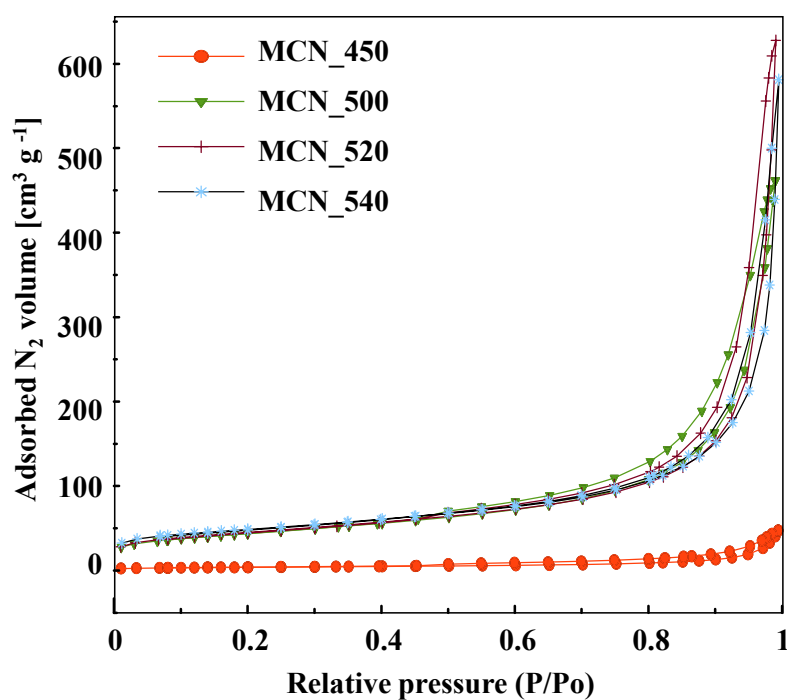
Figure S9. Adsorption-desorption N_2 isotherms obtained for the exfoliated (●) MCN_450, (▼) MCN_500, (+) MCN_520, and (*) MCN_540 g-C_3N_4 samples.
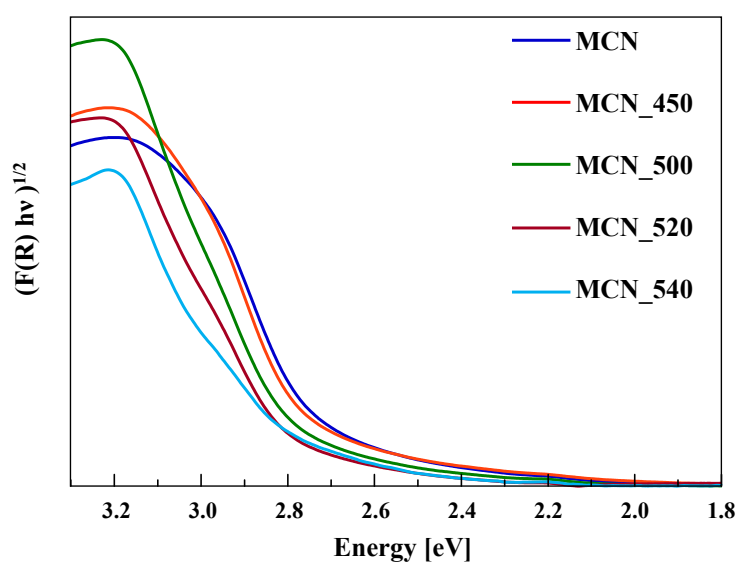
Figure S10. DR UV-vis spectra of the g-C_3N_4 and thermally exfoliated C_3N_4 samples
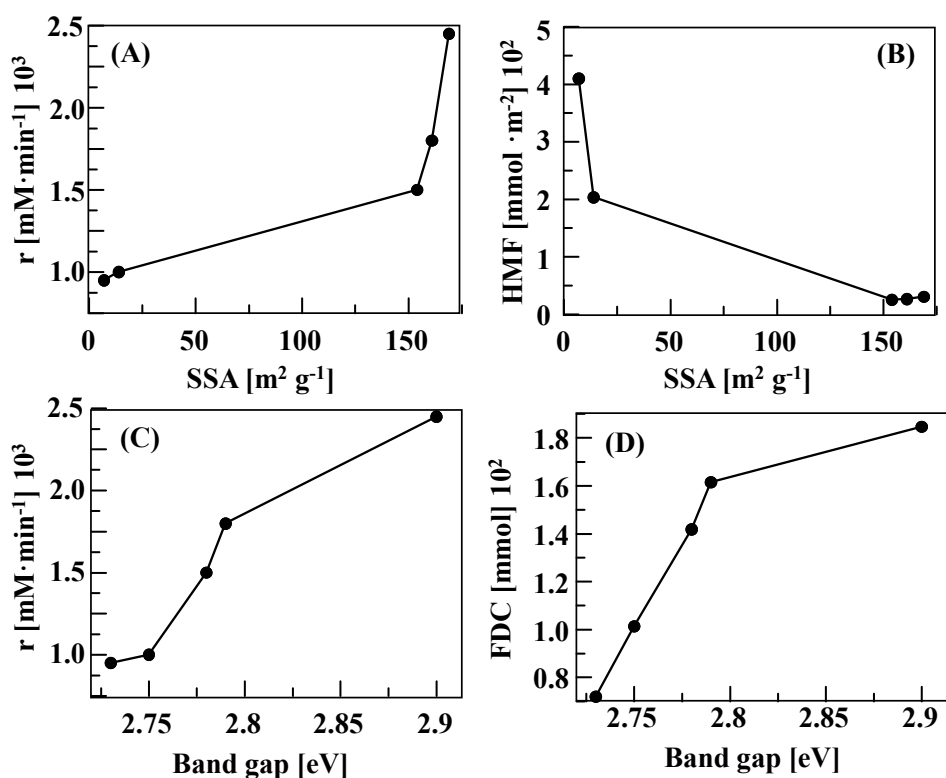
Figure S11. Correlation of SSA of the carbon nitride samples with the initial reaction rate (A) and with the HMF converted per m^2 of the photocatalyst (B). Correlation of the band gap energy of the carbon nitride samples with the HMF initial reaction rate (C), and FDC formation (D).
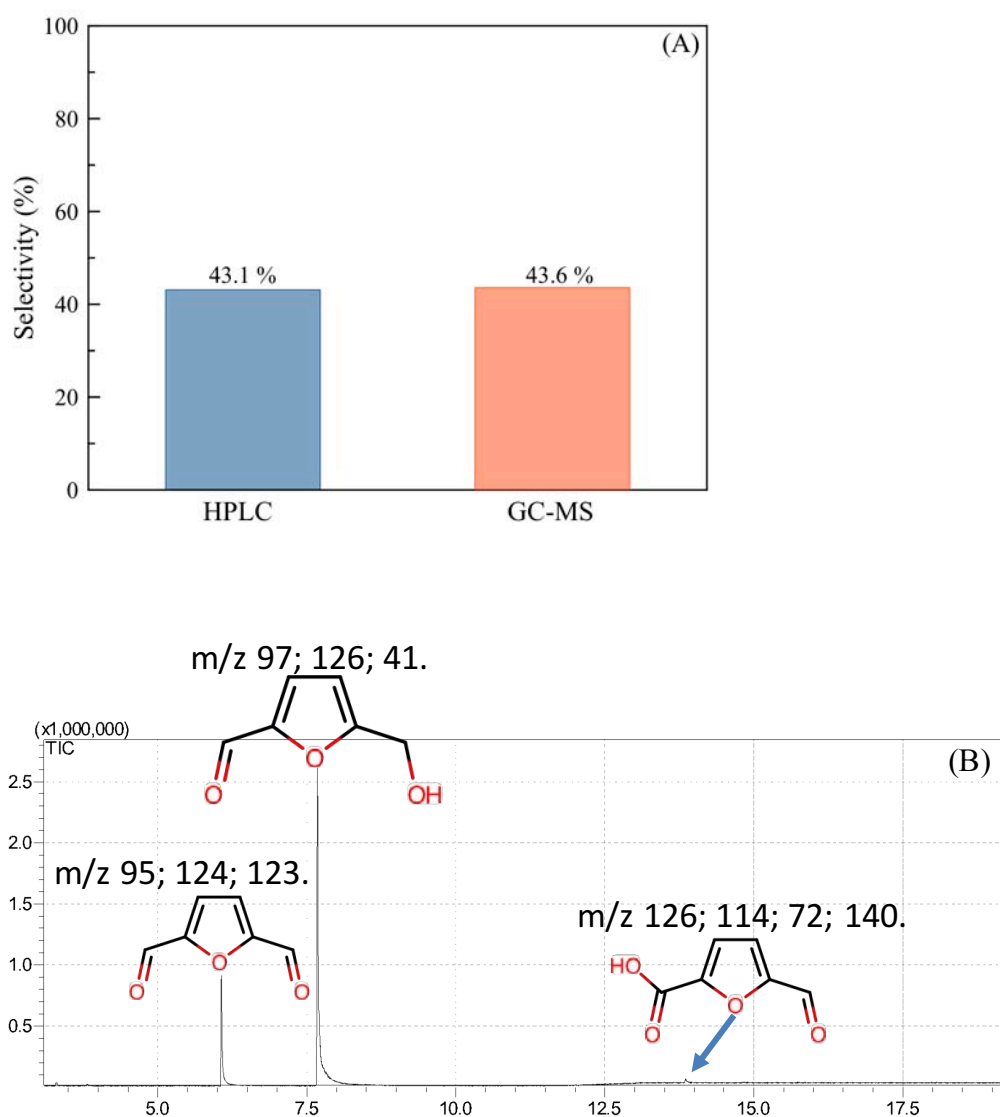
Figure S12. (A) Comparison of selectivity values for FDC formation obtained using HPLC and GC-MS techniques at 30 % of HMF conversion; (B) Identification of the HMF photooxidation reaction products by GC-MS method.
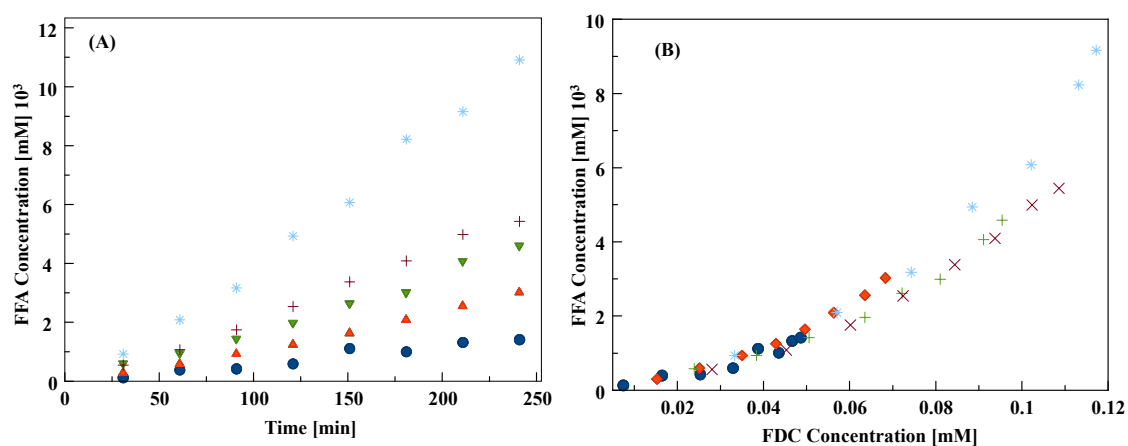
Figure S13. Evaluation of FFA concentration formed during the photocatalytic oxidation of HMF in the presence of the non exfoliated MCN (●), MCN_450 (▲), MCN_500 (▼), MCN_520 (+) and MCN_540 (*) (A) and concentration of FFA plotted versus the concentration of formed FDC in the reaction solution (B).
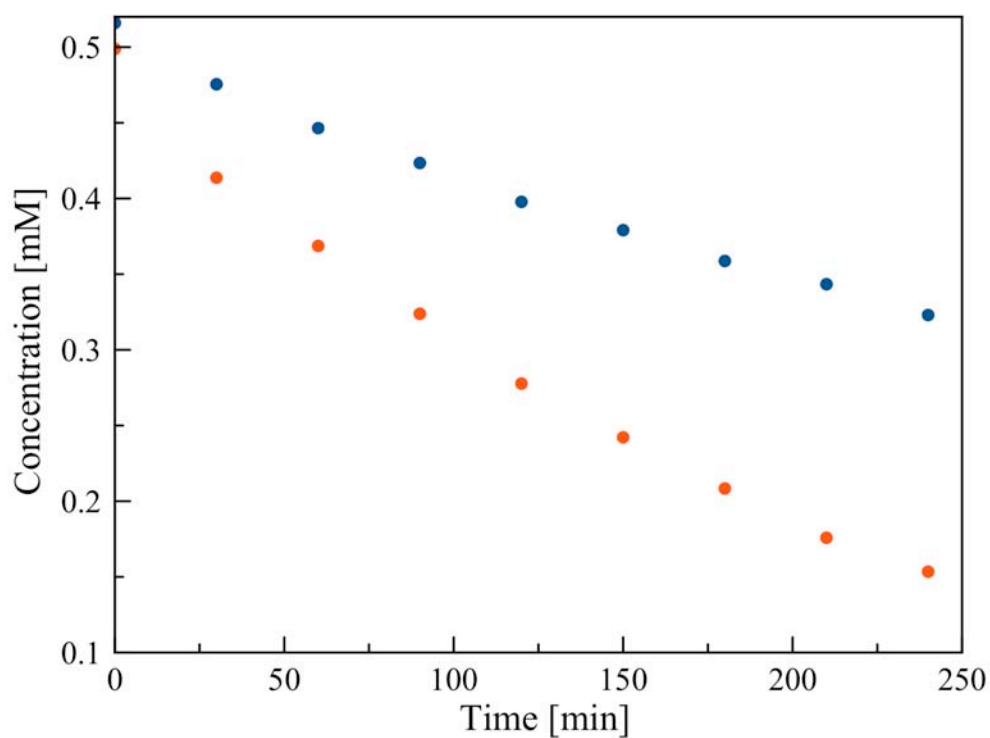
Figure S14. Photocatalytic decomposition of HMF (●) and FDC (●) over MCN_540.
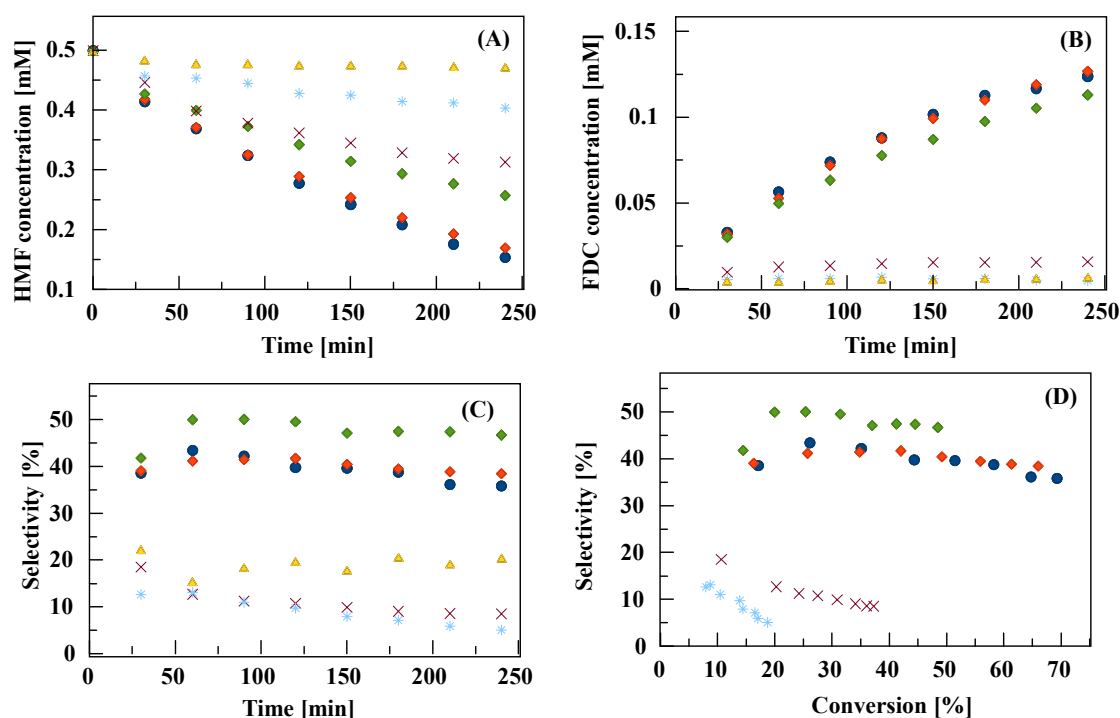
Figure S15. Effect of various scavengers on the photocatalytic conversion of HMF. MCN_540 in the absence of scavenger (●); t-BuOH (♦); NaCOOH (♦); p-benzoquinone (✗); N_2 (*); $CuCl_2/N_2$ (▲).

Stability tests of the material

The experimental procedure to test the material stability is reported in the following (MCN_520 was chosen as a representative sample). After the photocatalytic experiment described in the experimental section, the catalyst was left to settle and then the liquid was poured. Hence, water was added and the solid stirred for one hour and left to settle again

overnight. The liquid was poured and a solution of HMF 0.5 mM was added in the photoreactor to carry out the subsequent experiment. This procedure was repeated three times. Conversions and selectivities obtained in the runs are reported in Figure S16.
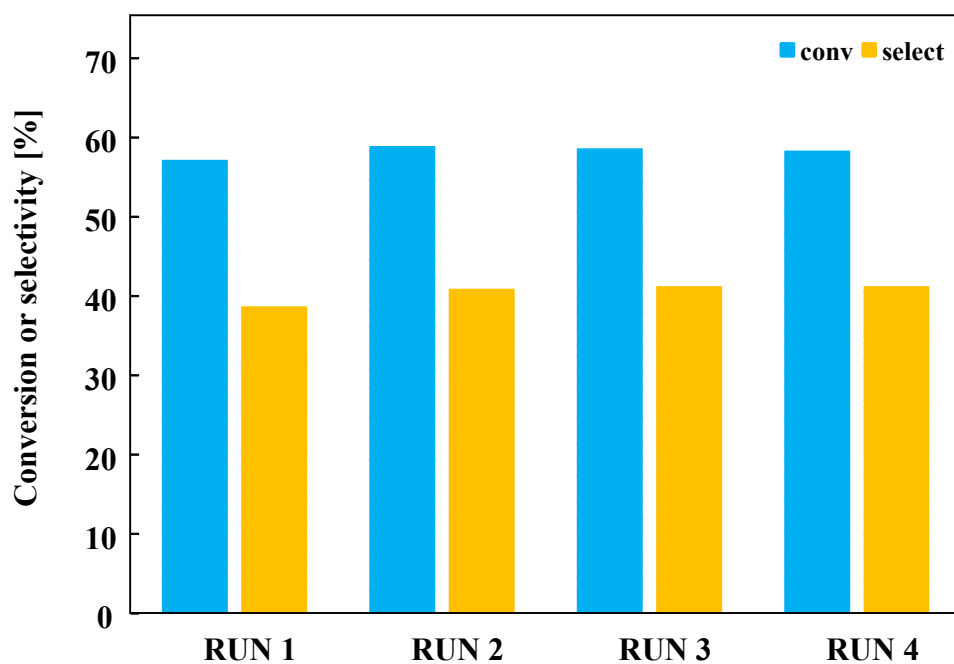
Figure S16. HMF conversion and the corresponding selectivity to FDC after 240 minutes of irradiation in the presence of MCN_520 by using the same powder.

Chapter 5   Conclusions

In the present Ph.D. Thesis, the methods of modification of the two most widespread photocatalysts TiO_2 and g-C_3N_4 via the synthetic as well as the post-synthetic approaches have been studied. It has been demonstrated that the rational design of the semiconductors' bulk and surface can tailor their photocatalytic properties toward better photo-degradation of organic pollutants in water medium or toward more efficient partial photo-oxidation of biomass platform molecules. Special attention has been paid to establish the relationship between the structural and surface properties of the materials with their photocatalytic performance in the photo-induced reactions.

1. With regard to the synthesis and photocatalytic application of silica-titania nanostructures:

    - A new two-step co-precipitation-hydrothermal procedure for the preparation of silica-titania nanoparticles using aqueous titanium peroxo complex and oligomeric silicic acid as sources of TiO_2 and SiO_2, respectively, has been developed.

    - In contrast to many conventional syntheses of SiO_2–TiO_2, silica in the developed method promotes titania crystal growth instead of supressing it, which is due to a low degree of Ti incorporation in SiO_2 and to the adsorption of silica species on the titania seeds separating them from each other, thus controlling the crystal growth.

    - The molar ratio of SiO_2 to TiO_2 equalling 0.4 in the mixed oxide is found to be the optimal for providing a uniform particle size distribution, and demonstrating the superior performance in photocatalytic decomposition of methylene blue under UV-irradiation.

- We attribute the enhanced photocatalytic activity of the synthesized mixed oxides in comparison to pure TiO_2 to the adsorption of methylene blue on the silanol groups belonging to the dispersed silica species located in the proximity of the crystalline anatase TiO_2 facilitating its subsequent decomposition.

2. With regard to the synthesis and photocatalytic application of thermally stable TiO_2 anatase nanoparticles:

  - A new solvent-exchange method for preparation of TiO_2 nanoparticles accomplished by the precipitation of hydrous titania from aqueous solution of ammonium peroxotitanate with organic solvent has been developed.

  - The prepared titania nanoparticles maintain high SSA of 34 $m^2 \, g^{-1}$ even after thermal treatment at 800 ℃.

  - The synthesized titania nanoparticles possess unprecedented thermal stability of anatase phase up to 1000 ℃. Even after thermal treatment at 1000 ℃ for 6 h the material is still composed of 60 % of anatase and 40% of rutile phases.

  - It has been confirmed by HR-TEM that the principal reason for the stabilization of a metastable anatase phase is the formation of defects in the titania nanostructure.

  - The photocatalytic activity of the prepared TiO_2 materials thermally treated at temperatures higher than 800 ℃ is superior to that of the commercial Aeroxide P25 photocatalyst treated at the same conditions.

  - The thermal stability of anatase up to the sintering temperatures, along with its high photocatalytic activity, offer new possibilities to prepare a wide range of self-cleaning and anti-bacterial TiO_2-based ceramic materials to meet medical and domestic needs.

3. With regard to the study of nitrogen-doped and oxygen-rich titania and their photocatalytic performance:

  - Detailed titanium local order investigation by applying XAS techniques has allowed us to reconsider the mechanism of the oxygen-rich titania formation.

- Thermal decomposition of ammonium peroxotitanate complex in the temperature range of 400–500 ℃ leads to the formation of nitrogen-doped TiO_2.

- Nitrogen has found to be present in the oxidised form in titania anatase structure and occupy interstitial positions located at a distance of 2.4 Å from the central Ti atom.

- The incorporation of nitrogen interstitials provokes the formation of oxygen vacancies in the first coordination shell of titanium.

- The nitrogen-dopants is removed if N-TiO_2 is treated at temperatures equal or higher than 600 ℃ in air. The elimination of the N-species causes a charge imbalance in the titanium environment, thus initiating the process of capture of atmospheric oxygen and formation of oxygen interstitial dopants.

- The incorporation of O_2 in titania provokes expansion of anatase crystallographic cell and increases the coordination number of Ti to 7 by forming peroxo-bridged oxygen species in the titanium environment.

- Nitrogen and oxygen interstitial dopants have a similar effect on the titania BG slightly reducing it to 3.10 eV in comparison to that of commercial titania anatase, which has BG of 3.20 eV. Apart from that, the presence of nitrogen interstitials causes formation of mid-gap states with energies of approximately 2.30 eV.

- Oxygen-rich titania demonstrate superior photo-degradation of *p*-cresol under UV-irradiation than its nitrogen-doped counterpart, while under visible light N-TiO_2 is found to be more efficient photocatalyst due to the presence of mid-gap states.

- Nitrogen-doped titania has found to be able to selectively oxidise HMF to FDC in water medium reaching the selectivity values in the range of 30% to 40%, while oxygen-rich TiO_2 tends to unselectively degrade the organic substrate.

- It has been proposed that the surface nitrogen species residing in N-TiO_2 suppress formation of hydroxyl radicals and adsorption of the reaction product

(FDC), thus contributing to higher selectivity in the partial photo-oxidation reaction.

4. With regard to the study of partial photo-oxidation of HMF to FDC using graphitic carbon nitride as photocatalyst:

- Among three most common carbon nitride precursors (melamine, urea, and thiourea), melamine has found to be the optimal choice due to higher yields of g-C_3N_4 obtained by its condensation and relatively high selectivity of HMF to FDC oxidation reaching 30% under UV irradiation.

- Thermal exfoliation of bulk g-C_3N_4 does not only lead to the enhancement of the rate of HMF conversion by a factor of 2.5, but also increases the selectivity for FDC production up to 43%.

- The selectivity increase observed for the thermally exfoliated carbon nitride is due to the partial elimination of uncondensed –NH_2 sites.

- The photocatalytic experiments under natural solar light irradiation have shown that, despite the band gap energy of the carbon nitride allows harvesting a small portion of visible light, the UV fraction of the solar spectrum contributed to a greater extent to the excitation of the photocatalytic material. It has also been observed that the exfoliated g-C_3N_4 shows even better activity and selectivity to FDC formation under real outdoor illumination, reaching 50% at 40% of HMF conversion in aqueous medium.

Conclusiones

En esta Tesis Doctoral se han desarrollado, aplicado y estudiado distintos métodos para la modificación de dos familias de foto-catalizadores, basadas en TiO_2 y $g\text{-}C_3N_4$ respectivamente, basados en medios sintéticos y tratamientos post-sintéticos. Se ha demostrado la influencia de las propiedades estructurales y texturales de los semiconductores en la optimización de sus propiedades foto-catalíticas en procesos de foto-degradación de contaminantes orgánicos en medio acuoso y de foto-oxidación parcial de moléculas plataforma derivadas de la biomasa, prestando atención especial a la búsqueda de conexiones entre las características estructurales y superficiales de los materiales y su actividad y selectividad en los procesos foto-catalíticos.

1. En lo que se refiere a la síntesis y aplicación foto-catalítica de nano-estructuras de sílica-titania:

   - Se ha desarrollado un nuevo método en dos etapas, que incluye la co-precipitación y el tratamiento hidrotermal, para obtener nanopartículas de sílica-titania, usando el complejo peróxido de titanio y ácido silícico oligomérico, como fuentes de TiO_2 y SiO_2, respectivamente.

   - En contraste con otros procedimientos convencionales para la síntesis de sistemas SiO_2–TiO_2, en el nuevo método, la sílica promueve el crecimiento de los cristales de la titania, como consecuencia del bajo nivel de incorporación de Ti en el SiO_2 y la presencia de especies de sílica en la superficie de los cristales de la titania, que controlan los procesos de la cristalización.

- Se ha establecido que el material de relación molar 0.4:1 (SiO_2:TiO_2) presenta una distribución de tamaño de partículas especialmente uniforme, mostrando la mayor actividad foto-catalítica de toda la serie en la degradación del azul de metileno bajo irradiación UV.

- El incremento de la actividad foto-catalítica observado en los materiales SiO_2–TiO_2, en comparación con la titania pura, se atribuye a la capacidad de adsorción del azul de metileno de los grupos hidroxilo de la sílica dispersa en las inmediaciones de anatasa cristalina.

2. En lo que se refiere a la síntesis y la aplicación foto-catalítica del TiO_2-anatasa térmicamente estable:

- Se ha descrito un nuevo método de intercambio de disolventes para la preparación de nano-partículas de TiO_2. La síntesis desarrollada implica la precipitación de titania hidratada desde una disolución acuosa de peroxotitanato de amonio, asistida por un disolvente orgánico.

- Las nanopartículas de titania obtenidas mantienen elevada área superficial específica (SSA = 34 m^2 g^{-1}) después de su tratamiento térmico a 800 ºC.

- Las nanoparticulas de titania sintetizadas poseen alta estabilidad térmica de la fase anatasa (después de tratamiento a 1000 ºC durante 6 horas, la relación anatasa:rutilo es 60:40).

- Estudios de microscopia electrónica de transmisión de alta resolución (HR-TEM) relacionan la estabilidad térmica de la fase metaestable (anatasa) con la existencia de defectos en la nano-estructura de la titania.

- Cuando la temperatura de tratamiento supera los 800 ºC, la actividad foto-catalítica de los nuevos materiales es superior a la del foto-catalizador comercial, Aeroxide P25, tratado en las mismas condiciones.

- El mantenimiento de la estabilidad térmica de la anatasa hasta temperaturas de sinterización, ofrece nuevas posibilidades para la preparación de materiales cerámicos basados en TiO_2 con actividad foto-catalítica y, por tanto, con propiedades auto-limpiantes y anti-bacterianas.

3. En lo que se refiere al estudio estructural de titania dopada con nitrógeno y titania oxigenada y sus propiedades foto-catalíticas:

- El estudio detallado del orden local utilizando métodos de espectroscopia de absorción de rayos X (XAS) ha permitido reconsiderar el mecanismo propuesto para la formación de titania oxigenada.

- La descomposición térmica del complejo de peroxotitanato de amonio en el rango de temperatura 400–500 ºC resulta en la formación de dióxido de titanio dopado con nitrógeno (N-TiO_2).

- El nitrógeno se incorpora a la estructura de la titania (anatasa) en forma oxidada, ocupando posiciones intersticiales a una distancia media de 2.4 Å del átomo Ti.

- La incorporación de nitrógeno intersticial en la titania produce vacantes de oxígeno en la primera esfera de coordinación del titanio.

- En aire, el tratamiento de N-TiO_2 a temperaturas superiores a los 600 ºC provoca la eliminación de las especies nitrogenadas, causando un desequilibrio de carga en el entorno del titanio, que propicia la captura de oxígeno atmosférico en los espacios intersticiales.

- La incorporación de especies O_2 a la titania provoca la expansión de la celdilla unidad de la anatasa y el aumento del número de coordinación del Ti hasta llegar a 7, con formación de puentes peroxo en su entorno.

- La separación de bandas (BG) de la titania se reduce (3.10 eV) en comparación con el valor característico de la titania (anatasa) comercial (3.20 eV) en muestras dopadas tanto con nitrógeno como con oxígeno. Además, la presencia de nitrógeno intersticial propicia la aparición de estados "mid-gap" con energías próximas a 2.30 eV.

- En comparación con las muestras N-TiO_2, la titania oxigenada presenta mayor actividad en la foto-degradación del *p*-cresol bajo radiación UV. Sin embargo, los estados "mid-gap" hacen que el foto-catalizador dopado con nitrógeno sea más eficiente bajo luz visible.

- La titania dopada con nitrógeno es capaz de oxidar selectivamente el 5-hidroximetil-2-furfural (HMF) hasta 2,5-furnadicarboxaldehido (FDC) en

medio acuoso, alcanzando selectividades del 30–40%. Por el contrario, el TiO_2 oxigenado degrada el sustrato no-selectivamente.

- Las especies nitrogenadas superficiales presentes en los materiales $N-TiO_2$ impiden la formación de radicales hidroxilo y la adsorción del producto de reacción (FDC), contribuyendo así a la alta selectividad en la reacción de foto-oxidación parcial.

4. En lo que se refiere al estudio de la foto-oxidación parcial del HMF hasta FDC utilizando nitruro de carbono grafitico ($g-C_3N_4$) como foto-catalizador:

- De los tres precursores más comunes del $g-C_3N_4$ (melamina, urea y tiourea), la melamina se ha mostrado como la mejor opción para la preparación de nitruro de carbono, proporcionando rendimientos satisfactorios y alta selectividad en la oxidación del HMF a FDC bajo irradiación UV.

- La exfoliación térmica del $g-C_3N_4$ genera un material más eficiente, con un notable incremento en el grado de conversión del HMF y un aumento en la selectividad hacia la producción de FDC.

- El aumento de selectividad observado en el nitruro de carbono exfoliado se atribuye a la eliminación parcial de fragmentos parcialmente condensados (grupos $-NH_2$).

- Bajo irradiación solar, el $g-C_3N_4$ exfoliado muestra una destacable actividad y selectividad en la obtención de FDC a partir de HMF, siendo la fracción UV del espectro la principal responsable de la excitación del material foto-catalítico, a causa de que el nitruro de carbono solo puede utilizar una pequeña porción de la luz visible.

References

1.   N. Serpone, A.V. Emeline, Suggested terms and definitions in photocatalysis and radiocatalysis, *Int. J. Photoenergy*, **2002**, 4, 91–131.

2.   C. Renz, Photoreactions of oxides of titanium, cerium and earth acids, *Helv. Chim. Acta*, **1921**, 4, 961–968.

3.   A. Fujishima, K. Honda, Electrochemical photolysis of water at a semiconductor electrode, *Nature*, **1972**, 238, 37–38.

4.   G. Knor, Recent progress in homogeneous multielectron transfer photocatalysis and artificial photosynthetic solar energy conversion, *Coordination Chem. Rev.* **2015**, 304-305, 102-108.

5.   Heterogeneous photocatalysis. From Fundamentals to Green Applications. Eds.: J.C. Colmenares, Y-J. Xu. Springer, **2016**.

6.   S. Banerjee, S.C. Pillai, P. Falaras, K.E. O'Shea, J.A. Byrne, D.D. Dionysiou, New insights into the mechanism of visible light photocatalysis, *J. Phys. Chem. Lett.* , **2014**, 5, 2543−2554.

7.   M.R. Hoffmann, S.T. Martin, W. Choi, D.W. Bahnemann, Environmental applications of semiconductor photocatalysis, *Chem. Rev.*, **1995**, 95, 69–96.

8.   T. Wu, G. Liu, J. Zhao, H. Hidaka, N. Serpone, Evidence for H_2O_2 generation during the TiO_2-assisted photodegradation of dyes in aqueous dispersions under visible light illumination, *J. Phys. Chem. B*, **1999**, 103, 4862–4867.

9.   T. Hirakawa, Y. Nosaka, Selective production of superoxide ions and hydrogen peroxide over nitrogen- and sulfur-doped TiO_2 photocatalysts with visible light in aqueous suspension systems, *J. Phys. Chem. C*, **2008**, 112, 15818–15823.

10. D. Tsukamoto, A. Shiro, Y. Shiraishi, Y. Sugano, S. Ichikawa, S. Tanaka, T. Hirai, Photocatalytic H_2O_2 production from ethanol/O_2 system using TiO_2 loaded with Au–Ag bimetallic alloy nanoparticles, *ACS Catal.*, **2012**, 2, 599–603.

11. M.A. Fox, M.T. Dulay. Heterogeneous photocatalysis, *Chem. Rev.*, **1993**, 93, 341–357.

12. C.S. Ong, W.J. Lau, P.S. Goh, B.C. Ng, A.F. Ismail, C.M. Choo, The impacts of various operating conditions on submerged membrane photocatalytic reactors (SMPR) for organic pollutant separation and degradation: A review, *RSC Adv.*, **2015**, 5, 97335–97348.

13. X. Wang, S. Blechert, M. Antonietti, Polymeric graphitic carbon nitride for heterogeneous photocatalysis, *ACS Catal.*, **2012**, 2, 1596−1606.

14. F.Z. Su, S.C. Mathey, G. Lipner, X.Z. Fu, M. Antonietti, S. Blechert, X.C. Wang, mpg-C_3N_4-catalyzed selective oxidation of alcohols using O_2 and visible light, *J. Am. Chem. Soc.,* **2010**, 132, 16299−16301.

15. S.G. Kumar, K.S.R.K. Rao, Polymorphic phase transition among the titania crystal structures in solution based approach: From precursor chemistry to nucleation process. *Nanoscale*, **2014**, 6, 11574−11632.

16. A.G. Dylla, G. Henkelman, K.J. Stevenson, Lithium insertion in nanostructured TiO_2(B) architectures, *Acc. Chem. Res.*, **2013**, 46, 1104–1112.

17. R. Marchard, L. Brochan, M. Tournoux, TiO_2(B) a new form of titanium dioxide and the potassium octatitanate $K_2Ti_8O_{17}$, *Mater. Res. Bull.*, **1980**, 15, 1129−1133.

18. H. Thi, T. Trana, H. Kosslicka, M.F. Ibada, C. Fischer, U. Bentrup, T.H. Vuong, L.Q. Nguyen, A. Schulz, Photocatalytic performance of highly active brookite in the degradation of hazardous organic compounds compared to anatase and rutile, *Appl. Catal. B: Environ.*, **2017**, 200, 647–658.

19. A. Di Paola, M. Bellardita, L. Palmisano, Brookite, the least known TiO_2 photocatalyst catalysts, *Catalyst,* **2013**, 3, 36−73.

20. T. Kotani, H.L. Tuller. Growth of TiO_2 single crystals and bicrystals by the laser-heated floating-zone method, *J. Am. Ceram. Soc.*, **1998**, 81, 592–596.

21. S.T. Aruna, S. Tirosh, A. Zaban, Nanosize rutile titania particle synthesis via a hydrothermal method without mineralizers, *J. Mater. Chem.*, **2000**, 10, 2388−2391.

22. W. Wang, B. Gu, L. Liang, W.A. Hamilton, D.J. Wesolowski, Synthesis of rutile (α-TiO$_2$) nanocrystals with controlled size and shape by low-temperature hydrolysis: Effects of solvent composition, *J. Phys. Chem. B*, **2004**, 108, 14789–14792.

23. L. Li, J. Yan, T. Wang, Z-J. Zhao, J. Zhang, J. Gong, N. Guan. Sub-10 nm rutile titanium dioxide nanoparticles for efficient visible-light-driven photocatalytic hydrogen production, *Nature Comm.*, **2015**, 6, 5881.

24. M. Krivec, R.A. Segundo, J.L. Faria, A.M.T. Silva, G. Dražić. Low-temperature synthesis and characterization of rutile nanoparticles with amorphous surface layer for photocatalytic degradation of caffeine*, Appl. Catal. B: Environ*., **2013**, 140–141, 9–15.

25. E. García-López, M. Addamo, A. Di Paola, G. Marcì, L. Palmisano. Preparation in mild conditions of photocatalytically active nanostructured TiO$_2$ rutile. *Stud. Surface Sci. Catal,*. **2006**, 162, 689–696.

26. A.S. Barnard, H. Xu. An environmentally sensitive phase map of titania nanocrystals, *ACS Nano*, **2008**, 2, 2237–2242

27. T. Luttrell, S. Halpegamage, J. Tao, A. Kramer, E. Sutter, M. Batzill. Why is anatase a better photocatalyst than rutile? Model studies on epitaxial TiO$_2$ films, *Sci. Reports,* **2014**, 4, 4043.

28. Y. Kakuma, A.Y. Nosaka, Y. Nosaka. Difference in TiO$_2$ photocatalytic mechanism between rutile and anatase studied by the detection of active oxygen and surface species in water, *Phys. Chem. Chem. Phys.*, **2015**, 17, 18691–18698.

29. M. Murdoch, G.I.N. Waterhouse, M.A. Nadeem, J.B. Metson, M.A. Keane, R.F. Howe, J. Llorca, H. Idriss. The effect of gold loading and particle size on photocatalytic hydrogen production from ethanol over Au/TiO$_2$ nanoparticles, *Nature Chem.,* **2013**, 3, 489–492.

30. D.C. Hurum, A.G. Agrios, K.A. Gray, T. Rajh, M.C. Thurnauer. Explaining the enhanced photocatalytic activity of Degussa P25 mixed-phase TiO$_2$ using EPR, *J. Phys. Chem. B*, **2003**, 107, 4545–4549.

31. D.O. Scanlon, C.W. Dunnill, J. Buckeridge, S.A. Shevlin, A.J. Logsdail, S.M. Woodley, C.R.A. Catlow, M.J. Powell, R.G. Palgrave, I.P. Parkin, G.W. Watson,

T.W. Keal, P. Sherwood, A. Walsh, A.A. Sokol. Band alignment of rutile and anatase TiO_2, *Nature Mater.*, **2013**, 12, 798–801.

32. Y. Mi, Y. Weng. Band alignment and controllable electron migration between rutile and anatase TiO_2, *Sci. Reports*, **2015**, 5, 11482.

33. I.K. Konstantinou, V.A Sakkas, T.A. Albanis. Photocatalytic degradation of the herbicides propanil and molinate over aqueous TiO_2 suspensions: Identification of intermediates and the reaction pathway, *Appl. Catal. B: Environ.*, **2001**, 227–239.

34. J.J. Testa, M.A. Grela, M.I. Litter. Heterogeneous photocatalytic reduction of chromium(VI) over TiO_2 particles in the presence of oxalate: Involvement of Cr(V) species, *Environ. Sci. Technol.*, **2004**, 38, 1589–1594.

35. Y.K. Kho, A. Iwase, W.Y. Teoh, L. Mädler, A. Kudo, R. Amal. Photocatalytic H_2 evolution over TiO_2 nanoparticles. The synergistic effect of anatase and rutile, *J. Phys. Chem. C*, **2010**, 114, 2821–2829.

36. A. Kubacka, M. Fernández-García, G. Colón. Advanced nanoarchitectures for solar photocatalytic applications, *Chem. Rev.*, **2012**, 112, 1555–1614.

37. K. Yan, G. Wu. Titanium dioxide microsphere-derived materials for solar fuel hydrogen generation. *ACS Sus. Chem. Eng.*, **2015**, 3, 779–791.

38. M. Cargnello, T.R. Gordon, C.B. Murray. Solution-phase synthesis of titanium dioxide nanoparticles and nanocrystals. *Chem. Rev.*, **2014**, 114, 9319–9345.

39. W. Li, Z. Wu, J. Wang, A.A. Elzatahry, D. Zhao. A perspective on mesoporous TiO_2 materials, *Chem. Mater.*, **2014**, 26, 287–298.

40. J. Tian, Z. Zhao, A. Kumar, R.I. Boughton, H. Liu. Recent progress in design, synthesis, and applications of one-dimensional TiO_2 nanostructured surface heterostructures: A review, *Chem. Soc. Rev.*, **2014**, 43, 6920–6937.

41. S. Ito, T.N. Murakami, P. Comte, P. Liska, C. Grätzel, M.K. Nazeeruddin, M. Grätzel. Fabrication of thin film dye sensitized solar cells with solar to electric power conversion efficiency over 10%, *Thin Solid Films*, **2008**, 516, 4613–4619.

42. G. Varshneya, S.R. Kanel, D.M. Kempisty, V. Varshney, A. Agrawal, E. Sahle-Demessie, R.S. Varma, M.N. Nadagoud. Nanoscale TiO_2 films and their application in remediation of organic pollutants, *Coordin. Chem. Rev.*, **2016**, 306, 43–64.

43.   S. Tanemura, L. Miao, W. Wunderlich, M. Tanemura, Y. Mori, S. Toh, K. Kaneko. Fabrication and characterization of anatase/rutile–TiO$_2$ thin films by magnetron sputtering: A review, *Sci. Technol. Adv. Mater.*, **2005**, 6, 11–17

44.   C. Quiñonez, W. Vallejo, G. Gordillo. Structural, optical and electrochemical properties of TiO$_2$ thin films grown by APCVD method, *Appl. Surf. Sci.*, **2010**, 256, 4065–4071.

45.   N. Arconadaa, A. Durán, S. Suárez, R. Portela, J.M. Coronado, B. Sánchez, Y. Castro. Synthesis and photocatalytic properties of dense and porous TiO$_2$-anatase thin films prepared by sol–gel, *Appl. Catal. B: Environ.*, **2009**, 86, 1–7.

46.   T. Oekermann, D. Zhang, T. Yoshida, H. Minoura. Electron transport and back reaction in nanocrystalline TiO$_2$ films prepared by hydrothermal crystallization, *J. Phys. Chem. B*, **2004**, 108, 2227–2235.

47.   E.J. Mezey, Pigments and reinforcing agents in Vapor Deposition, C.F Powell, J.H Oxley, J.M Blocher Jr. (Eds.), Wiley, New York, **1960**, 423‑451.

48.   P. Stamatakis, C.A Natalie, B.R Palmer, W.A Yuill. Research needs in aerosol processing, *Aerosol Sci. Technol.*, **1991,** 14, 316‑321.

49.   A.M Thayer. Titanium dioxide, *Chem. Eng. News*, **1998**, 9, 10–13.

50.   S.E. Pratsinisa, P.T. Spicer. Competition between gas phase and surface oxidation of TiCl$_4$ during synthesis of TiO$_2$ particles, *Chem. Eng. Sci.*, **1998**, 53, 1861–1868.

51.   Z. Seeley, Y.J. Choi, S. Bose. Citrate–nitrate synthesis of nano-structured titanium dioxide ceramics for gas sensors, *Sens. Actuator. B: Chem.*, **2009**, 140, 98–103.

52.   R. Menzel, B.F. Cottam, S. Ziemian, M.S.P. Shaffer. Two-stage, non-hydrolytic synthesis for improved control TiO$_2$ nanorod formation, *J. Mater. Chem.*, **2012**, 22, 12172–12178.

53.   J. Joo, S.G. Kwon, T. Yu, M. Cho, J. Lee, J. Yoon, T. Hyeon. Large-scale synthesis of TiO$_2$ nanorods via nonhydrolytic sol–gel ester elimination reaction and their application to photocatalytic inactivation of E. coli, *J. Phys. Chem. B*, **2005**, 109, 15297–15302.

54. R. Tanner, Y. Liang, E.I. Altman. Structure and chemical reactivity of adsorbed carboxylic acids on anatase TiO$_2$(001), *Surf. Sci.*, **2002**, 506, 251–271.

55. P.D. Cozzoli, A. Kornowski, H. Weller. Low-temperature synthesis of soluble and processable organic-capped anatase TiO$_2$ nanorods, *J. Am. Chem. Soc.*, **2003**, 125, 14539–14548.

56. Sol-gel science: The physics and chemistry of sol-gel processing. Eds.: C.J. Brinker, G.W. Scherrer. Academic Press. Boston, **1990,** 908**.**

57. C.-C. Wang, J.Y. Ying. Sol-gel synthesis and hydrothermal processing of anatase and rutile titania anocrystals, *Chem. Mater.*, **1999**, 11, 3113–3120.

58. S. Sahni, S.B. Reddy, B.S. Murty. Influence of process parameters on the synthesis of nano-titania by sol–gel route, *Mater. Sci. Eng.: A.,* **2007**, 452–453, 758–762.

59. M. Kakihana, M. Kobayashi, K. Tomita, V. Petrykin. Application of water-soluble titanium complexes as precursors for synthesis of titanium-containing oxides via aqueous solution processes, *Bull. Chem. Soc. Jpn.*, **2010**, 83, 1285–1308.

60. K. Tomita, V. Petrykin, M. Kobayashi, M. Shiro, M. Yoshimura, M. Kakihana. A water-soluble titanium complex for the selective synthesis of nanocrystalline brookite, rutile, and anatase by a hydrothermal method, *Angew. Chem.* **2006**, 188, 2438–2441.

61. Y. Zhang, L. Wu, Q. Zheng, J. Zhi. An approach for controllable synthesis of different-phase titanium dioxide nanocomposites with peroxotitanium complex as precursor, *J. Phys. Chem. C*, **2008**, 112, 16457–16462.

62. N. Murakami, Y. Kurihara, T. Tsubota, T. Ohno. Shape-controlled anatase titanium(IV) oxide particles prepared by hydrothermal treatment of peroxo titanic acid in the presence of polyvinyl alcohol, *J. Phys. Chem. C*, **2009**, 113, 3062–3069.

63. J.A. Chang, M. Vithal, I.C. Baek, S.I. Seok. Morphological and phase evolution of TiO$_2$ nanocrystals prepared from peroxotitanate complex aqueous solution: Influence of acetic acid, *J. Solid State Chem.*, **2009**, 182, 749–756.

64. V.R. De Mendoca, C. Ribeiro. Influence of TiO$_2$ morphological parameters in dye photodegradation: A comparative study in peroxo-based synthesis, *Appl. Catal. B: Environ.*, **2011**, 105, 298–305.

65. Y. Miao, J. Gao. Preparation of {010}-faceted anatase TiO$_2$ nanocuboids from peroxotitanium complex solution, *J. Solid State Chem.* **2012**, 196, 372–378.

66. M. Kobayashi, V. Petrykin, K. Tomita, M. Kakihana. Hydrothermal synthesis of brookite-type titanium dioxide with snowflake-like nanostructures using a water-soluble citratoperoxotitanate complex, *J. Cryst. Growth*, **2011**, 337, 30–37.

67. S. Jeon, P.V. Braun. Hydrothermal synthesis of Er-doped luminescent TiO_2 nanoparticles, *Chem. Mater.*, **2003**, 15, 1256–1263.

68. Y.V. Kolenko, K.A. Kovnir, A.I. Gavrilov, A.V. Garshev, J. Frantti, O.I. Lebedev, B.R. Churagulov, G. Van Tendeloo, M. Yoshimura. Hydrothermal synthesis and characterization of nanorods of various titanates and titanium dioxide, *J. Phys. Chem. B*, **2006**, 110, 4030–4038.

69. Á. Kukovecz, M. Hodos, E. Horváth, G. Radnóczi, Z. Kónya, I. Kiricsi. Oriented crystal growth model explains the formation of titania nanotubes, *J. Phys. Chem. B*, **2005**, 109, 17781–17783.

70. C.-C. Chung, T.-W. Chung, T. C.-K. Yang. Rapid synthesis of titania nanowires by microwave-assisted hydrothermal treatments, *Ind. Eng. Chem. Res.*, **2008**, 47, 2301–2307.

71. J-Q. Huang, Z. Huang, W. Guo, M.-l. Wang, Y-g. Cao, M-c. Hong. Facile synthesis of titanate nanoflowers by a hydrothermal route, *Cryst. Growth Des.*, **2008**, 8, 2444–2446.

72. S. Liu, J. Yu, M. Jaroniec. Anatase TiO_2 with dominant high-energy {001} facets: Synthesis, properties, and applications, *Chem. Mater.*, **2011**, 23, 4085–4093.

73. M. Hirano, K. Ota, H. Iwata. Direct formation of anatase (TiO_2) / silica (SiO_2) composite nanoparticles with high phase stability of 1300 °C from acidic solution by hydrolysis under hydrothermal condition, *Chem. Mater.*, **2004**, 16, 3725–3732.

74. J-Y. Kim, C-S. Kim, H-K. Chang, T-O. Kim. Effects of ZrO_2 addition on phase stability and photocatalytic activity of ZrO_2/TiO_2 nanoparticles, *Adv. Powder Technol.*, **2010**, 21, 141–144.

75. C. Anderson, A.J. Bard. Improved photocatalytic activity and characterization of mixed TiO_2/SiO_2 and TiO_2/Al_2O_3 materials, *J. Phys. Chem. B*, **1997**, 101, 2611–2616.

76. M.S.P. Francisco, V.R. Mastelaro. Inhibition of the anatase-rutile phase transformation with addition of CeO_2 to CuO-TiO_2 system: Raman spectroscopy, X-ray diffraction, and textural studies, *Chem. Mater.*, **2002**, 14, 2514–2518.

77. G. Marcì, L. Palmisano, A. Sclafani, A. M. Venezia, R. Campostrini, G. Carturan, C. Martín, V. Rives, G. Solana. Influence of tungsten oxide on structural and surface properties of sol–gel prepared TiO_2 employed for 4-nitrophenol photodegradation, *J. Chem. Soc., Faraday Trans.,* **1996**, 92, 819–829.

78. Y.T. Kwon, K.Y. Song, W. I. Lee, G. J. Choi, Y.R. Do. Photocatalytic behavior of WO_3-loaded TiO_2 in an oxidation reaction, *J. Catal.*, **2000**, 191, 192–199.

79. V. Puddu, R. Mokaya, G. Li Puma. Novel one step hydrothermal synthesis of TiO_2/WO_3 nanocomposites with enhanced photocatalytic activity. *Chem. Commun.,* **2007**, 45, 4749–4751.

80. A. Di Paola, G. Marcì, L. Palmisano, M. Schiavello, K. Uosaki, S. Ikeda, B. Ohtani. Preparation of polycrystalline TiO_2 photocatalysts impregnated with various transition metal ions: Characterization and photocatalytic activity for the degradation of 4-nitrophenol, *J. Phys. Chem. B*, **2002**, 106, 637–645

81. A. Kubacka, A. Fuerte, A. Martínez-Arias, M. Fernández-García. Nanosized Ti–V mixed oxides: Effect of doping level in the photo-catalytic degradation of toluene using sunlight-type excitation, *Appl. Catal. B: Environ.*, **2007**, 74, 26–33.

82. M. Lu, C. Shao, K. Wang, N. Lu, X. Zhang, P. Zhang, M. Zhang, X. Li, Y. Liu. p- MoO_3 nanostructures/n-TiO_2 nanofiber heterojunctions: Controlled fabrication and enhanced photocatalytic properties, *ACS Appl. Mater. Interfaces,* **2014**, 6, 9004–9012.

83. F. Galindo-Fernández, R. Gómez. Degradation of the herbicide 2,4-dichlorophenoxyacetic acid over TiO_2–CeO_2 sol–gel photocatalysts: Effect of the annealing temperature on the photoactivity, *J. Photochem. Photobiol. A: Chem.,* **2011**, 217, 383–388.

84. H.S. Kibombo, R. Peng, S. Rasalingam, R.T. Koodali. Versatility of heterogeneous photocatalysis: Synthetic methodologies epitomizing the role of silica support in TiO_2 based mixed oxides, *Catal. Sci. Technol.*, **2012**, 2, 1737–1766.

85. G. Liu, Y. Liu, G. Yang, S. Li, Y. Zu, W. Zhang, M. Jia. Preparation of titania–silica mixed oxides by a sol–gel route in the presence of citric acid, *J. Phys. Chem. C*, **2009**, 113, 9345–9351.

86. R.J. Davis, Z. Liu. Titania–silica: A model binary oxide catalyst system, *Chem. Mater.*, **1997**, 9, 2311–2324.

87. V. Torma, H. Peterlik, U. Bauer, W. Rupp, N. Husing, S. Bernstorff, M. Steinhart, G. Goerigk, U. Schubert. Mixed silica titania materials prepared from a single-source sol–gel precursor: A time-resolved SAXS study of the gelation, aging, supercritical drying, and calcination processes, *Chem. Mater.*, **2005**, 17, 3146–3153.

88. B.E. Yoldas. Formation of titania-silica glasses by low temperature chemical polymerization, *J. Non-Cryst. Solids*, **1980**, 38–39, 81–86.

89. V.G. Kessler. Aqueous route to TiO_2-based nanomaterials using pH-neutral carboxylate precursors, *J. Sol–Gel. Sci. Technol.*, **2013**, 68, 464–470.

90. I.V. Krivtsov, M.V. Ilkaeva, V.D. Samokhina, V.V. Avdin, S.A. Khainakov, D.A. Uchaev, J.R. Garcia. Synthesis of silica–titania composite oxide via "green" aqueous peroxo-route, *J. Sol–Gel. Sci. Technol.*, **2013**, 67, 665–669.

91. E. Pabon, J. Retuert, R. Quijada, A. Zarate. TiO_2–SiO_2 mixed oxides prepared by a combined sol–gel and polymer inclusion method, *Micropor. Mesopor. Mater.*, **2004**, 67, 195–203.

92. E. Borgarello, J. Kiwi, M. Gratzel, E. Pelizzetti, M. Visca. Visible light induced water cleavage in colloidal solutions of chromium-doped titanium dioxide particles, *J. Am. Chem. Soc.*, **1982**, 104, 2996–3002.

93. Z. Li, B. Hou, Y. Xu, D. Wu, Y. Sun, W. Hu, F. Deng. Comparative study of sol–gel-hydrothermal and sol–gel synthesis of titania–silica composite nanoparticles, *J. Solid State Chem.*, **2005**, 178, 1395–1405.

94. Z.Y. Wu, Y.F. Tao, Z. Lin, L. Liu, X.X. Fan, Y. Wang. Hydrothermal synthesis and morphological evolution of mesoporous titania–silica, *J. Phys. Chem. C*, **2009**, 113, 20335–20348.

95. B. Mahltig, E. Gutmann, D.C. Meyer. Solvothermal preparation of nanocrystalline anatase containing TiO_2 and TiO_2/SiO_2 coating agents for application of photocatalytic treatments, *Mater. Chem. Phys.*, **2011**, 127, 285–291.

96. V. Etacheri, C. Di Valentin, J. Schneider, D. Bahnemann, S.C. Pillai. Visible-light activation of TiO_2 photocatalysts: Advances in theory and experiments, *J. Photochem. Photobiol. C: Photochem. Rev.*, **2015**, 25, 1–29.

97. C. Di Valentin, G. Pacchioni. Trends in non-metal doping of anatase TiO_2: B, C, N and F, *Catal. Today.*, **2013**, 206, 12–18.

98. M. Peláez, N.T. Nolan, S.C. Pillai, M.K. Seery, P. Falaras, A.G. Kontos, P.S.M. Dunlop, J.W.J. Hamilton, J.A. Byrne, K. O'Shea, M.H. Entezari, D.D. Dionysiou. A review on the visible light active titanium dioxide photocatalysts for environmental applications, *Appl. Catal. B: Environ.*, **2012**, 125, 331–349.

99. L.G. Devi, R. Kavitha. A review on non-metal ion doped titania for the photocatalytic degradation of organic pollutants under UV/solar light: Role of photogenerated charge carrier dynamics in enhancing the activity, *Appl. Catal. B: Environ.*, **2013**, 140–141, 559–587.

100. C. Di Valentin, E. Finazzi, G. Pacchioni, A. Selloni, S. Livraghi, M.C. Paganini, E. Giamello. N-doped TiO_2: Theory and experiment, *Chem. Phys.,* **2007**, 339, 44-56.

101. N. Serpone. Is the band gap of pristine TiO_2 narrowed by anion- and cation-doping of titanium dioxide in second-generation photocatalysts? *J. Phys. Chem. B*, **2006**, 110, 24287-24293

102. J.C. Yu, W. Ho, J. Yu, H. Yip, P.K. Wong, J. Zhao. Efficient visible-light-induced photocatalytic disinfection on sulfur-doped nanocrystalline titania, *Environ. Sci. Technol.,* **2005**, 39, 1175–1179.

103. Y. Nosaka, M. Matsushita, J. Nishino, A.Y. Nosaka. Nitrogen-doped titanium dioxide photocatalysts for visible response prepared by using organic compounds, *Sci. Technol. Adv. Mater.*, **2005**, 6, 143–148.

104. J. Wang, D.N. Tafen, J.P. Lewis, Z. Hong, A. Manivannan, M. Zhi, M. Li, N. Wu. Origin of photocatalytic activity of nitrogen-doped TiO_2 nanobelts, *J. Am. Cchem. Soc.*, **2009**, 131, 12290–12297.

105. Y. Kuroda, T. Mori, K. Yagi, N. Makihata, Y. Kawahara, M. Nagao, S. Kittaka. Preparation of visible-light-responsive TiO_2-xNx photocatalyst by a sol-gel method: Analysis of the active center on TiO_2 that reacts with NH_3, *Langmuir*, **2005**, 21, 8026−8034.

106. C. Belver, R. Bellod, A. Fuerte, M. Fernández-García. Nitrogen-containing TiO_2 photocatalysts. Part 1. Synthesis and solid characterization, *Appl. Catal. B.: Environ.,* **2006**, 65, 301−308.

107. C. Belver, R. Bellod, S.J. Stewart, F.G. Requejo, M. Fernández-García. Nitrogen-containing TiO_2 photocatalysts. Part 2. Photocatalytic behaviour under sunlight excitation, *Appl. Catal. B.: Environ.*, **2006**, 65, 309−314.

108. R. Asahi, T. Morikawa, H. Irie, T. Ohwaki. Nitrogen-doped titanium dioxide as visible-light-sensitive photocatalyst: Designs, developments, and prospects, *Chem. Rev.*, **2014**, 114, 9824−9852.

109. T. Morikawa, R. Asahi, T. Ohwaki, K. Aoki, Y. Taga. Band-gap narrowing of titanium dioxide by nitrogen doping, *Jpn. J. Appl. Phys.*, **2001**, 40, L561–L563.

110. H. Irie, Y. Watanabe, K. Hashimoto. Nitrogen-concentration dependence on photocatalytic activity of $TiO_{2-x}N_x$ powders, *J. Phys. Chem. B*, **2003**, 107, 5483–5486.

111. C.H. Shin, G. Bugli, G.J. Djegamariadassou. Preparation and characterization of titanium oxynitrides with high specific surface areas, *Solid State Chem.,* **1991**, 95, 145–155.

112. S. Yin, Q.W. Zhang, F. Saito, T. Sato. Preparation of visible light-activated titania photocatalyst by mechanochemical method, *Chem. Lett.*, **2003**, 32, 358–359.

113. S. Yin, H. Yamaki, M. Komatsu, Q.W. Zhang, J.S. Wang, Q. Tang, F Saito, T.J. Sato. Preparation of nitrogen-doped titania with high visible light induced photocatalytic activity by mechanochemical reaction of titania and hexamethylenetetramine, *Mater. Chem.*, **2003**, 13, 2996–3001.

114. D. Mitoraj, R. Beránek, H. Kisch. Mechanism of aerobic visible light formic acid oxidation catalyzed by poly(tri-s-triazine) modified titania, *Photochem. Photobiol. Sci.,* **2010**, 9, 31-38.

115. S. Livraghi, M.C. Paganini, E. Giamello, A. Selloni, C. Di Valentin, G.J. Pacchioni. Origin of photoactivity of nitrogen-doped titanium dioxide under visible light, *J. Am. Chem. Soc.,* **2006**, 128, 15666–15671.

116. J.L. Gole, J.D. Stout, C. Burda, Y.B. Lou, X.B. Chen. Highly efficient formation of visible light tunable $TiO_{2-x}N_x$ photocatalysts and their transformation at the nanoscale, *J. Phys. Chem. B*, **2004**, 108, 1230–1240.

117. D. Wu, M. Long, W. Cai, C. Chen, Y. Wu. Low temperature hydrothermal synthesis of N-doped TiO_2 photocatalyst with high visible-light activity, *J. Alloy Compound.*, **2010**, 502, 289–294

118. H. Zhang, J.F. Banfield. Thermodynamic analysis of phase stability of nanocrystalline titania, *J. Mater. Chem.,* **1998**, 8, 2073−2076.

119. M. Machida, K. Norimoto, T. Kimura, Antibacterial activity of photocatalytic titanium dioxide thin films with photodeposited silver on the surface of sanitary ware, *J. Am. Ceram. Soc.*, **2005**, 88, 95−100.

120. A. Beltrán, L. Gracia, J. Andrés. Density functional theory study of the brookite surfaces and phase transitions between natural titania polymorphs, *J. Phys. Chem. B*, **2006**, 110, 23417−23423.

121. J. Muscat, V. Swamy, N.M. Harrison. First-principles calculations of the phase stability of TiO_2, *Phys. Rev. B,* **2002**, 65, 224112

122. M. Batzill, E.H. Morales, U. Diebold. Influence of nitrogen doping on the defect formation and surface properties of TiO_2 rutile and anatase, *Phys. Rev. Lett.*, **2006**, 96, 26103.

123. R.D. Shannon, J.A. Pask. Kinetics of the anatase-rutile transformation, *J. Am. Ceram. Soc.*, **1965**, 48, 391-398.

124. J. Craido, C. Real. Mechanism of the inhibiting effect of phosphate on the anatase → rutile transformation induced by thermal and mechanical treatment of TiO_2, *J. Chem. Soc. Faraday. Trans.*, **1983**, 79, 2765

125. C. Rao, A.G. Turner, J.M. Honeg. Some observations concerning the effect of impurities on the anatase-rutile transition, *Phys. Chem. Solids.*, **1959**, 11, 173.

126. S. Riyas, G. Krishnan, P.N. Mohandas. Anatase–rutile transformation in doped titania under argon and hydrogen atmospheres, *Adv. Appl. Ceram.*, **2007**, 106, 255-264.

127. Transition metal oxides: an introduction to their electronic structure and properties. Ed.: Cox PA, Clarendon Press, Oxford, **1992**.

128. W. Li, Y. Bai, C. Liu, Z. Yang, X. Feng, X. Lu, N.K. Van der Laak, K.Y. Chan. Highly thermal stable and highly crystalline anatase TiO_2 for photocatalysis, *Environ. Sci. Technol.*, **2009**, 43, 5423–5428.

129. Y. Mao, S.S. Wong. Size- and shape-dependent transformation of nanosized titanate into analogous anatase titania nanostructures, *J. Am. Chem. Soc.*, **2006**, 128, 8217–8226.

130. J. Choi, H. Park, M.R. Hoffmann. Effects of single metal-ion. Doping on the visible-light photoreactivity of TiO_2, *J. Phys. Chem. C*, **2010**, 114, 783−792.

131. K. Nagaveni, M.S. Hegde, G. Madras. Structure and photocatalytic activity of $Ti_{1-x}M_xO_{2\pm\delta}$ (M = W, V, Ce, Zr, Fe, and Cu) synthesized by solution combustion method, *J. Phys. Chem. B*, **2004**, 108, 20204–20212.

132. S.C. Padmanabhan, S.C. Pillai, J. Colreavy, S. Balakrishnan, D.E. McCormack, T.S. Perova, Y. Gun'ko, S.J. Hinder, J.M. Kelly. A simple sol−gel processing for the development of high-temperature stable photoactive anatase titania, *Chem. Mater.*, **2007**, 19, 4474–4481.

133. P. Periyat, S.C. Pillai, D.E. McCormack, J. Colreavy, S.J. Hinder. Improved high-temperature stability and sun-light-driven photocatalytic activity of sulfur-doped anatase TiO_2, *J. Phys.Chem. C*, **2008**, 112, 7644–7652.

134. S.C. Pillai, P. Periyat, R. George, D.E. McCormack, M.K. Seery, H. Hayden, J. Colreavy, D. Corr, S.J. Hinder, Synthesis of high-temperature stable anatase TiO_2 photocatalyst, *J. Phys. Chem. C*, **2007**, 111, 1605–1611.

135. J.V. Liebig, *Ann. Pharm.*, **1834**, 10, 10.

136. D.M. Teter, R.J. Hemley. Low-compressibility carbon nitrides, *Science*, **1996**, 271, 53–55.

137. D.C. Nesting, J.V. Badding. High-pressure synthesis of sp^2-bonded carbon nitrides, *Chem. Mater.* **1996**, 8, 1535–1539.

138. X. Wang, S. Blechert, M. Antonietti. Polymeric graphitic carbon nitride for heterogeneous photocatalysis, *ACS Catal.*, **2012**, 2, 1596−1606.

139. Y.J. Cui, Z.X. Ding, P. Liu, M. Antonietti, X.Z. Fu, X.C. Wang. Metal-free activation of H_2O_2 by g-C_3N_4 under visible light irradiation for the degradation of organic pollutants, *Phys. Chem. Chem. Phys*, **2012**, 14, 1455−1462.

140. F. Dong, L. Wu, Y. Sun, M. Fu, Z. Wu, S.C. Lee. Efficient synthesis of polymeric g-C_3N_4 layered materials as novel efficient visible light driven photocatalysts, *J. Mater. Chem.*, **2011**, 21, 15171–15174.

141. G. Zhang, J. Zhang, M. Zhang, X. Wang. Polycondensation of thiourea into carbon nitride semiconductors as visible light photocatalysts, *J. Mater. Chem.*, **2012**, 22, 8083–8091.

142. J. Liu, T. Zhang, Z. Wang, G. Dawson, W. Chen. Simple pyrolysis of urea into graphitic carbon nitride with recyclable adsorption and photocatalytic activity, *J. Mater. Chem.,* **2011**, 21, 14398–14401.

143. S.C. Yan, Z.S. Li, Z.G. Zou. Photodegradation performance of g-C_3N_4 fabricated by directly heating melamine, *Langmuir,* **2009**, 25, 10397–10401.

144. V.N. Khabashesku, J.L. Zimmerman, J.L. Margrave. Powder synthesis and characterization of amorphous carbon nitride, *Chem. Mater.,* **2000**, 12, 3264–3270.

145. J.L. Zimmerman, R. Williams, V.N. Khabashesku, J.L. Margrave. Synthesis of spherical carbon nitride nanostructures, *Nano Lett.,* **2001**, 1, 731–734.

146. H. Montigaud, B. Tanguy, G. Demazeau, I. Alves, M. Birot, J. Dunogues. Solvothermal synthesis of the graphitic form of C_3N_4 as macroscopic sample. *Diamond Relat. Mater.,* **1999**, 8, 1707–1710.

147. C-B. Cao, Q. Lv, H-S. Zhu. Carbon nitride prepared by solvothermal method, *Diamond Relat. Mater.,* **2003,** 12, 1070–1074.

148. Q. Lv, C. Cao, C. Li, J. Zhang, H. Zhu, X. Kong, X. Duan. Formation of crystalline carbon nitride powder by a mild solvothermal method, *J. Mater. Chem.*, **2003**, 13, 1241–1243.

149. C. Cao, F. Huang, C. Cao, J. Li, H. Zhu. Synthesis of carbon nitride nanotubes via a catalytic-assembly solvothermal route, *Chem. Mater.*, **2004**, 16, 5213–5215.

150. S. Dyjak, W. Kiciński, A. Huczko. Thermite-driven melamine condensation to $C_xN_yH_z$ graphitic ternary polymers: Towards an instant, large-scale synthesis of g-C_3N_4, *J. Mater. Chem. A*, **2015**, 3, 9621–9631.

151. Y. Wang, Y. Di, M. Antonietti, H. Li, X. Chen, X. Wang. Excellent visible-light photocatalysis of fluorinated polymeric carbon nitride solids, *Chem. Mater.*, **2010**, 22, 5119–5121.

152. S.C. Yan, Z.S. Li, Z.G. Zou. Photodegradation of Rhodamine B and Methyl Orange over boron-doped g-C_3N_4 under visible light irradiation, *Langmuir*, **2010**, 26, 3894–3901.

153. Y. Zhang, T, Mori, J. Ye, M. Antonietti. Phosphorus-doped carbon nitride solid: Enhanced electrical conductivity and photocurrent generation, *J. Am. Chem. Soc.*, **2010**, 132, 6294–6295.

154. J. Zhang, X. Chen, K. Takanabe, K. Maeda, K. Domen, J.D. Epping, X. Fu, M. Antonietti, X. Wang. Synthesis of a carbon nitride structure for visible-light catalysis by copolymerization, *Angew. Chem. Int. Ed.,* **2010**, 49, 441–444.

155. X. Li, G. Hartley, A.J. Ward, P.A. Young, A.F. Masters, T. Maschmeyer. Hydrogenated defects in graphitic carbon nitride nanosheets for improved photocatalytic hydrogen evolution, *J. Phys. Chem. C*, **2015**, 119, 14938–14946.

156. Y. Zhang, A. Thomas, M. Antonietti, X. Wang. Activation of carbon nitride solids by protonation: Morphology changes, enhanced ionic conductivity, and photoconduction experiments, *J. Am. Chem. Soc.*, **2009**, 131, 50–51.

157. X.C. Wang, K. Maeda, X.F. Chen, K. Takanabe, K. Domen, Y.D. Hou, X.Z. Fu, M. Antonietti. Polymer semiconductors for artificial photosynthesis: Hydrogen evolution by mesoporous graphitic carbon nitride with visible light, *J. Am. Chem. Soc.*, **2009**, 131, 1680–1681.

158. K. Wang, Q. Li, B. Liu, B. Cheng, W. Ho, J. Yu. Sulfur-doped g-C_3N_4 with enhanced photocatalytic CO_2-reduction performance, *Appl. Catal. B: Environ.,* **2015**, 176–177, 44–52.

159. Z. Yang, Y. Zhang, Z. Schnepp. Soft and hard templating of graphitic carbon nitride, *J. Mater. Chem. A*, **2015**, 3, 14081–14092.

160. Y. Wang, X. Wang, M. Antonietti, Y. Zhang. Facile one-pot synthesis of nanoporous carbon nitride solids by using soft templates, *ChemSusChem*, **2010**, 3, 435–439.

161. H. Yan. Soft-templating synthesis of mesoporous graphitic carbon nitride with enhanced photocatalytic H_2 evolution under visible light, *Chem. Comm.*, **2012**, 48, 3430–3432.

162. J.P. Paraknowitsch, J. Zhang, D. Su, A. Thomas, M. Antonietti. Ionic liquids as precursors for nitrogen-doped graphitic carbon, *Adv. Mater.,* **2010**, 22, 87–92.

163. A. Vinu, K. Ariga, T. Mori, T. Nakanishi, S. Hishita, D. Golberg, Y. Bando. Preparation and characterization of well-ordered hexagonal mesoporous carbon nitride, *Adv. Mater.,* **2005**, 17, 1648–1652.

164. X. Chen, Y. S. Jun, K. Takanabe, K. Maeda, K. Domen, X. Fu, M. Antonietti, X. Wang. Ordered mesoporous SBA-15 type graphitic carbon nitride: A semiconductor host structure for photocatalytic hydrogen evolution with visible light, *Chem. Mater.,* **2009**, 21, 4093–4095.

165. Y.S. Jun, W.H. Hong, M. Antonietti, A. Thomas. Mesoporous, 2D hexagonal carbon nitride and titanium nitride/carbon composites, *Adv. Mater.,* **2009**, 21, 4270–4274.

166. M. Groenewolt, M. Antonietti. Synthesis of g-C_3N_4 nanoparticles in mesoporous silica host matrices, *Adv. Mater.,* **2005**, 17, 1789–1792.

167. C.D. Liang, K.L. Hong, G.A. Guiochon, J.W. Mays, S. Dai. Synthesis of a large-scale highly ordered porous carbon films by self-assembly of block copolymers, *Angew. Chem., Int. Ed.,* **2004**, 43, 5785–5789.

168. A. Thomas, F. Goettmann, M. Antonietti. Hard templates for soft materials: Creating nanostructured organic materials, *Chem. Mater.*, **2008**, 20, 738–755.

169. X.-H. Li, J. Zhang, X. Chen, A. Fischer, A. Thomas, M. Antonietti, X. Wang. Condensed graphitic carbon nitride nanorods by nanoconfinement: Promotion of crystallinity on photocatalytic conversion, *Chem. Mater.*, **2011**, 23, 4344–4348.

170. J. Liu, H. Wang, M. Antonietti. Graphitic carbon nitride "reloaded": Emerging applications beyond (photo)catalysis, *Chem. Soc. Rev.,* **2016**, 45, 2308–2326.

171. Y. Zhang, Q. Pan, G. Chai, M. Liang, G. Dong, Q. Zhang, J. Qiu. Synthesis and luminescence mechanism of multicolor-emitting g-C_3N_4 nanopowders by low temperature thermal condensation of melamine, *Scientific Reports,* **2013**, 3, 1943.

172. E.Z. Lee, Y.S. Jun, W.H. Hong, A. Thomas, M.M. Jin. Cubic mesoporous graphitic carbon(IV) nitride: An all- in- one chemosensor for selective optical sensing of metal ions, *Angew. Chem., Int. Ed.,* **2010**, 49, 9706–9710.

173. S. Zhang, J. Li, M. Zeng, J. Xu, X. Wang, W. Hu, *Nanoscale*, **2014**, 6, 4157–4162.

174. T.Y. Ma, Y. Tang, S. Dai, S.Z. Qiao. Proton- functionalized two- dimensional graphitic carbon nitride nanosheet: An excellent metal- /label- free biosensing platform, *Small*, **2014**, 10, 2382–2389.

175. M. Rong, L. Lin, X. Song, Y. Wang, Y. Zhong, J. Yan, Y. Feng, X. Zeng, X. Chen. Fluorescence sensing of chromium(VI) and ascorbic acid using graphitic carbon nitride nanosheets as a fluorescent switch, *Biosens. Bioelectron.,* **2015**, 68, 210–217.

176. Y. Tang, H. Song, Y. Su, Y. Lv. Turn-on persistent luminescence probe based on graphitic carbon nitride for imaging detection of biothiols in biological fluids, *Anal. Chem.,* **2013**, 85, 11876–11884.

177. X. Zhang, X. Xie, H. Wang, J. Zhang, B. Pan, Y. Xie. Enhanced photoresponsive ultrathin graphitic-phase C_3N_4 nanosheets for bioimaging, *J. Am. Chem. Soc.*, **2012**, 135, 18–21.

178. X. Jin, V.V. Balasubramanian, S.T. Selvan, D.P. Sawant, M.A. Chari, G.Q. Lu, A. Vinu. Highly ordered mesoporous carbon nitride nanoparticles with high nitrogen content: A metal-free basic catalyst, *Angew. Chem.,* **2009**, 121, 8024 –8027.

179. X. Wang, K. Maeda, A. Thomas, K. Takanabe, G. Xin, J.M. Carlsson, K. Domen, M. Antonietti. A metal-free polymeric photocatalyst for hydrogen production from water under visible light, *Nature Mater.*, **2009**, 8, 76–80.

180. F.M. Bautista, J.M. Campelo, D. Luna, J. Luque, J.M. Marinas. Influence of the acid–base/redox properties of TiO_x-sepiolite supported vanadium oxide catalysts in the gas-phase selective oxidation of toluene, *Catal. Today*, **2006**, 112, 28–32.

181. L. Kesavan, R. Tiruvalam, M.H Ab Rahim, M.I. bin Saiman, D.I. Enache, R.L. Jenkins, N. Dimitratos, J.A. López-Sánchez, S.H. Taylor, D.W. Knight, C.J. Kiely, G.J. Hutchings. Solvent-free oxidation of primary carbon-hydrogen bonds in toluene using Au-Pd alloy nanoparticles, *Science*, **2011**, 331, 195–199.

182. N. Dimitratos, J.A. López-Sánchez, G.J. Hutchings. Selective liquid phase oxidation with supported metal nanoparticles, *Chem. Sci.*, **2012**, 3, 20–44.

183. N.A. Noureldin, D.G. Lee. Selective oxidation of unsaturated alcohols by potassium permanganate adsorbed on solid supports, *Tetrahedron Lett.,* **1981**, 22, 4889–4890.

184. S. Ghosh-Mukerji, H. Haick, M. Schvartzman, Y. Paz. Selective photocatalysis by means of molecular recognition, *J. Am. Chem. Soc.*, **2001**, 123, 10776−10777.

185. S. Ghosh-Mukerji, H. Haick, Y. Paz. Controlled mass transport as an means for obtaining selective photocatalysis, *J. Photochem. Photobiol. A,* **2003**, 160, 77−85.

186. S. Higashimoto, N. Kitao, N. Yoshida, T. Sakura, M. Azuma, H. Ohue, Y. Sakata. Selective photocatalytic oxidation of benzyl alcohol and its derivatives into corresponding aldehydes by molecular oxygen on titanium dioxide under visible light irradiation, *J. Catal.*, **2009**, 266, 279–285.

187. C-J. Lia, G-R. Xua, B. Zhanga, J.R. Gong. High selectivity in visible-light-driven partial photocatalytic oxidation of benzyl alcohol into benzaldehyde over single-crystalline rutile TiO_2 nanorods, *Appl. Catal. B: Environ.*, **2012,** 115–116, 201–208.

188. T.D. Giacco, M. Ranchella, C. Rol, G.V. Sebastiani. Photo-oxidation of some benzylic alcohols sensitized by colloidal TiO_2 in CH_3CN. A kinetic mechanistic study through quantum yield determinations, *J. Org. Phys. Chem.*, **2000**, 13, 745–751.

189. M. Zhang, Q. Wang, C. Chen, L. Zang, W. Ma, J. Zhao. Oxygen atom transfer in the photocatalytic oxidation of alcohols by TiO_2: Oxygen isotope studies, *Angew. Chem.*, **2009**, 121, 6197–6200.

190. X. Lang, H. Ji, C. Chen, W. Ma, J. Zhao. Selective formation of imines by aerobic photocatalytic oxidation of amines on TiO_2, *Angew. Chem. Int. Ed.*, **2011**, 50, 3934–3937.

191. X. Lang, W. Ma, Y. Zhao, C. Chen, H. Ji, J. Zhao. Visible-light-induced selective photocatalytic aerobic oxidation of amines into imines on TiO_2, *Chem. Eur. J.*, **2012**, 18, 2624–2631.

192. M-Q. Yang, Y. Zhang, N. Zhang, Z-R. Tang, Y-J. Xu. Visible-light-driven oxidation of primary C–H bonds over CdS with dual Co-catalysts graphene and TiO_2, *Scientific Reports*, **2013**, 3, 3314.

193. X. Li, G. Chen, Y. Po-Lock, C. Kutal. Photocatalytic oxidation of cyclohexane over TiO₂ nanoparticles by molecular oxygen under mild conditions, *J. Chem. Technol. Biotechnol.*, **2003**, 78, 1246–1251.

194. H. Park, W. Choi. Photocatalytic conversion of benzene to phenol using modified TiO₂ and polyoxometalates, *Catal. Today,* **2005**, 101, 291–297.

195. M. Zhang, Q. Wang, C. Chen, L. Zhang, W. Ma, J. Zhao. Oxygen atom transfer in the photocatalytic oxidation of alcohols by TiO₂: Oxygen isotope studies, *Angew. Chem. Int. Ed.*, **2009**, 48, 6081–6084.

196. Q. Wang, M. Zhang, C. Chen, W. Ma, J. Zhao. Photocatalytic aerobic oxidation of alcohols on TiO₂: The acceleration effect of a Bronsted acid, *Angew. Chem. Int. Ed.,* **2010**, 49, 7976–7979.

197. D. Spasiano, L.P.P Rodríguez, J.C. Olleros, S. Malato, R. Marotta, R. Andreozzi. TiO₂/Cu(II) photocatalytic production of benzaldehyde from benzyl alcohol in solar pilot plant reactor, *Appl. Catal. B: Environ.*, **2013**, 136–137, 56–63.

198. V. Augugliaro, H. Kisch, V. Loddo, M.J. López-Muñoz, C. Márquez-Álvarez, G. Palmisano, L. Palmisano, F. Parrino, S. Yurdakal. Photocatalytic oxidation of aromatic alcohols to aldehydes in aqueous suspension of home-prepared titanium dioxide: 1. Selectivity enhancement by aliphatic alcohols, *Appl. Catal. A: General,* **2008**, 349, 182–188.

199. L. Palmisano, V. Augugliaro, M. Bellardita, A. Di Paola, E. García-López, V. Loddo, G. Marcì, G. Palmisano, S. Yurdakal. Titania photocatalysts for selective oxidations in water, *ChemSusChem*, **2011**, 4, 1431–1438.

200. S. Yurdakal, V. Loddo, G. Palmisano, V. Augugliaro, H. Berber, L. Palmisano. Kinetics of 4-methoxybenzyl alcohol oxidation in aqueous solution in a fixed bed photocatalytic reactor, *Ind. Eng. Chem. Res.*, **2010**, 49, 6699−6708.

201. S. Yurdakal, G. Palmisano, V. Loddo, O. Alagöz, V. Augugliaro, L. Palmisano. Selective photocatalytic oxidation of 4-substituted aromatic alcohols in water with rutile TiO₂ prepared at room temperature, *Green Chem.*, **2009**, 11, 510−516.

202. S. Yurdakal, G. Palmisano, V. Loddo, V. Augugliaro, L. Palmisano. Nanostructured rutile TiO_2 for selective photocatalytic oxidation of aromatic alcohols to aldehydes in water, *J. Am. Chem. Soc.*, **2008**, 130, 1568−1569.

203. V. Augugliaro, H. Kisch, V. Loddo, M.J. López-Muñoz, C. Maŕquez-Álvarez, G. Palmisano, L. Palmisano, F. Parrino, S. Yurdakal. Photocatalytic oxidation of aromatic alcohols to aldehydes in aqueous suspension of home prepared titanium dioxide 2. Intrinsic and surface features of catalysts, *Appl. Catal. A: General*, **2008**, 349, 189−197.

204. V. Augugliaro, V. Loddo, M.J. López-Muñoz, C. Maŕquez-Álvarez, G. Palmisano, L. Palmisano, S. Yurdakal. Home-prepared anatase, rutile, and brookite TiO_2 for selective photocatalytic oxidation of 4-methoxybenzyl alcohol in water: Reactivity and ATR-FTIR study, *Photochem. Photobiol. Sci.* **2009**, 8, 663−669.

205. C. Anderson, A.J. Bard. An improved photocatalyst of TiO_2/SiO_2 prepared by a sol-gel synthesis, *J. Phys. Chem.*, **1995**, 99, 9882–9885.

206. Y.R. Do, W. Lee, K. Dwight, A. Wold. The effect of WO_3 on the photocatalytic activity of TiO_2, *J. Solid State Chem.*, **1994**, 108, 198–201.

207. J. Papp, S. Soled, K. Dwight, A. Wold. Surface acidity and photocatalytic activity of TiO_2, WO_3/TiO_2, and MoO_3/TiO_2 photocatalysts, *Chem. Mater.*, **1994**, 6, 496–500.

208. Y.T. Kwon, K.Y. Song, W.I. Lee, G.J. Choi, Y.R. Do. Photocatalytic behavior of WO_3-loaded TiO_2 in an oxidation reaction, *J. Catal.*, **2000**, 191, 192–199.

209. D. Tsukamoto, M. Ikeda, Y. Shiraishi, T. Hara, N. Ichikuni, S. Tanaka, T. Hirai. Selective photocatalytic oxidation of alcohols to aldehydes in water by TiO_2 partially coated with WO_3, *Chem.-Eur. J.*, **2011**, 17, 9816–9824.

210. F. Su, S.C. Mathew, L. Möhlmann, M. Antonietti, X. Wang, S. Blechert. Aerobic oxidative coupling of amines by carbon nitride photocatalysis with visible light, *Angew. Chem. Int. Ed.*, **2011**, 50, 657–660.

211. V. Augugliaro, M. Bellardita, V. Loddo, G. Palmisano, L. Palmisano, S. Yurdakal. Overview of oxidation mechanisms of organic compounds by TiO_2 in heterogeneous photocatalysis, *Photochem. Photobiol. C: Photochem. Rev.*, **2012**, 13, 224–245.

212. Y. Kofuji, Y. Isobe, Y. Shiraishi, H. Sakamoto, S. Tanaka, S. Ichikawa, T. Hirai. Carbon nitride−aromatic diimide−graphene nanohybrids: Metal-free photocatalysts

for solar-to-hydrogen peroxide energy conversion with 0.2% efficiency, *J. Am. Chem. Soc.,* **2016**, 138, 10019−10025.

213. Y. Shiraishi, S. Kanazawa, Y. Kofuji, H. Sakamoto, S. Ichikawa, S. Tanaka, T. Hirai. Sunlight-driven hydrogen peroxide production from water and molecular oxygen by metal-free photocatalysts, *Angew. Chem. Int. Ed.,* **2014**, 53, 13454–13459.

214. M.J. Lima, P.B. Tavares, A.M.T. Silva, C.G. Silva, J.L. Faria. Selective photocatalytic oxidation of benzyl alcohol to benzaldehydeby using metal-loaded g-C$_3$N$_4$ photocatalysts, *Catal. Today,* **2017**, 10.1016/j.cattod.2016.11.023.

215. B. Long, Z. Ding, X. Wang. Carbon nitride for the selective oxidation of aromatic alcohols in water under visible light, *ChemSusChem*, **2013**, 6, 2074–2078.

216. J.C. Colmenares, R. Luque. Heterogeneous photocatalytic nanomaterials: Prospects and challenges in selective transformations of biomass-derived compounds, *Chem. Soc. Rev.*, **2014**, 43, 765–778.

217. Biomass Sugars for Non-Fuel Applications, 1st Ed. Eds.: D. Murzin, O. Simakova. RSC, Cambridge, **2016**.

218. A.S. Amarasekara, D. Green, L.D. Williams. Renewable resources based polymers: Synthesis and characterization of 2,5-diformylfuran-urea resin, *Eur. Polym. J.*, **2009**, 45, 595–598.

219. Z. Hui, A. Gandini. Polymeric schiff bases bearing furan moieties, *Eur. Polym. J.*, **1992**, 28, 1461–1469.

220. Y. Kanetaka, S. Yamazaki, K. Kimura. Preparation of poly(ether ketone)s derived from 2,5-furandicarboxylic acid by polymerization in ionic liquid, *Macromol.,* **2016**, 49, 1252–1258.

221. T.S.A. Heugebaert, C.V. Stevens, C.O. Kappe. Singlet-oxygen oxidation of 5-hydroxymethylfurfural in continuous flow, *ChemSusChem.*, **2015**, 8, 1648–1651.

222. B. Liu, Y. Ren, Z. Zhang. Aerobic oxidation of 5-hydroxymethylfurfural into 2,5-furandicarboxylic acid in water under mild conditions, *Green Chem.*, **2015**, 17, 1610–1617.

223. J. Ma, Z. Du, J. Xu, Q. Chu, Y. Pang. Efficient aerobic oxidation of 5-hydroxymethylfurfural to 2,5-diformylfuran, and synthesis of a fluorescent material, *ChemSusChem.*, **2011**, 4, 51–54.

224. C. Carlini, P. Patrono, A.M.R. Galletti, G. Sbrana, V. Zima. Selective oxidation of 5-hydroxymethyl-2-furaldehyde to furan-2,5-dicarboxaldehyde by catalytic systems based on vanadyl phosphate, *Appl. Catal. A: General,* **2005**, 289, 197–204.

225. S. Yurdakal, B.S. Tek, O. Alagoz, V. Augugliaro, V. Loddo, G. Palmisano, L. Palmisano. Photocatalytic selective oxidation of 5-(hydroxymethyl)-2-furaldehyde to 2,5-furandicarbaldehyde in water by using anatase, rutile, and brookite TiO_2 nanoparticles, *ACS Sust. Chem. Eng.*, **2013**, 1, 456–461.

226. M. Ilkaeva, I. Krivtsov, V. Avdin, S. Khainakov, J.R. García. Comparative study of structural features and thermal behavior of mixed silica-titania xerogels prepared *via* the peroxo method the conventional co-precipitation technique, *Colloid. Surface. A: Physicochem. Eng. Aspects.,* **2014**, 456, 120–128.

227. V. Etacheri, M.K. Seery, S.J. Hinder and S.C. Pillai. Oxygen rich titania: A dopant free, high temperature stable, and visible-light active anatase photocatalyst, *Adv. Funct. Mater.,* **2011**, 21, 3744–3752.

228. Y.W. Zhang, J.H. Liu, G. Wu, W. Chen. Porous graphitic carbon nitride synthesized via direct polymerization of urea for efficient sunlight-driven photocatalytic hydrogen production, *Nanoscale*, **2012**, 4, 5300–5303.

229. P. Niu, L. Zhang, G. Liu, H.M. Cheng. Graphene-like carbon nitride nanosheets for improved photocatalytic activities, *Adv. Funct. Mater.,* **2012**, 22, 4763–4770.

230. G.R. Castro. Optical design of the general-purpose Spanish X-ray beamline for absorption and diffraction, *J. Synchrotron Rad.*, **1998**, 5, 657–660.

231. B. Ravel, M. Newville. ATHENA, ARTEMIS, HEPHAESTUS: Data analysis for X-ray absorption spectroscopy using IFEFFIT, *J. Synchrotron Rad.*, **2005**, 12, 537–541.

232. L. Tröger, D. Arvanitis, K. Baberschke, H. Michaelis, U. Grimm, E, Zschech. Full correction of the self-absorption in soft-fluorescence extended X-ray absorption fine structure, *Phys. Rev. B.*, **1992**, 46, 3283–3289.

233. W. Stober, A. Fink, E. Bohn. Controlled growth of monodisperse silica spheres in the micron size range, *J. Colloid Interface Sci.*, **1968**, 26, 62–69.

234. K.J.C. van Bommel, J.H. Jung, S. Shinkai. Poly(L-lisine) aggregates as templates for the formation of hollow silica spheres, *Adv. Mater.,* **2001**, 13, 1472–1476.

235. S. Kamaruddin, D. Stephan, The preparation of silica–titania core–shell particles and their impact as an alternative material to pure nano-titania photocatalysts, *Catal. Today*, **2011**, 161, 53–58.

236. X. Li, J. He. Synthesis of raspberry-like SiO_2–TiO_2 nanoparticles toward antireflective and self-cleaning coatings, *ACS Appl. Mater. Interfaces*, **2013**, 5, 5282–5290.

237. T. Leshuk, S. Linley, G. Baxter, F. Gu. Mesoporous hollow sphere titanium dioxide photocatalysts through hydrothermal silica etching, *ACS Appl. Mater. Interfaces*, **2012**, 4, 6062−6070.

238. Y. Ren, Y. Zhang, L. Wu. Fabrication of rattle-type TiO_2/SiO_2 core/shell particles with both high photoactivity and UV-shielding property, *Langmuir*, **2010**, 26, 11391–11396.

239. G.N. Shao, Y. Kim, S.M. Imran, S.J. Jeon, P.B. Sarawade, A. Hilonga, J-K. Kim, H.T. Kim. Enhancement of porosity of sodium silicate and titanium oxychloride based TiO_2–SiO_2 systems synthesized by sol–gel process and their photocatalytic activity, *Micropor. Mesopor. Mater.*, **2013**, 179, 111–121.